PHD

An analysis of high power stripline structures

Burchett, M. H.

Award date:
1994

Awarding institution:
University of Bath

An Analysis of High Power Stripline Structures

Submitted by M.H. Burchett
for the Degree of PhD.
of the University of Bath
1994

M.H.Burchett

ProQuest LLC
789 East Eisenhower Parkway
P.O. Box 1346
Ann Arbor, MI 48106-1346

Summary

This thesis presents a rigorous and efficient analysis of high power stripline structures of arbitrary dimensions. The analysis has been developed to improve the design of medium power beamforming networks that are commonly found in air surveillance radar antennas.

The thesis provides a review of electromagnetic analysis techniques and existing stripline analyses. The Transverse Resonance Diffraction (TRD) technique is introduced and developed in terms of a y-parameter network representation for coupled striplines, with the uniform line derived as a limiting case. The analysis yields a matrix equation in terms of a set of unknown fields in the structure. The equation is solved using Galerkin's method with the unknown fields discretised using basis functions that model the singularities present on the edge of the striplines.

Results have been computed for the cut-off frequency, impedance and attenuation factor for uniform and coupled stripline structures, and are compared to existing CAD packages, conformal mapping techniques and finite element analyses. The results illustrate improved accuracy over conformal mapping analyses, and comparable accuracy with numerical techniques, but achieved with a much reduced computation time and memory requirement.

Measured results are also presented for the cut-off frequency of uniform and coupled striplines and show excellent agreement with results computed using the TRD method and Hewlett Packard's High Frequency Structure Simulator (HFSS).

A generalised analysis of stripline discontinuities has also been developed. The analysis uses propagation constants and mode impedances calculated using the TRD method to compute the scattering parameters of discontinuities using a field matching method. The expressions for the uniform to coupled lines transition are evaluated as an example.

Acknowledgements

I would like to extend my thanks to Dr. Steve Pennock and Dr. Peter Shepherd for their helpful guidance as supervisors and their many valuable suggestions that have done much to enhance my research efforts.

Thanks must also go to past and present postgraduates and staff in the department for their interest and many useful conversations during the course of the research.

I would also like to express my gratitude to Dr. Jon Whitehurst for his supervision and support during my work at Siemens-Plessey Systems and the opportunity to use the High Frequency Structure Simulator (HFSS). I must also thank the other members of the Microwave Techniques Group at Siemens for their interest in the research and useful discussions, which have made my placements there both enjoyable and productive.

The research was undertaken under the Science and Engineering Research Council CASE programme in conjunction with Siemens-Plessey Systems and I am also indebted to both of these institutions for their financial support.

Publications Arising from the Work

1. *A Rigorous Analysis of the Higher Order Modes and Attenuation of Stripline of Arbitrary Dimensions*
   M.H. Burchett, S.R. Pennock, P.R. Shepherd
   Proc. IEEE MTT Symposium, Atlanta,
   June 1993, p1454 - p1456

2. *An Accurate Analysis of Coupled Striplines of Arbitrary Dimensions*
   M.H. Burchett, S.R. Pennock, P.R. Shepherd
   Proc. 23rd European Microwave Conference, Madrid,
   September 1993, p659 - p661

3. *A Rigorous Analysis of Uniform Stripline of Arbitrary Dimensions*
   M.H. Burchett, S.R. Pennock, P.R. Shepherd
   IEEE Transactions on Microwave Theory and Techniques,
   Vol. MTT-41, December 1993, p2074 - p2080

4. *A Rigorous Analysis of the Higher Order Modes, Impedance and Attenuation Factor of Coupled Striplines*
   M.H. Burchett, S.R. Pennock, P.R. Shepherd
   IEE Proceedings Part H.
   Vol. 141, No. 3, June 1994, p167 - p174

5. *An Improved Equivalent Circuit Representation of Stripline Step in Width Discontinuities*
   M.H. Burchett, C. Spillard, S.R. Pennock, P.R. Shepherd
   Proc. 24th European Microwave Conference, Cannes,
   Accepted for Publication.

Abbreviations

BEM	Boundary Element Method
CAD	Computer Aided Design
FD	Finite Difference
FD-TD	Finite Difference Time Domain
FE	Finite Elements
GTEM	GigaHertz Transverse Electro-Magnetic
HFSS	High Frequency Structure Simulator
IE	Integral Equation
MMIC	Monolithic Microwave Integrated Circuit
MMM	Mode Matching Method
MOM	Method of Moments
SDM	Spectral Domain Method
TE	Transverse Electric
TEM	Transverse Electro-Magnetic
TM	Transverse Magnetic
TRD	Transverse Resonance Diffraction
TRT	Transverse Resonance Technique
VLSI	Very Large Scale Integration

Glossary of Terms

A	Constant
A_k	Incident Wave Amplitude, Mode k
$A_k^{A,B}$	Orthonormalisation Coefficient, Mode k
$A_n^{R_i}$	Orthonormalisation Coefficient for Vector Potential, Sub-Region i, Mode n
A_p	Orthonormalisation Coefficient for Basis Function, Order p
b_i	Upper Airgap Spacing, Conductor i
B_k	Reflected Wave Amplitude, Mode k
C	Coupling between Striplines
$C_p^{\nu}(x)$	Gegenbauer Polynomial, Order p, Singularity ν
C_{pq}	Admittance Matrix Constant
$C_{\psi}^{R_i}$	Constant, Sub-Region i
d_i	Lower Airgap Spacing, Conductor i
e	Euler's Constant
e_{tk}	Transverse Electric Field, Mode k
e_x	$\hat{x}$ Directed Electric Field
e_y	$\hat{y}$ Directed Electric Field
$e_{xk}^{R_i}$	$\hat{x}$ Directed Electric Field, Sub-Region i, Mode k
$e_{yk}^{R_i}$	$\hat{y}$ Directed Electric Field, Sub-Region i, Mode k
$e_{zk}^{R_i}$	$\hat{z}$ Directed Electric Field, Sub-Region i, Mode k
E_{xkn}	$\hat{x}$ Directed Electric Field Amplitude, Field Expansion Mode n, Mode k
E_{ykn}	$\hat{y}$ Directed Electric Field Amplitude, Field Expansion Mode n, Mode k
f	Frequency
$f_p(x,y)$	Basis Function, Order p
F_i	Admittance Matrix Frequency Dependent Function
$F(x,\nu)$	Orthogonal Basis Function, Singularity ν
${}_nF_m\ (a_n; b_m; z)$	Hyper-Geometrical Function
f_{err}	Error Function for generalised Laguerre Polynomial
h	Stripline Ground Plane Spacing
h_{tk}	Transverse Magnetic Field, Mode k

h_x	$\hat{x}$ Directed Magnetic Field
h_y	$\hat{y}$ Directed Magnetic Field
$h_{xk}^{R_i}$	$\hat{x}$ Directed Magnetic Field, Sub-Region i, Mode k
$h_{yk}^{R_i}$	$\hat{y}$ Directed Magnetic Field, Sub-Region i, Mode k
$h_{zk}^{R_i}$	$\hat{z}$ Directed Magnetic Field, Sub-Region i, Mode k
H_{zkn}	$\hat{z}$ Directed Magnetic Field Amplitude, Field Expansion Mode n, Mode k
H_{pl}	Magnetic Field Amplitude Term, Basis Function p, Mode l
i	Summation Variable
I_n	Current Amplitude, Mode n
j	Square Root of -1
$J_p(x)$	Bessel Function, Order p
$\mathcal{J}(p,q,\psi)$	Admittance Matrix Frequency Independent Function
k	Mode Number
k_o	Free Space Wavenumber
k_t	Transverse Wavenumber
$k_x^{R_i}$	$\hat{x}$ Directed Wavenumber, Sub-Region i
$k_y^{R_i}$	$\hat{y}$ Directed Wavenumber, Sub-Region i
K	Total Number of Modes
K_i	Total Number of Modes, Region i
l	Mode Number
L	Arbitrary Length
$L_p^{\chi}(x)$	Generalised Laguerre Function, Order p, Singularity χ
m	Summation Variable
M	Number of Striplines in Analysed Structure
$\hat{n}$	Unit Normal Vector
n	Field Expansion Mode Number
N	Total Number of Field Expansion Modes -1
p	Basis Function Number
P	Total Number of Basis Functions -1
$P_p^{\nu,\eta}(x)$	Jacobi Polynomial, Order p, Singularities ν and η
P_{dis}	Power Dissipated in Structure
P_{flow}	Power Flow in Structure
$P_{pn(x)}$	$\hat{x}$ Directed Inner Product, Basis Function p, Field Expansion Mode n

$P_{pn(y)}$	$\hat{y}$ Directed Inner Product, Basis Function p, Field Expansion Mode n
$P_{pn}^{R_i}$	Inner Product, Basis Function p, Field Expansion Term, n
	Sub-Region, i
Q	Quality Factor
r	Radial Distance
R_i	Sub-Region Number i
R_s	Surface Resistance
s	Stripline Spacing
s_k	Constant, Mode k
S_{kl}	Scattering Parameter between Mode l and Mode k
t_i	Stripline Thickness, Conductor i
$T_p(x)$	Chebyshev Polynomial, Order p
$u_k(n,x,y)$	Field Shape Function, Mode k
U_{kn}	Field Amplitude Term, Field Expansion Mode n, Mode k
V^+	Forward Travelling Voltage Amplitude
V_n	Voltage Amplitude, Mode n
$V_{xkn}^{R_i}$	Voltage Amplitude, Field Expansion Mode n, Sub-Region i, Mode k
w_i	Stripline Width, Conductor i
$W(x,\nu)$	Weight Function for Orthogonal Basis Function , Singularity ν
x_o	Constant
X_{pk}	Basis Function Amplitude, Basis Function Order p, Mode k
y_o	Constant
y_{ij}	Greens Function y Parameter Admittance Operator
Y_{ij}	Y Parameter Admittance Matrix
Y_{ok}	Wave Admittance
$\mathcal{Y}(n)$	Mode Admittance, Mode n
Z_o	Characteristic Impedance
Z_{ck}	Mode Impedance, Mode k
Z_{ok}	Wave Impedance, Mode k
Z_{pi}	Power-Current Impedance
Z_{pv}	Power-Voltage Impedance
Z_{vi}	Voltage-Current Impedance
Z_{pq}	Impedance Matrix Element

$Z(x, x', y, y')$	Green's Function Impedance Operator
Z_L	Load Impedance
x,y,z	Cartesian Coordinates

Symbols

α	Attenuation Factor
α_c	Conductor Attenuation Factor
α_d	Dielectric Attenuation Factor
α_n	Normalised Attenuation Factor
β_k	Propagation Constant, Mode k
β_y	$\hat{y}$ Directed Propagation Constant.
δ	Material Loss
δ_n	Orthonormalisation Coefficient Delta Function, Mode n
$\delta_{k,l}$	Delta Function
δ_s	Skin Depth
Δ	RMS Surface Roughness
ϵ_o	Free Space Permittivity
ϵ_r	Relative Permittivity
λ	Eigenvalue
μ_o	Free Space Permeability
ρ	Reflection Coefficient
$\phi_{hk}^{R_i}$	Magnetic Scalar Potential for Sub-Region i, Mode k
$\phi_{ek}^{R_i}$	Electric Scalar Potential for Sub-Region i, Mode k
Ψ	Laguerre Polynomial Convergence Constant
ψ	Dimensional Constant
ω	Angular Frequency
σ	Conductivity
θ	Arbitrary Angle
χ	Laguerre Polynomial Singularity Order
ν	Basis Function Singularity Order
η	Basis Function Singularity Order

ε	Constant
φ	Constant
ϱ	Constant
ϑ	Constant

Operators

$\bullet$	Convolution
∂_x	Partial Derivative with respect to x
∂_y	Partial Derivative with respect to y
$\nabla_t \phi$	Gradient of ϕ with respect to x and y
$\nabla_z \phi$	Gradient of ϕ with respect to z
$\wedge$	Cross Product

Notation

$[A]$	Matrix Quantity, A
$\underline{A}$	Vector Quantity, A
$< \phi_h \ ; \ f(x) >$	Inner Product between Functions, ϕ_h and $f(x)$

Contents

Chapter 1

Introduction

1.1 Outline

This chapter provides background information on the stripline structure and its application to beamforming networks, and the motivation behind the research work. The chapter concludes with an outline of the work contained in the thesis.

1.2 Stripline and Related Structures

Historically, the term "stripline" has referred to structures where the signal conductor is separated from the ground plane by a dielectric. This encompasses the structures shown in Figure 1.1, which were referred to as micro-stripline (Figure 1.1(a)) and tri-plate stripline (Figure 1.1(b)), but have been abbreviated to microstrip and stripline respectively. Boxed stripline or rectangular co-axial line is shown in Figure 1.1(c) and is an important class of stripline structure. A simplifying assumption in many analyses is to increase the aspect ratio of the outer co-axial conductor, such that the side walls do not significantly interact with the stripline fields. The co-axial line structure can therefore be used to approximate the open tri-plate stripline structure. The rectangular co-axial line was one of the first structures to be analysed using Finite Difference

techniques.

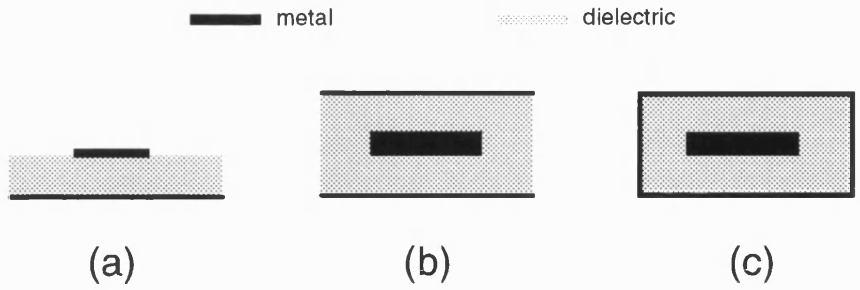

Figure 1.1: Microstrip (a), Stripline (b) and Rectangular Co-axial Line (c) Structures

The analysis of stripline structures has generated particular interest since it finds many applications. The interconnections in high speed printed circuit systems and MMIC's are essentially based on stripline structures where the conductor widths are a small fraction of the wavelength of operation ($1 \times 10^{-5}\lambda$ to $1 \times 10^{-3}\lambda$). Another application of stripline structures is in antenna beamforming networks at medium power levels ($< 4.5kW$ peak).

Beamforming networks connect a central antenna feed point to a number of radiating elements. Power splitting networks and line lengths are used to achieve a particular amplitude and phase variation across the set of radiating elements. The stripline structures used in these networks use central conductor widths of between 0.1λ to 0.4λ, and are typically air filled with the central conductor supported along its length by a number of dielectric blocks. The central conductor is not embedded in a dielectric for reasons of cost, weight and power dissipation. The central conductor and ground planes are normally manufactured from brass, although in some cases aluminium ground planes are used with a copper central conductor to reduce weight, but without increasing the overall power dissipation. The stripline used in these beamforming networks has a central conductor thickness which is an appreciable proportion of the ground plane spacing. The thickness of the central conductor is a compromise between weight, and cooling and ease of manufacture. In practice, most production systems use a standard thickness of brass plate (60 thousandths of an inch). This compares to stripline in MMIC structures,

and microstrip where the central conductor typically has a negligible thickness.

The power handling capability of these networks is specified as a peak power rating and a mean power rating. The peak power rating is set by the dielectric breakdown voltage, and the mean power rating is set by the allowable temperature rise of the central conductor. The mean power rating normally dictates the limit on the system operating power since high conductor temperatures cause problems with dielectric components in the network.

These limitations constrain the stripline to medium power operation, with high power networks being realised using waveguide. Low power networks are normally fabricated using printed circuit techniques (microstrip or stripline) for reasons of cost. Rectangular co-axial line is also used in medium power beamforming networks where the priority is for a compact network. The stripline network relies on the parallel arms of the network being spaced a sufficient distance apart such that no coupling, or crosstalk occurs. The rectangular co-axial structure enables parallel arms of the network to be more closely spaced, with the penalty of increased weight and power dissipation in the side walls between striplines.

1.3 Design of Beamforming Networks

The beampattern from an array of antenna elements consists of a summation of responses from each of the individual elements. The amplitude variation across the array weights this summation, and the phase variation controls the angle of the main lobe. Figure 1.2 shows the beampattern produced by a uniformly weighted linear array at broadside, i.e. perpendicular to the axis of the array.

The weighting of the array elements determines the 3dB beamwidth of the main lobe and the sidelobe level, and can be altered to optimise either of these parameters. The calculations assume that there are no gain and phase errors across the elements, or their feed network. In practice, phase errors produce a noise floor in the response and the gain errors degrade the main lobe gain. The design of the beamforming network is therefore critical to the performance of a sensor system. The optimum system performance is

achieved when the allowable gain and phase errors produce a noise floor equal to the sidelobe level. This often produces a very stringent specification on the phase and gain variations across a beamforming network, typically of the order of $\pm 5^o$ and $\pm$ 0.5dB for networks with lengths approaching 15λ. This requirement dictates a very accurate analysis of the elements in the beamforming network.

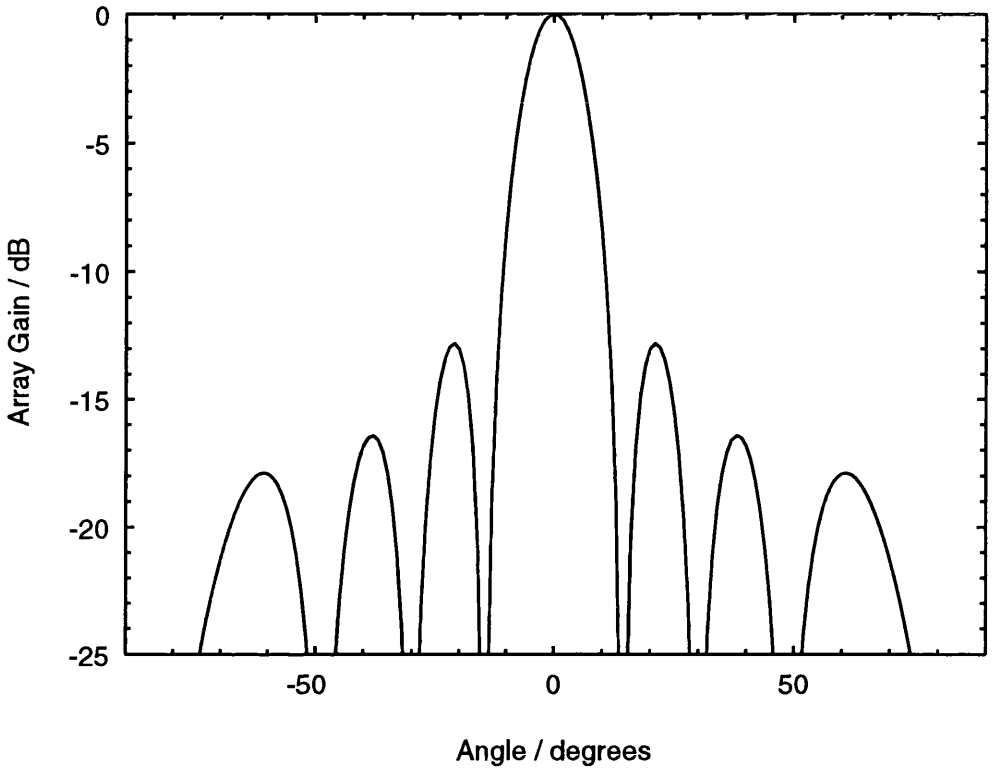

Figure 1.2: Beampattern of an Eight Element Array with Uniform Weighting for a Beam at 90^o to the Plane of the Array (Broadside)

The design of beamforming networks has traditionally been carried out using approximate design rules programmed into a CAD system, which produces a metallisation pattern that is machined, assembled and tested, with the results being used in the next iteration of the design. This process frequently can take up to nine iterations to produce a network with a correct response and is extremely inefficient in terms of development time and cost. Advances in manufacturing techniques and the use of common interfaces between CAD packages and computer controlled cutting machines has reduced the time

required to manufacture the networks. However, the greatest scope for improvement is in the development of accurate and efficient circuit models for inclusion into the CAD system. This would allow the network to be optimised and manufactured with the desired response met after very few iterations.

The current design of these networks has concentrated on a standard thickness of stripline supported symmetrically between ground planes. The principle design variable has been the width, and hence impedance of the stripline elements. The advent of an accurate and efficient means of analysing stripline enables the effects of manufacturing tolerances in the stripline dimensions to be ascertained. The design parameters of striplines with novel dimensional ratios can also be computed. Both of these calculations provide useful background information for the stripline designer.

The design parameters of greatest interest are the impedance and attenuation factor of the stripline. The networks are designed to operate as a monomode structure. An accurate calculation of the monomode bandwidth is therefore also required to check that higher order modes do not propagate on wide sections of stripline, such as the input of a power splitting network.

The principle elements that require modelling in a beamforming network are: uniform and coupled lines; uniform to coupled line transitions; uniform line step in widths; power splitters and mitred bends. The work described in this thesis considers the analysis of the first three elements with the notation used to describe the stripline dimensions shown in Figure 1.3.

1.4 Outline of the Thesis

This chapter has provided background information into the various types of stripline structure. The stripline used in medium power beamforming networks has also been described with a discussion of the design process and the motivation behind an accurate analysis of the structure.

The second chapter provides an overview of electromagnetic analysis techniques that have been used to analyse stripline structures, and their limitations and assumptions.

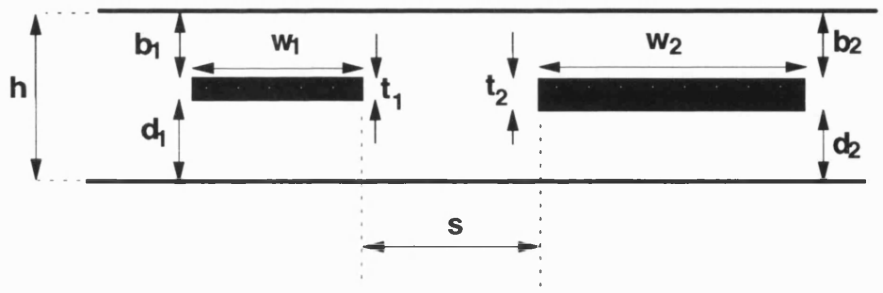

Figure 1.3: Definition of Stripline Dimensions

A review of the research work that has previously been undertaken to characterise the uniform and coupled stripline structures and stripline discontinuities is also given. The Transverse Resonance Diffraction (TRD) method is introduced and the choice of this method is discussed against the requirements of an accurate and efficient analysis technique.

The third chapter provides a detailed derivation of the TRD method applied to both uniform and coupled stripline structures, and illustrates the methods employed to produce a computationally efficient analysis. The extension of the technique to analyse any number of coupled striplines of arbitrary dimensions is also described. The practical aspects of solving the resulting equations are discussed in addition to means of expressing the determinant as a closed form expression. The parameters that are used to characterise the stripline structure are also defined and derived in terms of the computed fields.

Chapters four and five verify the TRD theory by comparison to a number of purely analytical and purely numerical techniques such as conformal mapping and finite element techniques. The comparison is primarily concerned with the relative accuracies of the methods. Typical computational times and memory requirements are also given to enable an assessment of the relative efficiencies of the methods. Measured results are also presented to verify the results computed by the TRD method. The results presented in these chapters are related, wherever possible, to the dimensions that are

used in practical circuits, and therefore provide an immediate source of information for stripline designers.

The sixth chapter utilises the TRD results computed for uniform and coupled lines as a basis for computing the scattering parameters of a number of stripline discontinuities. The technique again illustrates how a-priori information concerning the field singularity behaviour can provide a compact analysis. The limitations of the method in terms of its stability are also briefly discussed.

The thesis is concluded by a summary of the research work and an overview of results of particular interest. Future areas of research are also identified and discussed with respect to the TRD analysis and other methods of analysis.

An appendix is provided as a source of background information on the Hewlett Packard HP85180A High Frequency Structure Simulator (HFSS). The HFSS package has been used extensively as a means of verifying the TRD results and also as an example of a current commercial electromagnetic simulator. A number of appendices are also provided for the derivation mathematical expressions required in the evaluation of the uniform and coupled lines analysis and the stripline discontinuity analysis.

Chapter 2

Analyses of Stripline Structures

2.1 Outline

In this chapter various methods that have been used to analyse stripline and other passive microwave devices are briefly described. A review of published work on the analysis of uniform and coupled striplines, and stripline discontinuities is also presented. The chapter concludes with a description of the Transverse Resonance Diffraction (TRD) technique as an introduction to the theory derived in Chapter 3.

2.2 Review of Analysis Techniques

There are a large number of techniques available for the analysis of passive microwave components and a number of authors have provided reviews of the various methods [1, 2, 3, 4]. Many of the methods share common features, and are specific cases of a more general method e.g Boundary Element Method (BEM), or an extension of another method e.g. Spectral Domain Method (SDM). The majority of techniques use a combination of methods in order to analyse a structure e.g. Transverse Resonance Diffraction (TRD) technique.

The choice of an appropriate method depends on the accuracy required, the computer

power available, the amount of analytical pre-processing needed, and the generality of the analysis. For the purposes of this review, the methods are broadly classified as those techniques requiring little or no analytical pre-processing; those requiring analytical pre-processing; and techniques that require virtually no numeric processing.

2.2.1 Predominantly Numerical Techniques

Finite Difference (FD) methods and Finite Element (FE) methods can be categorised as predominantly numerical techniques, along with the Boundary Element Method (BEM). The small amount of pre-processing makes these methods ideal candidates for commercial electromagnetic analysis packages. Hewlett Packard's HP85180A High Frequency Structure Simulator (HFSS) is based on Finite Elements and is described further in Appendix A. Sonnet Software's EM Package is based on the Boundary Element Method. The disadvantages of these techniques are the computational requirement to run these packages, and the time taken to compute the results. This will be discussed in greater depth for HFSS in Chapters 4 and 5, where comparisons will be made with other methods. The generality of these methods is excellent with the HFSS FE software able to compute the field solution for arbitrary 3D structures. The BEM is currently applied commercially to structures that comprise of an arbitrary conductor pattern in the direction of propagation but the cross section consisting of layered media and conductor metallisations (planar 3D).

Finite Difference (FD) Method

The Finite Difference (FD) method requires no analytical pre-processing and is the oldest of the numerical methods. The structure is sub-divided into a regular mesh or grid (Figure 2.1(a)) and the derivative terms in Maxwell's equations are replaced by a Taylor Series expansion in terms of the potentials which are stored on the sides or vertices of the grid. This effectively transforms the problem into a set of linear equations in the unknown potential. The method is relatively inefficient due to the large number of grid points and hence the large order of the matrices, which contain mainly zeroes apart from a set of elements around the leading diagonal. The solutions are therefore

found using iterative techniques as opposed to matrix inversion techniques. A further limitation of the technique is that the mesh points must lie on the boundaries of the problem hence curved or irregular shaped structures require a large number of grid points. In addition, structures with field singularities also require a finely spaced grid to accurately model the rapid rate of change of the field. In order to decrease the matrix size, hence storage requirement, the graded mesh technique is used where the grid spacing is decreased only around the singularities. The efficiency of the FD method is also often improved by formulating the problem using variational expressions.

The finite difference technique has also been used to discretise the time derivative form of Maxwell's equations, termed Finite Difference Time Domain (FD-TD). This technique requires greater storage since a set of time steps are stored for the structure, hence the technique becomes feasible only with the increase in available computer storage and processing power. The overall time response of the structure can be converted into a frequency response by taking the Fourier transform, the cell dimensions limiting the range of the frequency data.

Finite Element (FE) Method

The finite element method [4, 5] differs from the finite difference technique in that the problem is cast in terms of a functional that has variational properties, i.e. for the correct solution a first order displacement produces a second order error. The structure is subdivided into polygons, normally triangular or rectangular elements for 2D problems and tetrahedra for 3D problems (Figure 2.1(b)) which are able to accurately model irregular shaped boundaries.

The functional is evaluated assuming an approximate solution, u_e for each element as a weighted sum of functions, g_p^e:

$$u_e = \sum_{p=0}^{p=P} X_p^e \, g_p^e \tag{2.1}$$

In the methods of moments, the problem is then solved for the unknown parameters, X_p for the structure, hence u_e. In the case of finite elements, a variable transformation is

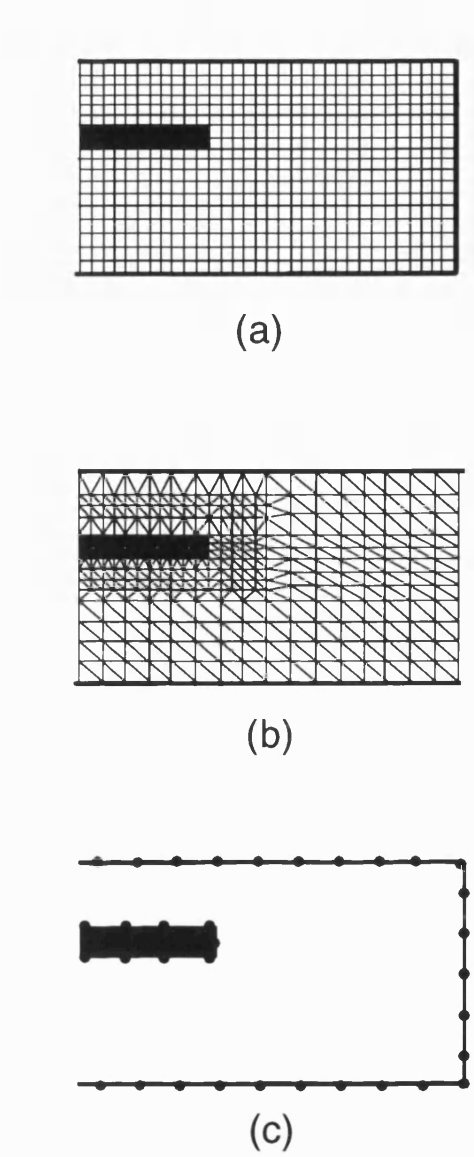

Figure 2.1: Meshes Generated by the Finite Difference (FD) Method (a); the Finite Element (FE) Method (b); and the Boundary Element Method (BEM) (c) for a Rectangular Stripline Structure

used to express the unknown function at the N nodes of the element, e. This essentially produces a set of N equations $\{u_{e,N}\}$ in P unknowns. This requires that P $\leq$ N, hence the number of nodes determines the order of the function, g_p^e. In this manner, convergence of the solution is achieved by increasing the number of elements used to discretise the structure, as opposed to increasing the order of the basis functions, P.

The finite element technique is readily suited to arbitrary structures with defined boundaries i.e. rectangular co-ax. Structures that are open in one dimension i.e. stripline have to be modelled in the cross section either by placing an electric wall at a sufficient distance, or using a system of "infinite elements". The former approach is the simplest but least efficient since the computation time is proportional to the cross sectional area which may be unnecessarily large. The infinite element approach sub-divides the cross section into a near field region and a far field region. The near field region is discretised as before, whereas the far field region is modelled by infinite elements parallel to the ground planes and with nodes defined on the boundary of near and far fields. These elements model the far field behaviour as a dipole field with dependence $\mid r \mid^{-1}$.

The existence of field singularities in the structure will also require many first order elements to model the rapid field change accurately. This problem has been circumvented by the introduction of singular elements. These elements introduce a scaling factor such that there is no longer a linear variation in potential between the singular node and the remaining two nodes of the triangle.

A further problem of finite elements are spurious modes, or numerical solutions that do not correspond to physical modes. These spurious modes are normally suppressed by incorporating Maxwell's divergence relations into the governing expressions derived from the curl relations.

Boundary Element Method (BEM)

The Boundary Element Method (BEM) can be shown to be a general case of the finite element method. Both techniques can be described as weighted residual techniques [4, 6] which are a general means of solving equations involving linear operators.

Stating the weighted residual expression [6] for Laplace's equation ($\nabla^2 u$) in domain Ω; with essential boundary conditions, $u = \bar{u}$ on contour C_1; and $q = \frac{\partial u}{\partial n} = \bar{q}$ on contour C_2; with weighting function, w:

$$\int_{\Omega} (\nabla^2 u)\ w d\Omega = \int_{C_1} (\bar{u} - u) \frac{\partial w}{\partial n}\ dC_1 + \int_{C_2} (q - \bar{q}) w\ dC_2 \tag{2.2}$$

The solution process for a number of methods can be described using the expression above. In the case of finite elements, the essential boundary conditions are satisfied i.e. $u = \bar{u}$ leaving a residual due to the approximation of u and a natural boundary condition term, thus the problem is cast in terms of the domain Ω and the contour C_2. However, it can be shown [6] that if a weighting function is used such that $\nabla^2 w = 0$, the problem is cast in terms of the essential and natural boundary conditions along the contour $C = C_1 + C_2$ which encloses domain Ω. Thus the substitution reduces the dimension of the problem by one. The resulting problem is therefore solved by sub-dividing the boundary of structure into discrete elements (Figure 2.1(c)) and solved using techniques similar to those described for finite elements.

A third possibility also arises from Equation 2.2, that both the essential and natural boundary conditions are satisfied, in this case setting the weighting function, w equal to the Dirac function specifying a point, i in domain Ω, Equation 2.2 becomes:

$$\int_{\Omega} (\nabla^2 u) \Delta_i\ d\Omega = 0 \tag{2.3}$$

The above expression is the general form of the Finite Difference method.

The main advantage of the BEM is that it requires less storage and processing due to the reduction in the number of dimensions of the problem. The method is therefore popular as a basis for commercial software e.g. Sonnet Software's EM package.

2.2.2 Analytical / Numerical Techniques

Techniques that require a degree of analytical pre-processing and numerical evaluation fall into this category. They are not widely used in commercial analysis packages since they do not have the generality of the predominantly numerical techniques.

Method of Moments (MOM)

The techniques of finite elements, finite differences and boundary elements are all linked by the weighted residual expression (Equation 2.2) by satisfying a combination of requirements. The method of moments is formulated from the weighted residual expression with the essential boundary conditions met. Stating the approximation for the unknown function as a summation of basis functions, f_p and amplitudes, X_p:

$$u = \sum_{p=1}^{p=P} X_p f_p \tag{2.4}$$

In the general case if f_p and the weighting function, w are different, the method is termed the Rayleigh-Ritz method; if f_p and w are identical the method is referred to as Galerkin's method. A further set of methods can then be defined by appropriate choice of the basis and weighting functions. The method of moments is widely used in conjunction with integral equation formulations. Hewlett Packard has recently introduced the Momentum Package based on MOM techniques [7].

Integral Equation (IE) and Spectral Domain (SD) Methods

The Integral Equation Method is a means of casting a problem such that a known field quantity i.e. the field at a boundary is linked to the unknown parameter by means of an integral operator. These techniques require the use of Green's Functions. A Green's Function is a function that expresses a relationship between a quantity at an observation point and a unity source. The derivation of an appropriate Green's Function can require a large amount of analytical pre-processing, after which the integral equation can be solved directly. An alternative method is to incorporate the integral equation into a variational expression.

A related technique to the Integral Equation method is the Spectral Domain Method (SDM) where the integral equation is transformed from the spatial to the spectral domain using a Fourier transform. The problem is frequently cast using a Green's function linking the electric field to the current density on the strip. The Green's function for the problem is derived by transforming the scalar potentials used to describe the fields,

using basis functions $\exp -j\beta_z z$ in the direction of propagation, and $\exp -j\beta_x x$ in the transverse direction. This yields a Fourier transformed vector Helmholtz equation as a partial differential equation in the y direction which can be solved by inspection to give expressions for the transformed fields.

The analysis is restricted to structures with infinitely thin central conductors such as microstrip embedded in a layered dielectric. The benefit of this approach is that the reduction of the problem by one dimension reduces the computation time.

Mode Matching Method (MMM)

The Mode Matching Method is a well established method applied to problems where an interface exists between two regions which contain different field shapes such as a waveguide, or stripline discontinuity. The fields are expressed on both sides of the interface as a summation of mode shapes with unknown amplitudes. A matrix expression for the amplitude terms can be found by utilising mode orthogonality and enforcing field continuity. These techniques can also be used in conjunction with generalised scattering matrix methods to analyse cascaded discontinuities.

Transverse Resonance Technique (TRT)

This technique is effectively the mode matching method applied in a direction transverse to the direction of propagation. The technique is therefore well suited to analysing structures like waveguides with transverse discontinuities. The mode matching method requires that the structure has a closed cross section, therefore electric walls are placed at set positions in the $\hat{z}$ direction. The technique does however require a knowledge of the propagation in the longitudinal direction of analysis i.e. transverse to the direction of propagation in the structure.

2.2.3 Predominantly Analytical Techniques

The previous sections have concentrated on methods that require an amount of numerical processing, with the benefit of being applicable to a wide range of structures.

An equally important set of techniques enable a closed form expression for the parameters of a structure to be derived using purely analytical techniques. These methods provide a closed form expression for the parameters that can be programmed into a CAD system and used for circuit optimisation. At the crudest level, this involves curve fitting to measured results to provide a database of known results which can then be interpolated. A more analytical technique is conformal mapping and will be described, since this technique is most commonly used to provide closed form expressions for CAD systems such as EEsof's Linecalc and Academy, and SuperCompact.

Conformal Mapping

The conformal mapping analysis essentially transforms the structure in one plane to a structure in another by means of a single, or a series of mathematical transforms. The parameters of the transformed structure are known as an exact expression in terms of the functions used in the mapping.

Figure 2.2 illustrates the conformal mapping transformations used by Bates [8] to calculate the impedance of finite thickness stripline which transforms the upper half of the stripline structure to a pair of co-axial cylinders.

Ideally, the expression for the impedance in the Q plane could be formulated as a function of the dimensions in the Z plane ($Z \rightarrow Q$). This assumes that the transforms $Z \rightarrow P$, $P \rightarrow S$ and $S \rightarrow Q$ are defined. For the case shown only the transforms $P \rightarrow Z$, $P \leftrightarrow S$ and $Q \rightarrow S$ are defined. Analytical inversion is therefore required to define the transforms $Z \rightarrow P$ and $S \rightarrow Q$, or alternatively, the inverse problem can be solved ($Q \rightarrow Z$). The inverse problem expresses the dimensions of the Z plane in terms of the impedance in the Q plane, yielding a synthesis expression for lines of a given impedance. This was the route chosen by Bates.

The transform $P \rightarrow Z$ is a Schwartz-Christoffel transformation [9] and transforms the points of the real axis of the P plane to a polygon in the Z plane, and yields an

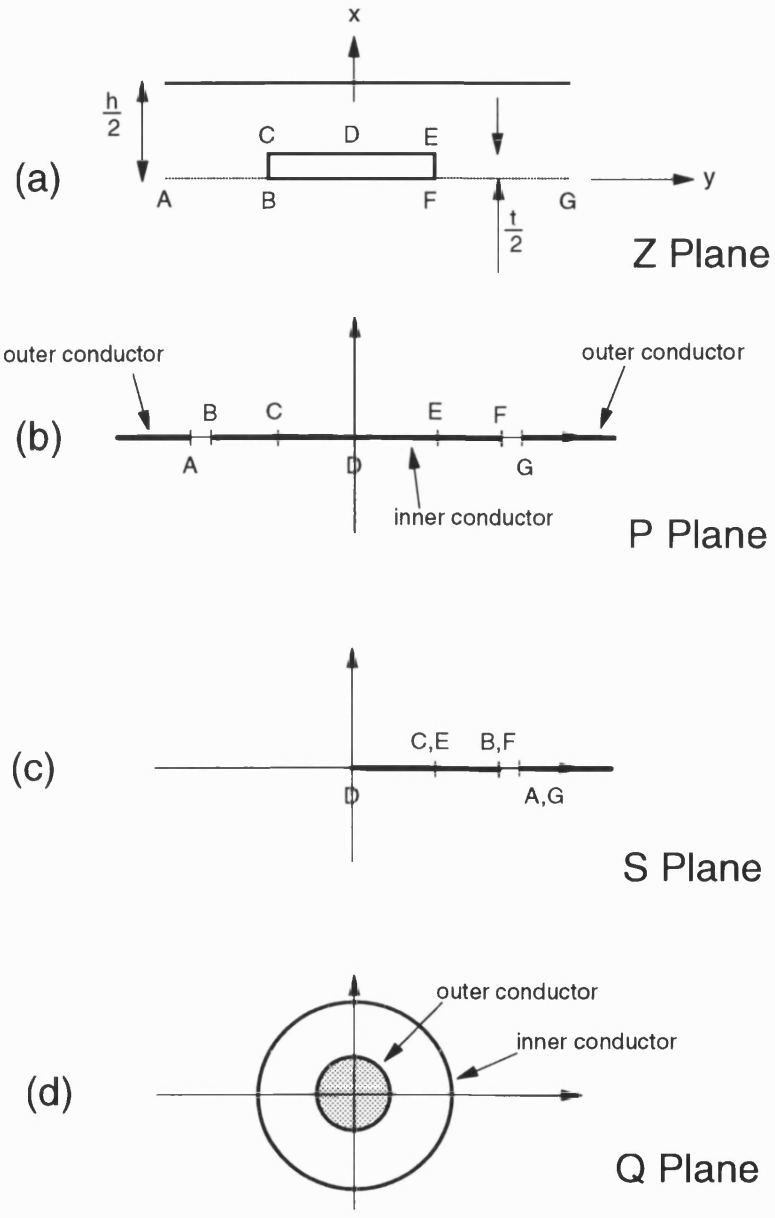

Figure 2.2: Conformal Mapping used in Analysis of Uniform Symmetrical Stripline

expression of the form [8]:

$$\frac{dz}{dp} = \frac{(1-p^2)^{\frac{1}{2}}}{(1-\xi_1^2 p^2)^{\frac{1}{2}}\,(1-\xi_2^2 p^2)} \tag{2.5}$$

where ξ_1 and ξ_2 are constants which depend on the geometry of the structure. The function on the right hand side requires integration which presents a further problem, since the integral must have an analytic form to provide a closed form expression for the impedance. In order to provide a practical expression the analytical form must be easily and accurately evaluated. This often leads to the analytical form being approximated and the closed form expressions limited to a restricted range of dimensions. These approximations can then be extended using curve fitting techniques.

Recently, numerical inversion of the Schwartz-Christoffel transform has been presented for arbitrary structures [10]. This enables the inverse transform $Z \rightarrow P$ and the standard transform $P \rightarrow Z'$ to be performed. This maps a polygon in the Z plane to another in the Z' plane whose parameters are known, via an arbitrary structure in the P plane.

Expressions from conformal mapping techniques can also be used in other analytical techniques such as the equivalent waveguide model technique [4] which is used for analysing discontinuities in terms of waveguides of equivalent cross section. This technique was first introduced as a means of calculating the cut-off frequencies of the higher order modes in stripline [11].

2.3 Analysis of Uniform Stripline

The first application of stripline, or flat strip transmission line was in antenna beamformers produced in the early 1940's [12]. The basic design information was not made widely available at the time. It was a number of years until further interest in flat strip transmission line, and the related microstrip structures, prompted research to be carried out into accurately evaluating the design parameters such as impedance and attenuation factor.

A number of researchers studied the problem of evaluating the impedance of stripline in the early fifties, and a special issue of the IEEE Transactions on Microwave Theory and Techniques in March 1955 presents a selection of their work. One of the most widely cited papers from this issue was written by Cohn [13]. This paper introduced a previously derived exact formula for the impedance of an infinitely thin stripline, and closed form expressions for the finite thickness stripline were developed from earlier work [14]. The finite thickness stripline expressions were developed for both wide ($\frac{w:b}{1-t:b} > 0.35$) and narrow ($\frac{w:b}{1-t:b} < 0.35$) striplines. The narrow strip expression was derived by approximating the rectangular conductor as a circular conductor of equivalent diameter and utilising a known expression for the impedance of a wire above a ground plane. The wide strip case was analysed using conformal mapping to provide a value of the fringing capacitance of a strip between infinite ground planes. Both expressions are limited to a strip thickness of less than a quarter of the ground plane spacing. Cohn also calculated the attenuation factor of stripline based on Wheeler's incremental inductance rule [15] which states the attenuation factor of a line is proportional to the ratio of the increase in line inductance to the decrease in dimension. The expression for the attenuation factors are again limited to a specific range of dimensions, and provide an overestimate of nominally ten percent since the edge singularities are not modelled accurately [13].

Finite thickness stripline was later analysed [8] to provide a set of equations for the synthesis of stripline i.e. expressions for the width and thickness of stripline in terms of the impedance. The analysis was based on conformal mapping using the Schwartz-Christoffel transformation [9] and the resulting integral evaluated in terms of elliptic functions. The expressions derived are exact but rely on tabulated values of the elliptic functions, or the relationships later given by Hilberg [16], however they cannot be analytically inverted to produce closed form formulae. The expressions were numerically inverted [17] to yield analysis data.

A very similar approach to the mapping used by Bates has also been used to calculate the attenuation factor of stripline [18] using a quasi-static formula for the attenuation factor. The approach evaluates the attenuation factor for a given impedance, hence provides synthesis information and analytically extracts the singularity of $\mid r^{-\frac{1}{2}} \mid$ at the corners of the stripline. This approach however is likely to result in errors as the

thickness of the strip becomes appreciable and the singularity behaviour approaches $| r^{-\frac{1}{3}} |$ [19]. The majority of the power flow in the structure occurs around the edges of the stripline, hence the evaluation around the singularities will strongly affect the results.

The benefit of having a closed form expression for the impedance and attenuation factor resulted in a number of authors providing expressions eliminating the need to use tabulated values of elliptic integrals [16], or providing further approximations to Cohn's analysis for a range of dimensions [20]. Research was also carried out into rectangular co-axial structures using conformal mapping [21, 22] resulting in similar equations to Cohn's.

An alternative approach was taken by Wheeler [23] to calculate the impedance and attenuation factor of finite thickness stripline. The structure was approximated as an infinitely thin stripline with an effective width correction to take account of the fringing fields. The previous application of this technique was for the calculation of the higher order mode cut-off frequencies [11]. Oliner's width correction only took into account the effect of the fringing fields as a function of the width of the stripline. Wheeler's formula further corrected the width of the stripline to take into account the thickness of the stripline, and resulted in a closed form expression for impedance that is quoted as having an accuracy of ± 0.5 percent [24], across a wide range of dimensional ratios. The incremental inductance rule can also be applied to obtain relationships for the attenuation factor of stripline. A number of expressions derived from Wheeler's work have also been presented [25].

The conformal mapping representations that have been described assume that the stripline is symmetrically placed between the ground planes. The impedance of asymmetrically placed striplines have also been studied with infinitely thin central conductors [26], and finite thickness conductors [27, 28]. Robrish's work provides a wider range of applicable dimensions than [27] and is an extension of Cohn's original conformal mapping representation [13]. In addition to modifying the conformal mapping the range of validity is improved by using curve fitting techniques.

Alternatively, the impedance of asymmetrically placed striplines can be calculated by

considering the impedance as the parallel addition of impedances due to a symmetrical stripline of ground plane spacing t+2b and one of ground plane spacing t+2d [29]. More recently the technique of the Numerical Inversion of the Schwartz Christoffel transform has been presented and applied to asymmetrical stripline [30].

The conformal mapping techniques were first developed due to a lack of adequate computing power available for more numerical, or rigorous approaches, and are governed by the assumption of monomode operation of the stripline. The conformal mapping techniques developed later are intended to provide accurate closed form expressions for the modelling of MIC interconnects using CAD systems [24, 31]. A further application of the infinitely thin symmetrical stripline is in the verification of electromagnetic simulators since the expressions stated are exact [32].

The first numerical technique to analyse stripline was the Finite Difference Method, approximately a decade after the first conformal mapping expressions were produced. The rectangular co-axial structure was one of the first structures to be analysed using this technique [33, 34, 35] since it is a closed structure supporting TEM propagation and can be easily discretised using a grid. A variational form of Finite Differences was also formulated to provide upper and lower bounds on the characteristic impedance [36] and therefore place error bounds on the earlier analyses.

Finite Element analysis has only comparatively recently been applied to stripline structures. Pantic and Mittra [37] analysed a set of Quasi-TEM structures using finite elements with infinite elements to model the propagation in the transverse direction of stripline, and also employed singular elements to model the fields at the corners of the stripline. The Finite Element approach has also been used to model stripline structures where the skin depth is a significant proportion of the strip thickness [38]. This problem has also been studied using an Integral Equation Technique [39] in order to characterise the attenuation factor in VLSI circuits.

The analyses presented have all assumed that the stripline is operating within its monomode range. The higher order mode cut-off frequencies were first investigated using an equivalent waveguide model with an effective width taking into account the fringing capacitance [11]. Finite element analysis has been applied to characterise the

monomode bandwidth of stripline using a rectangular co-axial structure approximation computed by Hewlett Packard's HFSS package [40]. More recently, algorithms which model the transverse wave propagation as an exponential decay have been used [41].

2.4 Analysis of Coupled Stripline

The analysis of coupled striplines has followed approximately the same path as that for uniform stripline. The first structures to be analysed were stripline that were symmetrically positioned between ground planes and had symmetrical strip widths. The physical symmetry of the problem enables half the structure to be analysed with an electric wall in the symmetry plane for odd mode excitation and a magnetic wall in the symmetry plane for even mode excitation. Cohn modified his paper [13] and provided exact expression for infinitely thin lines and approximate expressions for finite thickness lines [42]. The expressions however were only valid for strips with $\frac{w:b}{1-t:b} > 0.35$. The expressions for infinitely thin lines were later simplified by the use of closed form approximations for the elliptic integrals [16]. Getsinger [43] later provided synthesis equations for finite thickness stripline and modified the formulae to take into account fringing field interaction.

The assumption of physical symmetry provided severe limitations on the range of structures that could be analysed. Conformal mapping was therefore applied to infinitely thin stripline with equal widths, but positioned asymmetrically between ground planes (Figure 2.3) [44]. Shelton's analysis was formulated for tight coupling ($w_o < w$) and loose coupling ($w_o > w$). The analysis is limited to a range of dimensional ratios and provides synthesis information, although the expressions were later inverted to provide analysis equations [45].

Shelton's analysis provided results for offset striplines, however the characteristic impedances of the strips were still equal due to rotational symmetry about the centre of the structure. This enabled conventional even and odd mode analysis to be applied. The general case of couplers with unequal line impedances was investigated by Cristal [46], and later Tripathi [47]. Tripathi formalised the general case of lateral (C

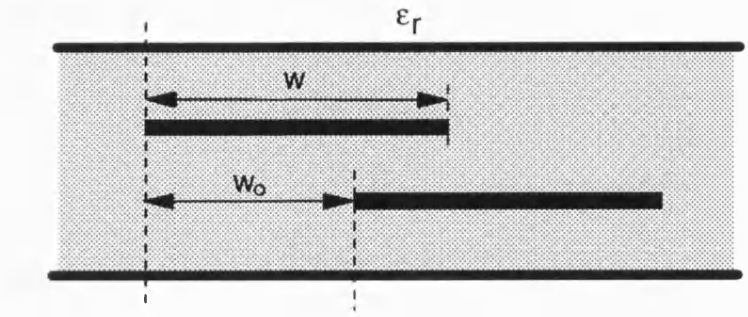

Figure 2.3: Asymmetrical Coupled Stripline Structure Analysed by Shelton

mode) excitation and diagonal (Π mode) excitation, which degenerate to even and odd mode excitations respectively for couplers with equal impedance striplines.

Multi-conductor lines of arbitrary width, but zero thickness and symmetrically placed between ground planes has been studied using conformal mapping techniques [48], providing results in terms of an impedance matrix relating the capacitance between strips. Synthesis information can then be derived using optimisation techniques.

Linner's analysis [48] provides a generalised, hence complex analysis of striplines, a more amenable approach was provided by Bedair [49] who sub-divided the capacitance of a general pair of coupled striplines of zero thickness into components modelling the fringing and parallel plate capacitances and a further component to take account of the capacitance due to the excitation (C or Π). These capacitances are then related to the known expressions for the capacitances of a symmetrical stripline.

A similar technique was used to calculate the coupling and impedances for finite thickness striplines [50]. The method differed in that the capacitances were evaluated directly from modified forms of expressions given in [42, 43]. This method however is again limited to symmetrical placement between the ground planes. In addition, expressions for the attenuation factor were also derived using the incremental inductance

rule [15].

The author is unaware of a general analysis to compute the coupling of any number of entirely arbitrarily dimensioned and positioned striplines. A number of analyses do exist however for infinitely thin striplines of arbitrary width and position in layered dielectric media, since these conductor configurations are commonly found in MMIC's. These analyses are formulated using an integral equation variational expression for the capacitance [51, 52, 53]. In addition the problem has also been approached using Spectral Domain analysis [54] and also a technique where the structure is conformally mapped and a variational technique employed on the transformed structure [55]. These techniques all rely on an estimate of the behaviour of the charge on the strip and assume a singularity of the order $| r^{-\frac{1}{2}} |$. A finite thickness integral equation technique has been presented [39] however this is limited to solving for the complex propagation constant.

Coupled striplines have also been analysed using purely numerical techniques. A finite difference approach was used by Gupta [56] which investigated means of improving the computational time of the method by the use of extrapolation and the use of graded meshes.

The generality of finite elements has meant that the coupled stripline structure can be readily analysed by algorithms used for uniform lines [37, 38, 40, 41] to provide coupling values and also higher order mode cut-off frequency information which has not been derived using predominantly analytical techniques.

2.5 Analysis of Stripline Discontinuities

The number of papers characterising stripline discontinuities is extremely limited. In part this is due to the complexity of modelling such structures and also the limited application of stripline elements. The majority of the discontinuity work has been concentrated on the microstrip structure [57]. The analysis of MMIC structures has mainly been restricted to computing the impedance of lines accurately and to quantify the coupling between lines to minimise crosstalk, as opposed to providing accurate circuit models for elements.

The first paper to characterise stripline discontinuities was presented by Oliner [11] with a second paper by Altschuler providing measured results [58]. Oliner's paper provided equivalent circuits for a number of symmetrical discontinuities in striplines of zero thickness conductors, and form the basis of the majority of models used in CAD systems [24, 31].

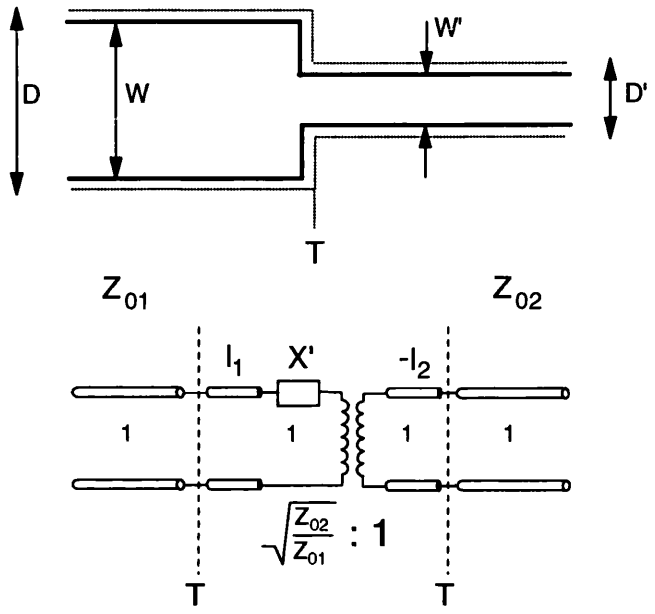

Figure 2.4: Symmetrical Step in Width Discontinuity and Equivalent Circuit

The discontinuities of interest in this work are the uniform and coupled line step in widths and the uniform to coupled line transition. The uniform line step in width analysis [11] calculated the effective widths of the stripline structure (D and D') and used Babinet's Principle to model the discontinuity as a parallel plate waveguide with a step in height of the ground planes (Figure 2.4). The waveguide structure has the property of a capacitive iris, hence the equivalent circuit of the stripline presents a series inductance, in addition to the impedance transformation. There is also a shift in the plane of the discontinuity by an amount equivalent to the increase in effective width of the stripline due to the fringing fields($\frac{D-W}{2}$). Altschuler's paper provided inconclusive experimental data to verify the equations derived for the inductance and line extension, and concluded since they were small they could be neglected, and the discontinuity

modelled by a single impedance transformation.

Altschuler extended the analysis to a single to coupled lines discontinuity by assuming that it could also be modelled simply by an impedance transformation. Babinet's Principle could also be applied to this discontinuity, and transformed into a finite thickness waveguide bifurcation, however no publications were found on the analysis of this discontinuity.

A more detailed study into the step in width discontinuity has been carried out [59] with some additional measurements and investigation into means of reducing the series reactance.

To the authors knowledge, no analyses exist for the unbalanced discontinuities, or discontinuities in finite thickness stripline.

2.6 Transverse Resonance Diffraction (TRD) Technique

The Transverse Resonance Diffraction (TRD) Technique is an Integral Equation technique formulated transverse to the direction of propagation in the structure. Equivalent circuits for the propagation in the transverse direction are found and solved using techniques which utilise knowledge about the singularities present in the cross section. The technique has been applied to a number of structures such as Inset Dielectric Guide (IDG) [60, 61]; the GTEM cell [62] and slotline [63] all of which have well defined interfaces with fields which exhibit singularity behaviour.

Stripline structures also fall into the above category and the TRD method was chosen since the technique yields accurate and compact expressions for the structure parameters, enabling the algorithms to be programmed on a desktop computer. The main benefit over the majority of existing stripline analyses is that the method is not restricted to TEM propagation. This enables higher order mode behaviour to be investigated and subsequently extended to provide an efficient and accurate analysis of stripline discontinuities. The method is also valid for striplines of arbitrary dimensions hence the sensitivity of the design parameters to dimensional variations can also be investigated.

The following sections provide a brief outline of the TRD method as an introduction to the theory described in Chapters 3 and 6.

2.6.1 TRD Technique Applied to Uniform and Coupled Lines

The uniform and coupled lines problem is solved by sub-dividing the structure into stripline and parallel plate regions (Figure 2.5). The fields on either side of the interfaces are derived using scalar potential functions. These consist of a summation of parallel plate modes in the x direction and a transverse variation in the y direction. The transverse variation is defined assuming an exponential decay in fields away from the striplines, at the sides of the structure; and assuming a variation of the form of a parallel plate transmission line terminating in an open or short circuit, for the remainder of the regions.

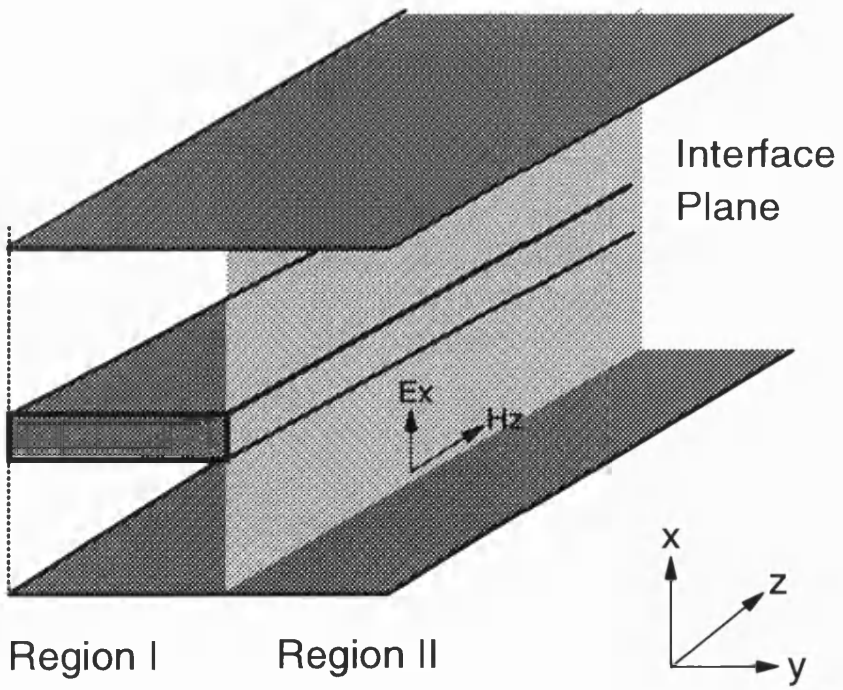

Figure 2.5: Sub-Division of Stripline Structure into Stripline (I) and Parallel Plate (II) Regions

In the case of the TE mode formulation, the magnetic field in the direction of propagation is linked to the x directed electric field by an admittance function at each of the interfaces. The aim is to enforce field continuity at the interfaces. This corresponds to the admittances at each side of the interface being equal, such that their sum is zero, i.e. the resonance condition. The transverse resonance condition is satisfied when the fields are matched across all the interfaces simultaneously. The admittance terms are written as a y-parameter matrices and cascaded. The resonance condition is then given when the determinant of the overall admittance matrix is equal to zero.

The problem cannot be solved directly and Galerkin's method is employed. The unknown field is expanded using basis functions that accurately model the singularity present at the interface. This yields a small admittance matrix, since a low number of basis terms are required to describe the field. The set of transverse propagation constants for which the determinant is zero yield the propagation constants for the modes of the structure. The fields and hence the parameters of the stripline can then be determined.

2.6.2 The Analysis of Stripline Discontinuities

The analysis of uniform and coupled lines computes the modes that can propagate in the structure, and their corresponding mode impedances. The analysis of the step in width and uniform to coupled lines transitions is carried out using a variational form of the field matching method [64] to determine the Scattering parameters of the discontinuity directly.

The discontinuity is characterised as the S parameters of an N port device, where N is the total number of modes present in the structure and is a sum of the modes propagating in the regions either side of the discontinuity plane. The field matching method is then applied, however the fields in the cross section of the discontinuity are expanded in terms of basis functions that model the singularities present in the cross sectional field. This differs from previous approaches when the fields at the discontinuity plane are expanded using the fields present on one side of the plane only.

2.7 Conclusions

The chapter has briefly introduced a number of techniques for analysing passive microwave structures, and considered in greater details some of the techniques that have been used to analyse stripline structures.

The choice of an appropriate analysis technique is a compromise between the amount of analytical pre-processing; the computing resources available and the accuracy required. The number of publications on uniform and coupled line analysis illustrate the range of techniques that have been used to meet particular compromises. The previous analyses of stripline have mainly concentrated on either a low computation time, closed form expressions at the expense of accuracy; or analyses with a higher degree of accuracy, but with a large computation time. The Transverse Resonance Diffraction (TRD) analysis offers a high degree of accuracy with a comparatively low computation time. The TRD method therefore meets the requirements of a tool for beamforming network design. The accuracy and low computation time are achieved by taking advantage of a-priori information concerning the edge singularities in the structure, at the expense of an amount of analytical pre-processing.

The ability to accurately and efficiently characterise the uniform and coupled stripline networks enables a compact theory to be developed to analyse stripline discontinuities, with a high degree of accuracy and again a relatively low computation time.

Chapter 3

Transverse Resonance Diffraction Analysis of Stripline Structures

3.1 Outline

This chapter describes the formulation of the Transverse Resonance Diffraction (TRD) method for striplines of arbitrary dimensions. A y-parameter model is developed for both uniform and coupled striplines, and solved using variational methods. The chapter concludes with an investigation of a reduced form of the analysis and definitions of the design parameters investigated in the later chapters.

3.2 Formulation of the Transverse Resonance Diffraction Problem

The Transverse Resonance Diffraction technique has been introduced in the previous chapter. The analysis will be carried out for a pair of coupled striplines and the corresponding expressions for a uniform stripline derived as a limiting case of the coupled

lines case.

The analysis assumes a uniform, isotropic and lossless dielectric filling and lossless conductors. The problem is formulated using potential functions with the propagating modes represented by a three field TE or TM mode description as opposed to a full five field description [60]. This is due to the structure containing a uniform dielectric as opposed to a structure with an air-dielectric, or dielectric-dielectric interface.

3.2.1 Description of Fields

The field solutions in the structure are governed by Maxwell's curl equations, assuming a time dependence of the form $\mathrm{Exp}(-j\omega t)$ and writing the fields for mode, k, in terms of transverse and longitudinal ($\hat{z}$ directed) components:

$$\left.\begin{aligned} \nabla \wedge \underline{e_{tk}} &= -j\omega\mu_o(\underline{h_{tk}} + \underline{h_{zk}}) \\ \nabla \wedge (\underline{h_{tk}} + \underline{h_{zk}}) &= j\omega\epsilon_o\epsilon_r\underline{e_{tk}} \end{aligned}\right\} \quad \text{TE Modes} \qquad (3.1)$$

$$\left.\begin{aligned} \nabla \wedge (\underline{e_{tk}} + \underline{e_{zk}}) &= -j\omega\mu_o\underline{h_{tk}} \\ \nabla \wedge \underline{h_t} &= j\omega\epsilon_o\epsilon_r(\underline{e_{tk}} + \underline{e_{zk}}) \end{aligned}\right\} \quad \text{TM Modes} \qquad (3.2)$$

Where, using the general vector notation, $\underline{a_k} = \hat{x}A_x + \hat{y}A_y + \hat{z}A_z = (A_x, A_y, A_z)$, the vector components $\underline{a_{tk}}$ and $\underline{a_{zk}}$ are given by:

$$\begin{aligned} \underline{a_{tk}} &= (A_{xk}, A_{yk}, 0) \\ \underline{a_{zk}} &= (0, 0, A_{zk}) \end{aligned}$$

Considering the TE modes in the structure, the above equations can be rewritten in terms of the transverse and longitudinal field components:

$$\nabla_t \wedge \underline{e_{tk}} = -j\omega\mu_o\underline{h_{zk}} \qquad (3.3)$$

$$\nabla_z \wedge \underline{e_{tk}} = -j\omega\mu_o\underline{h_{tk}} \qquad (3.4)$$

$$\nabla_t \wedge \underline{h_{tk}} = 0 \qquad (3.5)$$

$$(\nabla_t \wedge \underline{h_{zk}}) - (\nabla_z \wedge \underline{h_{tk}}) = j\omega\epsilon_o\epsilon_r\underline{e_{tk}} \qquad (3.6)$$

If the curl of a vector is equal to zero it can be represented as the gradient of a potential function ($\nabla \wedge \nabla\phi = 0$), the transverse magnetic field is expressed in terms of a magnetic scalar potential function, $\phi_{hk}(x, y, z)$:

$$\begin{aligned} \underline{h_{tk}} &= \nabla_t \phi_{hk}(x, y, z) \\ &= \nabla_t \phi_{hk}(x, y) \, \mathrm{Exp}(-j\beta_k z) \end{aligned} \tag{3.7}$$

Substituting the above expression into Equation 3.4:

$$\hat{z} \wedge \underline{e_{tk}} = \left(\frac{\omega\mu_o}{\beta_k}\right) \nabla_t \phi_{hk}(x, y) \tag{3.8}$$

$$\hat{z} \wedge (\hat{z} \wedge \underline{e_{tk}}) = \left(\frac{\omega\mu_o}{\beta_k}\right) [\hat{z} \wedge \nabla_t \phi_{hk}(x, y)] \tag{3.9}$$

Hence,

$$\underline{e_{tk}} = Z_{ok} \, [\hat{z} \wedge \nabla_t \phi_{hk}(x, y)] \tag{3.10}$$

where the wave impedance, Z_{ok} is given by:

$$Z_{ok} = \frac{\omega\mu_o}{\beta_k} \tag{3.11}$$

Substituting the expressions for $\underline{h_{tk}}$ and $\underline{e_{tk}}$ into Equation 3.6:

$$\nabla_t \wedge \underline{h_{zk}} = j\omega\epsilon_o\epsilon_r \left(\frac{\omega\mu_o}{\beta_k}\right) [\hat{z} \wedge \nabla_t \phi_{hk}(x, y)] - j\beta_k \, [\hat{z} \wedge \nabla_t \phi_{hk}(x, y)] \tag{3.12}$$

$$= -\left(\frac{k_t^2}{j\beta_k}\right) [\hat{z} \wedge \nabla_t \phi_{hk}(x, y)] \tag{3.13}$$

$$\text{where} \quad k_t^2 = \epsilon_r k_o^2 - \beta_k^2 \tag{3.14}$$

$$= k_x^2 + k_y^2 \tag{3.15}$$

It can be shown that the above equation can be satisfied when:

$$\underline{h_{zk}} = -\frac{k_t^2}{j\beta_k} \phi_{hk}(x, y) \tag{3.16}$$

Expressions for the TM fields can be found using an electric scalar potential function in a similar manner to the TE fields. Renormalising the expressions for the TE

modes, the fields in the structure are related to the potential functions by the following expressions:

$$\left.\begin{aligned} h_{zk}(x,y) &= \tfrac{k_t^2}{j\omega\mu_o}\phi_{hk}(x,y) \\ h_{tk}(x,y) &= -\tfrac{\beta_k}{\omega\mu_o}\nabla_t\phi_{hk}(x,y) \\ e_{tk}(x,y) &= \nabla_t\phi_{hk}(x,y)\wedge\hat{z} \end{aligned}\right\} \quad \text{TE Modes} \qquad (3.17)$$

$$\left.\begin{aligned} e_{zk}(x,y) &= \tfrac{k_t^2}{j\omega\epsilon_o\epsilon_r}\phi_{ek}(x,y) \\ e_{tk}(x,y) &= \tfrac{-\beta_k}{\omega\epsilon_o\epsilon_r}\nabla_t\phi_{ek}(x,y) \\ h_{tk}(x,y) &= \nabla_t\phi_{ek}(x,y)\wedge\hat{z} \end{aligned}\right\} \quad \text{TM Modes} \qquad (3.18)$$

Considering the TE modes, the fields can be derived from Equation 3.17:

$$h_{zk}(x,y) = \frac{k_t^2}{j\omega\mu_0}\phi_{hk}(x,y) \qquad (3.19)$$

$$e_{xk}(x,y) = \partial_y\phi_{hk}(x,y) \qquad (3.20)$$

$$e_{yk}(x,y) = -\partial_x\phi_{hk}(x,y) \qquad (3.21)$$

$$h_{xk}(x,y) = \frac{\beta_k}{\omega\mu_0}\partial_x\phi_{hk}(x,y) \qquad (3.22)$$

$$h_{yk}(x,y) = -\frac{\beta_k}{\omega\mu_0}\partial_y\phi_{hk}(x,y) \qquad (3.23)$$

3.2.2 Derivation of Scalar Potential Functions

The scalar potential functions used in the analysis are separable and consist of a summation of an infinite number of field shape terms for the $\hat{x}$, $\hat{y}$ and $\hat{z}$ directions, modified by an amplitude term in the form of a voltage for TE modes and a current for TM modes.

$$\phi_{hk}(x,y,z) = \sum_{n=0}^{n=\infty} V_{kn}\,\phi_{hx}(n,x)\phi_{hy}(n,y)\text{Exp } j(\omega t-\beta_k z) \qquad (3.24)$$

$$\phi_{ek}(x,y,z) = \sum_{n=1}^{n=\infty} I_{kn}\,\phi_{ex}(n,x)\phi_{ey}(n,y)\text{Exp } j(\omega t-\beta_k z) \qquad (3.25)$$

The contribution from the n=0 term of the electric scalar potential function has been omitted from the summation. The n=0 term in the TE analysis corresponds to the uniform field component, i.e. a constant electric field amplitude between the strip and

ground planes. An n=0 term in the TM analysis would therefore correspond to a constant magnetic field amplitude, or constant current flowing between the strip and ground plane, which is a non physical solution of the structure. The constant voltage term, V_o, represents the voltage of the central conductor with respect to the ground planes and is defined as a boundary condition of the problem.

The TEM mode of propagation is a limiting case of the TE analysis. Substitution of the transverse wavenumber, k_t, equal to zero into the field expressions derived from the scalar potentials yields zero values of the fields except the $\hat{x}$ directed electric field, and hence $\hat{y}$ directed magnetic field.

The stripline structure shown in Figure 3.1 is subdivided into five distinct Regions I to V. The overall field solution is found by enforcing field continuity across the four boundaries. Expressions for the fields, and hence scalar potentials have to be found on both sides of the boundaries. This requires further dividing the structure in to the sixteen sub-regions, R_1 to R_{16}.

The scalar potentials and fields for the sixteen sub-regions are derived fully in Appendix B for the TE and TM modes.

The analysis only considers the bound modes present in the structure, with the assumption that the continuum (radiating) modes do not radiate a significant amount of energy. The fields in Regions I and V are therefore represented as an exponential decay in the transverse ($\hat{y}$) direction.

The general form of the analysis means that the scalar potentials are similar, but distinct in the sixteen sub-regions. The formulation can be simplified, if required, by assuming a physical plane of symmetry at x=0, and an even or odd plane of symmetry at y=0 [61].

3.2.3 Y-Parameter Network Representation for TE Modes

The problem is analysed by enforcing field continuity in the $\hat{z}$ directed magnetic field, h_{zk}, and solving the resultant equations for the transverse $\hat{x}$ directed electric field, e_{xk}.

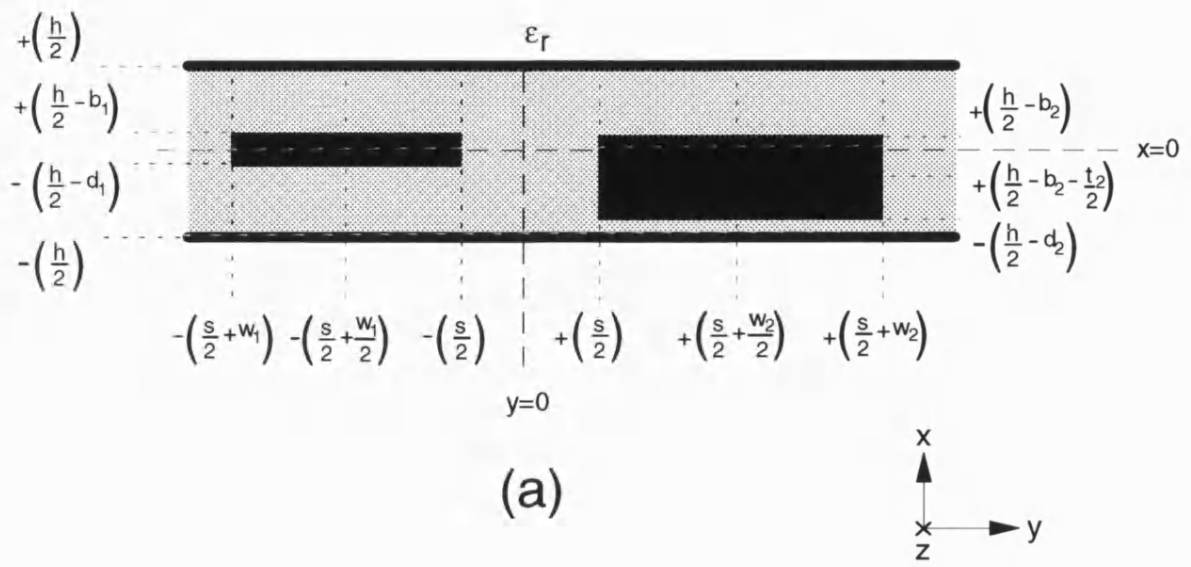

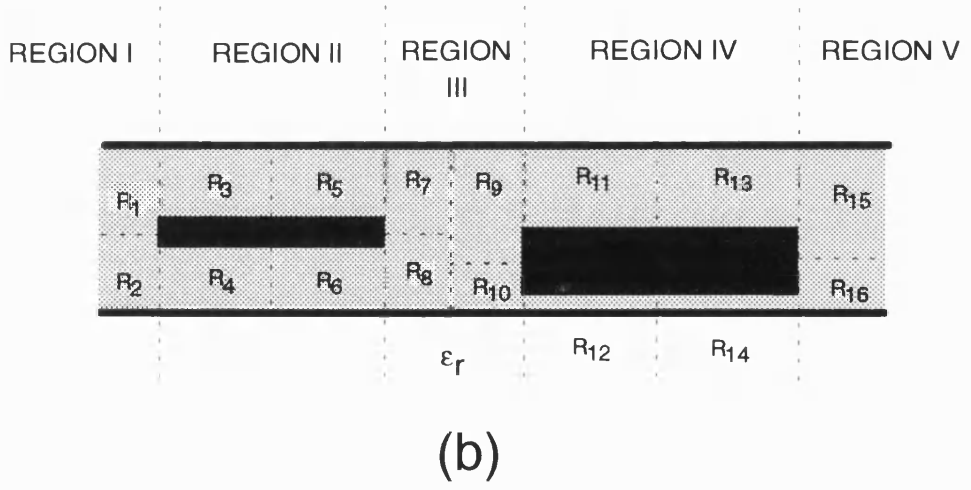

(b)

Figure 3.1: Definition of Dimensions (a) and Regions and Sub-Regions (b) of the Coupled Stripline Structure Analysed

The number of boundaries, across which field continuity has to be enforced, dictates that a network representation of the problem is used. This maintains a compact analytical form for the TRD formulation and enables the method to be easily extended for any number of arbitrarily dimensioned striplines.

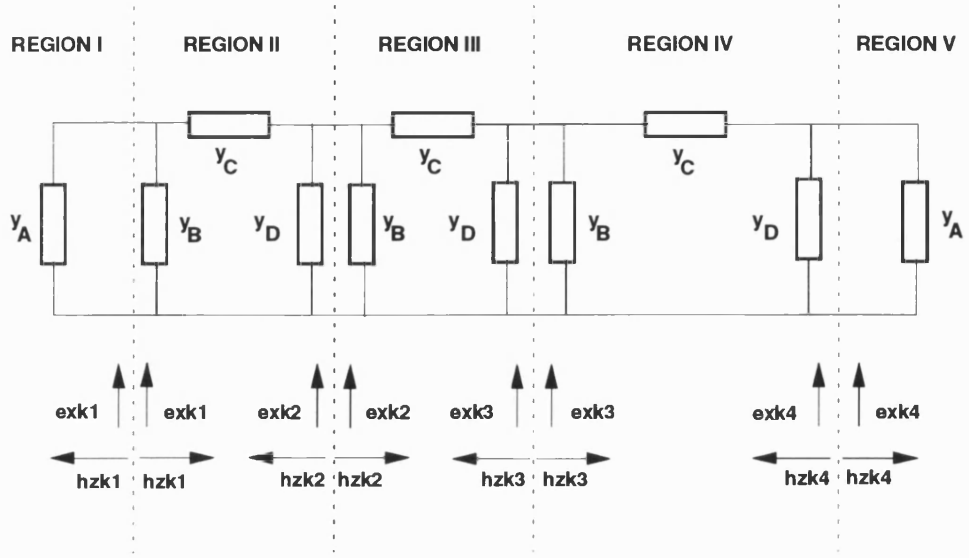

Figure 3.2: Equivalent y Parameter Circuit for TE Modes

The y-parameter equivalent circuit for the TE modes is shown in Figure 3.2. The elements, Y_A to Y_D can be expressed in terms the y-parameters of the structure:

$$Y_A = y_1 \qquad Y_B = y_{11} + y_{12}$$
$$Y_C = -y_{12} = -y_{21} \qquad Y_D = y_{22} + y_{21}$$

Considering the interface between Regions I and II, and linking the magnetic field, $h_{zk}(x, y)$, on the Region I side of the interface, to the electric field, $e_{xk}(x, y)$ on the Region II side of the interface; noting that the amplitude, H_{zkn} can be represented as $H_{zkn} = \mathcal{Y}(n)\, E_{xkn}$, the $h_{zk}(x, y)$ and $e_{xk}(x, y)$ fields are given by:

$$h_{zk1}\left(x,-\left(\frac{s}{2}+w_1\right)^-\right) = \frac{1}{j\omega\mu_o}\sum_{n=0}^{n=\infty}\mathcal{Y}(n)\,E_{xkn}\,\phi_{hx}\left(n,x,-\left(\frac{s}{2}+w_1\right)^-\right) \tag{3.26}$$

$$e_{xk1}\left(x',-\left(\frac{s}{2}+w_1\right)^+\right) = \frac{1}{j\omega\mu_o}\sum_{n=0}^{n=\infty}E_{xkn}\,\phi_{hx}\left(n,x',-\left(\frac{s}{2}+w_1\right)^+\right) \tag{3.27}$$

The E_{xkn} amplitude can be expressed as a Fourier expansion of Equation 3.27:

$$E_{xkn} = \int_{-\infty}^{+\infty} e_{xk1}\left(x',-\left(\frac{s}{2}+w_1\right)^+\right)\,\phi_{hx}\left(n,x',-\left(\frac{s}{2}+w_1\right)^+\right)dx' \tag{3.28}$$

Substituting the above equation in to the expression for $h_{zk1}(x,y)$:

$$h_{zk1}\left(x,-\left(\frac{s}{2}+w_1\right)^-\right) = y \bullet e_{xk1}\left(x',-\left(\frac{s}{2}+w_1\right)^+\right) \tag{3.29}$$

where $\bullet$ denotes convolution and y is of the form of a Greens Admittance Operator [19]:

$$y = \sum_{n=0}^{n=\infty}\mathcal{Y}(n)\,\phi_{hx}\left(n,x,-\left(\frac{s}{2}+w_1\right)^-\right)\phi_{hx}\left(n,x',-\left(\frac{s}{2}+w_1\right)^+\right) \tag{3.30}$$

The mode admittance terms $\mathcal{Y}(n)$ are derived for the sixteen sub-regions in Appendix B, using the notation of Figure 3.2 for the fields at the interface and rewriting Equation 3.29:

$$h^I_{zk1} = y^I_1 \bullet e^I_{xk1} \tag{3.31}$$

In a similar manner, the $\hat{z}$ directed magnetic field can be related to the $\hat{x}$ directed electric field for the remaining four regions.

$$\begin{bmatrix} h^{II}_{zk1} \\ h^{II}_{zk2} \end{bmatrix} = \begin{bmatrix} y^{II}_{11} & y^{II}_{12} \\ y^{II}_{12} & y^{II}_{22} \end{bmatrix} \bullet \begin{bmatrix} e^{II}_{xk1} \\ e^{II}_{xk2} \end{bmatrix} \tag{3.32}$$

$$\begin{bmatrix} h^{III}_{zk2} \\ h^{III}_{zk3} \end{bmatrix} = \begin{bmatrix} y^{III}_{11} & y^{III}_{12} \\ y^{III}_{12} & y^{III}_{22} \end{bmatrix} \bullet \begin{bmatrix} e^{III}_{xk2} \\ e^{III}_{xk3} \end{bmatrix} \tag{3.33}$$

$$\begin{bmatrix} h^{IV}_{zk3} \\ h^{IV}_{zk4} \end{bmatrix} = \begin{bmatrix} y^{IV}_{11} & y^{IV}_{12} \\ y^{IV}_{12} & y^{IV}_{22} \end{bmatrix} \bullet \begin{bmatrix} e^{IV}_{xk3} \\ e^{IV}_{xk4} \end{bmatrix} \tag{3.34}$$

$$h^V_{zk4} = y^V_1 \bullet e^V_{xk4} \tag{3.35}$$

Enforcing field continuity between the regions, the overall y-parameter representation is found:

$$\begin{bmatrix} 0 \\ 0 \\ 0 \\ 0 \end{bmatrix} = \begin{bmatrix} y_1^I + y_{11}^{II} & y_{12}^{II} & 0 & 0 \\ y_{12}^{II} & y_{11}^{III} + y_{22}^{II} & y_{12}^{III} & 0 \\ 0 & y_{12}^{III} & y_{22}^{III} + y_{11}^{IV} & y_{12}^{IV} \\ 0 & 0 & y_{12}^{IV} & y_{22}^{IV} + y_1^V \end{bmatrix} \bullet \begin{bmatrix} e_{xk1} \\ e_{xk2} \\ e_{xk3} \\ e_{xk4} \end{bmatrix} \tag{3.36}$$

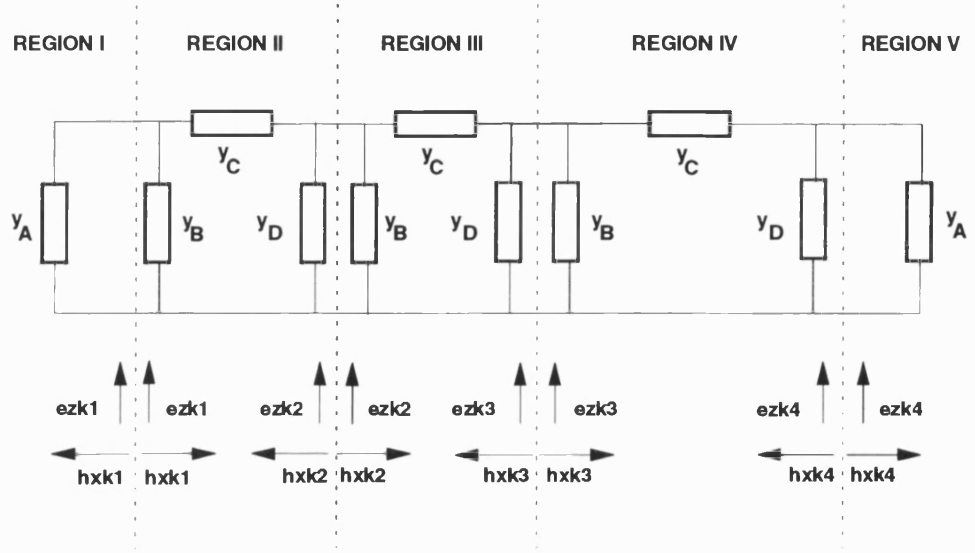

Figure 3.3: Equivalent Y-Parameter Circuit for TM Modes

3.2.4 Y-Parameter Network Representation for TM Modes

The total $\hat{x}$ and $\hat{z}$ directed fields in the interface plane between Regions I and II can be written as a general Green's Function Admittance Operator:

$$\begin{bmatrix} h_{zk1} \\ h_{xk1} \end{bmatrix}^I = \begin{bmatrix} y_{11} & y_{12} \\ y_{21} & y_{22} \end{bmatrix}^I \bullet \begin{bmatrix} e_{xk1} \\ e_{zk1} \end{bmatrix}^I \tag{3.37}$$

The y_{11} term equates to the TE admittance operator of Equation 3.31; and the y_{22} term to the corresponding TM admittance operator. The y_{12} and y_{22} terms represent the cross coupling between TE and TM modes and are therefore identically zero.

In order to simplify the TRD analysis it is beneficial to solve the TM problem for a field with the same shape as that used to solve the TE problem, since only one field shape has to be discretised. The matrix expression in Equation 3.37 is therefore modified to solve the TM modes in terms of the partial differential of the e_{zk} field with respect to the $\hat{x}$ direction, since this has the same singularity behaviour as the e_{xk} field, rewriting Equation 3.37, noting that the $\frac{A}{\pi}$ term is introduced to maintain the correct field scaling.

$$\begin{bmatrix} h_{zk1} \\ \int \frac{\pi}{A} h_{xk1} dx' \end{bmatrix}^I = \begin{bmatrix} y'_{11} & 0 \\ 0 & y'_{22} \end{bmatrix}^I \bullet \begin{bmatrix} e_{xk1} \\ \frac{A}{\pi} \partial_x e_{zk1} \end{bmatrix}^I \tag{3.38}$$

where the corresponding transformed admittance operators are given by:

$$\begin{aligned} y'_{11} &= y_{11} \\ y'_{22} &= -\int\int_{CrossSection} y_{22}\, dx\, dx' \end{aligned}$$

Enforcing field continuity, the overall y parameter representation for the TM modes is found:

$$\begin{bmatrix} 0 \\ 0 \\ 0 \\ 0 \end{bmatrix} = \begin{bmatrix} y_1^{I'} + y_{11}^{II'} & y_{12}^{II'} & 0 & 0 \\ y_{12}^{II'} & y_{11}^{III'} + y_{22}^{II'} & y_{12}^{III'} & 0 \\ 0 & y_{12}^{III'} & y_{22}^{III'} + y_{11}^{IV'} & y_{12}^{IV'} \\ 0 & 0 & y_{12}^{IV'} & y_{22}^{IV'} + y_1^{V'} \end{bmatrix} \bullet \begin{bmatrix} \frac{A}{\pi} \partial_x e_{zk1} \\ \frac{A}{\pi} \partial_x e_{zk2} \\ \frac{A}{\pi} \partial_x e_{zk3} \\ \frac{A}{\pi} \partial_x e_{zk4} \end{bmatrix} \tag{3.39}$$

where $'$ denotes operator $\int\int dx dx'$ and noting that the field scaling factor, $\frac{A}{\pi}$, will differ for the sub-regions.

3.3 Derivation of the Transverse Resonance Equation

The transverse resonance equations shown in Equations 3.36 and 3.39 cannot be directly solved since the exact form of the e_{xk} fields is unknown. Numerical techniques are

therefore used to indirectly solve for the unknown field. The method of solution will be described for the TE modes and a corresponding solution for TM modes will be derived.

Recalling Equation 3.36 and substituting the expressions for the Green's Admittance operators and rewriting in terms of matrices:

$$\begin{bmatrix} 0 \\ 0 \\ 0 \\ 0 \end{bmatrix} = \sum_{n=0}^{n=\infty} [\mathcal{Y}(n)]\,[\phi_{hk}(n,x,y)]\,[\phi_{hk}(n,x',y')] \bullet \begin{bmatrix} e_{xk1} \\ e_{xk2} \\ e_{xk3} \\ e_{xk4} \end{bmatrix} \tag{3.40}$$

where the mode admittance and scalar potential matrices are defined as:

$$[\mathcal{Y}(n)] = \begin{bmatrix} \mathcal{Y}_1^I(n)+\mathcal{Y}_{11}^{II}(n) & \mathcal{Y}_{12}^{II}(n) & 0 & 0 \\ \mathcal{Y}_{12}^{II}(n) & \mathcal{Y}_{11}^{III}(n)+\mathcal{Y}_{22}^{II}(n) & \mathcal{Y}_{12}^{III}(n) & 0 \\ 0 & \mathcal{Y}_{12}^{III}(n) & \mathcal{Y}_{22}^{III}(n)+\mathcal{Y}_{11}^{IV}(n) & \mathcal{Y}_{12}^{IV}(n) \\ 0 & 0 & \mathcal{Y}_{12}^{IV}(n) & \mathcal{Y}_{22}^{IV}(n)+\mathcal{Y}_1^V(n) \end{bmatrix} \tag{3.41}$$

$$[\phi_{hk}(n,x,y)] = \phi_{hx}(n,x) \begin{bmatrix} \phi_{hy}(-(\frac{s}{2}+w_1)^-) & 0 & 0 & 0 \\ 0 & \phi_{hy}(-(\frac{s}{2})^-) & 0 & 0 \\ 0 & 0 & \phi_{hy}(+(\frac{s}{2})^-) & 0 \\ 0 & 0 & 0 & \phi_{hy}(+(\frac{s}{2}+w_2)^-) \end{bmatrix} \tag{3.42}$$

$$[\phi_{hk}(n,x',y')] = \phi_{hx}(n,x') \begin{bmatrix} \phi_{hy}(-(\frac{s}{2}+w_1)^+) & 0 & 0 & 0 \\ 0 & \phi_{hy}(-(\frac{s}{2})^+) & 0 & 0 \\ 0 & 0 & \phi_{hy}(+(\frac{s}{2})^+) & 0 \\ 0 & 0 & 0 & \phi_{hy}(+(\frac{s}{2}+w_2)^+) \end{bmatrix} \tag{3.43}$$

Galerkin's method, a general form of the method of moments [65] was chosen as the numerical method to solve Equation 3.40 for the unknown fields. The method is based on approximating the unknown function using a weighted summation of basis functions. When the substitution is made in to the governing equation, there will be a small but finite error due to the approximation. This error is integrated with a second basis

function and the result assumed to vanish. The case when the first and second basis functions are identical is referred to as Galerkin's method.

The unknown e_{xk} field is approximated by the summation of basis functions. In the case of the stripline structure the $\hat{y}$ dependence of the e_{xk} fields is identical at all the interfaces and equal to unity, such that:

$$e_{xk}(x, y_o) = \sum_{p=0}^{p=\infty} X_{pk}\, f_p(x) \tag{3.44}$$

Therefore rewriting Equation 3.40 and evaluating the convolution as an inner product:

$$\begin{bmatrix} 0 \\ 0 \\ 0 \\ 0 \end{bmatrix} = \sum_{n=0}^{n=\infty} [\mathcal{Y}(n)]\ [\phi_{hk}(n, x', y')] \sum_{p=0}^{p=\infty} \int_{-\infty}^{+\infty} [\phi_{hk}(n, x, y)]\, f_p(x)\, dx \begin{bmatrix} X_{pk1} \\ X_{pk2} \\ X_{pk3} \\ X_{pk4} \end{bmatrix} \tag{3.45}$$

The integral $\int [\phi_{hk}(x, y)]\ f_p(x)\ dx$ is defined as an inner product, and is denoted by $< \phi_{hk}(x, y)\ ;\ f_p(x) >$. In addition, recalling that the $\hat{y}$ directed scalar potentials are normalised to unity at each of the interfaces (Appendix B), rewriting:

$$[\underline{0}] = \sum_{n=0}^{n=\infty} [\mathcal{Y}(n)]\ [\phi_{hk}(n, x', y')] \sum_{p=0}^{p=\infty} < \phi_{hx}(n, x)\ ;\ f_p(x) > \left[\underline{X_{pk}}\right] \tag{3.46}$$

A further inner product is then taken with the same basis functions:

$$[\underline{0}] = \sum_{n=0}^{n=\infty} \sum_{p=0}^{p=\infty} [\mathcal{Y}(n)] < \phi_{hx}(n, x')\ ;\ f_p(x') >< \phi_{hx}(n, x)\ ;\ f_p(x) > \left[\underline{X_{pk}}\right] \tag{3.47}$$

In order to practically solve the above equations, the infinite number of terms in the summations are replaced with a finite number of field expansion terms N, and a finite number of basis functions, P, and the above equation rewritten as a set of linear equations in matrix form such that:

$$\begin{bmatrix} \underline{0} \\ \underline{0} \\ \underline{0} \\ \underline{0} \end{bmatrix} = \begin{bmatrix} [Y_1^I + Y_{11}^{II}] & [Y_{12}^{II}] & [0] & [0] \\ [Y_{12}^{II}] & [Y_{11}^{III} + Y_{22}^{II}] & [Y_{12}^{III}] & [0] \\ [0] & [Y_{21}^{III}] & [Y_{22}^{III} + Y_{11}^{IV}] & [Y_{12}^{IV}] \\ [0] & [0] & [Y_{21}^{IV}] & [Y_{22}^{IV} + Y_1^V] \end{bmatrix} \begin{bmatrix} \underline{X_{k1}} \\ \underline{X_{k2}} \\ \underline{X_{k3}} \\ \underline{X_{k4}} \end{bmatrix} \tag{3.48}$$

The elements of the overall admittance matrix $[Y_{ij}]$ are themselves matrices, of order P×P, the elements of which are evaluated as:

$$[Y_{ij}]_{pq} = \sum_{n=0}^{n=\infty} [\mathcal{Y}(n)]_{ij} \; < \phi_{hx}(n,x) \; ; \; f_p(x) > < \phi_{hx}(n,x) \; ; \; f_q(x) > \tag{3.49}$$

The corresponding elements of the admittance matrix for the TM modes can be written:

$$[Y_{ij}]_{pq} = \sum_{n=0}^{n=\infty} \left(\int \int [\mathcal{Y}(n)]_{ij} dx dx' \right) \; < \phi_{ex}(n,x) \; ; \; f_p(x) > < \phi_{ex}(n,x) \; ; \; f_q(x) > \tag{3.50}$$

3.4 Evaluation of the Transverse Resonance Equation

3.4.1 Choice of Basis Functions

The efficiency of the TRD technique relies on expanding the unknown field using basis functions that can model the field using a small number of terms, since the computational time is proportional to the cube of the admittance matrix order [66].

The field singularities on the edges of the central conductor dominate the cross sectional fields. An efficient approach would therefore be to expand the fields using basis functions that model the order of the singularities on the edges of the conductors.

The term "singularity" suggests that the field strength is infinite at the edges of the strip. In practice, the energy stored must be a finite quantity, Collin [19] analysed a metallic wedge of arbitrary angle and produced an expression for the minimum order of the field singularity at the edge. For an angle of 90^o, found at the corners of a finite

thickness stripline, the singularity is of the order $\mid r \mid^{-\frac{1}{3}}$. For an infinitely thin stripline the order of the singularity is $\mid r \mid^{-\frac{1}{2}}$.

The basis functions take the form of a product of an orthonormalisation constant, A_p, a weight function to model the singularity, $W(x,\nu)$ and the orthogonal function, $F(x,\nu)$:

$$f_p(x) = A_p\, W(x,\nu)\, F(x,\nu) \tag{3.51}$$

Gegenbauer Polynomials (Figure 3.4) are used as basis functions to model the finite thickness stripline since the Gegenbauer Polynomial weight function is of the same form as the $\mid r \mid^{-\frac{1}{3}}$ field variation. Chebyshev Polynomials (Figure 3.5) are used as basis functions for infinitely thin stripline since their weight functions model the $\mid r \mid^{-\frac{1}{2}}$ field variation accurately.

3.4.2 Calculation of Inner Products

The inner products are derived in Appendix C between the scalar potentials and Gegenbauer polynomials for both the TE and TM modes.

Introducing the notation of an inner product as:

$$P_{pn}^{R_i} = < \phi_{hx,ex}^{R_i}(n,x)\ ;\ f_p(x) > \tag{3.52}$$

The general form of the inner products for the TE modes is given by:

$$P_{pn}^{R_i} = A_n^{R_i}\, b_i^{\frac{1}{6}}\, (-1)^p \sqrt{\frac{\pi}{2}} A_{2p} \left[\frac{\Gamma(2p+\frac{1}{3})}{(2p)!}\right]^{\frac{1}{2}} \left[2p+\frac{1}{6}\right]^{\frac{1}{2}} \left(k_x^{R_i}\, b_i\right)^{-\frac{1}{6}} J_{2p+\frac{1}{6}}\left(k_x^{R_i}\, b_i\right)$$
$$x > \left(\frac{h}{2} - \left(b_i + \frac{t_i}{2}\right)\right) \tag{3.53}$$

$$= A_n^{R_i}\, d_i^{\frac{1}{6}}\, (-1)^p \sqrt{\frac{\pi}{2}} A_{2p} \left[\frac{\Gamma(2p+\frac{1}{3})}{(2p)!}\right]^{\frac{1}{2}} \left[2p+\frac{1}{6}\right]^{\frac{1}{2}} \left(k_x^{R_i}\, d_i\right)^{-\frac{1}{6}} J_{2p+\frac{1}{6}}\left(k_x^{R_i}\, d_i\right)$$
$$x < \left(\frac{h}{2} - \left(b_i + \frac{t_i}{2}\right)\right) \tag{3.54}$$

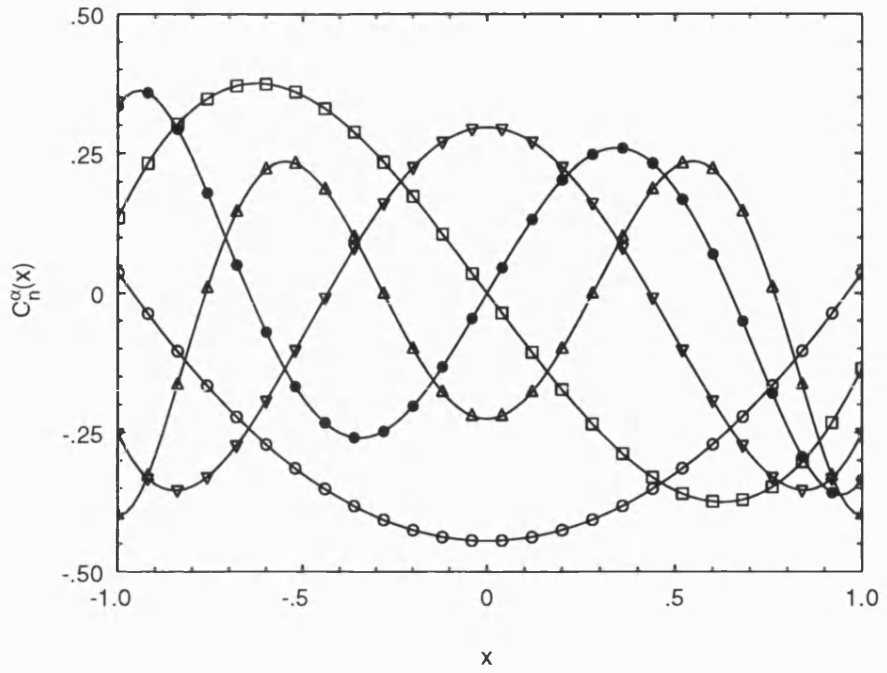

Figure 3.4: Second [○], Third [□], Fourth [∇], Fifth [•] and Sixth [△] Order Gegenbauer Polynomials of Singularity Order $\alpha = \frac{1}{6}$

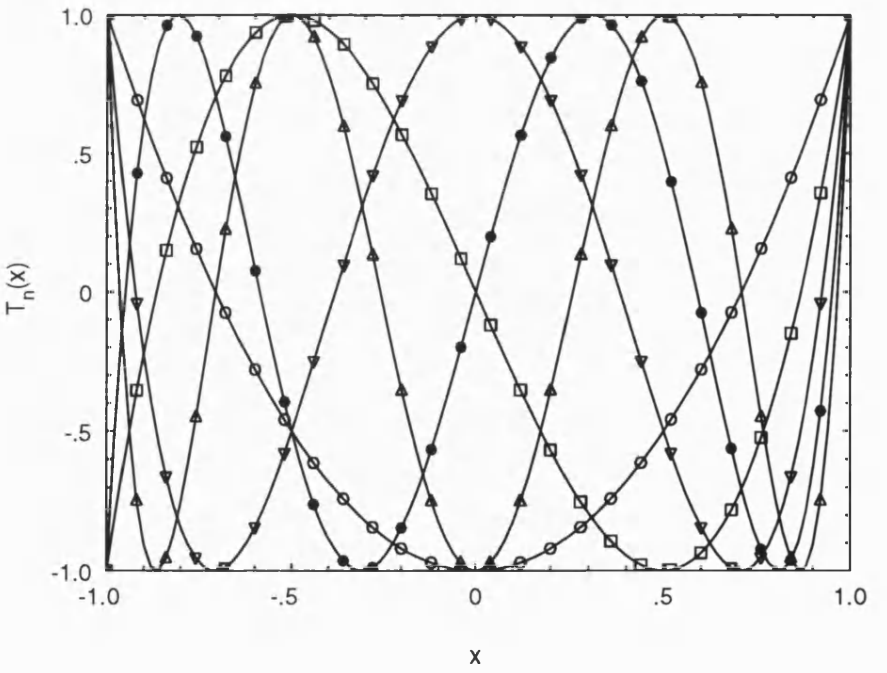

Figure 3.5: Second [○], Third [□], Fourth [∇], Fifth [•] and Sixth [△] Order Chebyshev Polynomials

The corresponding expressions for the TM modes are given as:

$$P_{pn}^{R_i} = A_n^{R_i} b_i^{\frac{1}{6}} (-1)^p \sqrt{\frac{\pi}{2}} A_{2p+1} \left[\frac{\Gamma(2p+\frac{4}{3})}{(2p+1)!}\right]^{\frac{1}{2}} \left[2p+\frac{7}{6}\right]^{\frac{1}{2}} \left(k_x^{R_i} b_i\right)^{-\frac{1}{6}} J_{2p+\frac{7}{6}}\left(k_x^{R_i} b_i\right) \quad x > \left(\frac{h}{2} - \left(b_i + \frac{t_i}{2}\right)\right) \quad (3.55)$$

$$= A_n^{R_i} d_i^{\frac{1}{6}} (-1)^p \sqrt{\frac{\pi}{2}} A_{2p+1} \left[\frac{\Gamma(2p+\frac{4}{3})}{(2p+1)!}\right]^{\frac{1}{2}} \left[2p+\frac{7}{6}\right]^{\frac{1}{2}} \left(k_x^{R_i} d_i\right)^{-\frac{1}{6}} J_{2p+\frac{7}{6}}\left(k_x^{R_i} d_i\right) \quad x < \left(\frac{h}{2} - \left(b_i + \frac{t_i}{2}\right)\right) \quad (3.56)$$

3.4.3 Transverse Resonance Admittance Matrix for TE Modes

Substituting the expressions for the inner products, P_{pn} and P_{qn}; and the expressions for the mode admittance terms, $\mathcal{Y}(n)$ from Appendix B into Equation 3.49 the transverse admittance matrix (Equation 3.48) can be evaluated.

Rewriting and factorising in terms of frequency independent functions, $\mathcal{J}(p,q,\psi)$ and C_{pq}; and frequency dependent functions, F_i, the matrix terms are found:

$$[Y_{11}]_{pq} = C_{pq} \sum_{n=0}^{n=N} F_1\left(k_y^{R_3}, k_y^{R_4}, w_1\right) \mathcal{J}(p,q,n\pi) + F_3\left(k_y^{R_1}\right) \mathcal{J}(p,q,k_x^{R_1} b_1) + F_3\left(k_y^{R_2}\right) \mathcal{J}(p,q,k_x^{R_2} d_1) \quad (3.57)$$

$$[Y_{12}]_{pq} = C_{pq} \sum_{n=0}^{n=N} F_2\left(k_y^{R_3}, k_y^{R_4}, w_1\right) \mathcal{J}(p,q,n\pi) \quad (3.58)$$

$$[Y_{21}]_{pq} = C_{pq} \sum_{n=0}^{n=N} F_2\left(k_y^{R_5}, k_y^{R_6}, w_1\right) \mathcal{J}(p,q,n\pi) \quad (3.59)$$

$$[Y_{22}]_{pq} = C_{pq} \sum_{n=0}^{n=N} \left[F_1\left(k_y^{R_5}, k_y^{R_6}, w_1\right) + F_1\left(k_y^{R_7}, k_y^{R_8}, s\right)\right] \mathcal{J}(p,q,n\pi) \quad (3.60)$$

$$[Y_{23}]_{pq} = C_{pq} \sum_{n=0}^{n=N} F_2\left(k_y^{R_5}, k_y^{R_6}, s\right) \mathcal{J}(p,q,n\pi) \quad (3.61)$$

$$[Y_{32}]_{pq} = C_{pq} \sum_{n} F_2\left(k_y^{R_7}, k_y^{R_8}, s\right) \mathcal{J}(p,q,n\pi) \quad (3.62)$$

$$[Y_{33}]_{pq} = C_{pq} \sum_{n=0}^{n=N} \left[F_1\left(k_y^{R_9}, k_y^{R_{10}}, s\right) + F_1\left(k_y^{R_{11}}, k_y^{R_{12}}, w_2\right)\right] \mathcal{J}(p,q,n\pi) \quad (3.63)$$

$$[Y_{34}^{IV}]_{pq} = C_{pq} \sum_{n=0}^{n=N} F_2\left(k_y^{R_{11}}, k_y^{R_{12}}, w_2\right) \mathcal{J}(p,q,n\pi) \tag{3.64}$$

$$[Y_{43}^{IV}]_{pq} = C_{pq} \sum_{n=0}^{n=N} F_2\left(k_y^{R_{13}}, k_y^{R_{14}}, w_2\right) \mathcal{J}(p,q,n\pi) \tag{3.65}$$

$$\begin{aligned}[Y_{44}^{IV}]_{pq} = {} & C_{pq} \sum_{n=0}^{n=N} F_1\left(k_y^{R_{13}}, k_y^{R_{14}}, w_2\right) \mathcal{J}(p,q,n\pi) + \\ & F_3\left(k_y^{R_{15}}\right) \mathcal{J}(p,q,k_x^{R_{15}} b_2) + F_3\left(k_y^{R_{16}}\right) \mathcal{J}(p,q,k_x^{R_{16}} d_2)\end{aligned} \tag{3.66}$$

Where the functions, F_1, F_2 and F_3, and the constant, C_{pq} are defined as:

$$C_{pq} = (-1)^{p+q} \frac{k_t^2 \pi}{2\omega\mu_o} \left[\frac{\Gamma(2p+\frac{1}{3})\Gamma(2q+\frac{1}{3})}{(2p)!\,(2q)!}\right]^{\frac{1}{2}} \left[\left(2p+\frac{1}{6}\right)\left(2q+\frac{1}{6}\right)\right]^{\frac{1}{2}} \tag{3.67}$$

$$F_1(k_y^{(R_l)}, k_y^{(R_m)}, \varphi) = -\left(\frac{\text{Cot}\,(k_y^{R_l}\frac{\varphi}{2})}{k_y^{R_l}} + \frac{\text{Cot}\,(k_y^{R_m}\frac{\varphi}{2})}{k_y^{R_m}}\right) \tag{3.68}$$

$$F_2(k_y^{R_l}, k_y^{R_m}, \varphi) = \left(\frac{\text{Cosec}\,(k_y^{R_l}\frac{\varphi}{2})}{k_y^{R_l}} + \frac{\text{Cosec}\,(k_y^{R_m}\frac{\varphi}{2})}{k_y^{R_m}}\right) \tag{3.69}$$

$$F_3(k_y^{R_i}) = -\frac{1}{jk_y^{R_i}} \tag{3.70}$$

$$\mathcal{J}(n,m,\psi) = J_{2n+\frac{1}{6}}(\psi)\, J_{2m+\frac{1}{6}}(\psi) \tag{3.71}$$

The wavenumbers for the different regions are defined from the equation:

$$k_t^2 = \left(k_x^{R_i}\right)^2 + \left(k_y^{R_i}\right)^2 \tag{3.72}$$

and are shown in Appendix B.

3.4.4 Transverse Resonance Admittance Matrix for TM Modes

The admittance matrix for TM modes is of an identical form to the expressions for the TE modes, however the lower limit of the summations in Equations 3.57 to 3.66 is n=1, as opposed to n=0.

The frequency dependent and independent functions are defined:

$$C_{pq} = (-1)^{p+q} \frac{k_t^2 \pi}{2\omega\epsilon_o\epsilon_r} \left[\frac{\Gamma(2p+\frac{4}{3})\Gamma(2q+\frac{4}{3})}{(2p+1)!\,(2q+1)!}\right]^{\frac{1}{2}} \left[\left(2p+\frac{7}{6}\right)\left(2q+\frac{7}{6}\right)\right]^{\frac{1}{2}} \tag{3.73}$$

$$F_1(k_y^{R_l}, k_y^{R_m}, \varphi) = -\left(\frac{jk_y^{R_l}\mathrm{Cot}\,(k_y^{R_l}\frac{\varphi}{2})}{n^2\,k_y^{(R_l)}} + \frac{jk_y^{R_m}\mathrm{Cot}\,(k_y^{R_m}\frac{\varphi}{2})}{n^2\,k_y^{R_m}}\right) \tag{3.74}$$

$$F_2(k_y^{R_l}, k_y^{R_m}, \varphi) = \left(\frac{jk_y^{R_l}\mathrm{Cosec}\,(k_y^{R_l}\frac{\varphi}{2})}{n^2} + \frac{jk_y^{R_m}\mathrm{Cosec}\,(k_y^{R_m}\frac{\varphi}{2})}{n^2}\right) \tag{3.75}$$

$$F_3(k_y^{R_i}) = -\frac{jk_y^{R_i}}{n^2} \tag{3.76}$$

$$\mathcal{J}(n, m, \psi) = J_{2n+\frac{7}{6}}(\psi)\,J_{2m+\frac{7}{6}}(\psi) \tag{3.77}$$

The $\hat{x}$ directed wavenumbers are again shown in Appendix B. The expressions for F_1, F_2 and F_3 for the TM modes are of the same form as the expressions for the TE modes. The denominators contain an additional n^2 term which also aids convergence of the method.

3.5 Solution of the Transverse Resonance Admittance Matrix

3.5.1 Solution for the Propagation Constant

The Transverse Resonance admittance equation (Equation 3.48) is of the form of a general eigenvalue problem:

$$[Y][X] = \lambda[X] \tag{3.78}$$

The solutions for the eigenvalue of zero ($\lambda = 0$) correspond to the resonance condition when the fields are matched across all interfaces. The corresponding eigenvectors give the basis amplitude terms for the mode. This eigenvalue solution, $\lambda = 0$ also corresponds to the determinant of the matrix $[Y]$ being equal to zero. This latter property was used to solve the TRD problem for the transverse wavenumber, k_t.

In order to determine the cut-off frequencies of a particular stripline geometry, the transverse wavenumber is replaced by the free space wavenumber, k_o ($\beta_k = 0$) in the expressions for the admittance matrix terms (Equations 3.57 to 3.66) . The wavenumber is then incremented and the sign of the determinant noted, when a change of sign is detected an interval halving technique [65] is used to determine the exact cut-off wavenumber. This is complicated by a number of poles satisfying the condition of a determinant change of sign, in addition to the determinant zeroes. The poles are due to the admittance matrix terms becoming undefined for values of $k_y^{R_i}\varphi = \pi$. These terms however can be easily identified by considering the relative values of the determinant during the interval halving search. The problem can also be cast to search for a set of unknown values of the propagation constant, β_k, at a fixed frequency.

The assumption of a lossless dielectric filling enables a straightforward interval halving technique to be used. An analysis for a dielectric permittivity with a complex component to model loss would require a two dimensional search technique to be used [60].

3.5.2 Solution for the Field Amplitudes

The propagation constant information can be computed in a straightforward manner. In order to calculate the circuit parameters such as impedance and power flow, the field amplitude terms have to be determined. Recalling the form of Equation 3.28 for TE modes:

$$E_{xkn} = \int_{-\infty}^{+\infty} e_{xk}(x,y)\ \phi_{hk}(n,x,y)\,dx \tag{3.79}$$

Substituting the expression for the unknown e_{xk} field,

$$E_{xkn} = \sum_{p=0}^{p=P} X_{pk} \int_{-\infty}^{+\infty} f_p(x)\ \phi_{hk}(n,x,y)\,dx \tag{3.80}$$

$$E_{xkn} = \sum_{p=0}^{p=P} X_{pk}\ P_{pn} \tag{3.81}$$

The solution of the field amplitude terms for the fundamental TEM mode of propagation, is complicated since the TEM case is a limiting case of the TE modes with $k_t = 0$. This substitution causes the admittance matrix to be equal to the null matrix, hence no field

information can be derived. However the field is assumed to be uniform and the field amplitudes are given by:

$$[X] = \begin{bmatrix} 1 \\ \underline{0} \end{bmatrix} \tag{3.82}$$

The corresponding field amplitudes for the remaining h_{zk} and e_{yk} fields are given by the following expressions:

$$H_{zkn} = \left(\frac{k_t^2}{j\omega\mu_o k_y}\right) E_{xkn} \tag{3.83}$$

$$E_{ykn} = \left(\frac{k_x}{k_y}\right) E_{xkn} \tag{3.84}$$

The field plots for the stripline structure can therefore be calculated from the expressions in Appendix B.

3.6 Extension to an Arbitrary Number of Striplines

The analysis has been presented for a pair of coupled striplines of arbitrary dimensions. The use of a y parameter network representation enables any number of coupled striplines to be analysed by cascading the two port networks of stripline elements together. The order of the overall admittance matrix is given by $2MP \times 2MP$ where M is the number of striplines and P is the number of basis terms. The efficiency of the analysis will demonstrate that this should not place a large requirement on the memory of a computer, however the computational time will be proportional to the cube of the matrix order.

3.7 Simplification for a Uniform Stripline

In addition to extending the analysis, the analysis can be simplified by inspection to produce the formulation for a uniform stripline.

The corresponding equation for a uniform line can be obtained by considering the three Regions in Figure 3.6.

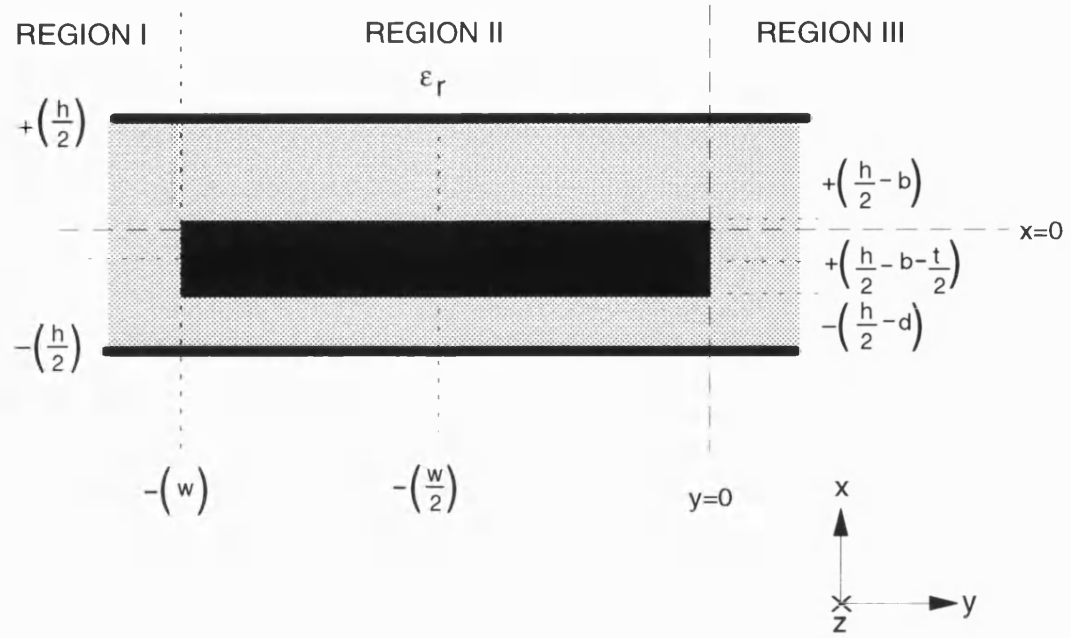

Figure 3.6: Uniform Stripline Structure Analysed

Recalling the expression for the transverse resonance equation given in Equation 3.48, the expressions for a uniform line can be written down by inspection:

$$\begin{bmatrix} \underline{0} \\ \underline{0} \end{bmatrix} = \begin{bmatrix} [Y_1^I + Y_{11}^{II}] & [Y_{12}^{II}] \\ [Y_{12}^{II}] & [Y_1^{III} + Y_{22}^{II}] \end{bmatrix} \begin{bmatrix} \underline{X_{k1}} \\ \underline{X_{k2}} \end{bmatrix} \tag{3.85}$$

The elements of the matrix are written as:

$$[Y_{11}]_{pq} = C_{pq} \sum_{n=0}^{n=N} F_1\left(k_y^{R_3}, k_y^{R_4}, w\right) \mathcal{J}(p,q,n\pi) + F_3\left(k_y^{R_1}\right) \mathcal{J}(p,q,k_x^{R_1} b) + F_3\left(k_y^{R_2}\right) \mathcal{J}(p,q,k_x^{R_2} d) \tag{3.86}$$

$$[Y_{12}]_{pq} = C_{pq} \sum_{n=0}^{n=N} F_2\left(k_y^{R_3}, k_y^{R_4}, w\right) \mathcal{J}(p,q,n\pi) \tag{3.87}$$

$$[Y_{21}]_{pq} = C_{pq} \sum_{n=0}^{n=N} F_2\left(k_y^{R_5}, k_y^{R_6}, w\right) \mathcal{J}(p,q,n\pi) \tag{3.88}$$

$$[Y_{22}^{IV}]_{pq} = C_{pq} \sum_{n=0}^{n=N} F_1\left(k_y^{R_5}, k_y^{R_6}, w\right) \mathcal{J}(p,q,n\pi) + F_3\left(k_y^{R_7}\right) \mathcal{J}(p,q,k_x^{R_7} b) + F_3\left(k_y^{R_8}\right) \mathcal{J}(p,q,k_x^{R_8} d) \tag{3.89}$$

$$F_3\left(k_y^{R_7}\right)\mathcal{J}(p,q,k_x^{R_7}b) + F_3\left(k_y^{R_8}\right)\mathcal{J}(p,q,k_x^{R_8}d) \qquad (3.89)$$

The frequency dependent and independent functions are defined in Equations 3.67 to 3.71 for TE modes and Equations 3.73 to 3.77 for TM modes.

An alternative derivation is possible by considering the TRD equation for coupled lines and substituting the limiting value for two identical striplines as the separation, s, tends to infinity, or the reflection coefficient in Region III tends to zero, i.e. a field match. The resulting matrix equation will have a symmetry plane along the non-leading diagonal due to the physical symmetry. Considering the top left hand quadrant, or the bottom right quadrant a similar equation to Equation 3.85 is found. The elements however will have a dimensional offset of $\frac{s}{2}$ in the $\hat{y}$ direction.

This alternative derivation is important as it gives an intuitive verification of the single line formulation and provides an insight into the behaviour of the structure as the dimensions are varied.

3.8 Reduced Form of the Determinant Expression

The existing expressions used to calculate the parameters of both uniform and coupled striplines are presented as closed form equations. The method defined in Section 3.5 is an iterative method, however computational savings could be made if the determinant was written as an explicit expression which could then be evaluated directly.

Computational savings can be gained by identifying the frequency dependent and independent components. This has been done to a certain extent through the separation of the orthonormalisation coefficients and the inner products from the Green's Admittance Operators.

The determinant of the admittance matrix can also be rewritten as an explicit expression containing the matrix terms and then simplified as a polynomial in the admittance operator. The formulation used for stripline relies on each admittance matrix term being a summation over the number of field expansion terms, N. The corresponding determinant expression is therefore complicated for a relatively small matrix order and value

of N, requiring an algebraic routine such as REDUCE [67] to factorise the expression.

The reduction of the determinant to a closed form expression can also be considered intuitively. The analysis yields a determinant value characterised by a number of poles, P and zeroes, Z, hence the minimum order of the polynomial to characterise this must be P+Z. The number of poles and zeroes will clearly be set by the maximum frequency of interest for a search at given propagation constant, or the maximum propagation constant for a search at a given frequency. The coefficients of the polynomial will depend on all the admittance matrix terms.

Reducing the determinant to a closed form is also equivalent to representing the problem using ABCD network representation, where the resonance condition is given by element C being equal to zero [9].

The lack of a compact form of the determinant expression suggests that an efficiently written algorithm using a small number of basis terms and field expansion terms will provide a sufficiently fast means of computing the propagation constant for a structure.

3.9 Stripline Parameters

The calculation of the field amplitude terms enables the impedance and attenuation factor of the stripline structures to be determined.

3.9.1 Definition of Impedance Measures

The impedances of the stripline structures can be calculated using three measures: the power-voltage impedance, Z_{pv}; the power-current impedance, Z_{pi} and the voltage-current impedance, Z_{vi}.

The expressions are defined below:

$$Z_{pv} = \frac{V_o^2}{P_{flow}} \tag{3.90}$$

$$Z_{pi} = \frac{P_{flow}}{I^2} \tag{3.91}$$

$$Z_{vi} = \sqrt{Z_{pv}\, Z_{pi}} \tag{3.92}$$

The power flow in the $\hat{z}$ direction, P_{flow}, is given by the Poynting vector:

$$P_{flow} = \int_{CrossSection} \underline{e_{tk}} \wedge \underline{h_{tk}} \;\; \underline{da} \tag{3.93}$$

The voltage, V_o represents the voltage between the stripline and ground planes, noting the total voltage is given by:

$$V = \int \underline{e_{tk}} \;\; \underline{dl} \tag{3.94}$$

The field, $\underline{e_{tk}}$ consists of a summation of N field amplitude and shape terms, however it can be shown that contributions to the integral are zero for all modes, except the $n = 0$ term. The corresponding expression for the current flowing in the conductors for the kth mode is given by:

$$I = \oint \underline{h_{tk}} \;\; \underline{dl} \tag{3.95}$$

The power flow, voltage and currents integrals are evaluated for the stripline structure in Appendix D.

Theoretically, the three different measures of the impedances should give identical results, this however assumes that all the integrals are calculated to an equal accuracy by the analysis method.

3.9.2 Definition of Coupled Stripline Modes

The expressions for the impedances (Equations 3.90 to 3.92) can be evaluated for all the modes present in the structure. The modes for the coupled striplines are denoted as C and Π, for lines excited with balanced and unbalanced voltages respectively [47]. For structures where there is a physical plane of symmetry at $y = 0$ the characteristic impedances are equal and the C and Π modes degenerate to the conventional even and odd modes respectively.

The expressions for the coupling, S_{21}; isolation, S_{31}; and transmission, S_{41} can be derived by considering the ABCD matrices of the modes separately [57]. The expression for the maximum coupling is noted here:

$$C = 20\log_{10}\left(\frac{Z_{o(C)} - Z_{o(\Pi)}}{Z_{o(C)} + Z_{o(\Pi)}}\right) \qquad \text{Units : dB} \qquad (3.96)$$

3.9.3 Definition of Attenuation Factor

The attenuation factor for the structure consists of contributions from the conductor attenuation factor, α_c, and the dielectric attenuation factor, α_d.

$$\alpha = \alpha_c + \alpha_d \qquad (3.97)$$

The conductor attenuation factor is calculated assuming a small perturbation method. In this approach the structure is analysed assuming a lossless propagation constant. The fields around the structure and hence the power flow (Equation 3.93) and power dissipation are calculated. The method has the advantage that only a one dimensional search is required to determine the propagation constant . The approach is only constrained by the requirement that the thickness of the conductors in the structure is approximately 2 - 3 times the skin depth. For a brass stripline network operating at C band (2.7-3.1 GHz) the analysis is limited to striplines with thicknesses greater than $10\mu m$.

The power dissipation assumes a current density on the surface of the material and an effective surface resistance, R_s, [9], such that:

$$P_{dis} = \frac{1}{2}R_s \int_{CrossSection} \left(\hat{n} \wedge \underline{h_{tk}}\right)^2 \ \underline{da} \qquad (3.98)$$

The material surface resistance is given by the expression:

$$R_s = \sqrt{\frac{\omega\mu_o}{2\sigma}} \qquad (3.99)$$

The attenuation factor in nepers per metre is then given as the ratio:

$$\alpha_c = \frac{P_{dis}}{2 \times P_{flow}} \tag{3.100}$$

The attenuation factor is normalised to remove the effect of frequency and surface resistance, since this enables the effects due to the structure dimensions to be characterised more readily:

$$\alpha_n = 20 \log_{10} e \left(\frac{h}{R_s}\right) \alpha_c \qquad \text{Units} : dB\Omega^{-1}m^2 \tag{3.101}$$

The dielectric attenuation factor is derived from an alternative form of Equation 3.100 [68]:

$$\alpha = \frac{k_o}{2Q} \left(\frac{\beta}{k_o}\right)^{-1} \tag{3.102}$$

Recalling that for a material with a loss given by Tan δ, the attenuation factor in dBm^{-1} can be written:

$$\alpha_d = [20 \log_{10} e] \, \pi \sqrt{\mu_o \epsilon_o} \sqrt{\epsilon_r} \, f \, [\text{Tan}\, \delta] \left(\frac{\beta}{k_o}\right)^{-1} \tag{3.103}$$

Chapter 4

Numerical and Measured Results for Uniform Striplines

4.1 Outline

This chapter presents numerical results for the convergence of the Transverse Resonance Diffraction (TRD) method for both TE and TM modes for uniform stripline. Results are also presented for the higher order mode cut-off frequencies, impedance and attenuation factor for uniform lines over a wide range of dimensional ratios. The values are compared to both purely numerical and purely analytical results, and differences highlighted between the TRD results and values computed by existing CAD systems. The sensitivity of the design parameters to variations in the dimensional ratios is also investigated. Higher order mode cut-off frequencies and attenuation factor measurements are also presented to verify the simulated results.

4.2 Convergence of the Method

The TRD method derived in Chapter 3 is formulated in terms of an admittance matrix of variable dimension, with the elements consisting of a summation of a finite number of

terms (Equations 3.49 and 3.50). The convergence of the formulation with the number of basis functions, P, and the number of field expansion terms, N, has to be determined in order to verify that the analysis is numerically stable.

4.2.1 Convergence of the TE Mode Formulation

The convergence of the first higher order mode is shown in Table 4.1 for a nominal 50Ω stripline. The results are calculated to four decimal places to illustrate the relative degree of convergence and do not imply accuracy to the same degree.

The values clearly indicate that two basis function terms and five field expansion terms are sufficient to calculate the cut-off frequencies to within one percent, and two basis function terms and twenty five field expansion terms to calculate the results to within 0.1 percent.

N	Cut-off Frequency (GHz)					
	No. of Basis Functions, P					
	1	2	3	4	5	6
5	7.0294	7.0402	7.0574	7.0802	7.0919	7.2380
10	6.9958	7.0001	7.0056	7.0130	7.0219	7.0276
15	6.9869	6.9900	6.9930	6.9966	7.0009	7.0053
25	6.9800	6.9823	6.9839	6.9853	6.9868	6.9885
50	6.9753	6.9771	6.9780	6.9786	6.9790	6.9795
75	6.9740	6.9756	6.9764	6.9768	6.9770	6.9773
100	6.9734	6.9750	6.9757	6.9760	6.9762	6.9764
200	6.9727	6.9742	6.9748	6.9751	6.9752	6.9753

Table 4.1: Convergence of the First Higher Order TE Mode Cut-off Frequency with the Number of Field Expansion Terms, N, and the Number of Basis Functions, P for a Nominal 50Ω Stripline (t=1.60mm, b=d=5.55mm, h=14.00mm and w=12.70mm)

4.2.2 Convergence of the TM Mode Formulation

The convergence for the first higher order TM mode is shown in Table 4.2, again for a nominal 50Ω stripline.

The results for the TM mode indicate that for the first higher order mode, two basis function terms and five field expansion terms are required to calculate the cut-

off frequencies to within one percent, and three basis function terms and fifteen field expansion terms are required to compute the frequency to within 0.1 percent.

The results illustrate the difference in convergence between the TE and TM mode formulations. Compared with the TE formulation, the TM analysis shows a strong convergence with the number of field expansion terms, as would be expected from the form of the mode admittance functions (Appendix B). The convergence with the number of basis functions is poorer than the TE formulation, with significant errors of between ten and fifteen percent for low numbers of basis functions. However, the rate of convergence of the TM analysis with the number of basis functions is better than the TE mode formulation.

The results for the convergence of the two formulations demonstrate that the TE and TM fields surrounding the stripline can be expressed accurately using a relatively low number of basis terms. The results indicate that the first higher order TM mode has a more complicated field shape than the TE mode, requiring a larger number of basis terms to calculate the fields to the desired accuracy.

4.3 Higher Order Mode Cut-Off Frequencies of Uniform Stripline

Results have been calculated for the variation in cut-off frequency with strip width (w:h); strip thickness (t:h); and strip position asymmetry (b:b+d). The results are compared to Oliner's conformal mapping analysis [11] which models the finite thickness stripline as a waveguide with an effective width. In addition, results for the variation in the strip width are compared to recently published data computed using finite elements [41] with an assumed exponential field decay in the transverse direction.

4.3.1 Variation in Cut-Off Frequency with Strip Width

Figure 4.1 shows the variation in the first higher order mode cut-off frequency with strip width for a range of strip thicknesses. The TRD results illustrate convergence to

N	Cut-off Frequency (GHz)					
	No. of Basis Functions, P					
	1	2	3	4	5	6
5		18.0853	18.0160	18.0069	17.9983	17.9973
10	20.2955	18.1139	18.0218	18.0200	18.0142	18.0078
15	20.4066	18.1188	18.0234	18.0226	18.0199	18.0161
25	20.4852	18.1217	18.0244	18.0245	18.0229	18.0214
50	20.5330	18.1234	18.0249	18.0248	18.0242	18.0236
75	20.5463	18.1239	18.0251	18.0250	18.0245	18.0241
100	20.5523	18.1241	18.0251	18.0251	18.0246	18.0243
200	20.5601	18.1243	18.0252	18.0252	18.0248	18.0245

Table 4.2: Convergence of the First Higher Order TM Mode Cut-off Frequency with the Number of Field Expansion Terms, N, and the Number of Basis Functions, P for a Nominal 50Ω Stripline (t=1.60mm, b=d=5.55mm, h=14.00mm and w=12.70mm)

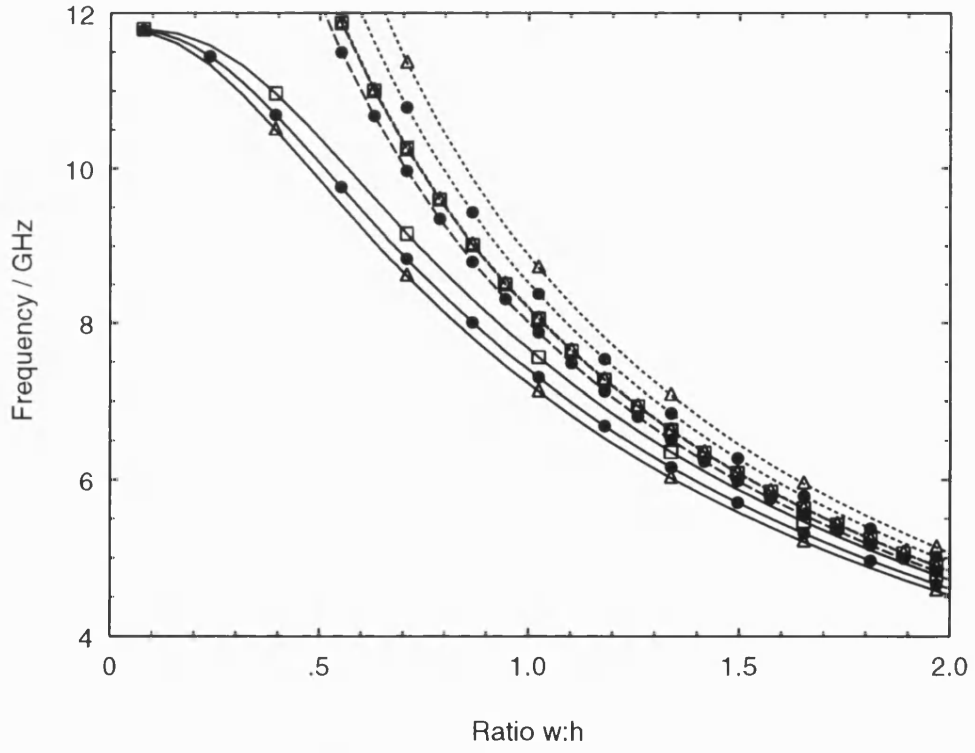

Figure 4.1: First Higher Order Mode Cut-Off Frequency versus Strip Width (w:h) computed by TRD (——) and Oliner's Finite Thickness Approximation (- - -) and Infinitely Thin Approximation (·····) for Various Strip Thicknesses (t:h=0.001[□]; t:h=0.126[•] and t:h=0.250[△]), b=d and h=12.70mm

the cut-off frequency of the parallel plate waveguide (11.803 GHz) as the strip becomes infinitely thin, as opposed to Oliner's analysis which increases rapidly. The agreement improves as the strip becomes wider, however Oliner's finite thickness analysis computes very similar results for thick strips (t:h=0.250) or very narrow strip (t:h=0.001). This is due to the finite thickness correction being unable to compensate for the overall trend in the cut-off frequency with strip thickness, the thickness (t:h=0.250) marking the upper bound of Oliner's analysis [11]. The correction does however reverse the trend of the cut-off frequencies for moderate values of strip thickness, agreeing with the TRD analysis and illustrating a decrease in cut-off frequency for an increase in strip thickness.

The variation with strip width is also compared to results computed using the finite element method [41], and plotted in Figure 4.2 as a percentage difference with respect to the TRD method to highlight the differences between the methods.

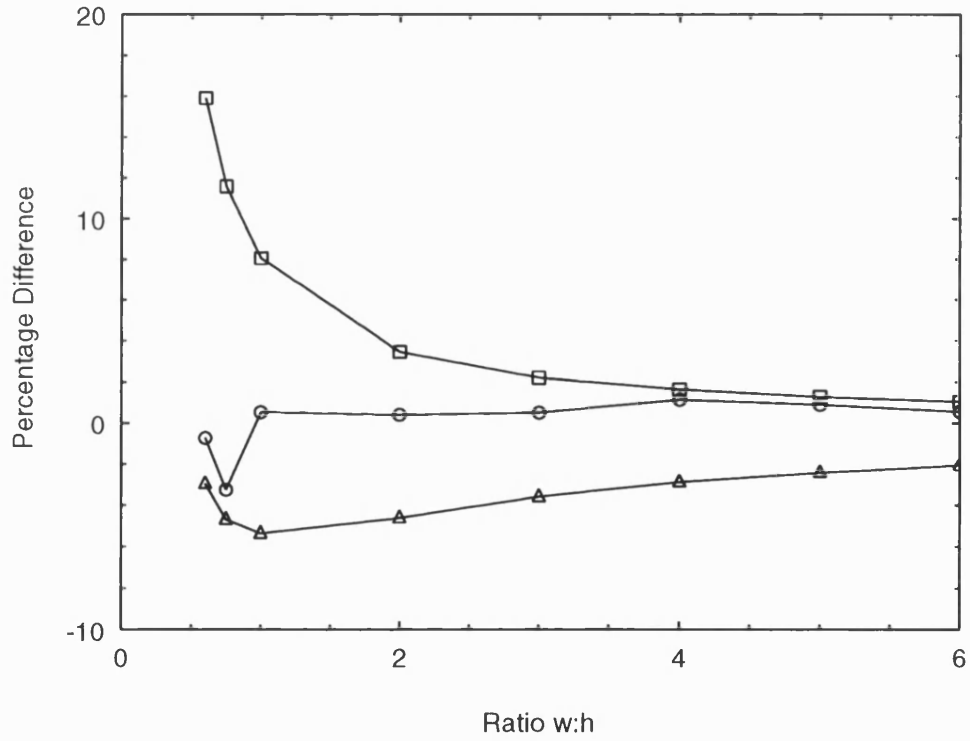

Figure 4.2: Percentage Difference between the First Higher Order Mode Cut-Off Frequency versus Strip Width (w:h) computed by the TRD Method and Oliner's Analysis [□];TRD and a Conformal Mapping Effective Width Correction [△]; and TRD and a Finite Element Analysis [○] for b=d=5.55mm, t=1.60mm and h=12.70mm

The results illustrate that Oliner's conformal mapping analysis produces significant differences of between one and sixteen percent, with agreement improving as the strip becomes wider. The errors for narrow strips are due to errors in the evaluation of the conformal mapping by approximate functions, and interaction of the fringing fields at the ends of the strip. Oliner suggests a minimum strip width of w:h=0.5, however the finite element and TRD analyses which typically agree to within one percent, indicate that this is over optimistic. The effective width correction [41] applied to the conformal mapping appears to give a lower bound on the solution with improved agreement for narrow strips compared with Oliner's analysis.

4.3.2 Variation in Cut-Off Frequency with Strip Thickness

Figure 4.3 illustrates the variation in first higher order mode cut-off frequency with strip thickness (t:h) for a range of strip widths. The TRD results show a comparatively small variation with strip thickness, suggesting the cut-off frequency is dominated by the width of the strip. This contrasts with Oliner's finite thickness approximation which shows a stronger variation with thickness. The agreement between the methods improves with strip width, indicating that the effective width correction should be a function of strip width as well as strip thickness [23].

4.3.3 Variation in Cut-Off Frequency with Strip Position Asymmetry

Figure 4.4 shows the variation in first higher order mode cut-off frequency with strip position asymmetry (b:b+d) for various strip thicknesses (t:h). The results show improved agreement between the methods for moderate strip thicknesses by using a finite thickness correction, which again corrects the trend in cut-off frequency with thickness for symmetrical stripline (b:b+d=0.5). The TRD analysis illustrates a smoother variation of cut-off frequency around the symmetric strip position than the conformal mapping analysis. This suggests that manufacturing tolerances in strip position will not alter the monomode bandwidth significantly.

Figure 4.5 illustrates the variation in the cut-off frequency with strip position asym-

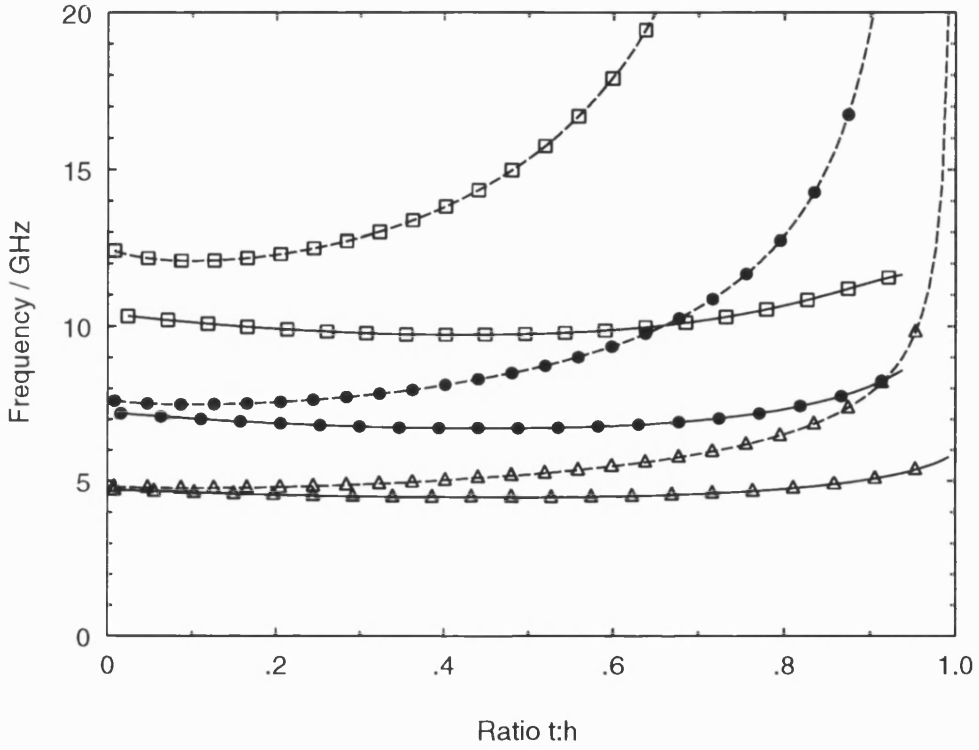

Figure 4.3: First Higher Order Mode Cut-Off Frequency versus Strip Thickness (t:h) computed by TRD (——) and Oliner's Finite Thickness Approximation (- - -) for Various Strip Widths (w:h=0.50[□]; w:h=1.10[•] and w:h=2.00[△]), b=d and h=12.70mm

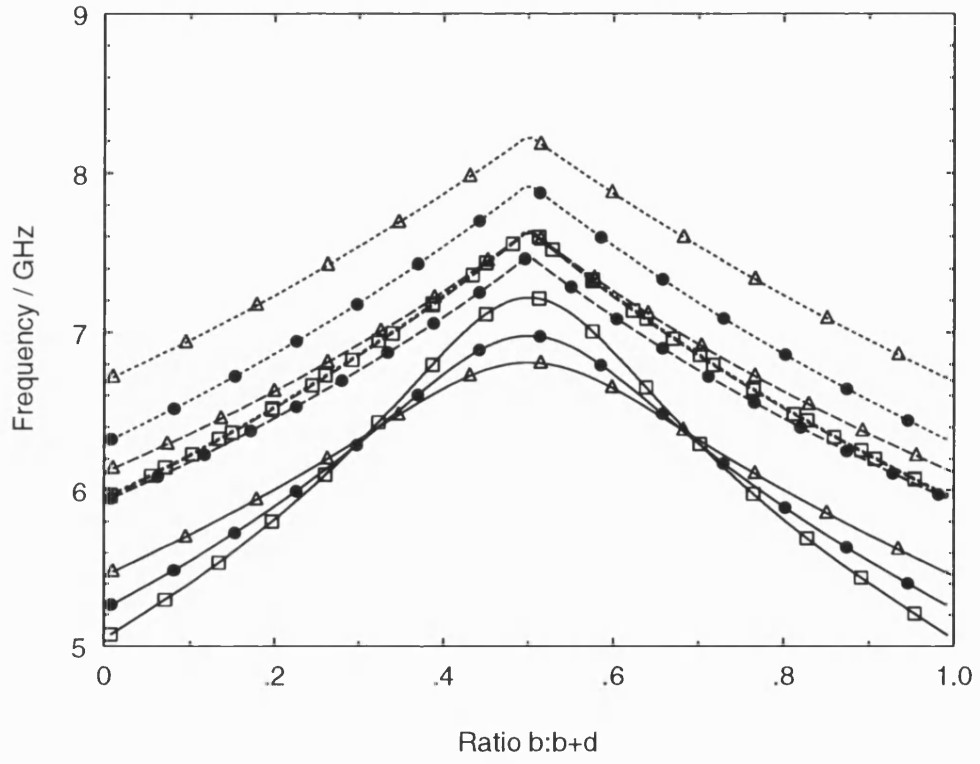

Figure 4.4: First Higher Order Mode Cut-Off Frequency versus Strip Position Asymmetry (b:b+d) computed by TRD (——) and Oliner's Finite Thickness Approximation (- - -) and Infinitely Thin Approximation (·····) for Various Strip Thicknesses (t:h=0.001[□]; t:h=0.126[•] and t:h=0.250[△]), w=14.00mm and h=12.70mm

metry for various strip widths and emphasises the points above and showing that for strip widths in excess of w:h=2.0 the agreement in comparatively good.

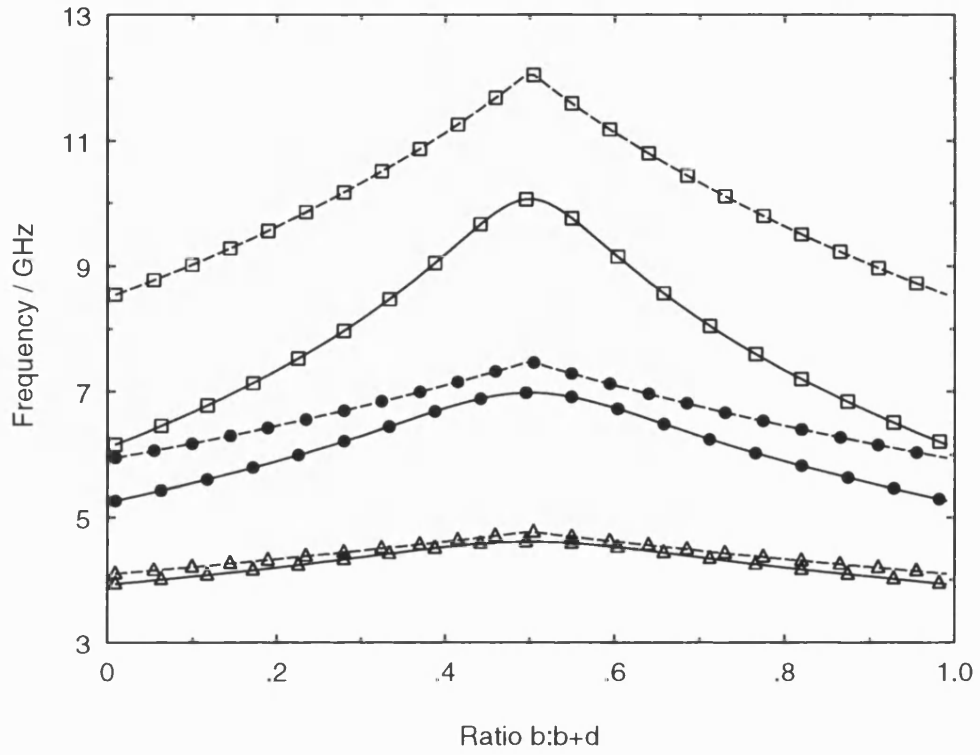

Figure 4.5: First Higher Order Mode Cut-Off Frequency versus Strip Position Asymmetry (b:b+d) computed by TRD (——) and Oliner's Approximation (- - -) for Various Strip Widths (w:h=0.50[□]; w:h=1.10[•] and w:h=2.00[△]), t=1.60mm and h=12.70mm

4.3.4 Calculation of Monomode Bandwidth in Practical Systems

The results illustrate that traditional conformal mapping techniques provide a significant overestimate of the first higher order mode of striplines with commonly used dimensions. Historically this has not been significant since the monomode bandwidth of a system is set by the widest strip, which corresponds to a width of w:h=2.80 for a typical system. The error between the conformal mapping and TRD values (Figure 4.2) is therefore low. The conformal mapping result will be an overestimate, which may become important for networks designed with a small or non-existent safety factor between the operating frequency and the monomode bandwidth.

4.4 Impedance of Uniform Stripline

TEM impedances are calculated using the TRD method and compared to values computed using conformal mapping techniques [13, 23, 28] for a range of dimensions. Results are also compared to EEsof's Linecalc package and Hewlett Packard's HP85180A High Frequency Structure Simulator (HFSS) Finite Elements package for a limited set of striplines.

4.4.1 Convergence of Impedance Measures

The three impedance measures that can be calculated for the stripline structure: the power-voltage impedance, Z_{pv}; the power-current impedance Z_{pi}; and the voltage-current impedance, Z_{vi} are defined in Chapter 3. Ideally the three measures should give consistent results. However, for a given number of field expansion terms the accuracy with which the voltage, current and power flow can be calculated will differ. Figure 4.6 shows the percentage difference between the impedance measures and Cohn's conformal mapping results [13] for nominal 30Ω, 50Ω and 75Ω striplines.

The power-voltage formulation converges fastest since the problem is formulated in terms of the magnetic scalar potentials with the $\hat{x}$ directed electric field as the discretised field that is solved for. Provided a sufficient number of terms are chosen, the power-current and hence the voltage-current measures converge to the power-voltage calculation. Figure 4.6 also shows that the rate of convergence differs depending on the stripline dimensions. The convergence behaviour is due to the current components from the edges of the stripline. The TRD analysis assumes a singularity behaviour based on a finite thickness stripline. Collin [19] derives the minimum order of the singularity required to model a metallic wedge of given internal angle. The actual order of the singularity present will differ if there is significant interaction between the edge singularities, as is the case for very thin or narrow conductors. The current calculation is very sensitive to the exact order of the edge singularity and if the order is incorrect more field expansion terms are required for convergence. It can be shown for very thin strips that a singularity behaviour of $\mid r \mid^{-\frac{1}{2}}$ gives a significantly improved convergence.

The impedance comparisons in the following sections use the power-voltage impedance measure computed with twenty five field expansion terms.

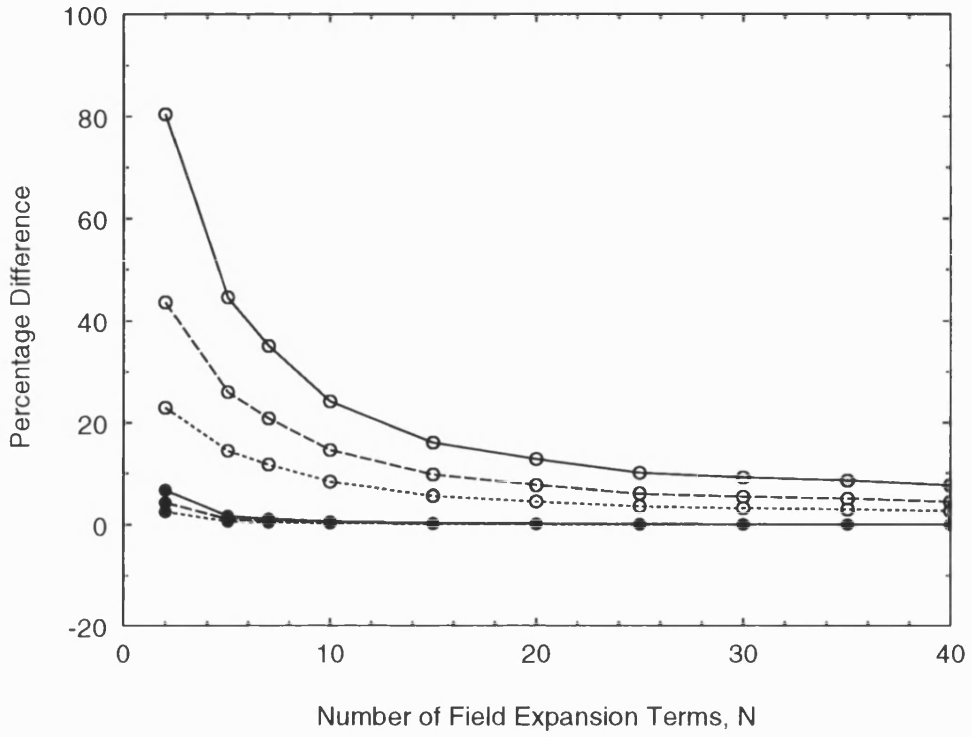

Figure 4.6: Percentage Difference between Cohn's Impedance Calculation and Z_{pv} [•] and Z_{pi} [o] Impedances for a Nominal 75Ω Stripline (——), 50Ω Stripline (- - -) and 30Ω Stripline (· · · · · ·)

4.4.2 Variation in Impedance with Strip Width

Figure 4.7 shows the variation in impedance with strip width calculated by the TRD analysis and Wheeler's analysis [23]. The percentage difference with respect to Wheeler's analysis is also shown. The results show a decrease in percentage difference as the width increases as the impedance is dominated by the parallel plate capacitance, with the error for wide strips within the 0.5% bound on Wheeler's results.

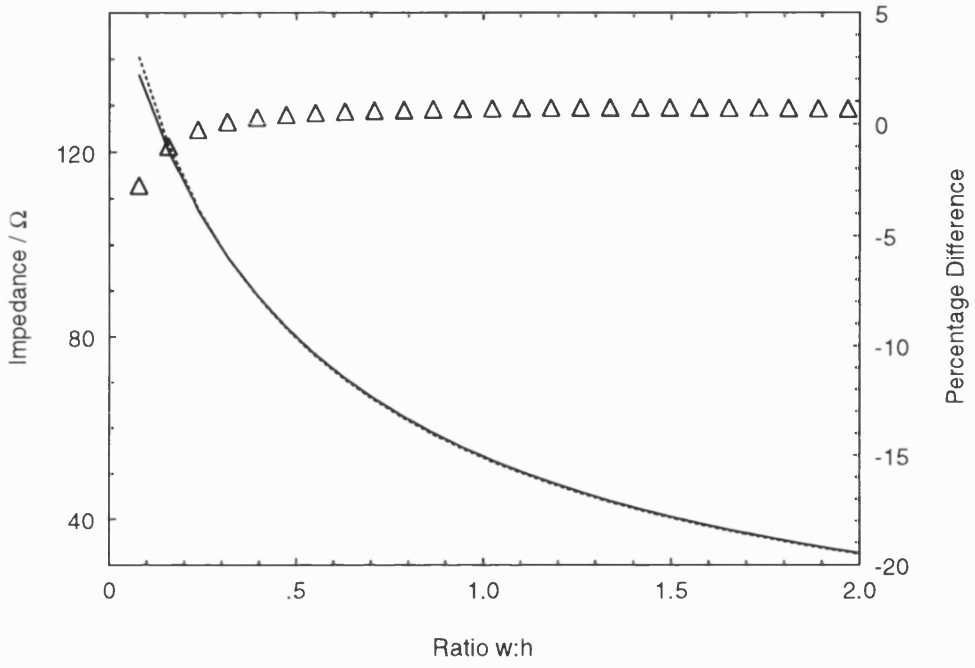

Figure 4.7: Impedance and Percentage Difference in Impedance [△] between TRD Power-Voltage Impedance, (Z_{pv}), (——); and Wheeler's Analysis (· · · · · ·) for a Variation in Strip Width for b=d, t=1.60mm and h=12.70mm

4.4.3 Variation in Impedance with Strip Thickness

Figure 4.8 shows the variation in impedance and percentage difference between Wheeler's results and the TRD results for a range of strip thicknesses. The agreement is reasonable across for a range of strip thicknesses up to t:h=0.8, beyond this value the percentage difference rapidly rises as small absolute differences in the impedance produce very large percentage differences between the methods.

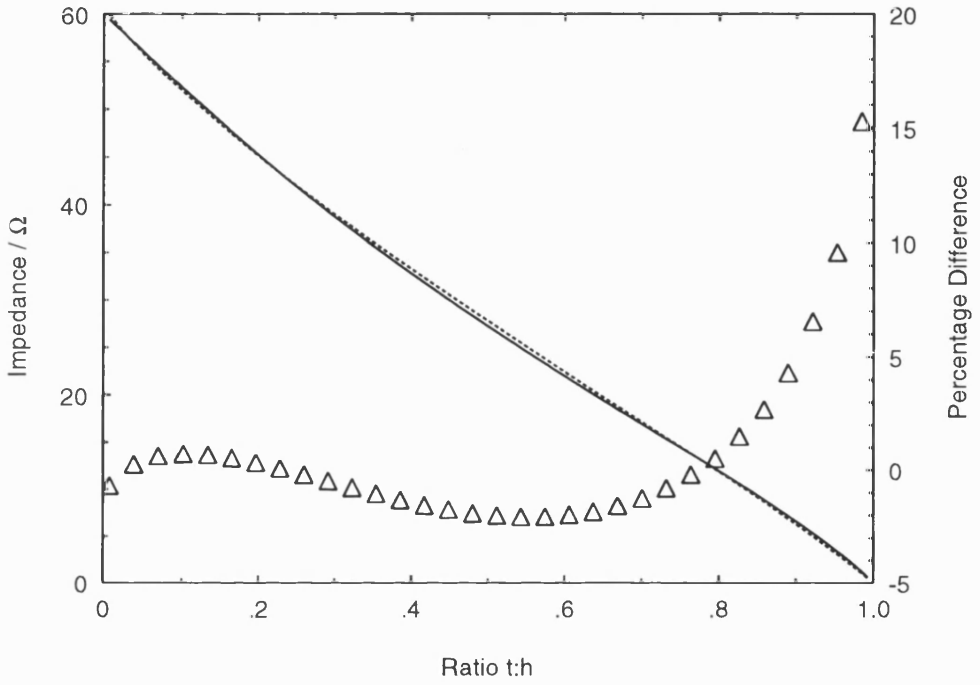

Figure 4.8: Impedance and Percentage Difference in Impedance [△] between TRD Power-Voltage Impedance, (Z_{pv}), (——); and Cohn's Analysis (· · · · · ·) for a Variation in Strip Thickness for b=d, w=14.00mm and h=12.70mm

4.4.4 Variation in Impedance with Strip Position Asymmetry

Figure 4.9 shows the variation in impedance and percentage difference between Robrish's results [28] for a wide strip and the TRD results for a range of strip position asymmetries (b:b+d). Robrish's analysis is accurate to ±2% for $0.2 < b : b + d < 0.8$ and t:h< 0.2. The TRD results are within these limits for the range of values stated, however the

differences increase relatively rapidly outside these bounds.

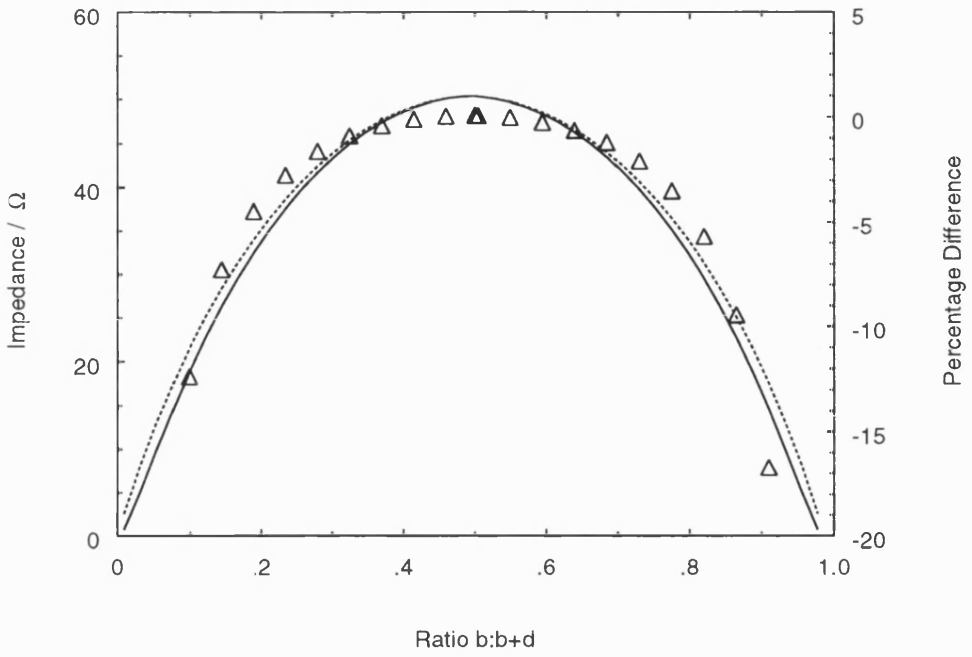

Figure 4.9: Impedance and Percentage Difference in Impedance [△] between TRD Power-Voltage Impedance, (Z_{pv}), (——); and Robrish's Analysis (· · · · · ·) for a Variation in Strip Position Asymmetry for t=1.60mm, w=14.00mm and h=12.70mm

4.4.5 Comparison of the TRD Impedance Results with Commercial Software

The TRD results are compared to values computed by Hewlett Packard's HFSS (Version A1.29) and EEsof Linecalc (Version 3.0) packages in Table 4.3. The values are quoted to four significant figures in order to compare the relative accuracies of the three methods. The agreement is excellent between the different techniques, with a maximum difference of 0.8%. The HFSS results are computed as a "ports only" 2D solution, and are shown for both of the ports.

Dimension (mm)				Impedance (Ω)			
t	b	d	h	TRD	HFSS		EEsof
				Z_{pv}	Port 1	Port 2	Linecalc
1.600	5.550	5.550	14.08	50.18	50.19	50.26	50.15
1.600	5.520	5.580	14.08	50.18	49.77	49.83	50.15
1.600	5.000	6.100	14.08	50.05	49.74	49.73	49.77
1.600	5.550	5.550	28.00	30.08	30.07	30.11	30.07
1.600	5.550	5.550	42.00	21.44	21.45	21.46	21.44
0.800	5.950	5.950	14.08	54.84	54.73	54.36	54.79
1.602	5.549	5.549	14.08	50.17	50.06	50.16	50.14
2.400	5.150	5.150	14.08	45.77	46.15	46.15	46.03

Table 4.3: Comparison of Impedances Calculated by the TRD Method and Commercial Software Packages for a Range of Dimensions

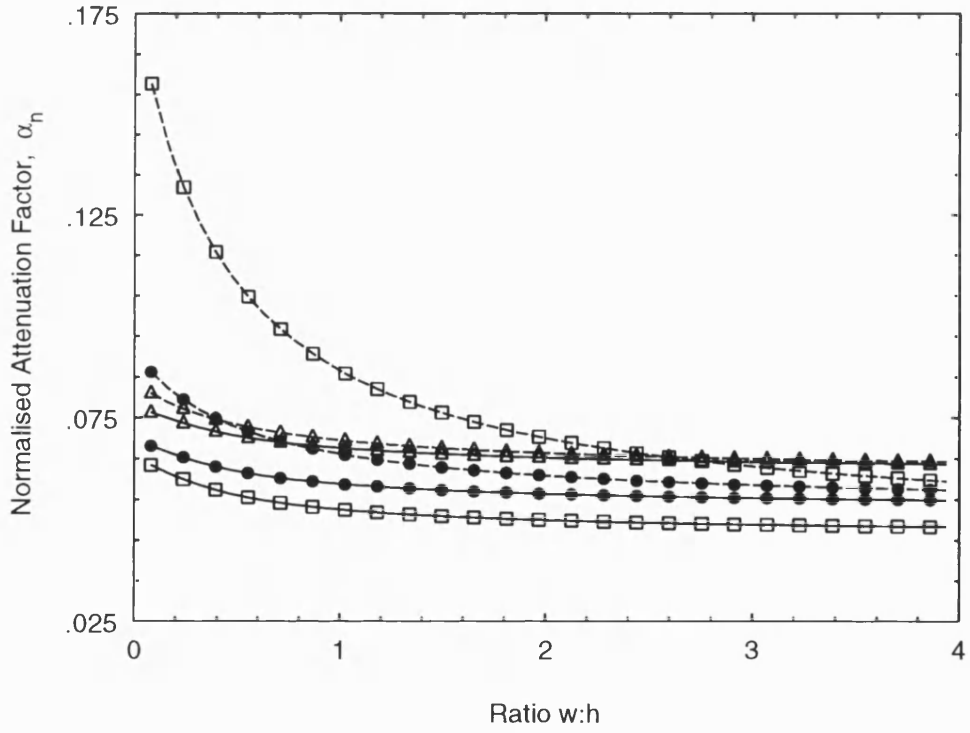

Figure 4.10: Normalised Attenuation Factor versus Strip Width (w:h) computed by TRD(——) and Cohn's Analysis (- - -) for Various Strip Thicknesses t:h=0.001, [□]; t:h=0.126, [•]; and t:h=0.250, [△]; b=d and h=12.70mm

4.5 Attenuation Factor of Uniform Stripline

The normalised attenuation factors of uniform stripline have been computed using the TRD method and compared with Cohn's conformal mapping analysis for variations in strip width, strip thickness and strip position asymmetry. In addition, the TRD results are compared with Hewlett Packard's HFSS software for a given structure, and also an integral equation formulation [39].

4.5.1 Variation in Attenuation Factor with Strip Width

Figure 4.10 shows the variation in normalised attenuation factor with strip width for a range of strip thicknesses. The graph shows that the difference between Cohn's analysis for the wide strips case (w:h> 0.40) and the TRD analysis decreases as the strips become progressively thicker and the effects of the edge singularities decrease. The TRD results also show a consistent trend of increasing attenuation factor with increasing strip thickness, contrary to Cohn's analysis for very narrow strips, but in agreement for very wide strips.

4.5.2 Variation in Attenuation Factor with Strip Thickness

Figure 4.11 shows the variation in normalised attenuation factor with strip thickness for various strip widths. The upper limit of Cohn's analysis is t:h=0.25, with the agreement between the two methods improving up to this point. The results also show decreasing attenuation with increasing strip width. Cohn's results also show an increase in attenuation as the strips become narrow suggesting the power flow is decreasing faster than the dissipation, as opposed to the TRD method which gives a monatonic decrease. This is attributable to the TRD analysis accurately modelling the singularities at the edge of the strip, around which the majority of the power flows. This suggests that the power flow will not be as sensitive to a variation in strip dimensions as the conformal mapping analysis which models the stripline as a co-axial cylinder of effective diameter [18]. The TRD and conformal mapping results increase rapidly as the strip becomes thicker, due to the increase in power dissipation in the ground planes.

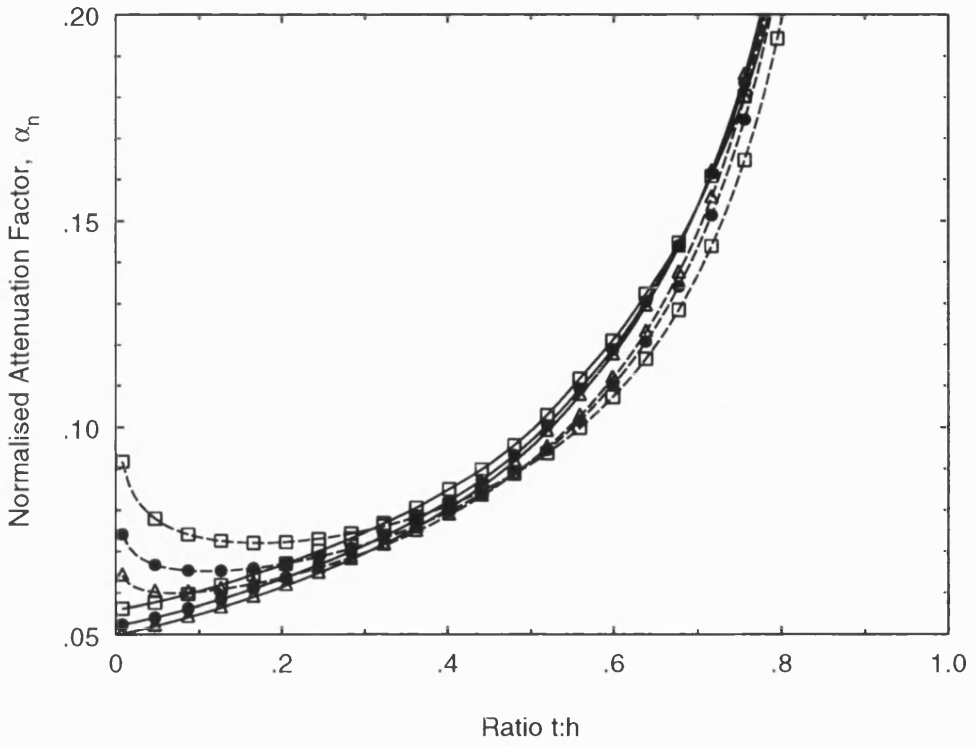

Figure 4.11: Normalised Attenuation Factor versus Strip Thickness (t:h) computed by TRD(——) and Cohn's Analysis (- - -) for Various Strip Widths w:h=0.50, [□]; w:h=1.102, [•]; and w:h=2.00, [△]; b=d, h=12.70mm.

4.5.3 Variation in Attenuation Factor with Strip Position Asymmetry

Figure 4.12 shows the variation in normalised attenuation factor with strip position asymmetry for a range of strip thicknesses between t:h=0.001 and t:h=0.250. Cohn's values are only valid for the symmetrical position and again emphasise the comments made in the previous sections. The TRD results showing a decrease in attenuation factor as the asymmetry increases with a rapid rise for very large asymmetries as the dissipation in the ground planes becomes significant.

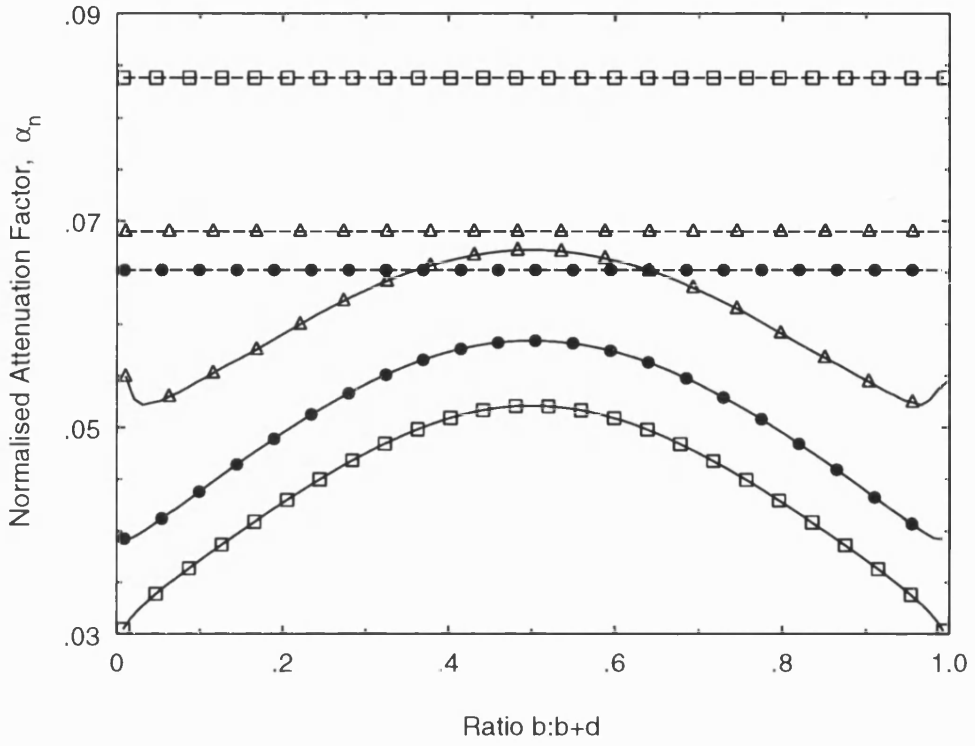

Figure 4.12: Normalised Attenuation Factor versus Strip Position Asymmetry (b:b+d) computed by TRD(——) and Cohn's Analysis (- - -) for Various Strip Thicknesses t:h=0.001, [□];t:h=0.126, [•]; and t:h=0.250, [△]; w:h=1.102, h=12.70mm.

Method	α_n $(dB\Omega^{-1}m^2)$	α (dBm^{-1})
Cohn	0.065	0.17
TRD	0.059	0.15
HFSS (Port 1)	0.065	0.17
(Port 2)	0.068	0.18
EEsof Linecalc	0.064	0.17

Table 4.4: Table of Normalised and Un-Normalised Attenuation Factor Computed by the TRD analysis; Cohn's Conformal Mapping analysis; EEsof's Linecalc and Hewlett Packard's HFSS analysis for a Stripline of Resistivity $\rho = 90n\Omega m$, w=14.00mm, b=d=5.55mm, t=1.60mm at 3.00GHz

4.5.4 Comparison of TRD Attenuation Factor Results with Commercial Packages

The TRD results are compared in Table 4.4 with results obtained by conformal mapping [13], EEsof's Linecalc Package (Version 3.0) and Hewlett Packard's HFSS (Version A1.29). The Linecalc value has a significant uncertainty since it is only quoted as an attenuation factor to two decimal places. The results quoted for HFSS are the imaginary component of the propagation constant computed at each of the ports for a full 3D solution. The attenuation factors are in agreement to within ± 0.02dB which corresponds to an attenuation of between 3.5% and 4.2% of signal power.

4.5.5 Comparison of Attenuation Factor Calculation with An Integral Equation Method

The TRD and conformal mapping results presented in the earlier sections use a small perturbation method i.e. the loss is calculated from the field computed for a lossless structure. Integral equation methods can be used to compute the complex propagation constant of a stripline [39]. Results are presented for structures with materials and dimensions that are normally found in printed circuit interconnections, and hence the skin depth is of a comparable order to the stripline dimensions at lower frequencies.

Figure 4.13 shows the attenuation factor versus frequency for symmetrically positioned copper and molybdenum striplines. Figure 4.14 shows the attenuation factor for an asymmetrical case. The TRD results are calculated assuming a frequency dependence of $\sqrt{f}$, and show excellent agreement with Kiang's results for frequencies approaching 1GHz, where the ratio of the skin depth, δ_s, to the strip thickness, t, is δ_s:t=0.083 for copper and δ_s:t=0.145 for molybdenum. This compares to ratios of δ_s:t=0.83 and δ_s:t=1.45 respectively at 10MHz, with significant differences between the results. The small perturbation methods (TRD and Cohn's analysis [13]) will give a d.c value of zero, whereas Kiang's results converge to a finite attenuation.

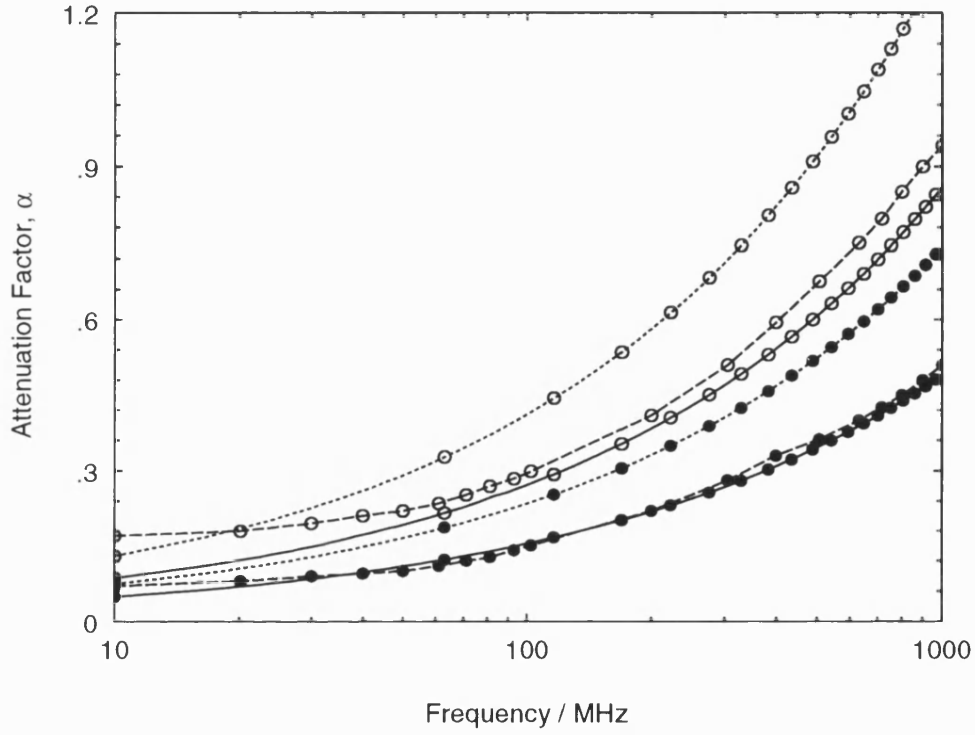

Figure 4.13: Attenuation Factor versus Frequency computed by TRD Analysis (——), Kiang's Integral Equation Method (- - -) and Cohn's Conformal Mapping Method (· · · · · ·) for a Copper Stripline, ($\rho = 17.2n\Omega m$), [•]; and a Molybdenum Stripline, ($\rho = 52.1n\Omega m$), [○] for w=100μm, b=d=287.5μm and t=25μm

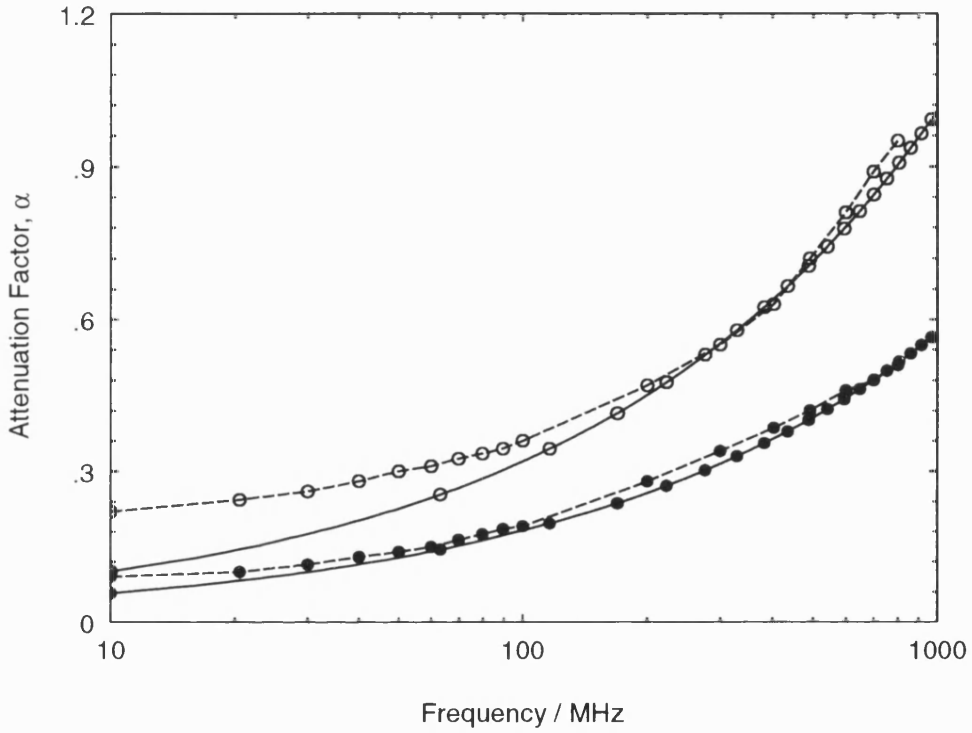

Figure 4.14: Attenuation Factor versus Frequency computed by TRD Analysis (——) and Kiang's Integral Equation Method (- - -) for a Copper Stripline, (ρ = 17.2$n\Omega m$), [•]; and a Molybdenum Stripline, (ρ = 52.1$n\Omega m$), [○] for w=100μm, b=387.5μm, d=187.5μm and t=25μm

4.6 Comparison of TRD Results with Measured Data

4.6.1 Method of Measurement

The cut-off frequencies and attenuation factor have been measured using a lightly coupled probe resonator technique. This has been described for the Inset Dielectric Guide structure [69]. The method involves exciting the test fixture shown in Figure 4.15 with the rotatable probes either parallel or perpendicular to the strip to excite the even or odd symmetric modes respectively (Figure 4.16(a) and (b)). The transmission through the structure (S_{21}) was measured using an HP8510B Network Analyser. A typical plot is shown in Figure 4.17 for a nominal 50Ω stripline.

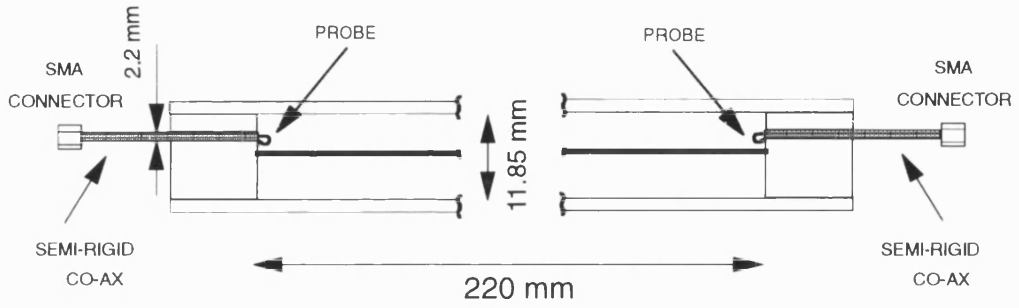

Figure 4.15: Side View of Uniform Line Test Fixture used to take Measurements

4.6.2 Measured Data for the Higher Order Mode Cut-off Frequencies

The local maxima in Figure 4.17 correspond to an integral number of half guide wavelengths. The position of the localised maxima, f_n are given by:

$$f_n = \frac{c}{2\pi}\left[k_c^2 + \left(\frac{n\pi}{L}\right)^2\right]^{\frac{1}{2}} \tag{4.1}$$

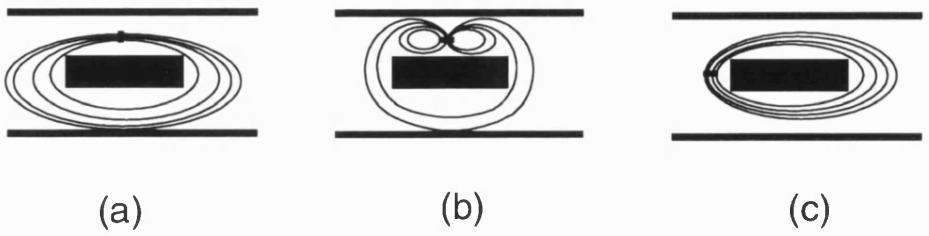

Figure 4.16: Magnetic Field Excitation for Probes Placed Above the Strip; Perpendicular to the Strip (a) and Parallel to the Strip (b); and Beside the Strip (c)

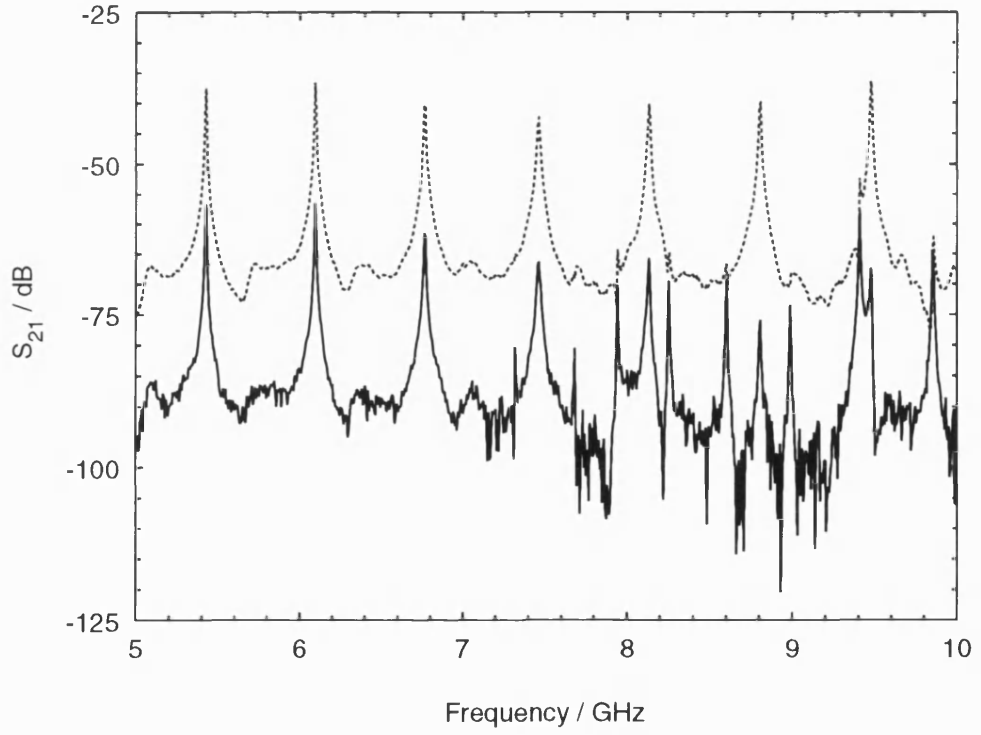

Figure 4.17: Plot of Transmission through Test Fixture versus Frequency for Probe Orientation (a) (- - -) and Probe Orientation (b) (———) for a Nominal 50Ω Stripline, b=4.965mm, d=5.265mm t=1.64mm, w=14.00mm and L=220mm taken using an HP8510B (801 Points and Averaging=100)

The maxima for the fundamental mode of propagation are therefore spaced at 681 MHz intervals, and clearly identifiable in Figure 4.17(- - -). The second set of maxima present in Figure 4.17 (——) are due to the first higher order mode, and propagate initially with a low amplitude and high Q, with the amplitude increasing and Q decreasing with frequency.

The determination of the cut-off frequency relies on the value of n in Equation 4.1 being determined for each of the maxima. The values are found by trial and error since some of the maxima may be missing due to the overall frequency response of the test fixture, or maxima coinciding with the maxima of the dominant mode.

The measured cut-off frequencies, the standard deviation of the measured values and number of maxima measured, N, are shown in Table 4.5 for a range of striplines with varying width.

Ratio w:h	Frequency (GHz)	Std. Dev. (GHz)	Std. Dev. (%)	No. of Maxima N
0.604	10.149	0.014	0.14	21
1.179	7.165	0.007	0.08	11
1.769	5.374	0.041	0.75	16
2.358	4.239	0.041	0.94	12
2.948	3.581	0.052	1.45	7
3.538	3.051	0.029	0.92	7

Table 4.5: Measured Results for the First Higher Order Mode Cut-off Frequency for a stripline with t=1.64mm, b=4.965mm, d=5.265mm, h=11.87mm

The measured data is compared to the TRD method; a finite thickness central conductor conformal mapping analysis [11] and Hewlett Packard's HP85180A High Frequency Structure Simulator (HFSS) finite elements package.

Figures 4.18 and 4.19 illustrate that the TRD results are in excellent agreement with the measured data for the first higher order mode cut-off frequency, agreeing to within two percent and typically within one percent. The maximum errors coincide with the largest percentage standard deviations suggesting that the error is due to measurement inaccuracy as opposed to the TRD method. Oliner's finite thickness central conductor conformal mapping analysis gives an error of between three and eighteen percent, with a decreasing error as the strip becomes wider. This is expected as the conformal mapping approximation improves as the overall effect of the singularities decreases. Results are

computed for two versions of the HFSS software for a 2D "ports only" solution with a 0.1% convergence. The HFSS Version A1.29 results have previously been published [70] and illustrate differences of up to nine percent. The results were recalculated using Version A2.06 which gives significantly improved results with differences comparable to that of the TRD method. The HFSS results however do include one result that has a four percent difference from the measured values.

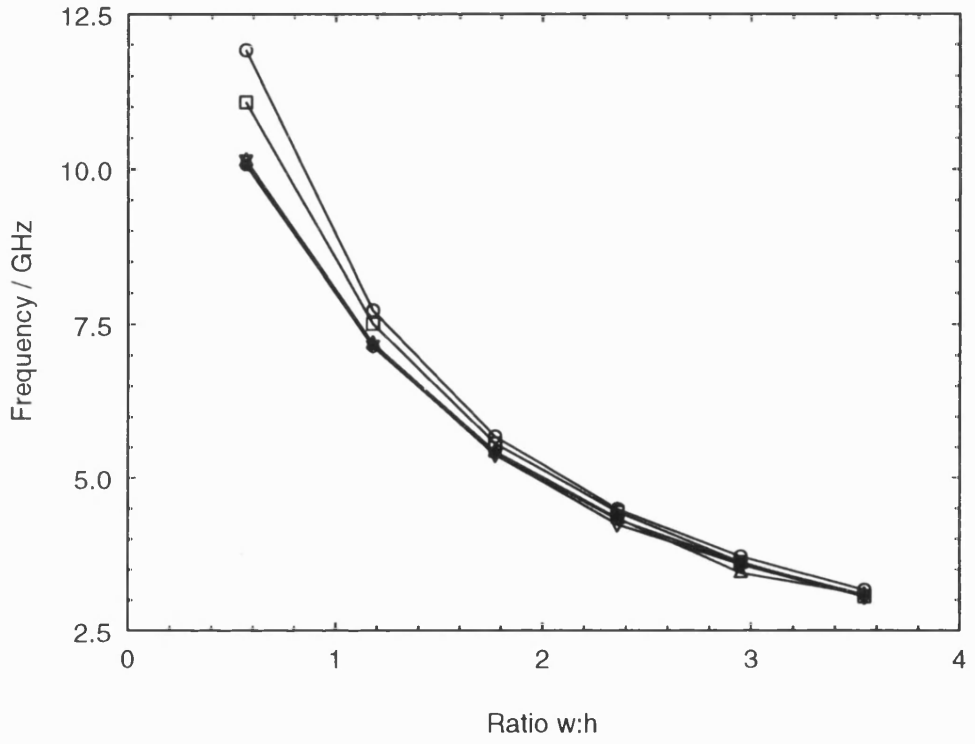

Figure 4.18: First Higher Order Mode Cut-Off Frequency versus Strip Width (w:h) for Measured Data [∇]; TRD Analysis, [$\bullet$]; Oliner's Finite Thickness Analysis, [$\circ$]; HFSS Ver. A1.29, [$\square$] and HFSS Ver. A2.06, [$\triangle$] for b=4.965mm, d=5.265mm, t=1.64mm and h=11.87mm

The repeatability of the method was also studied. The greatest variation was in the transmission level between successive experiments since the probes have to be carefully aligned to achieve a given level. The repeatability of the cut-off frequency measurements however, is very good since they rely on the determination of well defined resonant frequencies which are largely unaffected by the absolute level of the transmission provided it is sufficiently low (< -25dB [69]).

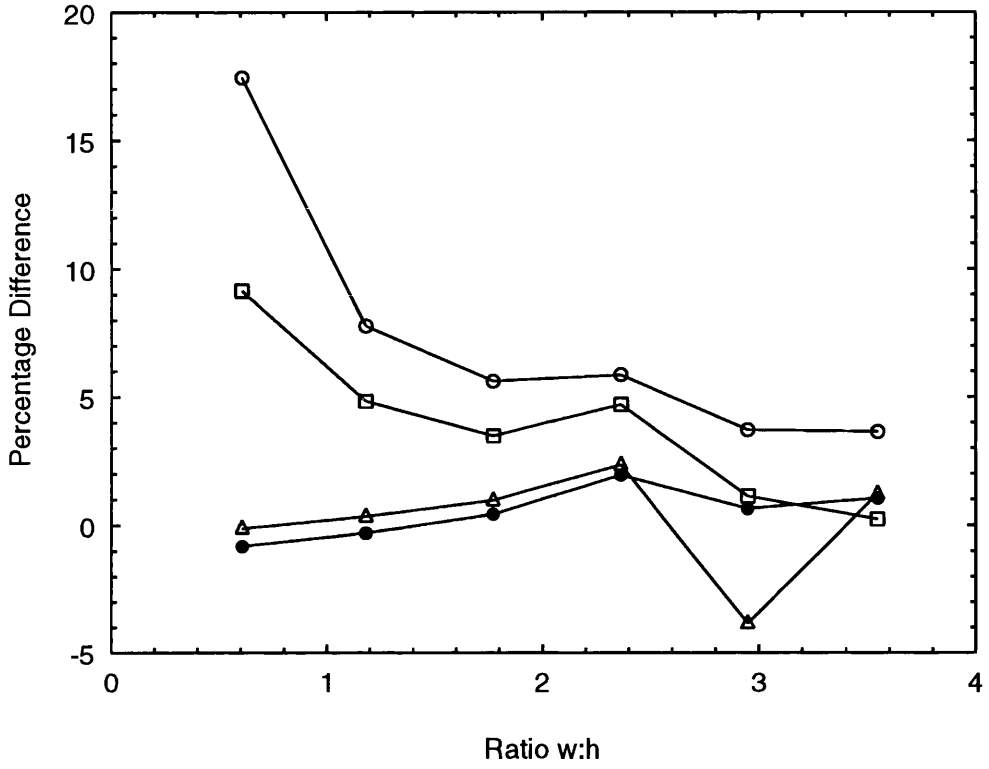

Figure 4.19: Percentage Variation between Measured Cut-Off Frequencies and Computed Cut-Off Frequencies for the First Higher Order Mode Calculated by TRD Analysis, [•]; Oliner's Finite Thickness Analysis, [o]; HFSS Ver. A1.29, [□] and HFSS Ver. A2.06, [△] for b=4.965mm, d=5.265mm, t=1.64mm and h=11.87mm

Method	Details	CPU Time (Secs)	Storage	Platform
HFSS Ver. A2.06	Ports Only Computation 0.1 % Convergence	660	23.6 MBytes	HP 715/50
TRD	3 Basis Terms 25 Field Expansion Terms	37	64kBytes	HP 710

Table 4.6: Comparison of Computational Requirements for the Calculation of the First Two Higher Order Mode Cut-Off Frequencies for a Nominal 50Ω Stripline

Table 4.6 compares the computational requirement to calculate the first two higher order mode cut-off frequencies for the HFSS Version A2.06 and TRD methods. Oliner's conformal mapping analysis can be evaluated as a closed form expression, hence is excluded from the comparison. The timing results show that the TRD method calculates the frequencies a factor of 25 times faster than the HFSS analysis after taking into account the computing performance. In addition the storage requirement is a factor of 350 times less.

4.6.3 Measured Data for the Attenuation Factor

The attenuation factor for the stripline structure is calculated from the measured Q factor, assuming the measured value is the unloaded Q of the structure.

A transmission line excited by one mode of propagation has a Q factor and attenuation factor given by:

$$Q = \omega \frac{\text{Time Averaged Total Energy Stored in Structure}}{\text{Time Averaged Power Dissipation in Structure}} \tag{4.2}$$

$$\alpha = \frac{1}{2} \frac{\text{Power Dissipated in Structure}}{\text{Power Flow in Structure}} \tag{4.3}$$

Substituting Equation 4.3 into Equation 4.2:

$$Q = \frac{1}{2\alpha} \omega \frac{\text{Time Averaged Total Energy in Structure}}{\text{Power Flow}} \tag{4.4}$$

$$= \frac{\omega}{2\alpha V_g} \tag{4.5}$$

The group velocity is defined as the ratio of the power flow to the time averaged total energy in the structure [68], hence it can be shown that:

$$Q = \frac{1}{2\alpha} k_o \left(\frac{\beta}{k_o}\right)^{-1} \tag{4.6}$$

Recalling that the attenuation factors are expressed as normalised values in units of dB's per metre and rearranging in terms of the measured Q factor, Q_m:

$$\alpha_n = [20 \log_{10} e] \frac{k_o}{2Q_m} \left(\frac{h}{R_s}\right) \left(\frac{\beta}{k_o}\right)^{-1} \tag{4.7}$$

A further correction is introduced for the surface roughness of the material, Δ, [57]:

$$\alpha_n = \frac{[20\log_{10}e]\ k_o\ h}{2Q_m\left[1+\frac{2}{\pi}\mathrm{Tan}^{-1}\left(1.4\frac{\Delta}{\delta_s}\right)^2\right]}\left(\frac{\beta}{k_o}\right)^{-1} \tag{4.8}$$

$$= \frac{h\sqrt{\pi}\sqrt{\epsilon_o}\,[20\log_{10}e]}{Q_m\left[1+\frac{2}{\pi}\mathrm{Tan}^{-1}\left(1.4\frac{\Delta}{\delta_s}\right)^2\right]}\sqrt{\frac{f}{\rho}}\left(\frac{\beta}{k_o}\right)^{-1} \tag{4.9}$$

The average measured Q factors and the calculated normalised attenuation factors are shown in Table 4.7 for the fundamental TEM mode of propagation with the standard deviation of the measured and calculated values and the number of maxima measured. The attenuation factors are normalised assuming a resistivity of brass of $\rho = 90n\Omega\ m$. The results are compared with values computed by the TRD method and also a finite thickness central conductor conformal mapping analysis [13] in Figure 4.20. The error bars mark one standard deviation either side of the average measured Q factor.

Figure 4.20 illustrates that the TRD method is between four and fourteen percent lower than Cohn's results. This supports Cohn's prediction of an overestimate of up to ten percent from the conformal mapping analysis due to approximations in the evaluation of the elliptic integrals.

The measurements were taken first with the probes placed above the stripline. The results for very thin strips shows reasonable agreement with the calculated values, however the results for wider strips show a considerable error and the measurements appeared to be sensitive to absorber placed at the edges of the test fixture. This is due to the probes exciting the TM transverse propagating mode of the parallel plate, in addition to the magnetic field surrounding the strip. The propagation of energy in the transverse direction appears as an additional loss of the structure, hence the measured attenuation factor is increased. The measurements were repeated using the coupled lines test fixture which excites the fields from the side of the strip, as shown in Figure 4.16(c), as opposed to exciting the fields from above the strip as shown in Figures 4.16(a) and (b). The position of the probe at the side of the strip reduces the coupling to the transverse propagating mode with the results in Figure 4.20 showing improved agreement.

The measurements exhibit a relatively large standard deviation which limits the

Ratio w:h	Probe Above Strip					Probe Beside Strip				
	Q_{meas}	σ_{meas}	α_n	σ_α	N	Q_{meas}	σ_{meas}	α_n	σ_α	N
0.604	714.2	226.2	0.078	0.029	10	563.4	143.8	0.123	0.062	12
1.179	769.1	230.9	0.085	0.030	15	408.8	113.2	0.146	0.066	9
1.769	420.3	139.3	0.114	0.031	7	650.7	123.6	0.076	0.030	6
2.358	255.0	49.1	0.160	0.043	5	493.1	96.9	0.089	0.022	5
2.948	179.4	43.2	0.183	0.018	3					
3.538	131.6	32.5	0.268	0.108	3					

Table 4.7: Measured Results for the Q Factor and Normalised Attenuation Factor for a probe placed above the strip and beside the strip for t=1.64mm, b=4.965mm, d=5.265mm, h=11.87mm

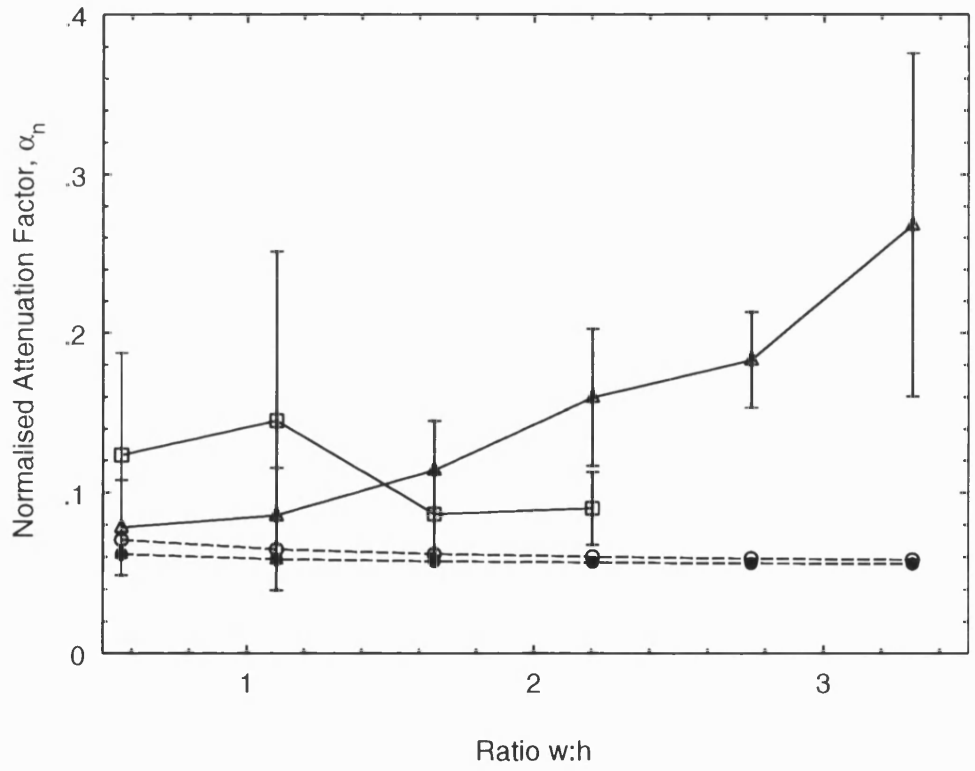

Figure 4.20: Measured Values (——)[$\rho = 90n\Omega m$] for a probe above the strip [△] and beside the strip [□], and Computed Values (- - -) of Normalised Attenuation Factor Calculated by Cohn's Analysis [○] and TRD Analysis [•] for h=11.87mm, t=1.64mm, b=4.965mm and d=5.265mm

conclusions that can be drawn from the results. The variation in the measured values and the agreement with theoretical results suggests that the assumptions of monomode propagation and the measurement of unloaded Q factor may be flawed.

The analysis assumes that the only mode of propagation is the fundamental, and that no other modes are excited. This has shown to be incorrect, for the probe placed above the strip where power is radiated from the sides of the structure. The assumption of monomode operation places another constraint on the standard deviation since the monomode bandwidth of the stripline decreases with increasing width, therefore the number of averaged Q factors will fall with increasing strip width (Table 4.7).

The analysis also assumes that the unloaded Q factor of the stripline is being measured, whereas in practice, the loaded Q is measured. This is less significant for structures with larger losses [60], but does present problems for air-filled stripline. The loading on the cavity varies with frequency and hence gives rise to significant variations in Q Factor. The additional loading can be attributed to losses in the probe mechanism (connectors, semi-rigid coax and poor grounding) in addition to grounding of the other fixture components. The frequency variation is due to variation in the coupling between the probes and cavity modes as well as stray probe capacitance.

The repeatability of the attenuation factor measurements is poor compared to the cut-off frequency measurements since the Q factor is altered by the repeatability of the contact between the stripline and test cavity; and the contact between the probe and the test fixture end pieces.

The standard deviation of the measured results could be improved by repeating the measurements with a longer test fixture, hence reducing the frequency spacing of the maxima and the increasing the number of points available for averaging. The proportion of the loss due to the stripline should also be larger hence reducing the effect of the probe connections.

4.7 Conclusions

The Transverse Resonance Diffraction (TRD) results have been compared to purely analytical and purely numerical techniques, and have demonstrated improved accuracy with significantly lower computation times over the latter.

The conformal mapping analyses have traditionally been used to design stripline networks. The results for the first higher order mode cut-off frequency illustrate that the results computed using this technique are in significant error when compared to the TRD method, measured results and numerical techniques.

The results for the impedance illustrate the wide range of dimensions that can be analysed using the TRD technique, whereas the conformal mapping representations are restricted to a limited range of dimensions. Within the range of dimensions the TRD results are in agreement with the conformal mapping results to within one to two percent, with comparable agreement with the HFSS results.

The attenuation factor results most clearly demonstrate the differences in the techniques that include an accurate representation of the edge singularities and those that do not. A comparison between the TRD and conformal mapping results illustrate improved agreement as the striplines become thicker and the effect of the edge singularities decreases. The use of measured data for the attenuation factor has demonstrated the difficulties in measuring low values of attenuation factor where other circuit effects provide a significant contribution to the loss of the structure.

Chapter 5

Numerical and Measured Results for Coupled Striplines

5.1 Outline

The previous chapter has reported numerical and measured results for uniform striplines. This section presents results for the convergence, higher order mode cut-off frequency, mode impedance, coupling and attenuation factor of coupled stripline structures for typical dimensional ratios. The Transverse Resonance Diffraction (TRD) results are compared with values computed using a number of methods, including existing CAD packages and Hewlett Packard's HP85180A High Frequency Structure Simulator (HFSS). The sensitivity of the design parameters to variations in the dimensional ratios is also studied and the results for the higher order mode cut-off frequencies are verified by measurement.

The ability of the coupled lines analysis to model striplines of arbitrary dimensions enables the parameter behaviour to be studied for a large number of dimensional variations. The results however have only been computed for the four main dimensional ratios of the structure: strip separation, (s:h); strip thickness, (t:h); strip position asymmetry, (b1:b+d); and strip width asymmetry, (w1:w1+w2).

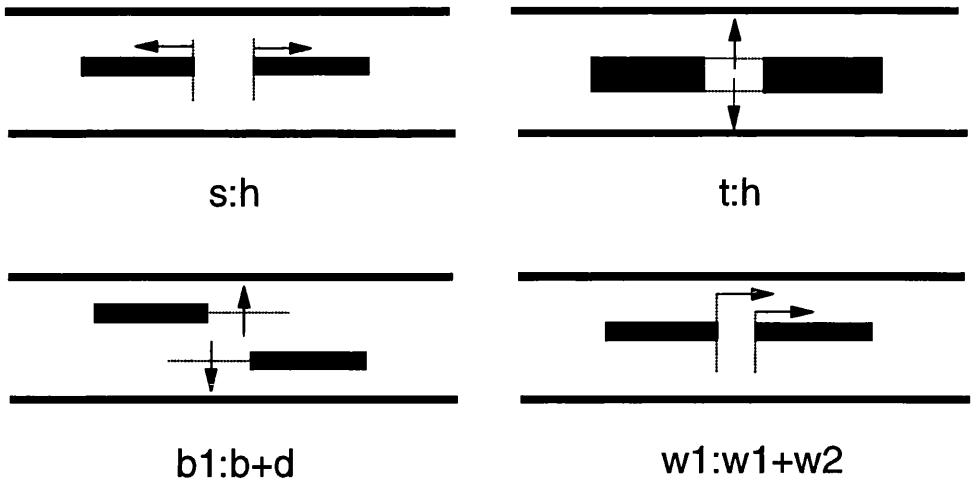

Figure 5.1: Stripline Dimensional Ratios varied in the Analysis of Coupled Striplines

The variations in the stripline dimensional ratios is shown in Figure 5.1 with the arrows denoting increasing ratios. The strip separation is varied with striplines of equal width and thickness placed symmetrically between the ground planes. The strip thickness is varied assuming an entirely symmetrical structure i.e. striplines of equal width and thickness placed symmetrically between the ground planes. The strip position asymmetry measure varies the strip position asymmetry of two strips, identical in width and thickness, simultaneously such that b1:b+d=d2:b+d i.e. the structure maintains rotational symmetry about the (x,y) origin. The strip width asymmetry is varied with the total width of the two, symmetrically placed, equal thickness striplines remaining constant. These measures have been chosen since they reflect the dimensions that are of interest to the stripline designer in terms of component design and sensitivity to manufacturing tolerances. The measures also enable the TRD theory to be compared with existing analyses.

5.2 Convergence of the Method

The convergence of the first and second higher order TE mode cut-off frequencies with the number of field expansion terms, N, and the number of basis functions, P, are shown in Tables 5.1 and 5.2 for a nominal 50Ω coupler.

The results indicate that five field expansion terms and two basis function terms are sufficient to compute the cut-off frequencies to within 1%. Twenty five field expansion terms and two basis functions terms are needed to compute the cut-off frequencies to within 0.1%. The results also verify that the coupled lines analysis is numerically stable.

The remainder of the results in this chapter are computed using three basis functions and twenty five field expansion terms.

5.3 Higher Order Mode Cut-Off Frequencies of Coupled Striplines

Results have been calculated for the variation in the first and second higher order mode cut-off frequencies with strip separation, (s:h); strip thickness, (t:h); strip position asymmetry, (b1:b+d); and strip width asymmetry, (w1:w1+w2).

The TRD results for strip separation are compared with results computed using a finite element program which assumes an exponential field decay in the transverse direction [41]. The TRD results for strip position asymmetry and strip width asymmetry are compared to HFSS which models the stripline as a rectangular co-axial structure (Appendix A).

The conformal mapping analyses of stripline structures assume TEM propagation, hence information on the higher order mode cut-off frequencies cannot be computed.

5.3.1 Variation in Cut-Off Frequency with Strip Separation

Figure 5.2 shows the variation in computed cut-off frequencies with strip separation for strips of equal width, and Figure 5.3 shows the same variation for striplines of unequal widths.

It is instructive to consider the two limiting cases of zero separation of strips and infinite separation, in order to intuitively verify the behaviour. In the case of zero separation the first two higher order modes of the coupled striplines should correspond

N	Cut-off Frequency (GHz)					
	No. of Basis Functions, P					
	1	2	3	4	5	6
2	6.8507	7.1293	7.1635			
5	6.7352	6.8546	6.8800	6.9134	6.9305	7.1327
10	6.7106	6.8114	6.8205	6.8298	6.8413	6.8489
25	6.6990	6.7917	6.7954	6.7971	6.7990	6.8010
50	6.6955	6.7850	6.7885	6.7892	6.7898	6.7904
75	6.6945	6.7844	6.7867	6.7872	6.7876	6.7879
100	6.6941	6.7837	6.7859	6.7863	6.7866	6.7868
200	6.6936	6.7828	6.7848	6.7852	6.7854	6.7855

Table 5.1: Convergence of the First Higher Order TE Mode Cut-off Frequency with the Number of Field Expansion Terms, N, and the Number of Basis Functions, P, for a Nominal 50Ω Stripline (t=1.60mm, b=d=5.55mm, w1=w2=12.00mm, s=4.00mm and h=12.70mm)

N	Cut-off Frequency (GHz)					
	No. of Basis Functions, P					
	1	2	3	4	5	6
2	8.7136	8.8046	8.8168			
5	8.4963	8.5395	8.5570	8.5792	8.5906	8.7369
10	8.4470	8.4941	8.4996	8.5074	8.5166	8.5223
25	8.4238	8.4742	8.4758	8.4773	8.4789	8.4806
50	8.4169	8.4684	8.4693	8.4699	8.4704	8.4708
75	8.4149	8.4669	8.4676	8.4680	8.4683	8.4685
100	8.4141	8.4662	8.4668	8.4672	8.4674	8.4675
200	8.4130	8.4652	8.4658	8.4661	8.4662	8.4663

Table 5.2: Convergence of the Second Higher Order TE Mode Cut-off Frequency with the Number of Field Expansion Terms, N, and the Number of Basis Functions, P, for a Nominal 50Ω Stripline (t=1.60mm, b=d=5.55mm, w1=w2=12.00mm, s=4.00mm and h=12.70mm)

to the first two higher order modes of a uniform stripline, of width w1+w2. When the separation is increased towards infinity, i.e. zero coupling, the first two higher order modes of the coupled stripline structure correspond to the first two higher order modes of a structure comprising of two uniform striplines of widths w1 and w2.

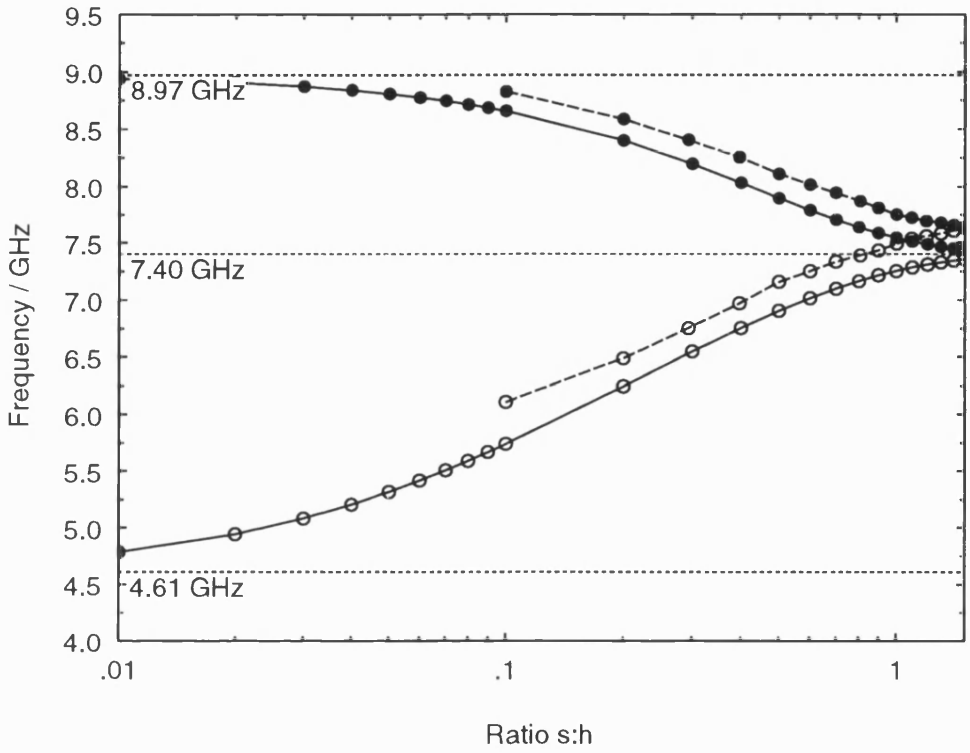

Figure 5.2: Calculated Cut-Off Frequencies for the First [o] and Second [•] Higher Order Modes Computed by the TRD Method (——) and the Finite Element Method (– – –) versus Strip Separation (s:h) for b=d=5.55mm, t=1.60mm, w=12.70mm and h=12.70mm

The TRD results are compared to results computed using the finite element method [41]. These results have been plotted directly from the paper, and are therefore subject to a ± 0.1 GHz inaccuracy. The results illustrate the behaviour described intuitively, and are plotted on a log scale to highlight the convergence to the asymptotic limits that have been calculated using the TRD uniform lines analysis. The results show good agreement with differences of the order of 2 to 4 percent for Figure 5.2, after taking into account the error bounds of the finite element results. The first higher order mode results in Figure 5.3 show agreement of between -1 to 2 percent, and the second higher

order mode results show a difference of between 2 and 4 percent.

The behaviour of the first and second higher order mode cut-off frequencies has been shown to be governed by the coupling between the striplines, and will exhibit odd field symmetry in the case of the first higher order mode, and even symmetry in the case of the second higher order mode. The behaviour between the asymptotic limits can also be described in terms of stripline structures with effective widths, which further suggests that the first and second higher order modes represent the first odd and even higher order modes, in a similar manner to the concept of even and odd mode impedances.

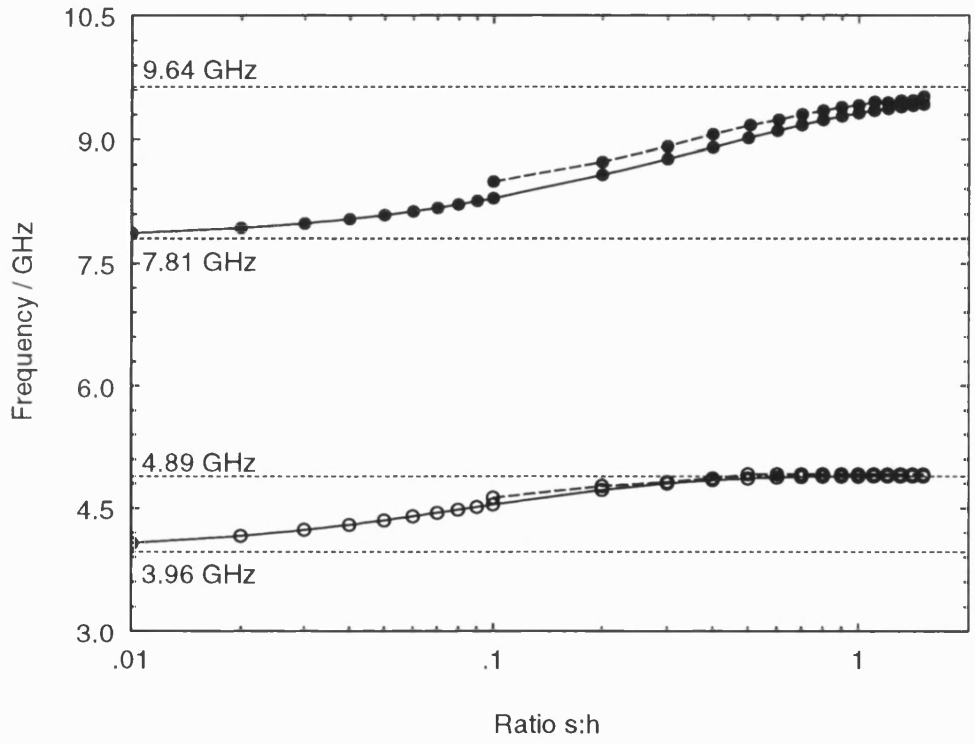

Figure 5.3: Calculated Cut-Off Frequencies for the First [○] and Second [●] Higher Order Modes Computed by the TRD Method (——) and the Finite Element Method (– – –) versus Strip Separation (s:h) for b=d=5.55mm, t=1.60mm, w1=7.25mm, w2=23.50mm and h=12.70mm

The finite element paper [41] does not state any timing information, hence the compromise between the computational time and accuracy cannot be investigated further.

5.3.2 Variation in Cut-Off Frequency with Strip Thickness

The variation in the cut-off frequencies of the first two higher order modes with strip thickness is shown in Figure 5.4. This variation has not been studied using other techniques, therefore the behaviour is only verified intuitively.

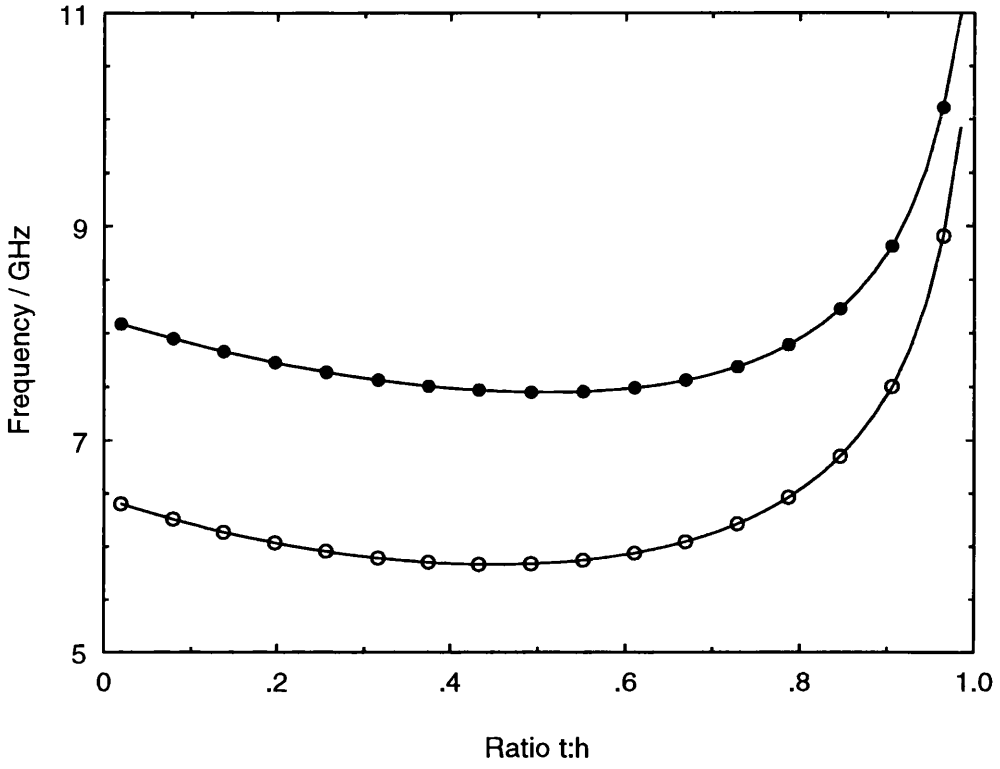

Figure 5.4: Calculated Cut-Off Frequencies for the First [o] and Second [•] Higher Order Modes Computed by the TRD Method (——) versus Strip Thickness (t:h) for b=d=5.55mm, s=4.00mm, w=12.70mm and h=12.70mm

The behaviour of the first two higher order mode cut-off frequencies illustrate the same trends as the first higher order mode cut-off frequency of a uniform line. The cut-off frequencies appear relatively insensitive to moderate variations in strip thickness, with a rapid rise in cut-off frequency when the striplines are in close proximity to the ground planes, suggesting the dominant mode switches from a variation in the $\hat{y}$ direction to a variation in the $\hat{x}$ direction. The identical trends for the first two higher order modes, and the similarity to the plot for a uniform line, further supports the intuitive approach of considering the modes as the modes of uniform striplines with

effective widths, governed by the coupling between the striplines.

5.3.3 Variation in Cut-Off Frequency with Strip Position Asymmetry

The variation in the cut-off frequency of the first two higher order modes with strip position asymmetry, (b1:b+d), is shown in Figure 5.5. The TRD results are compared with results computed using Hewlett Packard's HFSS package (Ver. A2.06), which models the coupled stripline structure as a rectangular co-axial structure (Appendix A). The HFSS results are computed using a two percent convergence criteria.

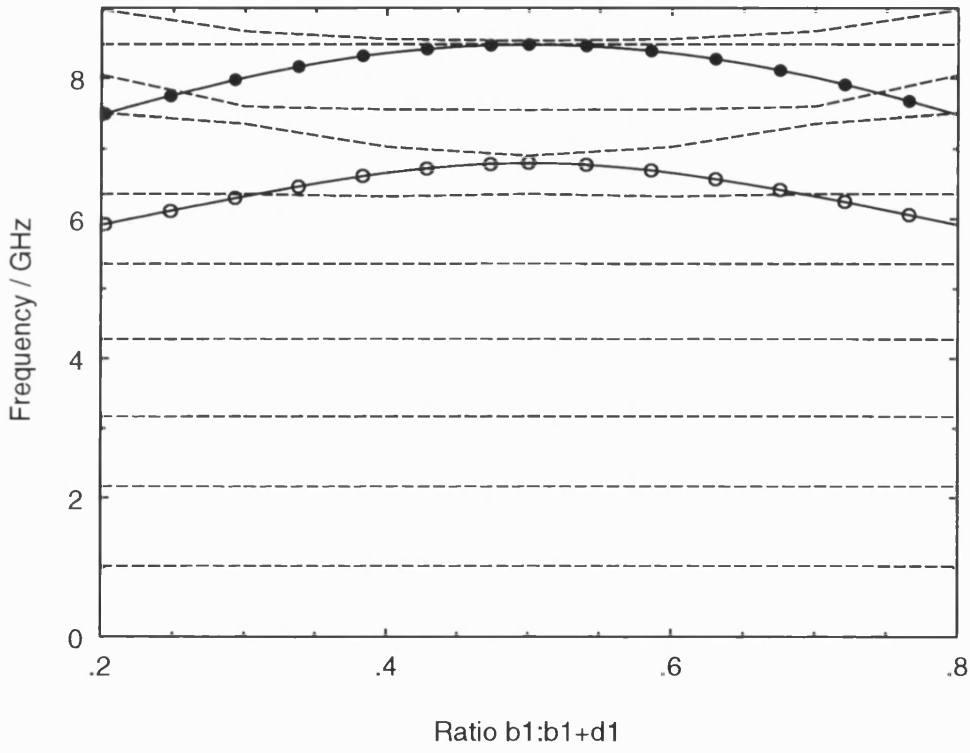

Figure 5.5: Calculated Cut-Off Frequencies for the First [o] and Second [•] Higher Order Modes Computed by the TRD Method (——) and Mode Solutions Computed by HFSS Ver. A2.06 (- - -) versus Strip Position Asymmetry (b1:b+d) for s=4.00mm, t=1.60mm, w=12.00mm, and h=12.70mm

The HFSS package calculates the modes of the defined port, hence a number of box modes are present in the structure, these will appear at a regular frequency spacing and in general will be independent of stripline position. The TRD results illustrate that the

cut-off frequency decreases with increasing strip position asymmetry, suggesting that as the striplines approach the ground planes the fields concentrate on one face, which is equivalent to a stripline of a larger equivalent width placed symmetrically between ground planes.

The HFSS mode solutions that do not correspond to the box modes appear to increase with increasing strip position asymmetry, contrary to the TRD analysis, although the cut-off frequencies for symmetrical strip placement agree. The behaviour of the HFSS package is also intuitively correct, since if the asymmetry is increased until the strips touch the ground planes, only the box modes of the structure will remain. For strips of negligible thickness this is equivalent to computing the cut-off frequencies of a waveguide. The trends are therefore a direct consequence of the excitation of the structure as a waveguide type structure for HFSS and a stripline structure for the TRD method.

The number of modes computed by HFSS, in order to calculate the cut-off frequencies of the striplines, is considerably greater than the TRD method. The total computational time for the HFSS package is 1560 CPU seconds on an HP 715/50, as opposed to 37 CPU seconds on an HP 710 for the TRD method. This equates to a speed difference of a factor of 64 after the performance of the machines are taken into account.

5.3.4 Variation in Cut-Off Frequency with Strip Width Asymmetry

The variation in the cut-off frequency of the first two higher order modes with strip width asymmetry, (w1:w1+w2), is shown in Figure 5.6.

The TRD results are again compared with results computed using Hewlett Packard's HFSS package. The HFSS package analysed the structure with a magnetic symmetry plane placed along the y axis, hence the box mode solutions start at a considerably higher frequency.

The TRD results are in excellent agreement with the HFSS results for the first higher order mode, and the second higher order mode for moderate strip width asymmetry. The remainder of the results show a similar trend, but with a significant error. The behaviour of the first higher order mode of the coupled structure represents the first higher order

mode of the widest stripline, hence decreases as the strip width asymmetry deviates from the symmetrical position. The second higher order mode behaviour, for variations around the symmetrical position, represents the first higher order mode of the narrower of the two striplines hence increases as the asymmetry increases. The asymmetry reaches a point where the second higher order mode of the widest strip propagates at a lower frequency than the first higher order mode of the narrower stripline, hence the second higher order mode cut-off frequency decreases with increasing asymmetry. The HFSS results appear to model this trend, but maintain the first higher order mode of the narrower stripline as the second preferential mode of propagation as opposed to the second higher order mode of the widest stripline.

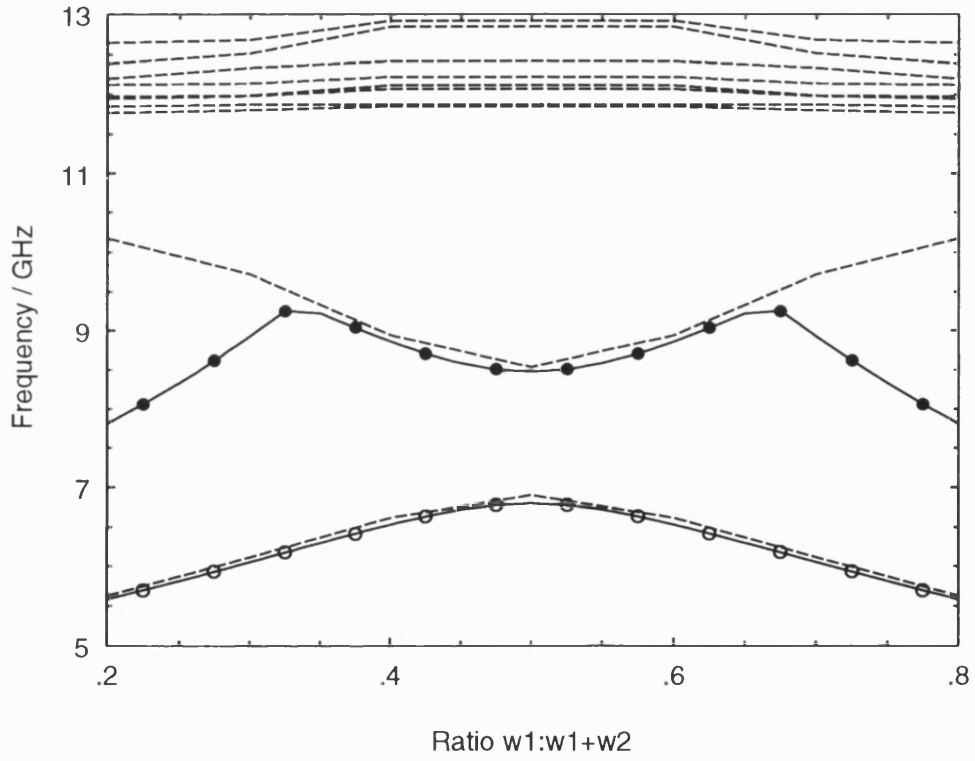

Figure 5.6: Calculated Cut-Off Frequencies for the First [o] and Second [•] Higher Order Modes Computed by the TRD Method (——); Mode Solutions Computed by HFSS Ver. A2.06 (- - -) versus Strip Width Asymmetry (w1:w1+w2) for s=4.00mm, t=1.60mm, w1+w2=24.00mm, and h=12.70mm

5.4 Impedance and Coupling of Coupled Striplines

The even and odd TEM mode impedances and coupling factors have been calculated for variations in the strip separation, (s:h); strip thickness, (t:h); strip position asymmetry (b1:b+d) and strip width asymmetry, (w1:w1+w2). The analysis has again been restricted to these cases since they correspond to the dimensions most commonly varied in stripline design. The TRD results are compared to both conformal mapping and variational approaches [50, 52], in addition to results computed by EEsof's Linecalc package [45]. A selected number of cases have also been analysed using Hewlett Packard's HFSS package (Appendix A), as a "ports only" 2D solution and also as a full 3D analysis.

5.4.1 Variation in Impedance and Coupling with Strip Separation

Figure 5.7 shows the computed even and odd mode impedances for two identical strips for a variation in strip separation. The TRD results are compared with results computed by Perlow's modified conformal mapping analysis [50]; the EEsof Linecalc package Ver.3.0, which is also based on a modified conformal mapping approach, and Hewlett Packard's HFSS package Ver. A2.06. The HFSS results are computed as a "ports only" solution with a 0.1 percent convergence limit.

The even mode impedances show good agreement between the TRD, Linecalc and HFSS methods for a wide range of separations, whereas the odd mode impedances show significant variations. The odd mode impedances are very dependent on the interaction, of the fields along the inside edges of the stripline, hence this effect has to be modelled accurately. The HFSS and TRD methods show consistently lower values indicating a stronger interaction between the striplines than predicted using the closed form expressions, and is the result of the more accurate modelling of the edge singularities. The impedances converge to the limiting case of uncoupled i.e uniform striplines, however Perlow's analysis appears to converge to a different value from that of the remaining analyses.

The coupling factors are computed from the mode impedances using Equation 3.96,

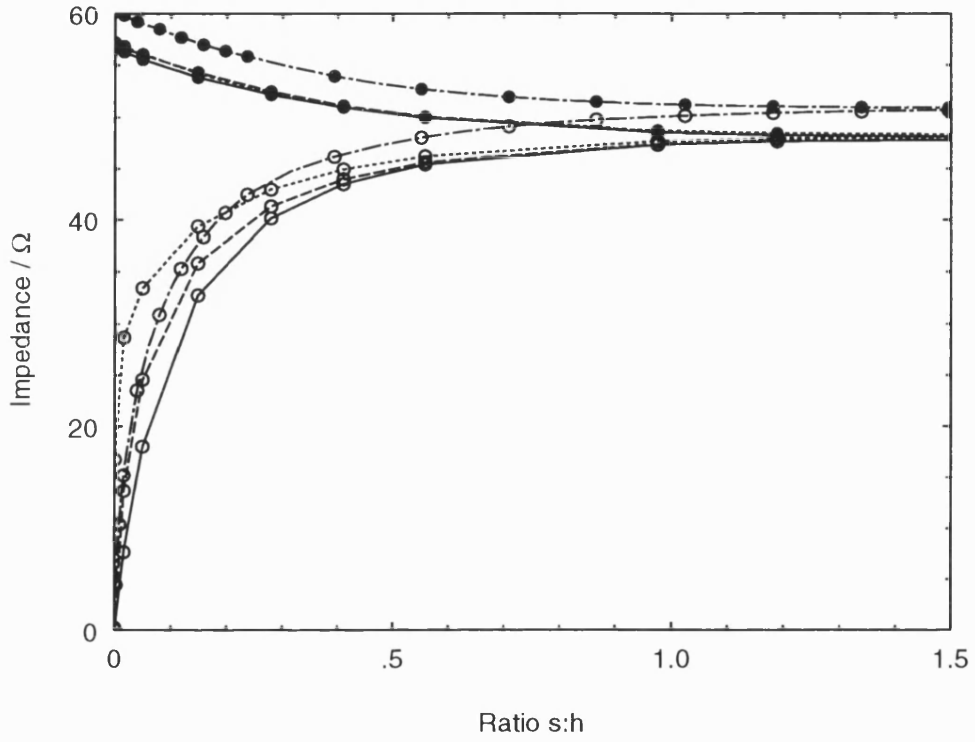

Figure 5.7: Even (Zoe [•]) and Odd (Zoo [○]) Mode Impedances versus Strip Separation (s:h) Computed by TRD (——); HFSS Ver. A2.06 (- - -); EEsof's Linecalc Ver. 3.0 (· · · · · ·) and Perlow's Analysis (- · -) for t=1.60mm, h=12.70mm, w=14.00mm and b=d

and are shown in Figure 5.8. The graph indicates that the TRD, HFSS and Perlow's analysis all show excellent agreement for weak coupling, however the difference increases as the separation decreases. Perlow's and the HFSS results also illustrate good agreement, despite a significant difference in mode impedances. The EEsof Linecalc values show a consistent underestimate of the coupling values when compared to the other analyses for the entire range of coupling values.

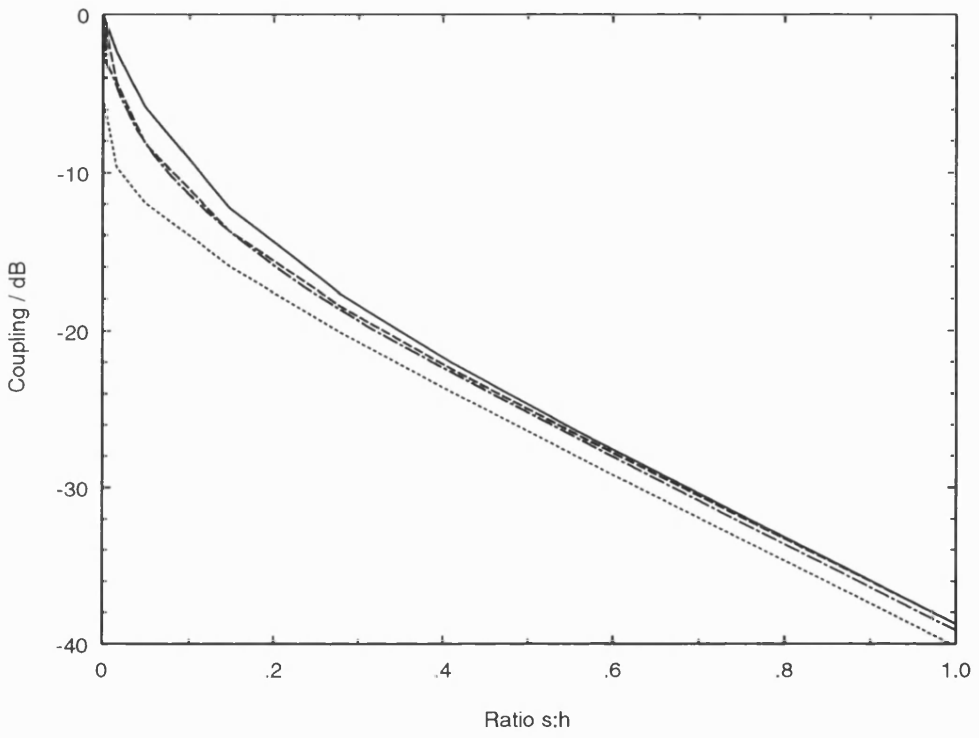

Figure 5.8: Coupling versus Strip Separation (s:h) Computed by TRD (——); HFSS Ver. A2.06 (- - -); EEsof's Linecalc Ver. 3.0 (· · · · · ·) and Perlow's Analysis (- · -) for t=1.60mm, h=12.70mm, w=14.00mm and b=d

The HFSS values were further verified by computing the full 3D field solution for a number of small strip separations and computing the coupling from the S parameters of the structure. These results are shown in Figure 5.9, where they are compared with the other analyses. The 3D results for the 5th and 6th adaptive passes are shown to demonstrate the convergence of the solution. The 3D HFSS results illustrate a more linear variation in coupling than the other results, however with a smaller variation in coupling with strip separation. A greater number of points would also have to be

computed to enable further conclusions to be drawn.

The range of couplings achievable by altering the separation, and the sensitivity of the coupling to the separation, suggests that this dimension has to be closely controlled in a practical network.

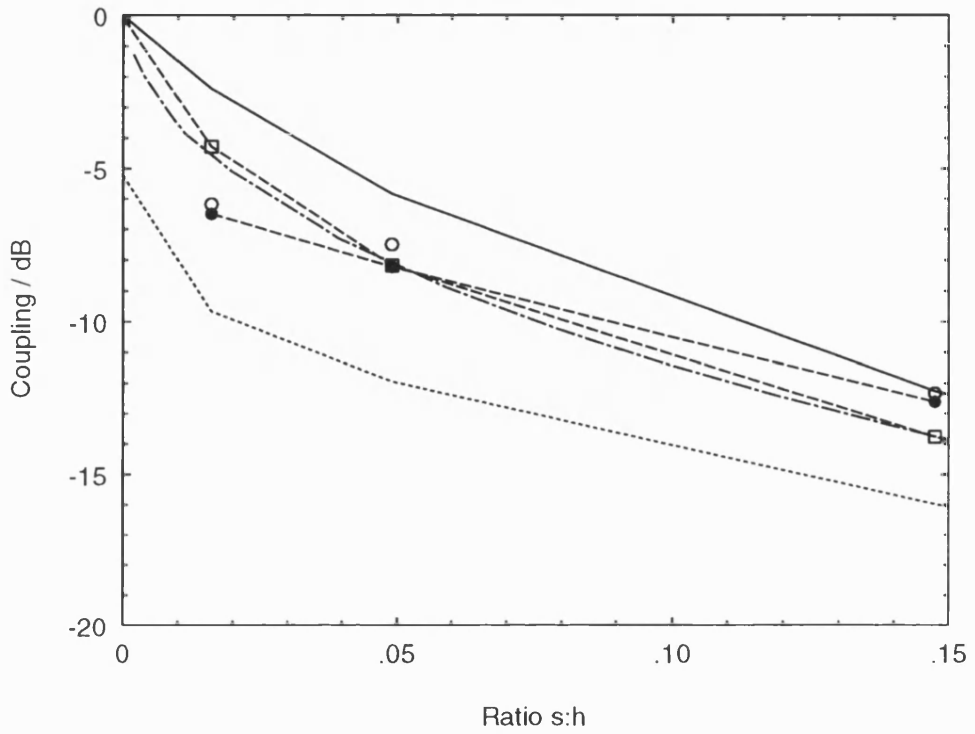

Figure 5.9: Coupling versus Strip Separation (s:h) Computed by TRD (——); HFSS Ver. A2.06 (- - -), 2D [□], 3D (5th Adaptive Pass [○]), 3D (6th Adaptive Pass [•]); EEsof's Linecalc Ver. 3.0 (·····) and Perlow's Analysis (- · -) for t=1.60mm, h=12.70mm, w=14.00mm and b=d

5.4.2 Variation in Impedance and Coupling with Strip Thickness

Figure 5.10 shows the computed even and odd mode impedances for two identical strips with a variation in strip thickness, (t:h). The TRD results are compared with EEsof's Linecalc package Ver.3.0 [45] and Perlow's modified conformal mapping analysis [50]. The mode impedance results show good agreement for the even order mode impedance for moderate strip thicknesses, with again a larger variation in the odd order mode

impedance between the methods.

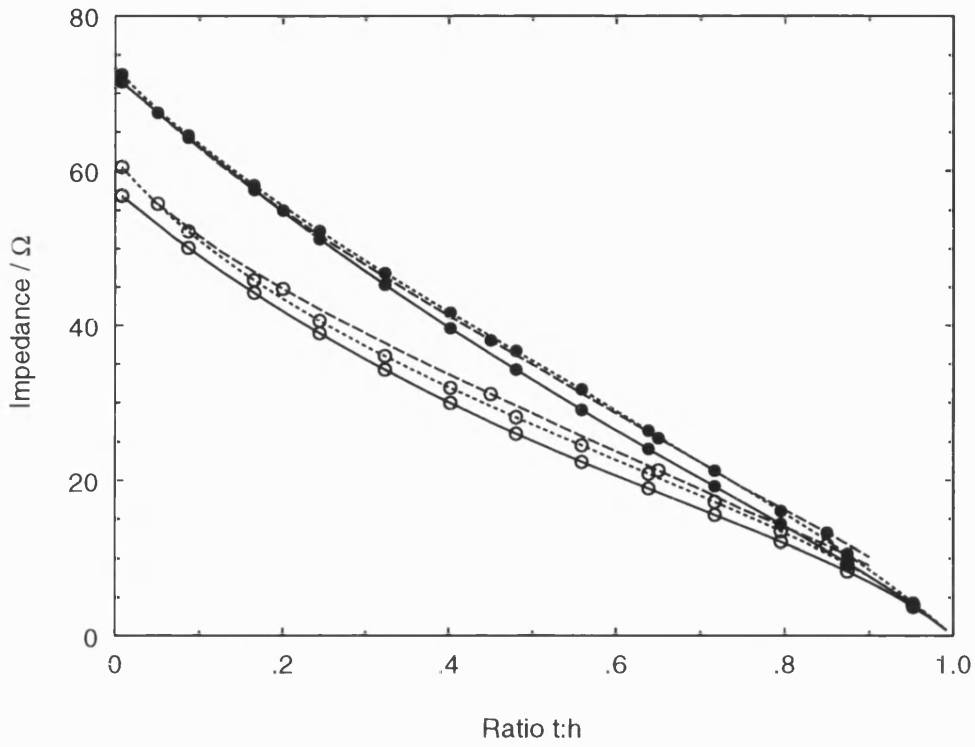

Figure 5.10: Even (Zoe [•]) and Odd (Zoo [○]) Mode Impedances versus Strip Thickness (t:h) computed by TRD (——); Perlow's Analysis (· · · · · ·) and EEsof's Linecalc Ver. 3.0 (– – –) for b=d, h=12.70mm, s=4.00mm and w=12.00mm

Figure 5.11 shows the coupling computed from the mode impedances for the TRD analysis, Perlow's analysis and EEsof's Linecalc. The results illustrate that the agreement between Perlow's analysis and the TRD analysis improves as the thickness of the strip increases and the coupling capacitance is dominated by the inside faces of the striplines, as opposed to the inside edge singularities. Both sets of results show a rapid decrease in coupling as the thickness increases and the interaction between the top faces of the striplines and the ground planes becomes stronger than the interaction between the striplines. The EEsof Linecalc results show a consistently lower value of coupling, and suggests a more linear variation in coupling than the other methods. The overestimate of the coupling values computed by the TRD method for thin striplines may be attributable to the singularity behaviour being modelled as a finite thickness stripline i.e. with two $\mid r \mid^{-\frac{1}{3}}$ singularities as opposed a single $\mid r \mid^{-\frac{1}{2}}$ singularity of an infinitely

thin strip. This is an important effect since the coupling for very thin striplines will be dominated by this edge effect.

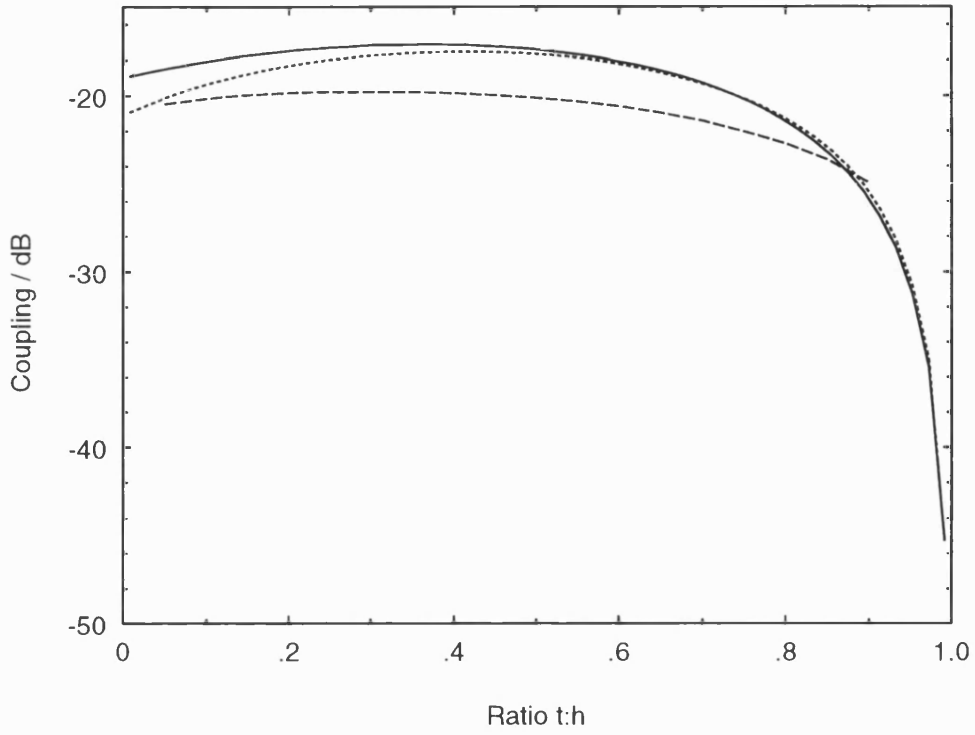

Figure 5.11: Coupling versus Strip Thickness (t:h) computed by TRD (——); Perlow's Analysis (· · · · · ·) and EEsof's Linecalc Ver. 3.0 (– – –) for b=d, h=12.70mm, s=4.00mm and w=12.00mm

5.4.3 Variation in Impedance and Coupling with Strip Position Asymmetry

The computed even and odd mode impedances for a variation in strip position asymmetry, (b1:b+d) are shown in Figure 5.12. The TRD results are compared to Das' Green's function analysis [52], which finds a variational form for the quasi-static capacitances of a system of infinitely thin conductors. The results are also compared to EEsof's Linecalc package which is based on a modified form of Shelton's conformal mapping approach [44]. The impedance results show the same overall trend, however the TRD values are in closest agreement with EEsof's values at the symmetric strip position and

in closest agreement with Das' analysis for large degrees of asymmetry. The even and odd mode impedances computed by the TRD method also show the least sensitivity to small changes in the strip position asymmetry than the other two methods.

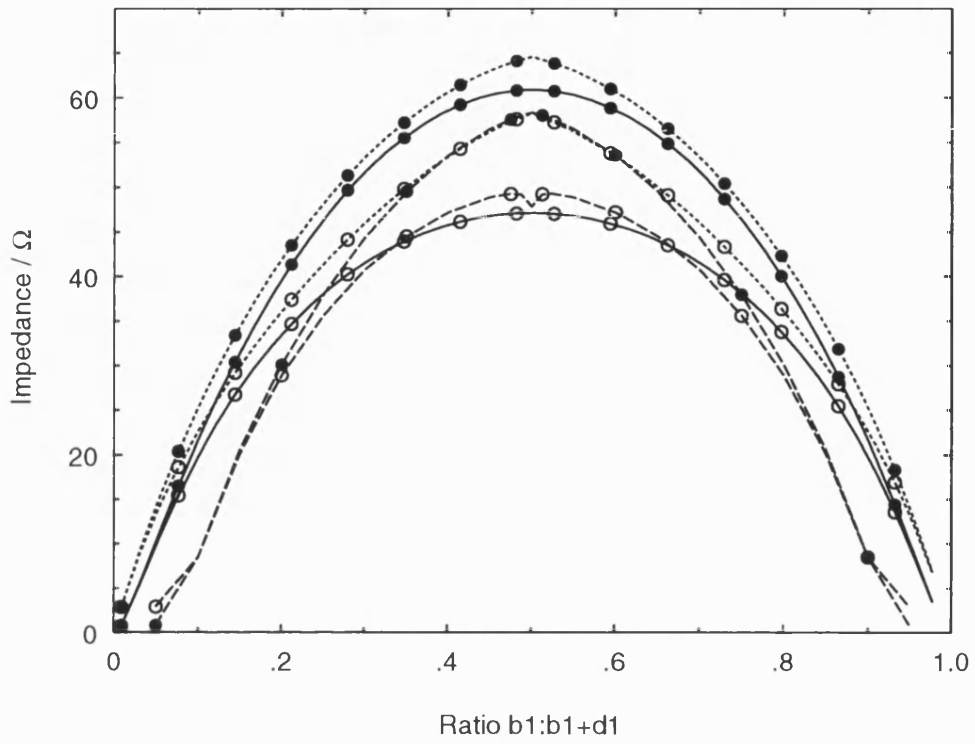

Figure 5.12: Even (Zoe [•]) and Odd (Zoo [○]) Mode Impedances versus Strip Position Asymmetry (b1:b+d) computed by TRD (——); Das' Analysis (· · · · · ·) and EEsof's Linecalc Ver. 3.0 (– – –) for t=1.60mm, h=12.70mm, s=4.00mm, w=12.70mm and b1=d2

The results for the coupling values computed from the mode impedances are shown in Figure 5.13, and demonstrate the differences between the methods more clearly. The graph illustrates the low sensitivity of the coupling computed by the TRD method to variations in strip position asymmetry, which would be expected for finite thickness striplines. The EEsof Linecalc results show significantly lower values of coupling computed by the SOCLIN element [45] for asymmetrical strip position, and the SCLIN element for symmetrical strip position. Das' analysis shows reasonable agreement with the TRD method for large stripline position asymmetries, but significant errors for symmetrical strip placement. This is due to the analysis accurately modelling the capacitances

between the top and bottom faces of the stripline, but inadequately modelling the edge to edge coupling, resulting in a minimum coupling value for the symmetric strip position. Coupling values were also computed using a full 3D HFSS analysis and are shown for the fifth and sixth adaptive passes. The HFSS results indicate reasonable agreement with the TRD results and again verify the underestimate of the EEsof results. The sensitivity of the HFSS results to a change in the strip position asymmetry cannot be quantified due to the relative difference between the fifth and six adaptive passes and the low number of structures analysed.

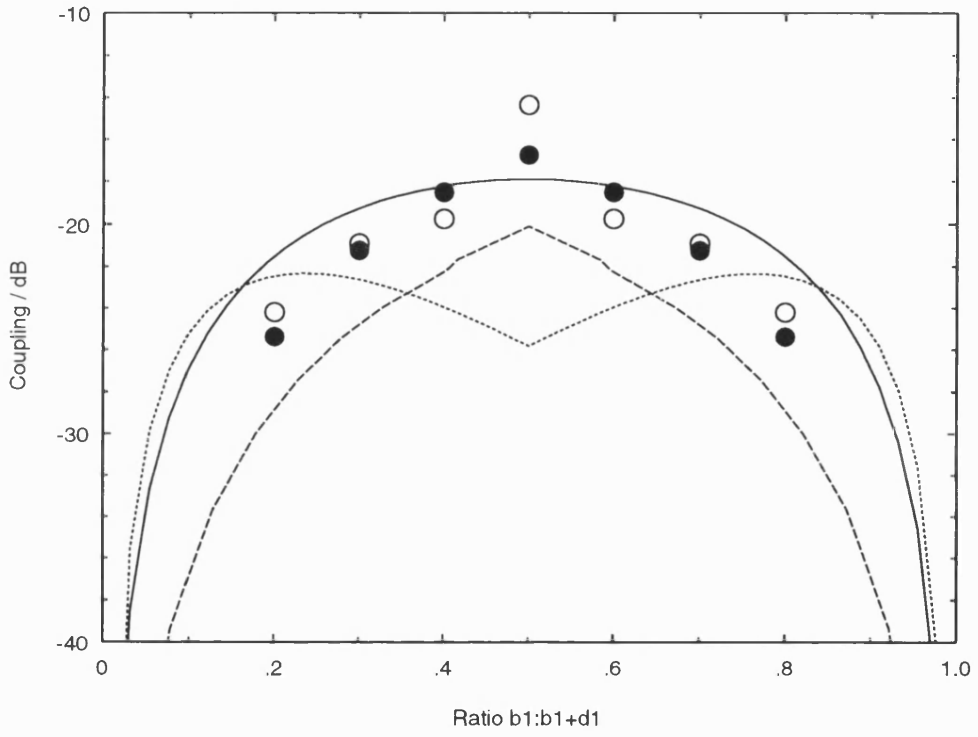

Figure 5.13: Coupling versus Strip Position Asymmetry (b1:b+d) computed by TRD (——); Das' Analysis (· · · · · ·), EEsof Linecalc Ver. 3.0 (– – –) and HFSS (5th Adaptive Pass [○]) and (6th Adaptive Pass [●]) for t=1.60mm, h=12.70mm, s=4.00mm, w=12.70mm and b1=d2

5.4.4 Variation in the Impedance and Coupling with Strip Width Asymmetry

The computed Π and C mode impedances, which correspond to the even and odd mode impedances for lines of unbalanced impedance, are shown in Table 5.3, and the coupling values are plotted in Figure 5.14, for the TRD method and Perlow's analysis [50]. Results are also shown for a number of cases computed using a full 3D HFSS solution, with again the fifth and six adaptive passes shown. The mode impedances illustrate a very small variation across the range of strip width asymmetries, and again the even mode (Π) impedances are in closer agreement than the odd order (C) mode impedances. The coupling values are therefore approximately constant across the range of asymmetries with the TRD results showing only a very small variation. This demonstrates that the coupling is dominated by the edge to edge interaction, and is largely independent of the width of the strip, a result that is intuitively correct. The HFSS results appear to be converging to a constant value across the range, although a larger number of iterations would be required to verify this.

Method	Π Mode Impedance (Ω)	C Mode Impedance (Ω)
TRD	53.63 $\pm$ 0.07	47.17 $\pm$ 0.05
Perlow's Analysis	54.77	48.94

Table 5.3: Π and C Mode Impedances for a Variation in Strip Width Asymmetry between $0.05 < w1 : w1 + w2 < 0.95$ for t=1.60mm, b=d, h=12.70mm, w1+w2=24.00mm and s=4.00mm

5.4.5 Comparison of Computation Times between the TRD Method and HFSS

The TRD results have been compared to conformal mapping closed form expressions [45, 50] and closed form expressions computed using other analytical techniques [52] and HFSS. The closed form expressions can be easily programmed on personal computers, and calculated virtually instantaneously. The comparison of timings for the TRD and HFSS methods is shown in Table 5.4 for a typical point computed in Figure 5.9. The

timings clearly illustrate the efficiency of the TRD method when compared to a 2D "ports only" solution and a full 3D HFSS solution.

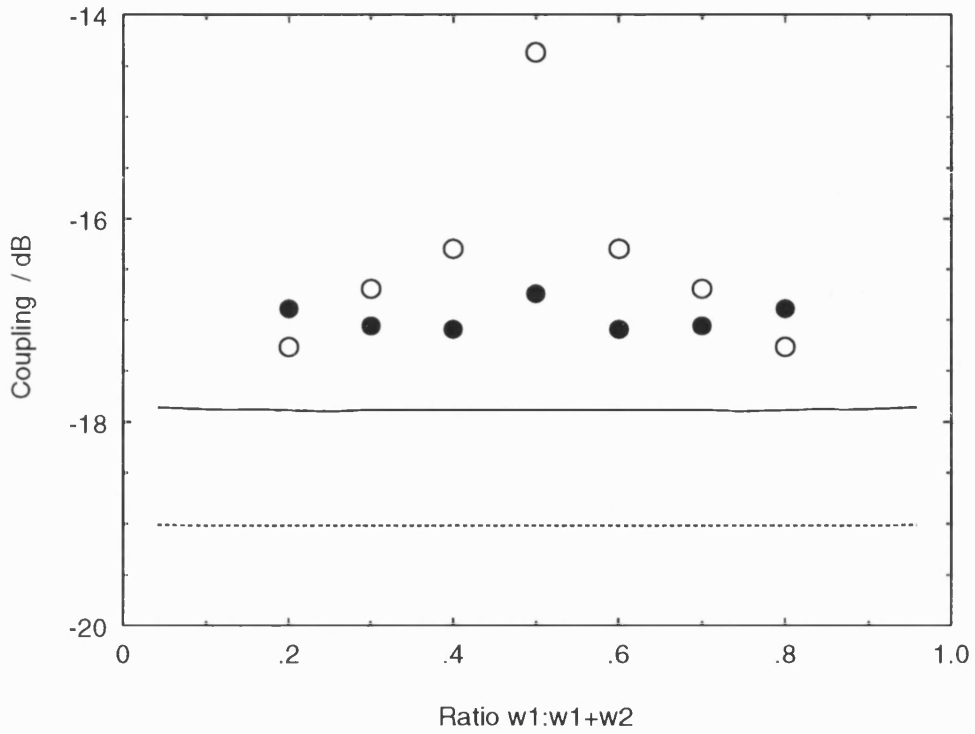

Figure 5.14: Coupling versus Strip Width Asymmetry (w1:w1+w2) computed by TRD (——); Perlow's Analysis (· · · · · ·), and HFSS (5th Adaptive Pass [○]) and (6th Adaptive Pass [•]) for t=1.60mm, h=12.70mm, s=4.00mm, w1+w2=12.00mm and b=d

Method	Details	CPU Time (Secs)	Storage	Platform
HFSS Ver. A2.06	Ports Only Computation 0.1 % Convergence	330	34.3 MBytes	HP 715/50
	3D Field Computation	2100	202 MBytes	
TRD	3 Basis Terms 25 Field Expansion Terms	1.6	33kBytes	HP 710

Table 5.4: Comparison of Computational Requirements for the Calculation of the Mode Impedances and Coupling for a Typical Point in Figure 5.9

5.5 Attenuation Factor of Coupled Striplines

The normalised attenuation factor of the even and odd modes have been calculated for variations in strip separation, (s:h); strip thickness, (t:h); strip position asymmetry, (b1:b+d); and strip width asymmetry, (w1:w1+w2). The results are compared with Perlow's modified conformal mapping approach [50] for all the variations except the strip asymmetry case. EEsof's Linecalc calculates the attenuation for particular elements, however the values cannot be normalised to a suitable precision for comparison.

5.5.1 Variation in Normalised Attenuation Factor with Strip Separation

The computed normalised attenuation factors are shown in Figure 5.15 for a variation in strip separation, (s:h), for TRD and Perlow's analysis. Both sets of results show similar trends, although Perlow's results illustrate the problems of taking a piece-wise approximation and curve fitting the capacitances. The non-monatonic behaviour is due to the loss being calculated using an incremental inductance rule approach [15], where the attenuation factor is proportional to the difference in inductance between the lossless case, with the charge on the surface of the conductors, and a structure with the charge at a distance of half the skin depth inside the conductors. The low attenuation factors for the stripline structures ensure that any error in the piece-wise approximation of the capacitance will significantly alter the calculated attenuation.

Perlow's analysis also suggests a significantly higher attenuation factor for the odd mode, and a greater rate of change of the even order mode attenuation factor for low separations. This behaviour is a result of the attenuation factor being modelled as a function of the change in overall inductance (capacitance) which changes rapidly with separation. The TRD analysis however, calculates the dissipation and storage terms from the fields and directly models the singularities on the edges of striplines, around which the majority of the power flows. The change in strip interaction is therefore smaller, for a given change in stripline separation, and only becomes significant for small strip separations. The TRD results also converge to a constant value, whereas

Perlow's analysis converges to a steady decrease in attenuation factor with separation, which is intuitively incorrect. At a separation ratio, s:h=2, the two methods differ by twelve percent in normalised attenuation factor.

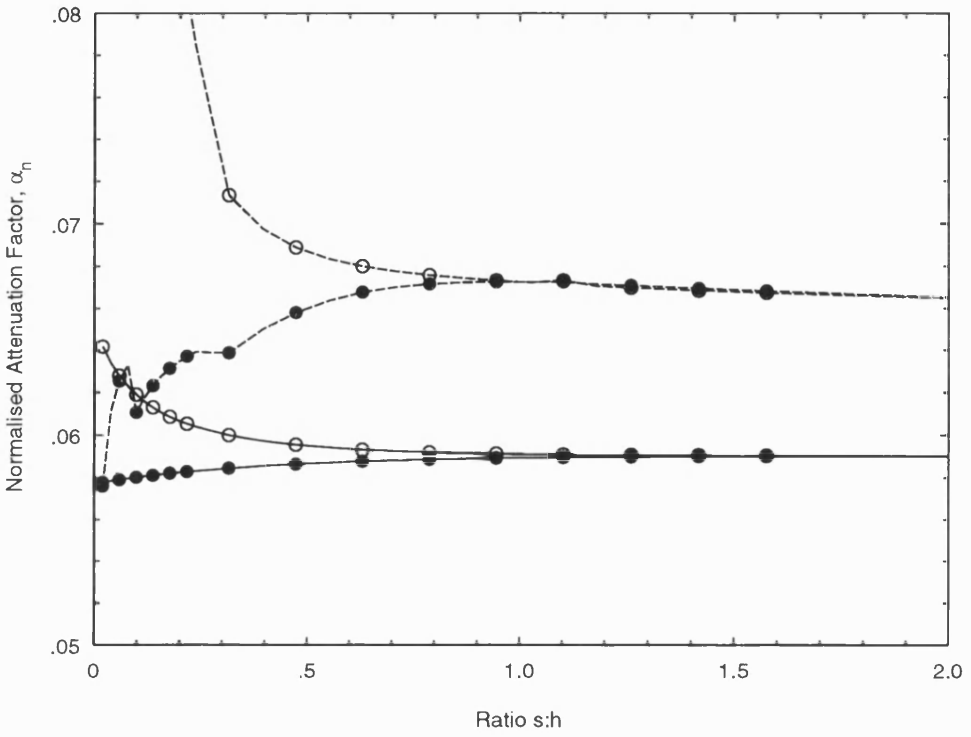

Figure 5.15: Normalised Attenuation Factor of Even [•] and Odd [o] Modes versus Strip Separation (s:h) computed by TRD (——) and Perlow's Analysis (- - -); for t=1.60mm, h=12.70mm, w=12.00mm and b=d

5.5.2 Variation in Normalised Attenuation Factor with Strip Thickness

Figure 5.16 shows the normalised attenuation factor for a variation in strip thickness, (t:h) computed using the TRD analysis and Perlow's analysis [50]. Perlow's results again suffer from a discontinuity due to the curve fitting approach at a strip thickness, (t:h≈0.55). The discontinuity also corresponds to the even order mode attenuation becoming greater than the odd order mode attenuation. This "crossover" point appears at significantly lower values of thickness for the TRD method. The "crossover" is due

to the changing interaction between the striplines (odd order mode) and the interaction between the striplines and the ground planes (even order mode). This can be again attributed to the accurate modelling of the singularities. The difference between even and odd mode attenuation factors is also greater for Perlow's analysis below "crossover" than the TRD method, with the opposite occurring above "crossover". Perlow's analysis also suggests a very high attenuation factor for narrow strips, contrary to the TRD results. Perlow's results suggest that the power flow decreases more sharply than the dissipation, whereas, with the TRD method the decrease in thickness of the strip, brings the edge singularities closer together, but the power flow is not significantly reduced.

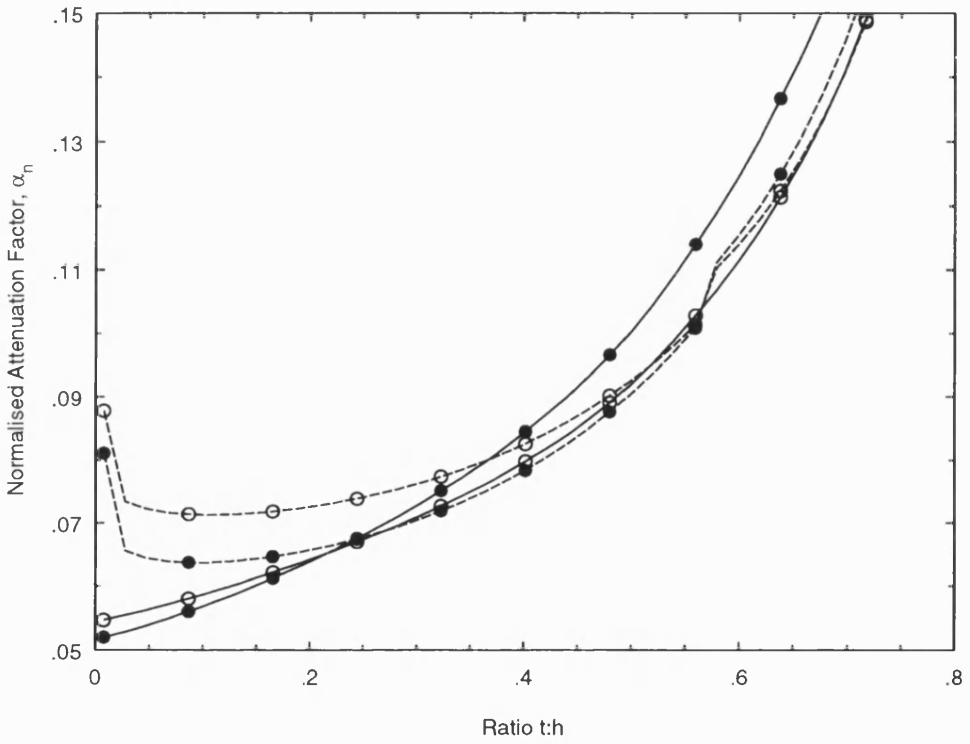

Figure 5.16: Normalised Attenuation Factor of Even [•] and Odd [○] Modes versus Strip Thickness (t:h) computed by TRD (——) and Perlow's Analysis (- - -); for t=1.60mm, h=12.70mm, w=12.00mm and b=d

5.5.3 Variation in Normalised Attenuation Factor with Strip Position Asymmetry

The normalised attenuation factor calculated by the TRD method for a variation in strip position asymmetry, (b1:b+d) is shown in Figure 5.17. The graph shows a clear minimum at the symmetric position, with a rapid rise as the asymmetry increases and the contribution from dissipation in the ground planes increases with a small increase in power flow. The results again exhibit a crossover point between the even and odd attenuation factors for the same reasons explained in the previous sections.

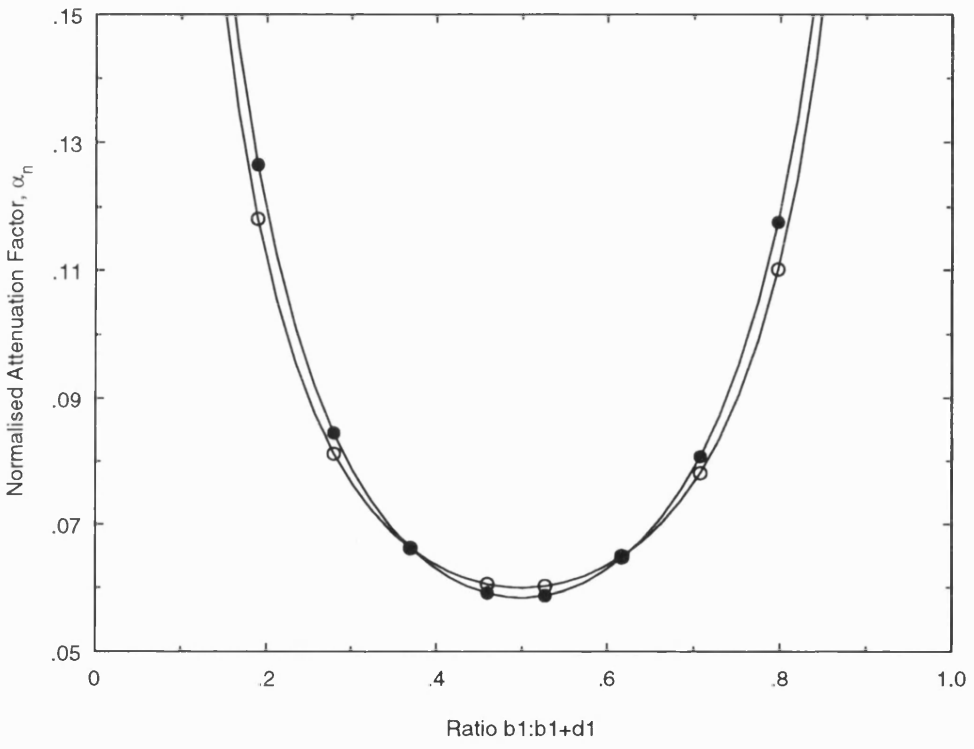

Figure 5.17: Normalised Attenuation Factor of Even [•] and Odd [○] Modes versus Strip Position Asymmetry (b1:b+d) computed by the TRD method (——) for t=1.60mm, h=12.70mm, w=12.00mm and b=d

5.5.4 Variation in Normalised Attenuation Factor with Strip Width Asymmetry

The normalised attenuation factor results are tabulated in Table 5.5 for the range of strip width asymmetries $0.1 < w1 : w1 + w2 < 0.9$. The results further verify the comments made in the previous sections. Perlow's results however do indicate a sharp increase in attenuation for structures with extreme asymmetry.

Method	Even Mode Normalised Attenuation Factor	Odd Mode Normalised Attenuation Factor
TRD	0.06002 ± 0.00005	0.05850 ± 0.00005
Perlow's Analysis	0.07135	0.06387

Table 5.5: Even and Odd Mode Normalised Attenuation Factors Mode for a Variation in Strip Width Asymmetry, (w1:w1+w2) between $0.1 < w1 : w1 + w2 < 0.9$ for t=1.60mm, b=d, h=12.70mm, w1+w2=24.00mm and s=4.00mm

5.6 Comparison of TRD Results with Measured Data

The cut-off frequencies for a number of pairs of coupled lines have been measured using the same method employed for measuring the cut-off frequencies of the uniform lines. The plan view of the coupled lines test fixture is shown in Figure 5.18. The variation in the separation of the striplines was achieved by inserting different "T" pieces of variable width into the structure. The possible modes of excitation of the strips is shown in Figure 5.19(a) for a probe placed perpendicular to the striplines; and Figure 5.19(b) for a probe placed parallel to the striplines.

A typical plot of the transmission through the structure for both probe orientations is shown in Figure 5.20 for a separation ratio, $s:h \approx 1$. The plot illustrates some clear differences from the uniform lines measurement (Figure 4.17). The overall transmission level is higher, with a small difference between the probe orientations. This can be attributed to the position of the probes in close proximity to the edges of the stripline, which enables energy to be reflected between the strips, in addition to between the ground planes. The different mode of excitation also gives rise to shift in frequency of

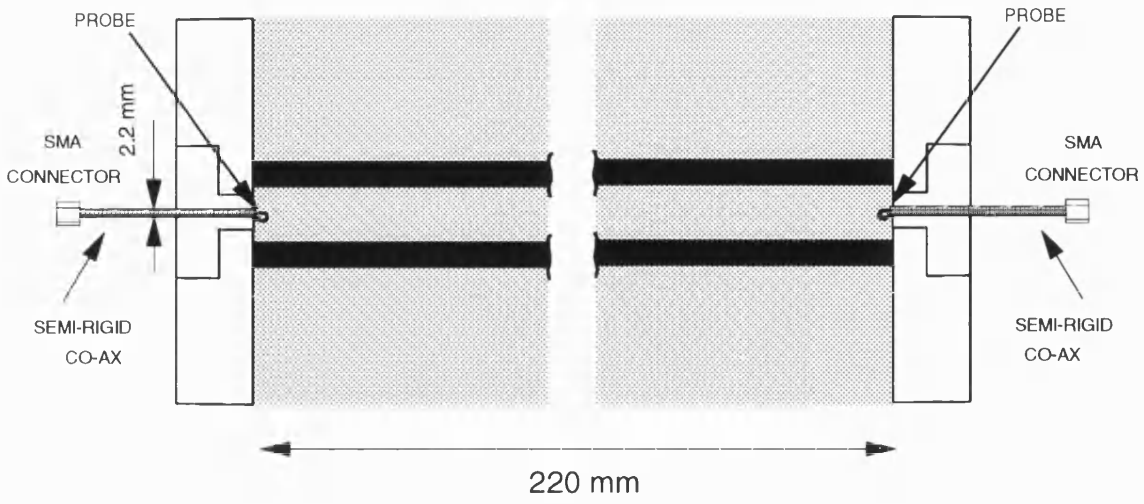

Figure 5.18: Plan View of the Coupled Lines Test Fixture

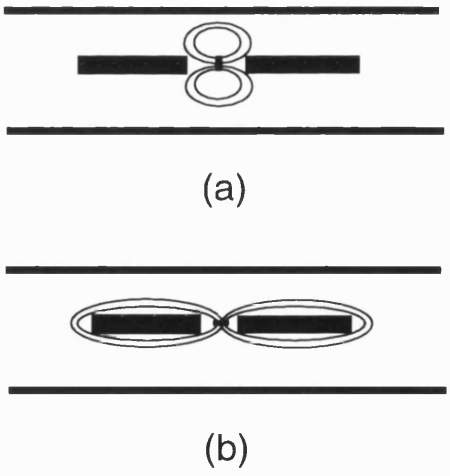

Figure 5.19: Magnetic Field Excitation for the Coupled Lines Test Fixture with probe placed perpendicular to the striplines (a), and parallel to the striplines (b)

the fundamental mode of propagation. Probe orientation (b) was used for all of the measurements, and the secondary set of maxima shown correspond to both the first and second higher order mode resonances. This illustrates the increased complexity in identifying the resonance number, n, (Equation 4.1) although the coupled lines structure does allow modes to be distinguished despite their similar propagation constant.

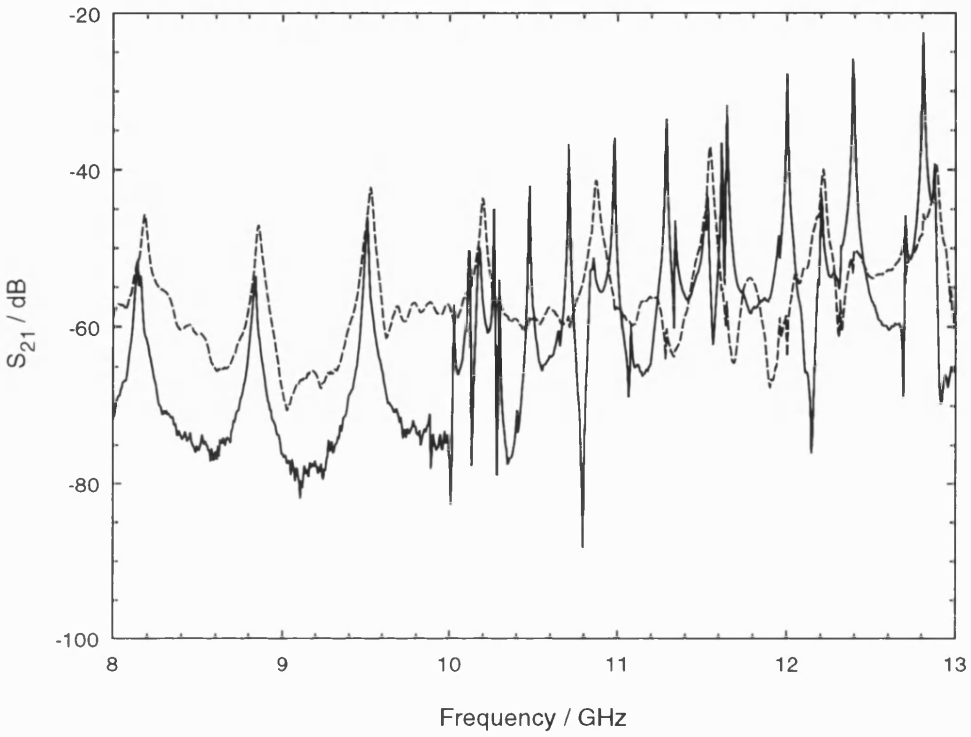

Figure 5.20: Plot of Transmission through the Test Fixture versus Frequency for Probe Orientation (a) (- - -) and Probe Orientation (b) (——) for Coupled Striplines with w=7.00mm, b=5.10mm, d=5.10mm, t=1.64mm and s=11.15mm, L=220mm, using an HP8510B Network Analyser (Averaging=100, 801 Points)

The measured and TRD results are directly compared to results computed by a 2D "ports only" solution computed using HFSS Ver A2.06 in Figure 5.21, the TRD and HFSS results are also compared as percentage differences of the measured data in Figure 5.22.

The graphs illustrate the excellent agreement between the TRD, HFSS and measured results with the difference between the three values typically of the order of one percent. The comparatively large error between the measured and computed results for a separa-

tion of s:h=0.738 suggests that the measured value is in error. The measured values are also tabulated in Tables 5.6 and 5.7 with the standard deviation of the measurements. The repeatability of the measurements is also good since the position of the resonant peaks of the first two higher order modes is largely independent of exact probe position.

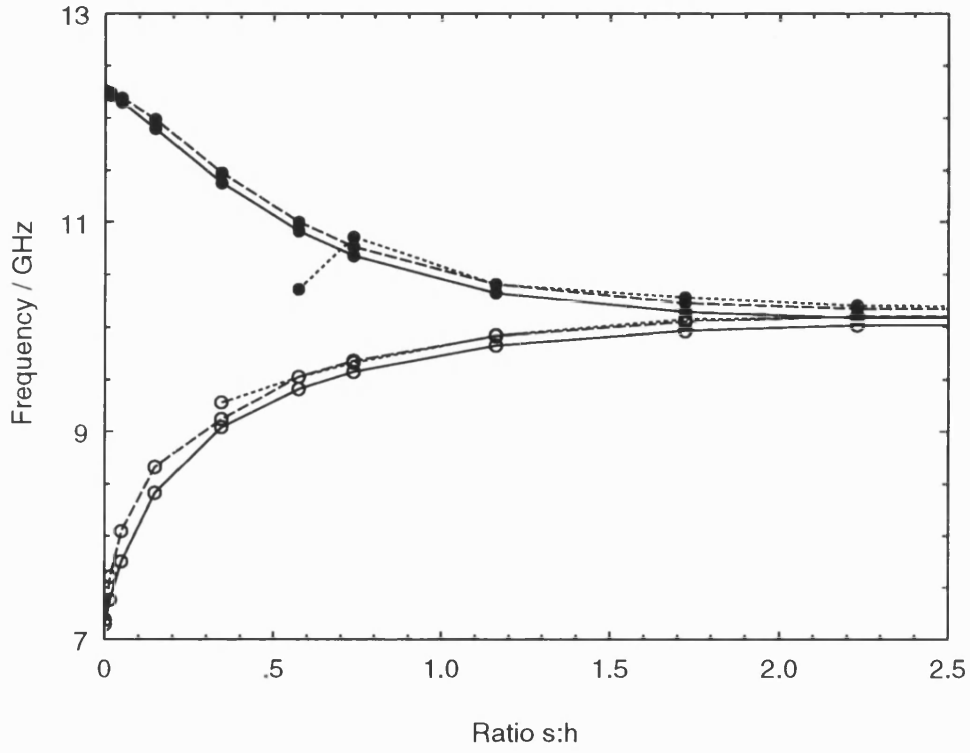

Figure 5.21: First [o] and Second [•] Higher Order Mode Cut-Off Frequencies versus Strip Separation (s:h) for Measured Data (· · · · · ·); TRD Analysis, (——); HFSS Ver. A2.06, (- - -) for b=5.10mm, d=5.10mm, t=1.64mm and h=11.84mm

5.7 Conclusions

The results presented in this Chapter have illustrated the ability of the TRD analysis to compute the parameters of coupled stripline structures of entirely arbitrary dimensions. Existing analytical techniques are restricted to variations in certain dimensions over a limited range, and numerical analyses provide results at the expense of a large

Ratio s:h	Frequency (GHz)	Std. Dev. (GHz)	Std. Dev. (%)	No. of Maxima N
0.348	9.281	0.035	0.38	12
0.574	9.527	0.033	0.35	11
0.738	9.665	0.044	0.46	12
1.160	9.923	0.023	0.23	11
1.172	10.075	0.043	0.43	13
2.238	10.096	0.021	0.21	9
8.000	10.104	0.032	0.31	11

Table 5.6: Measured Results for the First Higher Order Mode Cut-off Frequency for t=1.64mm, b=5.10mm, d=5.10mm, h=11.84mm

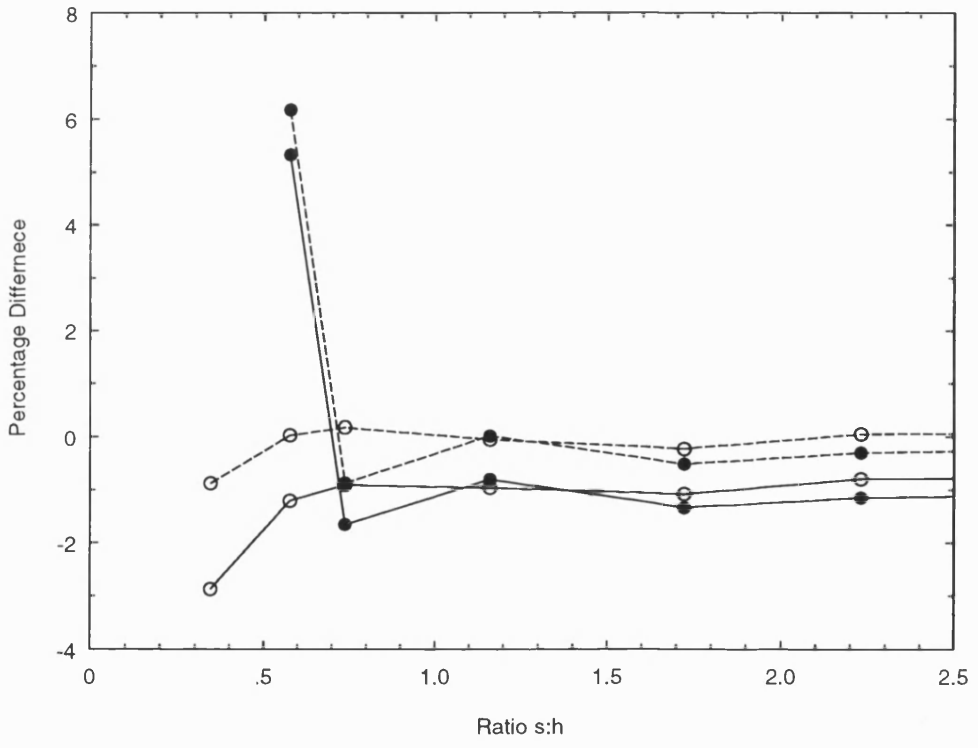

Figure 5.22: Percentage Variation between Measured Cut-Off Frequencies and Computed Cut-Off Frequencies for the First [o] and Second [•] Higher Order Modes Calculated by TRD Analysis, (——) and HFSS Ver. A2.06 (- - -), for b=5.10mm, d=5.10mm, t=1.64mm and h=11.84mm

computation time.

The complexity of the coupled lines structure compared with the uniform structure has meant that the monomode bandwidth of the structure has had to be computed using purely numerical methods. The TRD method provides a significantly faster means of calculation, without compromising the accuracy of the results.

The results for the coupling between the striplines has indicated that the TRD method predicts stronger coupling than the conformal mapping technique and HFSS 2D "ports only" solution due to the strong effect of the edge singularities. The results also illustrate that the comparatively small differences between the mode impedances can lead to large differences in the coupling values. The results also highlight the problems of using piece-wise approximations for accurate conformal mapping results, since this leads to non monatonic variations in the attenuation factor.

Ratio s:h	Frequency (GHz)	Std. Dev. (GHz)	Std. Dev. (%)	No. of Maxima N
0.348				
0.574	10.360	0.033	0.32	7
0.738	10.856	0.030	0.28	6
1.160	10.406	0.018	0.18	6
1.172	10.281	0.036	0.35	11
2.238	10.204	0.031	0.30	10
8.000	10.104	0.032	0.31	11

Table 5.7: Measured Results for the Second Higher Order Mode Cut-off Frequency for t=1.64mm, b=5.10mm, d=5.10mm, h=11.84mm

Chapter 6

Analysis of Stripline Discontinuities

6.1 Outline

The analysis of uniform and coupled stripline structures has been described in Chapter 3, and the theory verified in Chapters 4 and 5 by measurement and comparison with other analysis techniques. This section presents an extension to the TRD analysis to analyse stripline discontinuities of the type shown in Figure 6.1. The analysis is applicable to a number of types of discontinuity, but the case of a uniform to coupled lines transition is specifically treated. The analysis is carried out for stripline discontinuities with an infinitely thin central conductor, as is commonly found in MMIC's. Expressions for finite thickness discontinuities can be evaluated provided singularity orders for three dimensional corners in space can be found.

6.2 Formulation of the Discontinuity Problem

The stripline discontinuities are modelled using a technique introduced by Rozzi [64] for a dielectric waveguide. The methodology is identical, but the analysis is complicated by

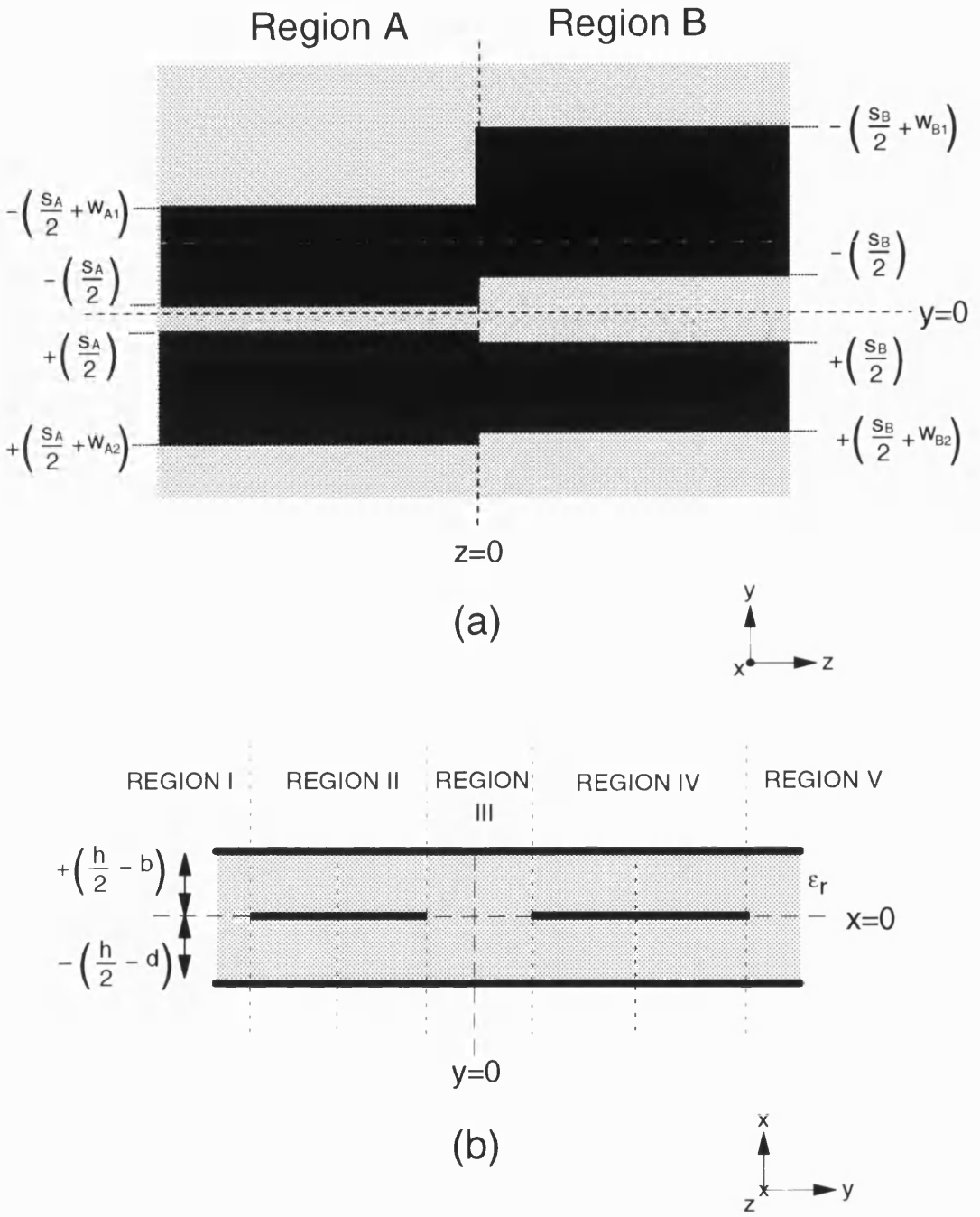

Figure 6.1: Plan View (a) and Cross Section View (b) of the General Form of the Stripline Discontinuity Analysed

the form of the cross-sectional fields in the stripline structure, and the expansion of the discontinuity fields to take into account the singularities on the strip. The analysis will be shown for the TE modes present in the structure with corresponding expressions for the TM modes derived later.

Recalling the expressions for the fields in terms of the vector potentials (Equations 3.24 and 3.25), and denoting the partial derivative by a primed quantity, the $\hat{x}$ directed electric and $\hat{y}$ directed magnetic TE fields in the cross section of the discontinuity can be written for mode, k:

$$e_{xk}(x,y,z) = A_k^{A,B} \sum_{n=0}^{n=\infty} A_n \, V_{xkn} \, \phi_h(n,x) \, \phi_h'(n,y) \, \phi(z) \tag{6.1}$$

$$h_{yk}(x,y,z) = -Y_{ok} \, e_{xk}(x,y,z) \tag{6.2}$$

Rewriting the $\hat{x}$ directed electric field as a summation of amplitude terms, U_{kn}, and field shape functions, $u_k(n,x,y)$, and omitting the $\hat{z}$ directed dependency for simplification:

$$e_{xk}(x,y) = A_k^{A,B} \sum_{n=0}^{n=\infty} U_{kn} \, u_k(n,x,y) \tag{6.3}$$

The orthonormalisation coefficient for the kth mode discontinuity field, $A_k^{A,B}$, is found from the expression:

$$\left[A_k^{A,B}\right]^2 \int_{CrossSection} \left[\sum_{n=0}^{n=\infty} U_{kn} \, u_k(n,x,y)\right]^2 d\underline{a} = 1 \tag{6.4}$$

The evaluation of this integral results in an orthonormalisation coefficient which is a function of the mode propagation constant, in addition to the stripline dimensions. In practice, the above integral is evaluated using a piece-wise description of the fields in the sixteen sub-regions shown in Figure 3.1. The derivation of the orthonormalisation coefficient is shown in Appendix E.

6.2.1 Network Representation

The discontinuity is analysed as a K port device shown in Figure 6.2, where the number of ports is given by the total number of modes propagating in Regions A and B:

$$K = K_A + K_B \tag{6.5}$$

The scattering parameters of the device are calculated using a modified form of the mode matching method, where the fields at the discontinuity plane (z=0) are described in terms of K incident waves with amplitudes A_k; and K reflected waves with amplitudes, B_k.

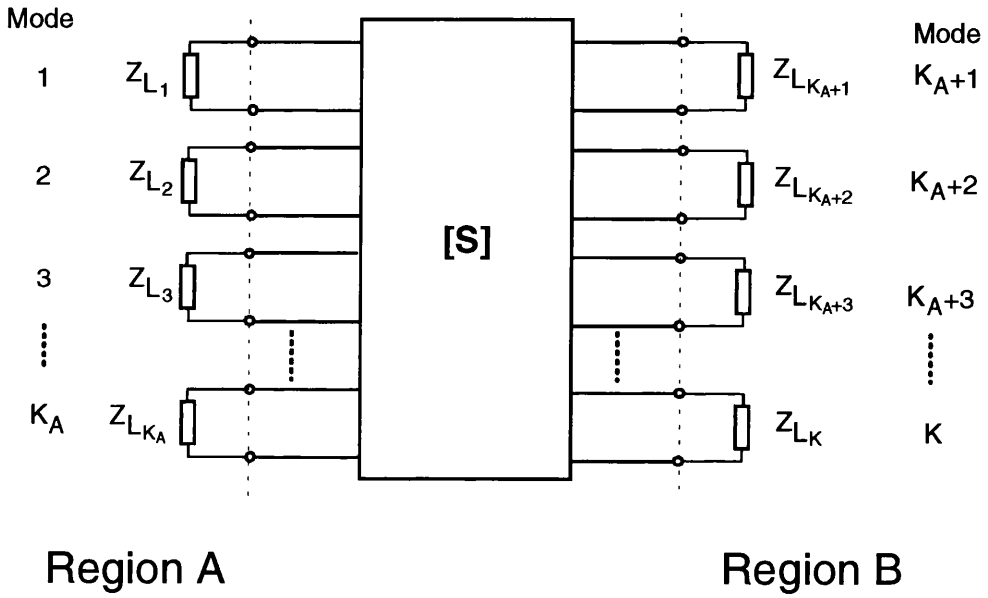

Figure 6.2: Equivalent Network Representation of the Stripline Discontinuity

The reflection and incident amplitude terms are related through the elements of the scattering matrix of the discontinuity.

$$[B] = [S][A] \tag{6.6}$$

The matrices are all of order $K \times K$, and if the discontinuity is excited with the lth mode of the structure, the incident amplitudes, A_k, are given by the lth row of [A], which is defined as:

$$A_k = \delta_{k,l} = \begin{cases} 1 & k = l \\ 0 & k \neq l \end{cases} \tag{6.7}$$

The lth column of the scattering parameter matrix, $[S]$ is then given by the resulting reflected amplitudes, B_k.

6.2.2 Derivation of Incident and Reflected Waves at the Discontinuity

The fields at the discontinuity plane can be written satisfying the field continuity conditions:

$$e_x(x,y) = \sum_{k=1}^{k=K_A} (A_k + B_k) \left[\sum_{n=0}^{n=\infty} U_{kn}\ u_k(n,x,y) \right] \tag{6.8}$$

$$= \sum_{k=K_A+1}^{k=K} (A_k + B_k) \left[\sum_{n=0}^{n=\infty} U_{kn}\ u_k(n,x,y) \right] \tag{6.9}$$

$$h_y(x,y) = \sum_{k=1}^{k=K_A} -Y_{ok}(A_k - B_k) \left[\sum_{n=0}^{n=\infty} U_{kn}\ u_k(n,x,y) \right] \tag{6.10}$$

$$= \sum_{k=K_A+1}^{k=K} -Y_{ok}(-A_k + B_k) \left[\sum_{n=0}^{n=\infty} U_{kn}\ u_k(n,x,y) \right] \tag{6.11}$$

Rewriting the expression for the $\hat{y}$ directed magnetic field, h_y (Equation 6.10):

$$h_y(x,y) + \sum_{k=1}^{k=K_A} Y_{ok} A_k \left[\sum_{n=0}^{n=\infty} U_{kn}\ u_k(n,x,y) \right] = \sum_{k=1}^{k=K_A} Y_{ok} B_k \left[\sum_{n=0}^{n=\infty} U_{kn}\ u_k(n,x,y) \right] \tag{6.12}$$

Integrating to form an inner product with the field shape function, normalised by the mode impedance, Y_{ok}:

$$\frac{1}{Y_{ok}} \int_{-\infty}^{+\infty} \int_{-\infty}^{+\infty} h_y(x,y) \left[\sum_{n=0}^{n=\infty} U_{kn}\ u_k(n,x,y) \right] dxdy$$
$$+ \sum_{k=1}^{k=K_A} \int_{-\infty}^{+\infty} \int_{-\infty}^{+\infty} A_k \left[\sum_{n=0}^{n=\infty} U_{kn}\ u_k(n,x,y) \right] dxdy \left[\sum_{n=0}^{n=\infty} U_{kn}\ u_k(n,x,y) \right]$$

$$= \sum_{k=1}^{k=K_A} \int_{-\infty}^{+\infty} \int_{-\infty}^{+\infty} B_k \left[\sum_{n=0}^{n=\infty} U_{kn}\ u_k(n,x,y) \right] dxdy \left[\sum_{n=0}^{n=\infty} U_{kn}\ u_k(n,x,y) \right] \tag{6.13}$$

Simplifying the above expression in terms of the incident and reflected amplitudes for each mode, k:

$$B_k = A_k + \frac{1}{Y_{ok}} \int_{-\infty}^{+\infty} \int_{-\infty}^{+\infty} h_y(x,y) \left[\sum_{n=0}^{n=\infty} U_{kn}\ u_k(n,x,y) \right] dxdy \tag{6.14}$$

A similar approach can be employed to simplify Equation 6.11, and both the resulting equations can be summarised as:

$$B_k = A_k - \frac{s_k}{Y_{ok}} \int_{-\infty}^{+\infty} \int_{-\infty}^{+\infty} h_y(x,y) \left[\sum_{n=0}^{n=\infty} U_{kn}\ u_k(n,x,y) \right] dxdy \tag{6.15}$$

where:

$$s_k = \begin{cases} -1 & 1 \leq k \leq K_A \\ +1 & K_A < k \leq K \end{cases} \tag{6.16}$$

6.2.3 Derivation of the Green's Function Impedance Operator

Equating the two expressions for the $\hat{x}$ directed electric field , e_x, given in Equations 6.8 and 6.9:

$$\sum_{k=1}^{k=K} -s_k \left(A_k + B_k\right) \left[\sum_{n=0}^{n=\infty} U_{kn}\ u_k(n,x',y') \right] = 0 \tag{6.17}$$

Substituting the expression for B_k (Equation 6.15) into Equation 6.17 and simplifying:

$$\sum_{k=1}^{k=K} 2\ s_k\ A_k \left[\sum_{n=0}^{n=\infty} U_{kn}\ u_k(n,x',y') \right] =$$
$$\sum_{k=1}^{k=K} \frac{s_k^2}{Y_{ok}} \int_{-\infty}^{+\infty} \int_{-\infty}^{+\infty} h_y(x,y) \left[\sum_{n=0}^{n=\infty} U_{kn}\ u_k(n,x,y) \right] dxdy \left[\sum_{n=0}^{n=\infty} U_{kn}\ u_k(n,x',y') \right] \tag{6.18}$$

Hence rewriting the right hand side as a Green's Function Impedance Operator linking the $\hat{x}$ directed electric field to the $\hat{y}$ directed magnetic field:

$$\sum_{k=1}^{k=K} s_k A_k \left[\sum_{n=0}^{n=\infty} U_{kn}\ u_k(n, x', y') \right] = \int_{-\infty}^{+\infty} \int_{-\infty}^{+\infty} Z(x, x', y, y')\ h_y(x, y)\ dxdy \quad (6.19)$$

where:

$$Z(x, x', y, y') = \frac{1}{2} \sum_{k=1}^{k=K} \frac{1}{Y_{ok}} \left[\sum_{n=0}^{n=\infty} U_{kn}\ u_k(n, x, y) \right] \left[\sum_{n=0}^{n=\infty} U_{kn}\ u_k(n, x', y') \right] \quad (6.20)$$

The $\hat{y}$ directed magnetic field can be written as a linear sum of the contributions from each of the modes excited independently, which correspond to the excitation matrix, $[A]$ (Equation 6.6):

$$h_y(x, y) = \sum_{l=1}^{l=K} A_l\ h_{yl}(x, y) \quad (6.21)$$

Hence, rewriting Equation 6.19 using Equation 6.21, for an incident excitation of mode, l, noting that $A_l = 1$:

$$s_l \left[\sum_{n=0}^{n=\infty} U_{ln}\ u_l(n, x', y') \right] = \int_{-\infty}^{+\infty} \int_{-\infty}^{+\infty} Z(x, x', y, y')\ h_{yl}(x, y)\ dxdy \quad (6.22)$$

6.2.4 Discretisation of Fields

Substituting the incident excitation conditions into Equation 6.15 and recalling the relationship between the reflected amplitudes and the S parameters:

$$S_{k,l} = \delta_{k,l} - \frac{s_k}{Y_{ok}} \int_{-\infty}^{+\infty} \int_{-\infty}^{+\infty} h_{yl}(x, y) \left[\sum_{n=0}^{n=\infty} U_{kn}\ u_k(n, x, y) \right] dxdy \quad (6.23)$$

The above equation therefore expresses the S parameters of the discontinuity in terms of an inner product between the field shapes of the Regions A and B and the unknown magnetic field distribution for mode l.

The fields at the interface can be expressed in terms of the field shapes in Regions A or

B, however a more efficient method is to expand the unknown fields at the discontinuity plane in terms of functions that take into account the singularity behaviour of the structure. Writing the field shape as a weighted summation of amplitude terms, X_{pk}, and basis functions, $f_p(x,y)$:

$$\sum_{n=0}^{n=\infty} U_{kn}\ u_k(n,x,y) = \sum_{p=0}^{p=\infty} X_{pk}\ f_p(x,y) \tag{6.24}$$

The amplitude terms can be expressed in a standard manner as:

$$X_{pk} = \sum_{n=0}^{n=\infty} U_{kn} \int_{-\infty}^{+\infty}\int_{-\infty}^{+\infty} f_p(x,y)\ u_k(n,x,y)\ dxdy \tag{6.25}$$

The unknown $\hat{y}$ directed magnetic field can be similarly written as a weighted summation of basis functions:

$$h_{yl}(x,y) = \sum_{p=0}^{p=\infty} H_{pl}\ f_p(x,y) \tag{6.26}$$

$$H_{pl} = \int_{-\infty}^{+\infty}\int_{-\infty}^{+\infty} f_p(x,y)\ h_{yl}(x,y)\ dxdy \tag{6.27}$$

Substituting the expression for the field shape function into Equation 6.23

$$S_{k,l} = \delta_{k,l} - \frac{s_k}{Y_{ok}} \sum_{p=0}^{p=\infty} X_{pk} \int_{-\infty}^{+\infty}\int_{-\infty}^{+\infty} f_p(x,y)\ h_{yl}(x,y)\ dxdy \tag{6.28}$$

Hence the S parameters can be expressed as:

$$S_{k,l} = \delta_{k,l} - \frac{s_k}{Y_{ok}} \sum_{p=0}^{p=\infty} X_{pk}\ H_{pl} \tag{6.29}$$

The Green's Function Impedance Operator (Equation 6.20) can also be written using the basis function expressions for the discontinuity fields:

$$Z(x,x',y,y') = \sum_{p=0}^{p=\infty}\sum_{q=0}^{q=\infty} Z_{pq}\ f_p(x,y)\ f_q(x',y') \tag{6.30}$$

where the impedance amplitude terms, Z_{pq} are defined by the inner product:

$$Z_{pq} = \int_{-\infty}^{+\infty}\int_{-\infty}^{+\infty} Z(x,x',y,y')\ f_p(x,y)\ f_q(x',y')\ dxdy' \tag{6.31}$$

$$= \frac{1}{2}\sum_{k=1}^{k=K} Z_{ok}\ X_{pk}\ X_{qk} \tag{6.32}$$

Substituting the above results into Equation 6.22:

$$s_l \sum_{p=0}^{p=\infty} X_{pl}\ f_p(x,y) = \int_{-\infty}^{+\infty}\int_{-\infty}^{+\infty} \sum_{p=0}^{p=\infty}\sum_{q=0}^{q=\infty} Z_{pq}\ h_{yl}(x,y)\ f_p(x,y)\ f_q(x',y')\ dxdy \tag{6.33}$$

$$s_l \sum_{p=0}^{p=\infty} X_{pl}\ f_p(x,y) = \sum_{p=0}^{p=\infty}\sum_{q=0}^{q=\infty} Z_{pq}\ H_{pl}\ f_q(x',y') \tag{6.34}$$

6.2.5 Matrix Representation of the S Parameter Expressions

The infinite limits of the summations in the previous expressions are truncated to finite values to enable the equations to be represented using matrices. Equation 6.29 can be rewritten and simplified assuming that the maximum values of p and q are equal to P, yielding a square matrix:

$$[S_l] = [\delta_l] - s_k[Z_{ok}][X_k]^T[H_l] \tag{6.35}$$

$$= [\delta_l] - s_k[Z_{ok}][X_k]^T[Z]^{-1}[Z][H_l] \tag{6.36}$$

Expressing Equation 6.34 in a similar manner, and evaluating the set of S parameters for the lth column of the overall S matrix,

$$s_l[X_l] = [Z][H_l] \tag{6.37}$$

Hence substituting Equation 6.37 into the S parameter expression:

$$[S_l] = [\delta_l] - s_k s_l[Z_{ok}][X_k]^T[Z]^{-1}[X_l] \tag{6.38}$$

where the matrices are defined:

$[S_l]$ is a matrix order K $\times$ 1, element S_{kl}

$[\delta_l]$ is a matrix order K $\times$ 1, element δ_{kl}

$[Z_{ok}]$ is a diagonal matrix, order K $\times$ K, element Z_{ij} such that the diagonal elements $Z_{ii} = Z_{oi}$

$[X_k]$ is a matrix order P$\times$K, element X_{pk}

$[Z]$ is a matrix order P$\times$P, element Z_{pq}

$[X_l]$ is a matrix order P$\times$1, element X_l

The normalised scattering matrix is defined for unity resistance terminations, whereas the problem is defined by assuming each mode is terminated by its mode impedance. The S parameters have to be related to the mode impedances in the structure, $[Z_{ck}]$.

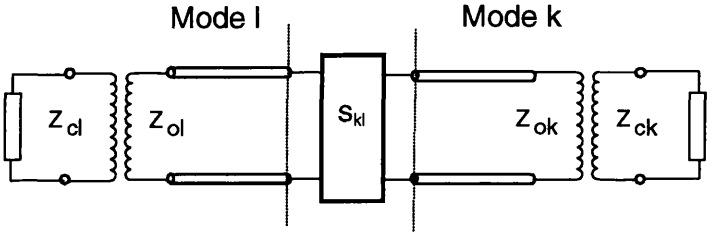

Figure 6.3: Equivalent Circuit of Impedance Transformers Connected at each of the outputs of the network

These conditions are met by inserting an ideal transformer at the ports of the network representation such that the wave impedance terminations are transformed to mode impedances. There is also the additional condition of reciprocity that has to be maintained between the modes, hence, defining the normalised S parameter matrix, with unity terminations, $\overline{[S]}$, the S parameter matrix of the discontinuity for TE modes is given as:

$$\overline{[S]} = [Z_{ok}]^{-\frac{1}{2}} \, S \, [Z_{ol}]^{\frac{1}{2}} \tag{6.39}$$

$$[S] = [Z_{ck}]^{\frac{1}{2}} \, [Z_{ok}]^{-\frac{1}{2}} \, S \, [Z_{ol}]^{\frac{1}{2}} \, [Z_{cl}]^{-\frac{1}{2}} \tag{6.40}$$

Summarising the overall equation for the S parameters of the discontinuity:

$$[S_l] = [\delta_l] - s_k s_l \, [Z_{ck}]^{\frac{1}{2}} \, [Z_{ok}]^{-\frac{1}{2}} \, [Z_{ol}]^{\frac{1}{2}} \, [Z_{cl}]^{-\frac{1}{2}} \, [X_k]^T \, [Z]^{-1} \, [X_l] \qquad (6.41)$$

6.2.6 Formulation of the Discontinuity Problem for TM Modes

A similar expression for the S parameter terms for the TM modes can also be derived. The theory for these modes is formulated in terms of the $\hat{y}$ directed electric field and the $\hat{x}$ directed magnetic field.

In the case of the uniform and coupled lines the behaviour of the edge singularities was identical for both the $\hat{x}$ and $\hat{y}$ directed electric fields, with the fields related through the vector potential expressions. The singularity expressions for the discontinuity fields differ between the $\hat{x}$ and $\hat{y}$ directed electric fields, hence different functions are used to discretise the fields. Identical matrix expressions for the S parameters are therefore derived with the evaluation of those terms differing between the TE and TM modes.

6.3 Evaluation of the S Parameter Expressions

The previous section has derived a compact expression for the S parameters in terms of matrices for an arbitrary stripline discontinuity of the form shown in Figure 6.1.

This section outlines the general calculation methodology for computing the S parameters of a discontinuity. The choice of basis functions is discussed for a number of types of discontinuity, and the inner product terms that are required to compute the amplitude matrices, $[X_k]$ are derived for the TE modes, however TM mode expressions can be found in a similar manner.

6.3.1 General Calculation Methodology

The steps in the calculation of the S parameters expression are shown in Figure 6.4. The operations marked • represent calculations carried out to characterise uniform and coupled stripline structures, whereas operations marked □ represent calculations carried out specifically to compute the S parameters of the discontinuity.

Figure 6.4 illustrates that a prerequisite for this type of analysis is an accurate and efficient means of calculating the propagation constants, mode impedances and field amplitude terms of the stripline structures.

The computational efficiency of the discontinuity analysis is governed by the number of modes, K, required to obtain convergence of the S parameters in addition to the number of field expansion terms, N, and the number of basis functions, P, required to discretise the fields in the cross-section of the discontinuity. In general, the number of modes and field expansion terms required is set by the structure being analysed. An improvement in computational efficiency can therefore be achieved by a suitable choice of the basis functions for the discontinuity fields.

6.3.2 Choice of Basis Functions

The appropriate choice of two-dimensional basis functions is important to ensure an efficient discretisation of the unknown fields. This minimises the order of the impedance matrix to be inverted, and hence the time required to carry out this operation which is proportional to the cube of the matrix order [66].

The singularity behaviour of the uniform line step in width, and the uniform to coupled lines transition (Figure 6.5) are shown in Figures 6.6 and 6.7 respectively, with the basis functions used to discretise the unknown fields tabulated in Tables 6.1 and 6.2 respectively.

The values quoted to one decimal place are minimum orders for the singularity, derived by Collin [19], whereas the values quoted to six decimal places were computed by Marchetti [71] for 2D planar metallisations. The weight functions, range and validity

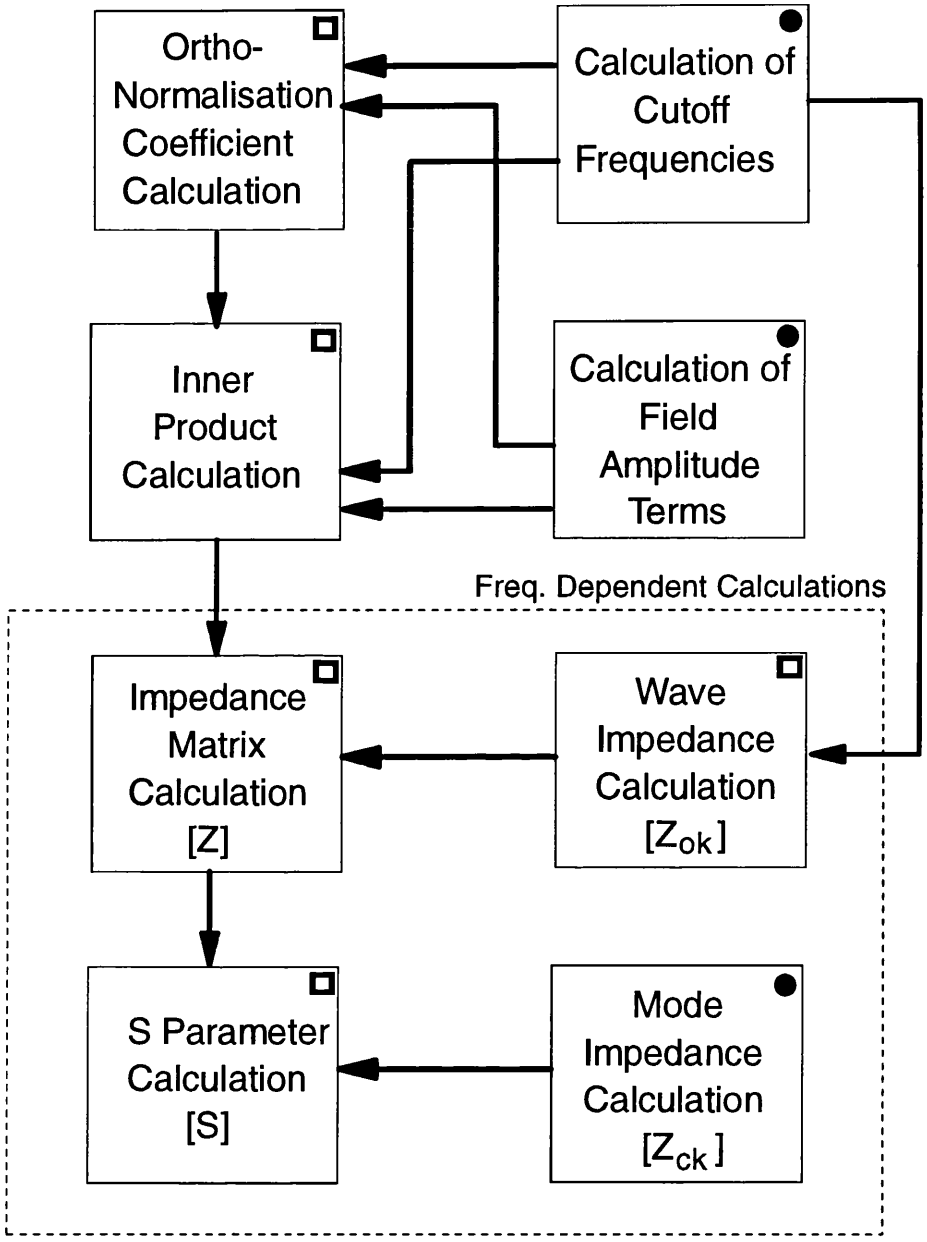

Figure 6.4: Calculation Methodology for the Computation of the S Parameters of a Stripline Discontinuity

Range	Singularity Order	
	$\hat{x}$	$\hat{y}$
$-\infty < y < -w_{B1}$	$\nu = -0.703416$	$\nu = -0.703416$
$-w_{B1} < y < -w_{A1}$	$\nu = -0.703416$ $\nu = -0.185345$	$\nu = -0.203416$ $\eta = +0.314655$
$-w_{A1} < y < w_{A2}$	$\nu = -0.185345$	$\nu = -0.185345$
$w_{A2} < y < w_{B2}$	$\nu = -0.185345$ $\nu = -0.703416$	$\nu = +0.314655$ $\eta = -0.203416$
$w_{B2} < y < +\infty$	$\nu = -0.703416$	$\nu = -0.703416$

Table 6.1: Basis Functions used to Model the $\hat{x}$ Directed Electric Field Singularities at the Plane of the Uniform Lines Step in Width Discontinuity Calculated by Marchetti

Range	Singularity Order	
	$\hat{x}$	$\hat{y}$
$-\infty < y < -w_{A1}$	$\nu = -0.5(*)$	$\nu = -0.5(*)$
$-w_{A1} < y < -(w_{A1} - w_{B1})$	$\nu = -0.5(*)$ $\nu = -0.185345(\dagger)$	$\nu = -0.5(*)$ $\eta = -0.185345(\dagger)$
$-(w_{A1} - w_{B1}) < y < (w_{A2} - w_{B2})$	$\nu = -0.185345(\dagger)$	$\nu = +0.314655(\dagger)$
$(w_{A2} - w_{B2}) < y < w_{A2}$	$\nu = -0.185345(\dagger)$ $\nu = -0.5(*)$	$\nu = -0.185345(\dagger)$ $\eta = -0.5(*)$
$w_{A2} < y < +\infty$	$\nu = -0.5(*)$	$\nu = -0.5(*)$

Table 6.2: Basis Functions used to Model the $\hat{x}$ Directed Electric Field Singularities at the Plane of the Uniform Line to Coupled Line Transition Calculated by Marchetti ($\dagger$) and Collin ($*$)

Polynomial		Weight Function	Range	Validity
Chebyshev	$T_n(x)$	$(1-x^2)^{-\frac{1}{2}}$	$-1 < x < +1$	
Gegenbauer	$C_n^{\nu}(x)$	$(1-x^2)^{\nu-\frac{1}{2}}$	$-1 < x < +1$	$\nu > -\frac{1}{2}$
Jacobi	$P_n^{\nu,\eta}(x)$	$(1-x)^{\nu}(1+x)^{\eta}$	$-1 < x < +1$	$\nu > -1, \eta > -1$
Laguerre	$L_n^{\nu}(x)$	$e^{-x}x^{\nu}$	$0 < x < +\infty$	$\nu > -1$

Table 6.3: Basis Functions used to Model the Singularities Present in the Fields in the Discontinuity Plane of Various Stripline Structures

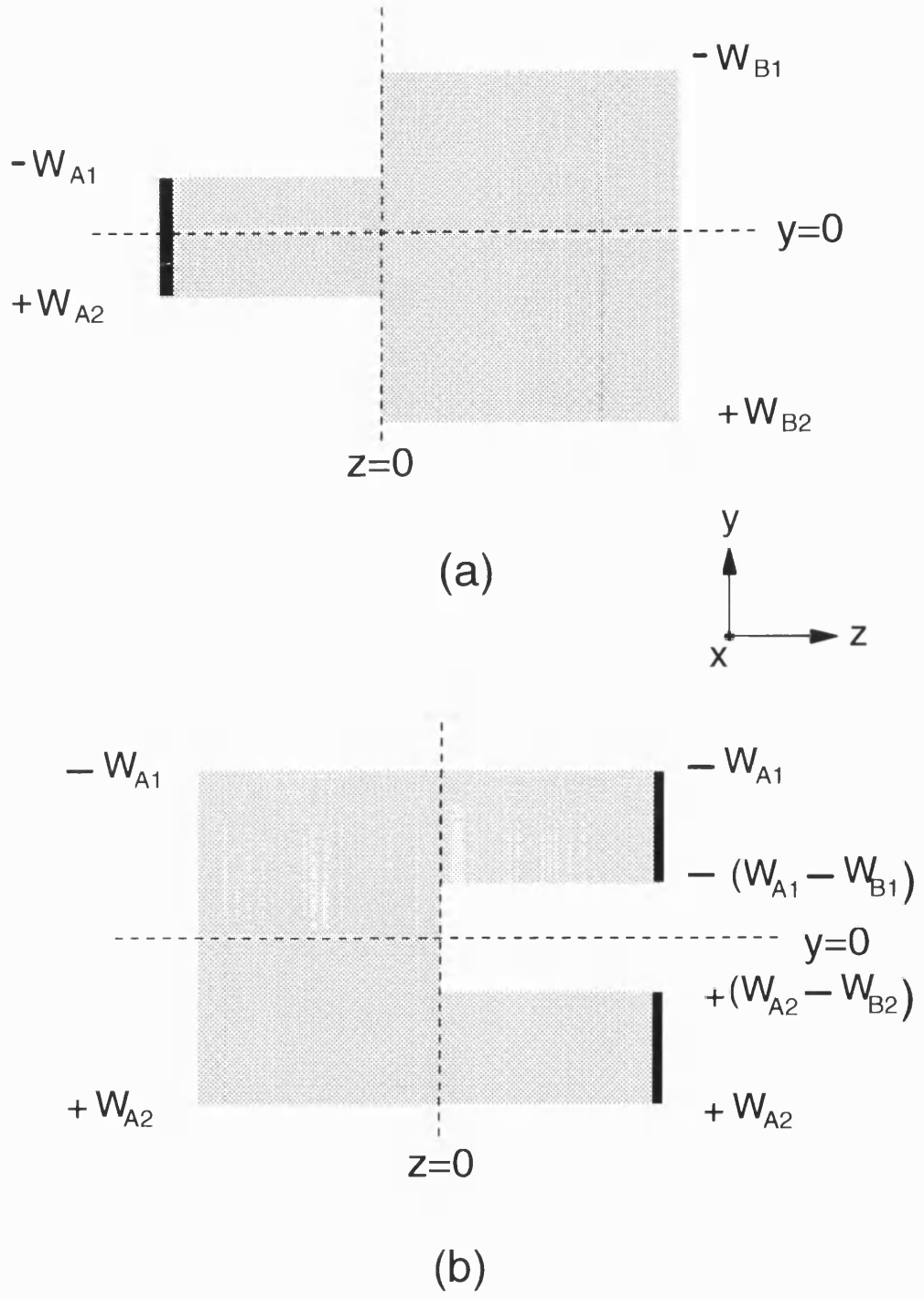

Figure 6.5: Uniform Line Step in Width Discontinuity (a) and Uniform to Coupled Lines Discontinuity (b)

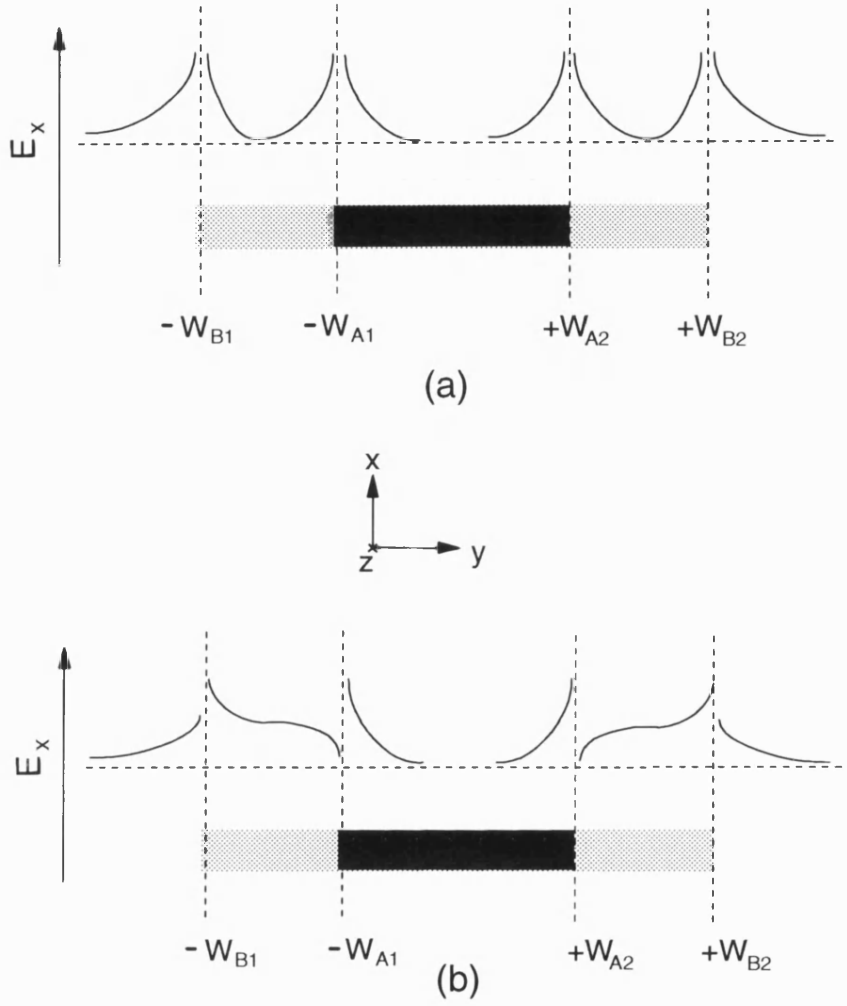

Figure 6.6: $\hat{x}$ Directed Singularity Behaviour (a) and the $\hat{y}$ Directed Singularity Behaviour (b) of the $\hat{x}$ Directed Electric Field at the Discontinuity Plane of a Uniform Lines Step in Width Discontinuity

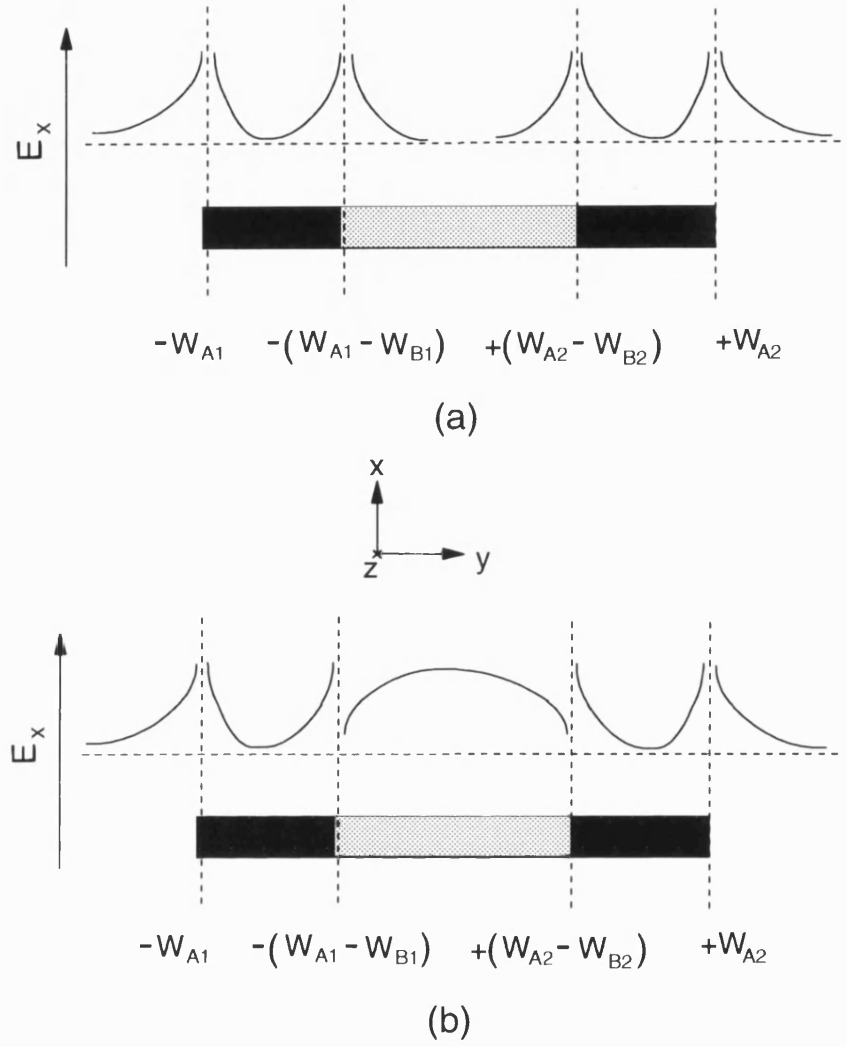

Figure 6.7: $\hat{x}$ Directed Singularity Behaviour (a) and the $\hat{y}$ Directed Singularity Behaviour (b) of the $\hat{x}$ Directed Electric Field at the Discontinuity Plane of a Uniform to Coupled Lines Transition

of the functions that are used to model the singularities are summarised in Table 6.3 [72].

Recalling the form of the basis functions used to discretise the unknown field (Equation 6.24):

$$\sum_{n=0}^{n=\infty} U_{kn}\ u_k(n,x,y) = \sum_{p=0}^{p=\infty} X_{pk}\ f_p(x,y) \tag{6.42}$$

The basis function, $f_p(x,y)$ is assumed separable in the $\hat{x}$ and $\hat{y}$ directions, such that:

$$f_p(x,y) = f_p(x)\ f_p(y) \tag{6.43}$$

and where in general:

$$f_p(x) = A_p\ W(x,\nu,\eta)\ F(x,\nu,\eta) \tag{6.44}$$

with a similar expression for the $\hat{y}$ directed variation.

It should be noted that the orders of the singularities strictly only apply at the singularity points. The results for the convergence of the uniform line impedances demonstrated that as the dimensions of the striplines were changed the singularity orders also changed. This is consistent with the minimum order of the singularity changing from $-\frac{1}{3}$ to $-\frac{1}{2}$ [19]. The singularity orders quoted in Tables 6.1 and 6.2 [71] to six significant figures assume isolated singularities. The effective order of the singularities will change if any interaction occurs between the edge singularities. In general, two significant figures is a more practical precision for this analysis.

6.3.3 Calculation of Amplitude Matrices

Recalling the expressions for the terms of the amplitude matrix, $[X]$:

$$X_{pk} = \sum_{n=0}^{n=\infty} U_{kn} \int_{-\infty}^{+\infty} \int_{-\infty}^{+\infty} f_p(x,y)\ u_k(n,x,y)\ dxdy \tag{6.45}$$

The above expression can be rewritten in terms of an inner product, P_{pn}, defined between the basis functions, $f_p(x,y)$ and the field shape functions, $u_k(x,y)$:

$$X_{pk} = \sum_{n=0}^{n=\infty} U_{kn} P_{pn} \tag{6.46}$$

The $\hat{x}$ and $\hat{y}$ variations of the basis and field shape functions are separated, resulting in $\hat{x}$ and $\hat{y}$ directed inner product contributions:

$$P_{pn} = \int_x u_k(n,x) f_p(x)\, dx \int_y u_k(n,y) f_p(y)\, dy \tag{6.47}$$

$$= P_{pn(x)} P_{pn(y)} \tag{6.48}$$

The expressions for the field shape functions $u_k(n,x,y)$ of the stripline structure are defined as a piece-wise approximation across a number of sub-regions which are defined in Figure 3.1 for a pair of coupled striplines. The uniform line is also represented as a pair of coupled lines with zero separation, hence this structure is also divided into sixteen sub-regions, with Region III having zero width. This assumption can be verified by the consistent behaviour of the cut-off frequencies with strip separation as shown in Chapter 5, Figure 5.2. The figure illustrates that as the coupled lines separation is reduced the cut-off frequencies tend towards those of a uniform line. The inner product integrals are therefore given by a summation of contributions over the sixteen sub-regions.

A number of inner product terms have been derived in Appendix E between general field shape functions and Laguerre, Chebyshev, Gegenbauer and Jacobi polynomials.

The calculation of the amplitude matrix terms is best illustrated using an example of a specific stripline discontinuity. The uniform to coupled lines transition is shown in Figure 6.5. The amplitude matrix terms for this structure can be written using notation introduced in the uniform and coupled lines analysis for TE modes:

$$X_{pk} = A_k^{A,B} \sum_{i=1}^{i=16} \sum_{n=0}^{n=\infty} \left(\frac{A_n^{R_i}\, V_{xkn}^{R_i}}{j\omega\mu_o} \right) P_{pn(x)}^{R_i}\; P_{pn(y)}^{R_i} \tag{6.49}$$

The inner product terms can then be derived for the five regions and sixteen sub-regions as shown in the following sections.

Regions I and V

The field components are identical in Regions A and B for Regions I and V since the outer dimensions for the uniform and coupled striplines are equal.

The $\hat{x}$ directed inner product for $x > (\frac{h}{2} - b_i)$ is given by the integral of the $\hat{x}$ directed field and Chebyshev polynomials and can be written as:

$$P_{pn(x)} = \int_{\frac{h}{2}-b_i}^{\frac{h}{2}} A_p b_i^{-1} \left[1 - \left(\frac{x - \frac{h}{2}}{b_i}\right)^2\right]^{-\frac{1}{2}} T_p\left(\frac{x - \frac{h}{2}}{b_i}\right) \text{Cos } k_x^{R_i}\left(x - \frac{h}{2}\right) dx \quad (6.50)$$

The above integral can then be evaluated (Appendix E) and a similar result derived for $x < (\frac{h}{2} - b_i)$:

$$P_{pn(x)} = A_{2p}\,(-1)^p \left[\frac{\pi}{2}\right] J_{2p}(b_i k_x^{R_i}) \qquad x > \left(\frac{h}{2} - b_i\right) \quad (6.51)$$

$$= A_{2p}\,(-1)^p \left[\frac{\pi}{2}\right] J_{2p}(d_i k_x^{R_i}) \qquad x < \left(\frac{h}{2} - b_i\right) \quad (6.52)$$

The orthonormalisation coefficient is derived in Appendix E.

The $\hat{y}$ directed component is given by the inner product of the fields with Laguerre polynomials with the integral for sub-region, R_1, written as:

$$P_{pn(y)} = \int_{-w_{A2}}^{-\infty} A_p \left(\frac{y + w_{A2}}{\Psi}\right)^{\nu} \text{Exp}\left[-\left(\frac{y + w_{A2}}{\Psi}\right)\right] L_p\left(\frac{y + w_{A2}}{\Psi}\right) \text{Exp}\left[-jk_y^{R_1}(y + w_{A2})\right] dy \quad (6.53)$$

The above integral is evaluated in general in Appendix E as:

$$P_{pn(y)} = A_{2p}\Psi(-1)^p \frac{\Gamma(\nu + 2p + 1)}{(2p)!}\left[\frac{(\Psi k_y^{R_i})^{2p}}{(1 + jk_y^{R_i})^{\nu+2p+1}}\right] \quad (6.54)$$

The value of the singularity term, ν, is defined in Table 6.2 as $\nu = -0.5$.

The orthonormalisation coefficient is shown in Appendix E, and the Laguerre Polynomial convergence constant, Ψ, is found by minimising the error function, f_{err} [73]:

$$f_{err} = -\sum_{k=1}^{k=K}\sum_{n=1}^{n=N}\left[\frac{1}{4[k_y^{R_i}]^2} + \Psi^2 \sum_{p=0}^{p=P} A_p^2 \frac{[\Gamma(\nu + 2p + 1)]^2}{[(2p)!]^2}\left(\frac{(\Psi k_y^{R_i})^{2p}}{(1 + jk_y^{R_i})^{\nu+2p+1}}\right)^2\right] \quad (6.55)$$

This constant is calculated using an interval halving technique similar to the one used to determine the propagation constant of uniform and coupled line structures (Chapter 3).

Regions II to IV

In Regions I and V, the outer dimensions for Regions A and B are equal hence the boundaries of the sub-regions coincide across the discontinuity plane, however in Regions II to IV the boundaries of the sub-regions do not coincide. This leads to a more complex form for the expressions for the inner products.

The $\hat{x}$ directed inner product is given by the integral for the regions $x > (\frac{h}{2} - b_i)$:

$$P_{pn(x)} = \int_{\frac{h}{2}-b_i}^{\frac{h}{2}} A_p b_i^{2\nu-1} \left[1 - \left(\frac{x - \frac{h}{2}}{b_i}\right)\right]^{\nu-\frac{1}{2}} C_p^{\nu}\left(\frac{x - \frac{h}{2}}{b_i}\right) \text{Cos } k_x^{R_i}\left(x - \frac{h}{2}\right) \, dx \quad (6.56)$$

The above integral can be solved using results derived in Appendix E:

$$P_{pn(x)} = j^p \, A_p \left[\frac{\pi 2^{1-\nu}\Gamma(2\nu + p)}{p!\Gamma(\nu)}\right] \left(k_x^{R_i} b_i\right)^{-\nu} \, J_{p+\nu}(k_x^{R_i} b_i) \left[\frac{\text{Cos } k_x^{R_i}[(\frac{h}{2} - b_i) - \frac{h}{2}]}{\text{Cos } k_x^{R_i}\frac{h}{2}}\right] \quad (6.57)$$

Recalling that the field shapes should exhibit even symmetry, the variable p is replaced with 2p, with a corresponding expression for $x < (\frac{h}{2} - b_i)$ found by substituting d_i for b_i:

$$P_{pn(x)} = A_{2p}(-1)^p \left[\frac{\pi 2^{1-\nu}\Gamma(2\nu + 2p)}{(2p)!\Gamma(\nu)}\right] \left(k_x^{R_i} b_i\right)^{-\nu} \, J_{2p+\nu}(k_x^{R_i} b_i) \left[\frac{\text{Cos } k_x^{R_i} b_i}{\text{Cos } k_x^{R_i}\frac{h}{2}}\right] \quad (6.58)$$

$$= A_{2p}(-1)^p \left[\frac{\pi 2^{1-\nu}\Gamma(2\nu + 2p)}{(2p)!\Gamma(\nu)}\right] \left(k_x^{R_i} d_i\right)^{-\nu} \, J_{2p+\nu}(k_x^{R_i} d_i) \left[\frac{\text{Cos } k_x^{R_i} d_i}{\text{Cos } k_x^{R_i}\frac{h}{2}}\right] \quad (6.59)$$

The value of the singularity order, ν, is given in Table 6.2 for the sub-regions as:

$$\nu = -0.185345 \quad R_5 \text{ to } R_{12}$$
$$\nu = -0.5 \quad \text{otherwise}$$

The $\hat{y}$ directed inner products are defined by the following integrals for Regions II,

III and IV respectively:

$$P^{II}_{pn(y)} = \int_{-w_{A1}}^{-(w_{A1}-w_{B1})} A_p \left(\frac{w_{B1}}{2}\right)^{\nu+\eta} \left[1-\left(\frac{y+(w_{A1}+\frac{w_{B1}}{2})}{\frac{w_{B1}}{2}}\right)\right]^{\nu} \left[1+\left(\frac{y+(w_{A1}+\frac{w_{B1}}{2})}{\frac{w_{B1}}{2}}\right)\right]^{\eta} P_p^{\nu,\eta}\left(\frac{y+(w_{A1}+\frac{w_{B1}}{2})}{\frac{w_{B1}}{2}}\right) \left[\frac{\text{Exp}\ [-jk_y^{R_i}(y-\psi)]+\rho\ \text{Exp}\ [jk_y^{R_i}(y-\psi)]}{C_\psi^{R_i}}\right] dx \quad (6.60)$$

$$P^{III}_{pn(y)} = \int_{-(w_{A1}-w_{B1})}^{w_{A2}-w_{B2}} A_p \left(\frac{s}{2}\right)^{2\nu-1} \left[1-\left(\frac{y}{\frac{s}{2}}\right)\right]^{\nu-\frac{1}{2}} C_p^{\nu}\left(\frac{y}{\frac{s}{2}}\right) \left[\frac{\text{Exp}\ [-jk_y^{R_i}(y-\psi)]+\rho\ \text{Exp}\ [jk_y^{R_i}(y-\psi)]}{C_\psi^{R_i}}\right] dx \quad (6.61)$$

$$P^{IV}_{pn(y)} = \int_{w_{A2}-w_{B2}}^{w_{B2}} A_p \left(\frac{w_{B2}}{2}\right)^{\nu+\eta} \left[1-\left(\frac{y-(w_{A2}-\frac{w_{B2}}{2})}{\frac{w_{B2}}{2}}\right)\right]^{\nu} \left[1+\left(\frac{y-(w_{A2}+\frac{w_{B2}}{2})}{\frac{w_{B2}}{2}}\right)\right]^{\eta} P_p^{\nu,\eta}\left(\frac{y+(w_{A2}+\frac{w_{B2}}{2})}{\frac{w_{B2}}{2}}\right) \left[\frac{\text{Exp}\ [-jk_y^{R_i}(y-\psi)]+\rho\ \text{Exp}\ [jk_y^{R_i}(y-\psi)]}{C_\psi^{R_i}}\right] dx \quad (6.62)$$

where the constant, $C_\psi^{R_i}$ is given by:

$$C_{\psi_i}^{R_i} = \text{Exp}\ [-jk_y^{R_i}\psi_i]+\rho\ \text{Exp}\ [jk_y^{R_i}\psi_i] \quad (6.63)$$

The form of the inner products are derived in Appendix E, and the overall inner product found as:

$$P^{II}_{pn(y)} = A_p 2^{\nu_{II}+\eta_{II}+1} \frac{\Gamma(\eta+1)\Gamma(1)\Gamma(\nu+1)}{\Gamma(1-p)\Gamma(\nu+\eta+p+2)} {}_2F_2\left[1+\eta\ ,\ 1\ ;\ 1-p\ ,\ \nu+\eta+p+2\ ;\ 2jk_y^{R_i}\frac{w_{B1}}{2}\right] \left[\frac{\text{Exp}\ [jk_y^{R_i}[(w_{A1}+\frac{w_{B1}}{2})-\psi]]+\rho\ \text{Exp}\ [-jk_y^{R_i}[(w_{A1}+\frac{w_{B1}}{2})-\psi]]}{C_\psi^{R_i}}\right] \quad (6.64)$$

$$P^{III}_{pn(y)} = A_p j^p \left[\frac{\pi 2^{1-\nu}\Gamma(2\nu+p)}{p!\Gamma(\nu)}\right]\left(k_y^{R_i}\frac{s}{2}\right)^{-\nu} J_{p+\nu}\left(k_y^{R_i}\frac{s}{2}\right) \left[\frac{\text{Exp}\ [-jk_y^{R_i}\psi]+\rho\ \text{Exp}\ [jk_y^{R_i}\psi]}{C_\psi^{R_i}}\right] \quad (6.65)$$

$$P^{IV}_{pn(y)} = A_p 2^{\nu+\eta+1} \frac{\Gamma(\eta+1)\Gamma(1)\Gamma(\nu+1)}{\Gamma(1-p)\Gamma(\nu+\eta+p+2)}$$

$$ {}_2F_2\left[1+\eta\ ,\ 1\ ;\ 1-p\ ,\ \nu+\eta+p+2\ ;\ 2jk_y^{R_i}\frac{w_{B2}}{2}\right] \left[\frac{\text{Exp}\ \left[jk_y^{R_i}[(w_{A2}-\frac{w_{B2}}{2})-\psi]\right]+\rho\ \text{Exp}\ \left[-jk_y^{R_i}[(w_{A2}-\frac{w_{B2}}{2})-\psi]\right]}{C_\psi^{R_i}}\right] \tag{6.66} $$

The singularity orders are tabulated in Table 6.2, and summarised as:

$$ \left.\begin{array}{rcr} \nu &=& -0.5 \\ \eta &=& -0.185345 \end{array}\right\} \quad \text{Region II} $$

$$ \nu = +0.314655 \qquad \text{Region III} $$

$$ \left.\begin{array}{rcr} \nu &=& -0.185345 \\ \eta &=& -0.5 \end{array}\right\} \quad \text{Region IV} $$

The orthonormalisation coefficients, A_p are derived in Appendix E for the various basis functions:

$$ A_p = \frac{(w_{B1})^{1+\nu+\eta}\Gamma(\nu+p+1)\Gamma(\eta+p+1)}{p!(\nu+\eta+1+2p)\Gamma(\nu+\eta+p+1)}^{-\frac{1}{2}} \qquad \text{Region II} \tag{6.67} $$

$$ A_p = (s)^{-(1+2\nu)}\left[\frac{p!(p+\nu+\frac{1}{2})[\Gamma(\nu+\frac{1}{2})]^2}{\pi\Gamma(p+2\nu+1)}\right]^{-\frac{1}{2}} \qquad \text{Region III} \tag{6.68} $$

$$ A_p = \frac{(w_{B2})^{1+\nu+\eta}\Gamma(\nu+p+1)\Gamma(\eta+p+1)}{p!(\nu+\eta+1+2p)\Gamma(\nu+\eta+p+1)}^{-\frac{1}{2}} \qquad \text{Region IV} \tag{6.69} $$

6.3.4 Calculation of Impedance Matrices

The impedance matrix, $[Z]$ and hence its inverse, $[Z]^{-1}$ is calculated from the amplitude matrix terms and the wave impedances of the modes in the structure. An element of the impedance matrix, Z_{pq} is given by:

$$ Z_{pq} = \sum_{k=1}^{k=K} Z_{ok}\ X_{pk}X_{qk} \tag{6.70} $$

$$ = \omega\mu_o \sum_{k=1}^{k=K} \frac{1}{\beta_k} X_{pk}X_{qk} \tag{6.71} $$

6.3.5 Calculation of Wave and Mode Impedance Matrices

The wave and mode impedance matrices are found directly from the uniform and coupled lines computations with the matrices defined as:

$$[Z_{ok}] = \omega\mu_o \begin{bmatrix} \beta_1^{-1} & 0 & \cdots & 0 \\ 0 & \beta_2^{-1} & \cdots & 0 \\ \vdots & \vdots & \ddots & \vdots \\ 0 & 0 & \cdots & \beta_K^{-1} \end{bmatrix} \quad ; \quad [Z_{ck}] = \begin{bmatrix} Z_{c1} & 0 & \cdots & 0 \\ 0 & Z_{c2} & \cdots & 0 \\ \vdots & \vdots & \ddots & \vdots \\ 0 & 0 & \cdots & Z_{cK} \end{bmatrix} \tag{6.72}$$

where Z_{ck} represents the mode impedance for mode, k. The corresponding matrices, $[Z_{ol}]$ and $[Z_{cl}]$ are found by replacing the diagonal elements with the wave and mode impedances for the lth mode respectively.

6.4 Notes on the Implementation of the S Parameter Calculation

The implementation of the S parameter expression is relatively straightforward, and follows the calculation methodology outlined in Figure 6.4.

In order to check the implementation, the convergence of the Laguerre polynomial constant, Ψ; the amplitude matrix terms, X_{pk}; and the scattering parameter matrix, $[S]$ have to be determined. The convergence is studied with respect to the number of field expansion terms, N; the number of basis function terms, P; and the number of modes, K.

The calculation of the S parameters requires the inversion of the impedance matrix, $[Z]$, hence it relies on the matrix being non-singular. The conditions required to make $[Z]$ singular are briefly discussed to determine whether this will place a limitation on the type of discontinuity, or the range of dimensions of the structures that can be analysed.

6.4.1 Singular Behaviour of the Impedance Matrix

The discontinuity theory can be verified by analysing the limiting case of a stripline "discontinuity" of two uniform striplines of equal width, which should exhibit zero reflection (S_{11}) and unit transmission ($S_{(K_A+1)\,1}$) with zero scattering into the remaining modes.

Recalling the expression for the terms of the impedance matrix:

$$Z_{pq} = \sum_{k=1}^{k=K} Z_{ok}\ X_{pk} X_{qk} \tag{6.73}$$

The identical nature of the Regions A and B determines that:

$$X_{pk} = X_{p(k+K_A)} \tag{6.74}$$

It is assumed that the analysis is carried out at a frequency, much smaller than the cut-off frequency of the first higher order mode, such that the elements of the impedance matrix are given by:

$$Z_{pq} = 2\left[120\pi\ X_{p1} X_{q1} + j \sum_{2}^{K_A} \mid Z_{ok} \mid\ X_{pk} X_{qk}\right] \tag{6.75}$$

Assuming a simplified case of K=4, i.e. two modes on either side of the interface are required for convergence of the S parameters, and that the interface fields can be adequately described by two basis functions; the determinant of the impedance matrix is then found as:

$$|Z| = 240\pi \begin{vmatrix} X_{11}X_{11} + jZ'_{o1}X_{12}X_{21} & X_{11}X_{21} + jZ'_{o1}X_{12}X_{22} \\ X_{21}X_{11} + jZ'_{o1}X_{22}X_{12} & X_{21}X_{21} + jZ'_{o1}X_{22}X_{22} \end{vmatrix} \tag{6.76}$$

$$= 240\pi \Big(\left[X_{11}^2 X_{21}^2 - X_{11}^2 X_{21}^2\right] - \left[Z'_{o1}\right]^2 \left[X_{12}^2 X_{22}^2 - X_{12}^2 X_{22}^2\right] + jZ'_{o1}\left[X_{11}X_{22} - X_{12}X_{21}\right]^2 \Big) \tag{6.77}$$

where the normalised impedance is denoted by the primed quantity.

Two observations can be made from the expression for the determinant. Firstly,

if the minimum number of modes is used, which is by definition, two, the impedance matrix is singular. Secondly the imaginary part of the determinant is non zero provided the expression, $X_{11}X_{22} - X_{12}X_{21}$ is also non-zero.

The second condition can be interpreted as the requirement that the field shape functions must be linearly independent with mode number, i.e. $X_{11} \neq A\ X_{12}$. This condition appears to be satisfied since the modes will clearly have different field shapes in the $\hat{x}$ and $\hat{y}$ directions.

The inner products, however consist of a summation over the sixteen sub-regions, therefore a more general condition for numerical stability is that the inner product terms are not dominated by a contribution that is invariant with mode number.

In the case where the contributions are largely invariant with mode number, the determinant becomes small which in turn leads to an increased susceptibility to numerical errors in the computation.

The example illustrates that the limiting case of a uniform line "discontinuity" may be subject to potential inaccuracies at the limit.

6.4.2 Comparison of Timings between the TRD Based Method and HFSS

The algorithms required to compute the S parameters of uniform to coupled line discontinuities have been programmed, however at the time of writing the software is still under development. An approximate comparison of the timing to compute the S parameters can be made between the TRD based method and Hewlett Packard's HP85180A High Frequency Structure Simulator (HFSS) Ver. A2.06. Table 6.4 shows a comparison of the timings required to compute the S parameters of a discontinuity at a single frequency point.

The benefit of the TRD based analysis is that the inner products are independent of frequency, hence the variation in S parameters with frequency can be rapidly calculated, as opposed to the HFSS package that has to recalculate the full 3D field solution at each of the frequency points.

Method	Operation	Time (CPU Secs.)	Notes
TRD Based Method	Computation of Propagation Constants†	327	20 Modes
	Computation of Mode Impedances †	161	20 Freq. Pts.
	Computation of Inner Products ‡	2.7	
	Computation of S Parameters ‡	7.2	
	Total	**498**	
HFSS Ver. A2.06	Full 3D Computation of Fields and S Parameters	3600 Typ.	180 MBytes Storage

Table 6.4: Comparison of Approximate Timings Required to Compute the S Parameters of a Uniform to Coupled Lines Discontinuity using the TRD Based Method and HFSS Ver. A2.06 (†3 Basis Function Terms and 25 Field Expansion terms) (‡4 Basis Function Terms and 25 Field Expansion Terms)

Chapter 7

Conclusions and Further Work

7.1 Outline

This chapter reviews the work undertaken to characterise the uniform and coupled stripline structures, and various types of stripline discontinuity. The review highlights novel aspects of the research and results of particular interest, and also aims to comment on its significance compared to other published work.

7.2 Review of Research Undertaken

The introductory chapter of the thesis outlined the application of stripline structures to medium power beamforming networks. The motivation behind the requirement for an extremely accurate, but computationally efficient means of designing these networks was also explained, with the aim of developing CAD models for the network elements. The beamforming networks consist of uniform and coupled line sections, quarter wave impedance transformers, power splitting networks, mitred bends and curves. The research that has been undertaken has concentrated on the analysis of the uniform and coupled lines. The calculated parameters have been used as a basis for analysing the stripline discontinuities present in the network elements. In addition to improving the

design of stripline structures, an efficient analysis enables stripline with novel cross-sectional dimensions to be studied and to provide a verification of practical knowledge.

The range of analysis techniques available for electromagnetic analysis were reviewed in the second chapter. The methods were broadly characterised into three areas: techniques which are predominantly numerically based; those which are predominantly analytically based; and those which combine a degree of both analytical and numerical processing. The previously published research on stripline structures was also reviewed. The research illustrates that the existing analyses of stripline have mainly been based on conformal mapping expressions (CAD packages) that can be evaluated quickly, but at the expense of accuracy; or purely numerical techniques (full wave electromagnetic simulators) that provide accurate results for structures of arbitrary shape, but at the expense of a large hardware requirement and long computation time.

The Transverse Resonance Diffraction (TRD) technique was developed to combine the accuracy of a numerical technique with a compact analysis which can be evaluated efficiently. The technique uses a-priori information concerning the field singularities of the stripline to describe the fields using a small number of terms. The TRD method is limited to structures with well defined interfaces across which the analysis is undertaken, however, the dimensions of the structure can have arbitrary values. The variation in the stripline parameters for a number of dimensional ratios can therefore be computed, a feature which many of the previous applications of the TRD method have not fully exploited. The TRD technique is in contrast with conformal mapping analyses which are restricted to a limited range of dimensions. This constrains their use in computing stripline parameters although the range of validity can be extended by the use of curve fitting techniques. In the case of coupled stripline structures the symmetry requirements for conformal mapping techniques mean that analyses are not normally available for asymmetrical structures. The computation time for purely numerical techniques also makes a study of this nature infeasible.

The TRD theory for arbitrary uniform and coupled stripline structures was developed in Chapter Three in terms of an admittance matrix representation in the plane transverse to the direction of propagation. This approach enables an analysis for any number of coupled striplines to be formulated by cascading a series of y parameter net-

works, with the sole assumption that only adjacent striplines are coupled. This has been demonstrated by the derivation of the uniform stripline formulation as a limiting case of the analysis of a pair of coupled striplines. The calculation of the propagation constant as a closed form polynomial expression was also studied. The study concluded that the operation can be interpreted as a conversion of the y parameter network representation to an ABCD network representation. The solutions for the propagation constant are given by the zero Eigenvalue solutions of the y parameter matrix, which correspond to the solution of the polynomial expression C=0. This conversion however yields no improvement in calculation time.

The definition of impedance parameters as power-voltage, power-current and voltage-current measures was shown in Chapter Three. The derivation of the power dissipation and attenuation factor using a small perturbation method has also been carried out.

The theory that has been derived is generally applicable to any stripline structure with a dielectric filling, hence it can be scaled to analyse structures found in Monolithic Microwave Integrated Circuits (MMICs). The results that have been presented were calculated for air filled stripline with dimensions that are typically found in medium power beamforming networks.

The discussion of the TRD results has primarily concentrated on the accuracy compared with other analysis techniques. The relative performance of the methods can only be judged when the computation speed and hardware requirements are also taken into account. This information has also been given to enable a fairer comparison of the results to be made.

The convergence of the uniform and coupled line formulations has been calculated and has shown that the analysis is stable. The results illustrate that a small number of field expansion terms and basis function terms are required to obtain convergence to within one percent of the cut-off frequencies.

The results for monomode bandwidth, impedance and attenuation factor for uniform stripline structures were presented in Chapter Four. The results for the first higher order mode cut-off frequencies for uniform stripline illustrate the accuracy of the TRD method with agreement to within two percent of the measured values. Hewlett Packard's High

Frequency Structure Simulator (HFSS) finite elements software provides comparable accuracy, but at the expense of a computation time that is approximately twenty-five times longer. These results also illustrate the inaccuracies of the conformal mapping analysis where errors of between four and eighteen percent are present.

The results for the impedance of uniform stripline show an agreement of within two percent between the TRD results and those computed using conformal mapping, across the range of specified dimensions for the conformal mapping analysis. Significantly better agreement of within half a percent is achieved for typically used stripline dimensions.

The results for the attenuation factor clearly indicate the strong effect that the edge singularities have on the computation of the stripline parameters. This is shown by the agreement between TRD and conformal mapping results improving significantly as the thickness of the stripline is increased and the effect of the singularities decreases. The attenuation factor was also measured experimentally, however due to its small magnitude the measurements were very susceptible to probe position and the excitation of the cavity. The repeatability and the variation in the measurements was also comparatively poor. The measurements however indicate that the order of magnitude of the attenuation factor calculated by the analysis is correct.

The results for all the parameters indicate that the stripline structure is not particularly sensitive to variations in the strip position asymmetry around the symmetrical position, and the strip thickness around commonly used thicknesses. There is a large sensitivity to strip thickness when the strip occupies the majority of the space between the ground planes. The sensitivity to variations in strip width increases for very narrow strips where any variation is a significant proportion of the overall width.

The results for the first two higher order mode cut-off frequencies, coupling, and attenuation factor for coupled stripline structures were presented in Chapter Five.

The TRD results for the first two higher order mode cut-off frequencies versus strip separation show agreement to within two percent of measured values and values computed using HFSS. The conformal mapping results only provide information concerning the asymptotes of the variations where the structure can be approximated to a uniform stripline structure with an effective width. Values for the cut-off frequencies computed

by HFSS, for certain dimensional ratios, produced significant differences when compared to the TRD results. This can be attributed to HFSS modelling the stripline as a boxed structure therefore a number of box modes appear in the set of solutions.

The results for the coupling of striplines highlights the differences between the various analysis techniques. The EEsof Linecalc package produced a significant underestimate of coupling in all cases. The TRD method showed a stronger coupling than conformal mapping and HFSS values in the majority of cases. This is due to the TRD analysis predicting a stronger coupling effect of the edge singularities. A comparison of the timings between the TRD method and HFSS has also been presented with the TRD method a minimum of three hundred times faster with typically one thousand times less memory required.

The results for the attenuation factor illustrate the limitations of the conformal mapping approaches with curve fitting used to extend the range of validity. The attenuation factor variation clearly exhibits discontinuous behaviour at the boundary between two approximations.

The results for the coupled stripline parameters indicate that they are particularly sensitive to variations in the strip separation and are relatively insensitive to the strip width asymmetry, or "slot" position, which appears to be intuitively correct. The parameters are also relatively insensitive to strip thickness provided the strip does not account for a very large proportion of the ground plane spacing. The comparison of parameters for strip position asymmetry illustrate that existing analyses can provide significant errors. The TRD and HFSS results, however, suggest that the parameters are relatively insensitive to variations around the symmetric position.

The previously published characterisations of stripline discontinuities were reviewed in Chapter Two. The analyses are derived using conformal mapping techniques, and the only structure analysed which is of interest to beamforming network design is the symmetrical uniform line step in width.

The derivation of the analysis of a generalised stripline discontinuity has been described in Chapter Six, with the formulation evaluated to characterise a uniform to coupled lines transition. Uniform and coupled line step in widths, however, can also

be analysed. The method is based on a field matching technique applied at the plane of the discontinuity. The discontinuity is expressed as an N port network, where N is the total number of modes accessible at the plane of the discontinuity. This approach is made possible by the accurate and efficient calculation of the modes in the structure using the TRD method. The analysis of the stripline discontinuities differs from previously published work in that the form of the cross-sectional fields is significantly more complex than other structures analysed using this technique. The stability of the method has also been studied with the conditions for stability identified as the modes of the structure being significantly distinct (linearly independent). The initial stages of development have been completed with the algorithms implemented.

7.3 Further Work

The main aspect of the further work covers the development of the discontinuity theory. The algorithms based on the theory described in Chapter Six show errors in the calculated S parameters, hence further work is required to verify the implementation of the algorithms.

The development of the algorithms will be carried out in a similar way to the uniform and coupled line analysis, with a check on the convergence of the method as the first goal. The further verification of the method does present problems. Limiting cases of the discontinuity can result in an instability (singular matrix) in the formulation, for example when the slot width in the uniform to coupled line transition approaches zero. Results have been computed for a number of transitions using HFSS which will provide additional information.

The convergence check for the analysis is of particular interest due to the complexity of the cross-section discontinuity fields and singularities. Theoretical results for uniform stripline indicate that the minimum order of singularity at the edge of a finite thickness strip is $\mid r \mid^{-\frac{1}{3}}$, whereas on the edge of an infinitely thin strip it is $\mid r \mid^{-\frac{1}{2}}$. Clearly as the thickness of a strip is decreased, a gradual transition of the singularity order takes place due to the localised interaction of the singularities. This manifests itself as

a degradation in convergence of the finite thickness formulation as the strip thickness becomes small. The close proximity of singularities in the discontinuity plane suggests that singularity interaction may also take place in the discontinuity analysis.

The calculation of the S parameters is an intermediate step in the analysis with the eventual aim to calculate the equivalent circuit of a number of discontinuities for inclusion in a CAD package, hence further work is also required for this conversion process.

The current analysis is undertaken for an infinitely thin stripline hence the extension to finite thickness structures is of interest. The author, however, has not been able to identify any publications on the singularity orders for finite thickness 90^o corners.

The long term aim is to provide CAD models for the entire range of elements used in stripline beamforming networks. The analysis of power splitting networks is of particular interest to network designers, as are mitred bends and stripline curves, although this work is a significant extension of the stripline analysis.

7.4 Concluding Remarks

The initial brief of this work was to provide an efficient and accurate analysis of stripline structures. This has undoubtably been achieved for uniform and coupled lines where significant analytical pre-processing has produced a computational gain over numerical techniques.

The degree of analytical pre-processing required to analyse more complicated structures, and the numerical efficiency of the calculations should again be compared to the benefits of using a purely numerical technique, such as finite differences or finite elements. The advance of purely numerical techniques has been illustrated by the development of commercial packages such as HFSS and the increase in computing power available within the period of the research. In the case of the stripline discontinuities purely numerical methods offer an extremely attractive alternative since the aim is to calculate equivalent circuits for the elements, and there is no requirement for the evaluation of the algorithms in real time.

Appendix A

Hewlett Packard's HP85180A High Frequency Structure Simulator

A.1 Outline

The results computed by the Transverse Resonance Diffraction (TRD) method have been compared in a number of cases to values computed by Hewlett Packard's HP85180A High Frequency Structure Simulator (HFSS) finite element package [74, 75]. The following sections outline the capabilities and the limitations of the package and describe how it is used to compute various stripline parameters.

A.2 General Description

The HFSS package is a 3D field simulator for arbitrary structures based around finite element software developed by Ansoft. The user can specify whether HFSS computes the 2D "ports only" solution which determines the allowable modes at the ports of the structure, and their propagation constants and impedances; or to extend the analysis

to solve for the complete 3D fields present in the structure, and hence generate the S parameters. The package consists of a number of modules including a schematic capture module; a mesh generation module; a field excitation module; a field solving module and a post-processing module.

The schematic capture module provides tools for drawing the structure and also defining the ports of the structure and the boundary conditions. The HFSS package is limited to computing the field solutions of enclosed structures, hence the stripline structures are modelled as a rectangular co-axial structure. The side walls are placed at a sufficient distance (approximately three strip widths from the edge of the strip) so that they do not interact with the fields surrounding the strip. This enables a common type of element to be used for the mesh generation at the expense of computational efficiency. In addition, electric and magnetic walls can also be defined in the structure. Symmetry planes can therefore be used to reduce the cross sectional area of the structure, hence the overall computation time.

The finite element mesh is automatically computed by the mesh generation module. HFSS discretises the structure using tetrahedra with the port surfaces therefore discretised by triangular elements. The user is able to specify a seeding of the mesh to produce a uniformly spaced mesh on a given surface. This is of little practical use for stripline since the mesh has to be non-uniformly spaced near singularities to model the fields.

The field excitation module computes the modes that can propagate in the port cross sections. The initial mesh is solved for the 2D electric field, and then the 2D magnetic field for each of the first N modes specified by the user. Maxwell's curl equations are then used to compute the corresponding magnetic and electric fields. The results are then compared and if the values agree to within a user defined convergence limit the 2D problem is solved, if not the mesh is refined and the procedure repeated.

The field solver module is similar to the field excitation module, however, it computes the full 3D field solution for the structure for each of the combinations of modes and ports to generate the scattering parameters for the structure. The module uses the "ports only" solution as a further set of boundary conditions on the problem in conjunction

with the boundary conditions set by the user in the schematic capture. The convergence criteria for this module is based on the S parameter convergence required, with the number of adaptive passes also specified by the user. This process can be carried out for a frequency sweep based on the single frequency solution.

The post-processing module enables the fields to be displayed, and animated by incrementing the phase reference of the excitation. Related parameters such as power flow are also computed and the data reformatted for use with other packages. The module also computes the impedance of the structure using the impedance measures defined in Chapter 3.

A.3 Accuracy and Timing Considerations

The accuracy of the results obtained from the package will depend on size and number of elements used to discretise the structure, and the amount of processing time and memory storage available.

The convergence limit specified by the user for the 2D "ports only" solution is a relatively arbitrary value since it does not directly relate to the convergence criteria for the propagation constants, or mode impedances that are the practical outputs from the "ports only" solution. The convergence behaviour of these parameters therefore has to be determined to provide an appropriate choice of convergence criteria for a given application. The convergence criteria for the S parameters of the 3D solution, equally, will not apply to the fields from which the parameters are calculated, since the S parameters are variational on the field solutions. Chapter 3 will also differ since the 3D magnetic field solution is less accurate than the corresponding electric field. This is due to the magnetic field being computed from the electric field solution.

The effect on the solution time due to a change in the convergence limit or number of modes is difficult to predict. This is due to the differing field shapes of the higher order modes where convergence of all modes to a couple of percent may be possible in a small number of iterations but convergence to half a percent may take significantly longer. Equally, the situation may arise that one mode achieves convergence to two

percent after a significant number of iterations, whereas the remainder of the modes have achieved convergence to fractions of a percent after a few iterations. The effect on computation time for successive iterations of the 3D field solution is also difficult to predict. The solution time will rapidly increase with the number of iterations as the number of equations to be solved, hence matrix size increases. This will normally result in additional accessing of data from disc drives which further slows the solution process. The seeding of the initial mesh only has a limited effect on the overall solution timings as it reduces the computation time of the first iteration, which is the fastest and is typically computed in one fifth of the time of the later iterations.

A.4 Hardware and Software Configuration

The hardware used to compute the HFSS results is shown in Table A.1 and compared to the hardware used to compute the TRD results. The table enables the timings quoted in Chapters 3 and 4 to be compared on the same basis.

	HP 9000/710	HP 715/50
RAM	16MByte	128 MByte
Disc (Internal)	420 MByte	—
Disc (External)	1.4 GByte	1.4GByte 300MByte Magneto-Optic
Display	1280×1024	1280×1024
MIPS	57	57
MFLOPS	12	17
SPECmarks	50	55.5
Operating System	HP-UX 8.07	HP-UX 9.01

Table A.1: Comparison of the Computer Platforms used to Compute the TRD and HFSS Results

The results computed in Chapters 3 and 4 were all computed with HFSS Version A2.06 unless otherwise stated. This is an important consideration since particular problems have been reported with the previous versions A1.00 and A1.29 in calculating the propagation constant of the stripline structure, and the calculation of mode impedances with the use of symmetry planes [76].

Appendix B

Derivation of Scalar Potentials, Fields and Mode Admittance Functions

B.1 Outline

The scalar potential functions on which the Transverse Resonance Diffraction (TRD) analysis is based, are derived for the general coupled stripline structure shown in Figure 3.1

The fields present in the structure are then derived from the scalar potentials and the expressions given in Chapter 3. Finally the Mode Admittance Functions ($\mathcal{Y}$) are derived for each of the Regions shown in Figure 3.1.

B.2 Derivation of Scalar Potentials

B.2.1 Derivation of $\hat{x}$ Directed Scalar Potential Functions

The $\hat{x}$ directed scalar potential functions for the sixteen regions shown in Figure 3.1 can be written down by inspection. The derivative of the scalar potentials for the TE modes is zero on the strip and ground planes; and for the TM modes, the scalar potential is zero on the strip and ground planes.

Magnetic Scalar Potential Function

$$\phi_{hx}^{R_i}(n,x) = A_n^{R_i} \text{Cos } k_x^{R_i}\left[x-\frac{h}{2}\right] \qquad x > \left(\frac{h}{2}-\left(b_i+\frac{t_i}{2}\right)\right) \tag{B.1}$$

$$\phi_{hx}^{R_i}(n,x) = A_n^{R_i} \text{Cos } k_x^{R_i}\left[x+\frac{h}{2}\right] \qquad x < \left(\frac{h}{2}-\left(b_i+\frac{t_i}{2}\right)\right) \tag{B.2}$$

Electric Scalar Potential Function

The corresponding expressions for the electric scalar potential can also be written down:

$$\phi_{hx}^{R_i}(n,x) = A_n^{R_i} \text{Sin } k_x^{R_i}\left[x-\frac{h}{2}\right] \qquad x > \left(\frac{h}{2}-\left(b_i+\frac{t_i}{2}\right)\right) \tag{B.3}$$

(B.4)

$$\phi_{hx}^{R_i}(n,x) = A_n^{R_i} \text{Sin } k_x^{R_i}\left[x+\frac{h}{2}\right] \qquad x < \left(\frac{h}{2}-\left(b_i+\frac{t_i}{2}\right)\right) \tag{B.5}$$

The $\hat{x}$ directed wavenumbers are defined for the sixteen sub-regions as:

$$k_x^{R_i} = \frac{n\pi}{2(\psi_i+\frac{t_i}{2})} \qquad \text{Regions I, III and V} \tag{B.6}$$

$$= \frac{n\pi}{\psi_i} \qquad \text{Regions II and IV} \tag{B.7}$$

The constant, ψ_i is defined as:

$$\psi_i = \begin{cases} b_i & x > \left(\frac{h}{2}-\left(b_i+\frac{t_i}{2}\right)\right) \\ d_i & x < \left(\frac{h}{2}-\left(b_i+\frac{t_i}{2}\right)\right) \end{cases} \tag{B.8}$$

The orthonormalisation coefficient, $A_n^{R_i}$ is determined by the requirement for Region, R_i that:

$$\int_x A_n^{R_i} \left[\phi_{hx,ex}^{R_i}(n,x)\right]^2 dx = 1 \tag{B.9}$$

Which is evaluated for sub-region, R_1, as:

$$A_n^{R_1} = \left[\int_{\frac{h}{2}-b_1}^{\frac{h}{2}} \left[\phi_{hx,ex}^{R_1}(n,x)\right]^2 dx\right]^{-\frac{1}{2}} \tag{B.10}$$

The orthonormalisation coefficients for the sub-regions can therefore be summarised as:

$$A_n^{R_i} = \frac{2\delta_n}{\sqrt{b_i + d_i}} \qquad \text{Region II and IV} \tag{B.11}$$

$$A_n^{R_i} = \frac{2\delta_n}{\sqrt{h}} \qquad \text{Region I, III and V} \tag{B.12}$$

Where the constant, δ_n is defined as:

$$\delta_n = \frac{1}{2} \qquad n = 0 \tag{B.13}$$

$$= \frac{1}{\sqrt{2}} \qquad n \neq 0 \tag{B.14}$$

B.2.2 Derivation of $\hat{y}$ Directed Scalar Potential Functions

Regions II to IV

The $\hat{y}$ directed scalar potentials are derived by representing Regions II to IV by a transmission line as shown in Figure B.1. An analogy is drawn between the conventional current and voltage quantities, and the electric and magnetic fields present in the stripline structure. The odd and even modes present in each of the regions are modelled by a short circuit or open circuit at $y = \frac{L}{2}$ respectively.

The voltage and current at a point along the line can be represented as a summation of forward and backward travelling waves. Expressions for an excitation at port 1 are given by:

$$V_y = V^+ \text{Exp}\left[j\beta_y\left(y - \frac{L}{2}\right)\right] + \rho V^+ \text{Exp}\left[-j\beta_y\left(y - \frac{L}{2}\right)\right] \tag{B.15}$$

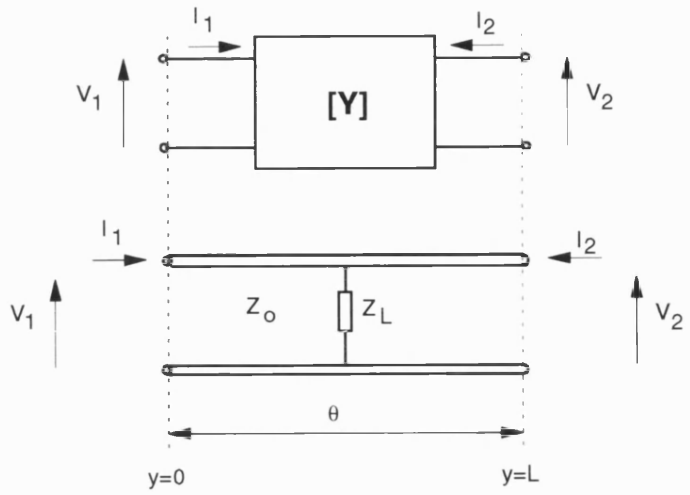

Figure B.1: General Transmission Line and y Parameter Representation

$$I_y = \frac{V^+}{Z_0}\text{Exp}\left[j\beta_y\left(y-\frac{L}{2}\right)\right] - \frac{\rho V^+}{Z_0}\text{Exp}\left[-j\beta_y\left(y-\frac{L}{2}\right)\right] \qquad \text{(B.16)}$$

Noting the standard expression for the reflection coefficient:

$$\rho = \frac{Z_L - Z_0}{Z_L + Z_0}$$

The expressions for the voltages and currents are normalised to unity at the excitation port:

$$V_y = \left[\frac{\text{Exp}\ [j\beta_y(y-\frac{L}{2})] + \rho\ \text{Exp}\ [-j\beta_y(y-\frac{L}{2})]}{\text{Exp}\ [-j\beta_y\frac{L}{2}] + \rho\ \text{Exp}\ [j\beta_y\frac{L}{2}]}\right] \qquad \text{(B.17)}$$

$$I_y = \left[\frac{\text{Exp}\ [j\beta_y(y-\frac{L}{2})] - \rho\ \text{Exp}\ [-j\beta_y(y-\frac{L}{2})]}{\text{Exp}\ [-j\beta_y\frac{L}{2}] - \rho\ \text{Exp}\ [j\beta_y\frac{L}{2}]}\right] \qquad \text{(B.18)}$$

The voltages and currents in the above expressions represent the voltages and currents in the transverse $\hat{x}$ direction. In order to extract the voltages and currents in the $\hat{z}$ direction and hence the scalar potential, the expressions have to be integrated with respect to the $\hat{y}$ direction.

The $\hat{y}$ directed propagation constant is replaced using the notation used in Chapter 3, with the propagation constant in Regions II to IV represented as a purely real quantity

and the propagation constant in Regions I and V represented as a purely imaginary quantity. The $\hat{y}$ directed magnetic scalar potentials for the TE modes are derived from Equation B.17 and given by:

$$\phi_{hy}^{R_3}(n,y) = \frac{1}{k_y^{R_3}}\left[\frac{\text{Exp}\ \left[jk_y^{R_3}(y+(\frac{s}{2}+\frac{w_1}{2}))\right]+\rho\text{Exp}\ \left[-jk_y^{R_3}(y+(\frac{s}{2}+\frac{w_1}{2}))\right]}{\text{Exp}\ \left[jk_y^{R_3}(\frac{s}{2}+\frac{w_1}{2})\right]+\rho\text{Exp}\ \left[-jk_y^{R_3}(\frac{s}{2}+\frac{w_1}{2})\right]}\right] \tag{B.19}$$

$$\phi_{hy}^{R_4}(n,y) = \frac{1}{k_y^{R_4}}\left[\frac{\text{Exp}\ \left[jk_y^{R_4}(y+(\frac{s}{2}+\frac{w_1}{2}))\right]+\rho\text{Exp}\ \left[-jk_y^{R_4}(y+(\frac{s}{2}+\frac{w_1}{2}))\right]}{\text{Exp}\ \left[jk_y^{R_4}(\frac{s}{2}+\frac{w_1}{2})\right]+\rho\text{Exp}\ \left[-jk_y^{R_4}(\frac{s}{2}+\frac{w_1}{2})\right]}\right] \tag{B.20}$$

$$\phi_{hy}^{R_5}(n,y) = \frac{1}{k_y^{R_5}}\left[\frac{\text{Exp}\ \left[jk_y^{R_5}(y+(\frac{s}{2}+\frac{w_1}{2}))\right]+\rho\text{Exp}\ \left[-jk_y^{R_5}(y+(\frac{s}{2}+\frac{w_1}{2}))\right]}{\text{Exp}\ \left[-jk_y^{R_5}(\frac{s}{2}+\frac{w_1}{2})\right]+\rho\text{Exp}\ \left[jk_y^{R_5}(\frac{s}{2}+\frac{w_1}{2})\right]}\right] \tag{B.21}$$

$$\phi_{hy}^{R_6}(n,y) = \frac{1}{k_y^{R_6}}\left[\frac{\text{Exp}\ \left[jk_y^{R_6}(y+(\frac{s}{2}+\frac{w_1}{2}))\right]+\rho\text{Exp}\ \left[-jk_y^{R_6}(y+(\frac{s}{2}+\frac{w_1}{2}))\right]}{\text{Exp}\ \left[-jk_y^{R_6}(\frac{s}{2}+\frac{w_1}{2})\right]+\rho\text{Exp}\ \left[jk_y^{R_6}(\frac{s}{2}+\frac{w_1}{2})\right]}\right] \tag{B.22}$$

$$\phi_{hy}^{R_7}(n,y) = \frac{1}{k_y^{R_7}}\left[\frac{\text{Exp}\ \left[jk_y^{R_7}y\right]+\rho\text{Exp}\ \left[-jk_y^{R_7}y\right]}{\text{Exp}\ \left[-jk_y^{R_7}(\frac{s}{2})\right]+\rho\text{Exp}\ \left[jk_y^{R_7}(\frac{s}{2})\right]}\right] \tag{B.23}$$

$$\phi_{hy}^{R_8}(n,y) = \frac{1}{k_y^{R_8}}\left[\frac{\text{Exp}\ \left[jk_y^{R_8}y\right]+\rho\text{Exp}\ \left[-jk_y^{R_8}y\right]}{\text{Exp}\ \left[-jk_y^{R_8}(\frac{s}{2})\right]+\rho\text{Exp}\ \left[jk_y^{R_8}(\frac{s}{2})\right]}\right] \tag{B.24}$$

$$\phi_{hy}^{R_9}(n,y) = \frac{1}{k_y^{R_9}}\left[\frac{\text{Exp}\ \left[jk_y^{R_9}y\right]+\rho\text{Exp}\ \left[-jk_y^{R_9}y\right]}{\text{Exp}\ \left[jk_y^{R_9}(\frac{s}{2})\right]+\rho\text{Exp}\ \left[-jk_y^{R_9}(\frac{s}{2})\right]}\right] \tag{B.25}$$

$$\phi_{hy}^{R_{10}}(n,y) = \frac{1}{k_y^{R_{10}}}\left[\frac{\text{Exp}\ \left[jk_y^{R_{10}}y\right]+\rho\text{Exp}\ \left[-jk_y^{R_{10}}y\right]}{\text{Exp}\ \left[jk_y^{R_{10}}(\frac{s}{2})\right]+\rho\text{Exp}\ \left[-jk_y^{R_{10}}(\frac{s}{2})\right]}\right] \tag{B.26}$$

$$\phi_{hy}^{R_{11}}(n,y) = \frac{1}{k_y^{R_{11}}}\left[\frac{\text{Exp}\ \left[jk_y^{R_{11}}(y-(\frac{s}{2}+\frac{w_2}{2}))\right]+\rho\text{Exp}\ \left[-jk_y^{R_{11}}(y-(\frac{s}{2}+\frac{w_2}{2}))\right]}{\text{Exp}\ \left[-jk_y^{R_{11}}(\frac{s}{2}+\frac{w_2}{2})\right]+\rho\text{Exp}\ \left[jk_y^{R_{11}}(\frac{s}{2}+\frac{w_2}{2})\right]}\right] \tag{B.27}$$

$$\phi_{hy}^{R_{12}}(n,y) = \frac{1}{k_y^{R_{12}}}\left[\frac{\text{Exp}\ \left[jk_y^{R_{12}}(y-(\frac{s}{2}+\frac{w_2}{2}))\right]+\rho\text{Exp}\ \left[-jk_y^{R_{12}}(y-(\frac{s}{2}+\frac{w_2}{2}))\right]}{\text{Exp}\ \left[-jk_y^{R_{12}}(\frac{s}{2}+\frac{w_2}{2})\right]+\rho\text{Exp}\ \left[jk_y^{R_{12}}(\frac{s}{2}+\frac{w_2}{2})\right]}\right] \tag{B.28}$$

$$\phi_{hy}^{R_{13}}(n,y) = \frac{1}{k_y^{R_{13}}}\left[\frac{\text{Exp}\ \left[jk_y^{R_{13}}(y-(\frac{s}{2}+\frac{w_2}{2}))\right]+\rho\text{Exp}\ \left[-jk_y^{R_{13}}(y-(\frac{s}{2}+\frac{w_2}{2}))\right]}{\text{Exp}\ \left[jk_y^{R_{13}}(\frac{s}{2}+\frac{w_2}{2})\right]+\rho\text{Exp}\ \left[-jk_y^{R_{13}}(\frac{s}{2}+\frac{w_2}{2})\right]}\right]$$

(B.29)

$$\phi_{hy}^{R_{14}}(n,y) = \frac{1}{k_y^{R_{14}}}\left[\frac{\text{Exp}\ \left[jk_y^{R_{14}}(y-(\frac{s}{2}+\frac{w_2}{2}))\right]+\rho\text{Exp}\ \left[-jk_y^{R_{14}}(y-(\frac{s}{2}+\frac{w_2}{2}))\right]}{\text{Exp}\ \left[jk_y^{R_{14}}(\frac{s}{2}+\frac{w_2}{2})\right]+\rho\text{Exp}\ \left[-jk_y^{R_{14}}(\frac{s}{2}+\frac{w_2}{2})\right]}\right] \tag{B.30}$$

The $\hat{y}$ directed propagation constants are given by:

$$\left(k_y^{R_i}\right)^2 = k_i^2 - \left(k_x^{R_i}\right)^2 \tag{B.31}$$

$$= k_o^2 - \beta_k^2 - \left(\frac{n\pi}{\psi_i}\right)^2 \tag{B.32}$$

where either the wavenumber, k_o, or the propagation constant, β_k, is fixed during the search for the set of solutions of the remaining variable.

The corresponding expressions for the electric scalar potentials for the TM modes are derived from the current expression, and are of the general form:

$$\phi_{ey}^{R_i}(n,y) = \frac{1}{k_y^{R_i}}\left[\frac{\text{Exp}\ \left[jk_y^{R_i}(y+\psi_i)\right]-\rho\text{Exp}\ \left[-jk_y^{R_i}(y+\psi_i)\right]}{\text{Exp}\ \left[jk_y^{R_i}(\psi_i)\right]-\rho\text{Exp}\ \left[-jk_y^{R_i}(\psi_i)\right]}\right] \tag{B.33}$$

Regions I and V

The remaining regions are characterised assuming that the $\hat{y}$ directed dependency is an exponential decay away from the striplines. This gives rise to an $\hat{x}$ directed scalar potential of the form for the sub-regions:

$$\phi_{hy,ey}^{R_1}(n,y) = \frac{\text{Exp}\ \left[jk_y^{R_1}(y+(\frac{s}{2}+w_1))\right]}{jk_y^{R_1}} \tag{B.34}$$

$$\phi_{hy,ey}^{R_2}(n,y) = \frac{\text{Exp}\ \left[jk_y^{R_2}(y+(\frac{s}{2}+w_1))\right]}{jk_y^{R_2}} \tag{B.35}$$

$$\phi_{hy,ey}^{R_{15}}(n,y) = \frac{\text{Exp}\ \left[jk_y^{R_{15}}(y-(\frac{s}{2}+w_2))\right]}{jk_y^{R_{15}}} \tag{B.36}$$

$$\phi_{hy,ey}^{R_{16}}(n,y) = \frac{\text{Exp}\ \left[jk_y^{R_{16}}(y-(\frac{s}{2}+w_2))\right]}{jk_y^{R_{16}}} \tag{B.37}$$

The overall scalar potentials are formed using the Equations 3.24 and 3.25.

B.3 Derivation of Fields

The three fields present in the coupled stripline structure for both the TE and TM modes can be derived from the relationships stated in Chapter 3, Equations 3.17 and 3.18.

B.3.1 Derivation of Fields for TE Modes

The fields are again derived as a piece-wise formulation for each of the sixteen regions leading to a total of forty eight field components.

$\hat{z}$ Directed Magnetic Field, h_{zk}

$$h_{zk}^{R_1}(x,y) = \frac{k_t^2}{j\omega\mu_o}\sum_{n=0}^{n=\infty}\frac{2\delta_n V_{xkn}^{R_1}}{\sqrt{h}}F_1\left[R_1,\left(\frac{h}{2}\right)\right]\frac{F_2\left[R_1,-(\frac{s}{2}+w_1)\right]}{jk_y^{R_1}} \quad \text{(B.38)}$$

$$h_{zk}^{R_2}(x,y) = \frac{k_t^2}{j\omega\mu_o}\sum_{n=0}^{n=\infty}\frac{2\delta_n V_{xkn}^{R_2}}{\sqrt{h}}F_1\left[R_2,-\left(\frac{h}{2}\right)\right]\frac{F_2\left[R_2,-(\frac{s}{2}+w_1)\right]}{jk_y^{R_1}} \quad \text{(B.39)}$$

$$h_{zk}^{R_3}(x,y) = \frac{k_t^2}{j\omega\mu_o}\sum_{n=0}^{n=\infty}\frac{2\delta_n V_{xkn}^{R_3}}{\sqrt{b_1+d_1}}F_1\left[R_3,\left(\frac{h}{2}\right)\right]\frac{F_3\left[R_3,-(\frac{s}{2}+\frac{w_1}{2})\right]}{jk_y^{R_3}} \quad \text{(B.40)}$$

$$h_{zk}^{R_4}(x,y) = \frac{k_t^2}{j\omega\mu_o}\sum_{n=0}^{n=\infty}\frac{2\delta_n V_{xkn}^{R_4}}{\sqrt{b_1+d_1}}F_1\left[R_4,-\left(\frac{h}{2}\right)\right]\frac{F_4\left[R_4,-(\frac{s}{2}+\frac{w_1}{2})\right]}{jk_y^{R_4}} \quad \text{(B.41)}$$

$$h_{zk}^{R_5}(x,y) = \frac{k_t^2}{j\omega\mu_o}\sum_{n=0}^{n=\infty}\frac{2\delta_n V_{xkn}^{R_5}}{\sqrt{b_1+d_1}}F_1\left[R_5,\left(\frac{h}{2}\right)\right]\frac{F_3\left[R_5,-(\frac{s}{2}+\frac{w_1}{2})\right]}{jk_y^{R_5}} \quad \text{(B.42)}$$

$$h_{zk}^{R_6}(x,y) = \frac{k_t^2}{j\omega\mu_o}\sum_{n=0}^{n=\infty}\frac{2\delta_n V_{xkn}^{R_6}}{\sqrt{b_1+d_1}}F_1\left[R_6,-\left(\frac{h}{2}\right)\right]\frac{F_4\left[R_6,-(\frac{s}{2}+\frac{w_1}{2})\right]}{jk_y^{R_6}} \quad \text{(B.43)}$$

$$h_{zk}^{R_7}(x,y) = \frac{k_t^2}{j\omega\mu_o}\sum_{n=0}^{n=\infty}\frac{2\delta_n V_{xkn}^{R_7}}{\sqrt{h}}F_1\left[R_7,\left(\frac{h}{2}\right)\right]\frac{F_3\left[R_7,-(\frac{s}{2})\right]}{jk_y^{R_7}} \quad \text{(B.44)}$$

$$h_{zk}^{R_8}(x,y) = \frac{k_t^2}{j\omega\mu_o}\sum_{n=0}^{n=\infty}\frac{2\delta_n V_{xkn}^{R_8}}{\sqrt{h}}F_1\left[R_8,-\left(\frac{h}{2}\right)\right]\frac{F_4\left[R_8,-(\frac{s}{2})\right]}{jk_y^{R_8}} \quad \text{(B.45)}$$

$$h_{zk}^{R_9}(x,y) = \frac{k_t^2}{j\omega\mu_o}\sum_{n=0}^{n=\infty}\frac{2\delta_n V_{xkn}^{R_9}}{\sqrt{h}}F_1\left[R_9,\left(\frac{h}{2}\right)\right]\frac{F_3\left[R_9,(\frac{s}{2})\right]}{jk_y^{R_9}} \quad \text{(B.46)}$$

$$h_{zk}^{R_{10}}(x,y) = \frac{k_t^2}{j\omega\mu_o}\sum_{n=0}^{n=\infty}\frac{2\delta_n V_{xkn}^{R_{10}}}{\sqrt{h}}F_1\left[R_{10},-\left(\frac{h}{2}\right)\right]\frac{F_4\left[R_{10},(\frac{s}{2})\right]}{jk_y^{R_{10}}} \quad \text{(B.47)}$$

$$h_{zk}^{R_{11}}(x,y) = \frac{k_t^2}{j\omega\mu_o}\sum_{n=0}^{n=\infty}\frac{2\delta_n V_{xkn}^{R_{11}}}{\sqrt{b_2+d_2}}F_1\left[R_{11},\left(\frac{h}{2}\right)\right]\frac{F_3\left[R_{11},+(\frac{s}{2}+\frac{w_2}{2})\right]}{jk_y^{R_{11}}} \quad \text{(B.48)}$$

$$h_{zk}^{R_{12}}(x,y) = \frac{k_t^2}{j\omega\mu_o}\sum_{n=0}^{n=\infty}\frac{2\delta_n V_{xkn}^{R_{12}}}{\sqrt{b_2+d_2}}F_1\left[R_{12},-\left(\frac{h}{2}\right)\right]\frac{F_4\left[R_{12},+(\frac{s}{2}+\frac{w_2}{2})\right]}{jk_y^{R_{12}}} \quad \text{(B.49)}$$

$$h_{zk}^{R_{13}}(x,y) = \frac{k_t^2}{j\omega\mu_o}\sum_{n=0}^{n=\infty}\frac{2\delta_n V_{xkn}^{R_{13}}}{\sqrt{b_2+d_2}}F_1\left[R_{13},\left(\frac{h}{2}\right)\right]\frac{F_3\left[R_{13},+(\frac{s}{2}+\frac{w_2}{2})\right]}{jk_y^{R_{13}}} \quad \text{(B.50)}$$

$$h_{zk}^{R_{14}}(x,y) = \frac{k_t^2}{j\omega\mu_o}\sum_{n=0}^{n=\infty}\frac{2\delta_n V_{xkn}^{R_{14}}}{\sqrt{b_2+d_2}}F_1\left[R_{14},-\left(\frac{h}{2}\right)\right]\frac{F_4\left[R_{14},+(\frac{s}{2}+\frac{w_2}{2})\right]}{jk_y^{R_{14}}} \quad \text{(B.51)}$$

$$h_{zk}^{R_{15}}(x,y) = \frac{k_t^2}{j\omega\mu_o}\sum_{n=0}^{n=\infty}\frac{2\delta_n V_{xkn}^{R_{15}}}{\sqrt{h}}F_1\left[R_{15},\left(\frac{h}{2}\right)\right]\frac{F_2\left[R_{15},+(\frac{s}{2}+w_2)\right]}{jk_y^{R_{15}}} \quad \text{(B.52)}$$

$$h_{zk}^{R_{16}}(x,y) = \frac{k_t^2}{j\omega\mu_o}\sum_{n=0}^{n=\infty}\frac{2\delta_n V_{xkn}^{R_{16}}}{\sqrt{h}}F_1\left[R_{16},-\left(\frac{h}{2}\right)\right]\frac{F_2\left[R_{16},+(\frac{s}{2}+w_2)\right]}{jk_y^{R_{16}}} \quad \text{(B.53)}$$

where the functions, F_1, F_2, F_3 and F_4 are denoted by the following expressions:

$$F_1(R_i,\psi) = \text{Cos}\, k_x^{R_i}(x-\psi) \quad \text{(B.54)}$$

$$F_2(R_i,\psi) = \text{Exp}\ \left[jk_y^{R_i}(y-\psi)\right] \quad \text{(B.55)}$$

$$F_3(R_i,\psi) = \left[\frac{\text{Exp}\ \left[jk_y^{R_i}(y-\psi)\right]+\rho\text{Exp}\ \left[-jk_y^{R_i}(y-\psi)\right]}{\text{Exp}\ \left[-jk_y^{R_i}(\psi)\right]+\rho\text{Exp}\ \left[jk_y^{R_i}(\psi)\right]}\right] \quad \text{(B.56)}$$

$$F_4(R_i,\psi) = \left[\frac{\text{Exp}\ \left[jk_y^{R_i}(y-\psi)\right]+\rho\text{Exp}\ \left[-jk_y^{R_i}(y-\psi)\right]}{\text{Exp}\ \left[jk_y^{R_i}(\psi)\right]+\rho\text{Exp}\ \left[-jk_y^{R_i}(\psi)\right]}\right] \quad \text{(B.57)}$$

$\hat{x}$ Directed Electric Field, e_{xk}

The e_{xk} fields are given by the partial derivative of the h_{zk} field with respect to the $\hat{y}$ direction, such that:

$$e_{xk}^{R_i}(x,y) = h_{zk}^{R_i}\, k_y^{R_i}\frac{j\omega\mu_o}{k_t^2} \quad \text{(B.58)}$$

$\hat{y}$ Directed Electric Field, e_{yk}

Similarly, the e_{yk} fields are given by the partial derivative with respect to the $\hat{x}$ direction:

$$e_{yk}^{R_i}(x,y) = h_{zk}^{R_i}\, k_x^{R_i}\frac{j\omega\mu_o}{k_t^2} \quad \text{(B.59)}$$

The definition of the function, F_1 is modified to:

$$F_1(R_i, \psi) = k_x^{R_i} \text{ Sin } k_x^{R_i}(x - \psi) \tag{B.60}$$

The remainder of the functions, F_2, F_3 and F_4 remain unchanged and given by the expressions in Equations B.55 to B.57.

B.3.2 Derivation of Fields for TM Modes

The fields for the TM modes are again derived in an analogous manner to those for the TE modes, using the electric scalar potentials as a base:

$\hat{z}$ Directed Electric Field, e_{zk}

The e_{zk} field components are similar to those of the h_{zk} fields for the TE modes in the sixteen sub-regions. For example, the expression for the sub-region, R_3 is given by:

$$e_{zk}^{R_3}(x, y) = \frac{k_t^2}{j\omega\epsilon_o\epsilon_r} \sum_{n=1}^{n=\infty} \frac{2\delta_n I_{xkn}^{R_3}}{\sqrt{b_1 + d_1}} F_1\left[R_3, \left(\frac{h}{2}\right)\right] \frac{F_3\left[R_3, -(\frac{s}{2} + \frac{w_1}{2})\right]}{jk_y^{R_3}} \tag{B.61}$$

where the voltage amplitude is replaced by an equivalent current amplitude. The functions F_1, F_2, F_3 and F_4 are given by the equations:

$$F_1(R_i, \psi) = \frac{\text{Sin } k_x^{R_i}(x - \psi)}{n^2} \tag{B.62}$$

$$F_2(R_i, \psi) = \text{Exp } \left[jk_y^{R_i}(y - \psi)\right] \tag{B.63}$$

$$F_3(R_i, \psi) = \left[\frac{\text{Exp } \left[jk_y^{R_i}(y - \psi)\right] - \rho\text{Exp } \left[-jk_y^{R_i}(y - \psi)\right]}{\text{Exp } \left[-jk_y^{R_i}(\psi)\right] - \rho\text{Exp } \left[jk_y^{R_i}(\psi)\right]}\right] \tag{B.64}$$

$$F_4(R_i, \psi) = \left[\frac{\text{Exp } \left[jk_y^{R_i}(y - \psi)\right] - \rho\text{Exp } \left[-jk_y^{R_i}(y - \psi)\right]}{\text{Exp } \left[jk_y^{R_i}(\psi)\right] - \rho\text{Exp } \left[-jk_y^{R_i}(\psi)\right]}\right] \tag{B.65}$$

$\hat{x}$ Directed Magnetic Field, h_{xk}

The h_{xk} field is given by the partial derivative of the e_{zk} with respect to y:

$$h_{xk}^{R_i}(x,y) = e_{zk}^{R_i}\, k_y^{R_i}\, \frac{j\omega\mu_o}{k_t^2} \tag{B.66}$$

$\hat{y}$ Directed Magnetic Field, h_{yk}

Similarly, the h_{yk} fields are given by the partial derivative with respect to the $\hat{x}$ direction:

$$h_{yk}^{R_i}(x,y) = e_{zk}^{R_i}\, k_x^{R_i}\, \frac{j\omega\mu_o}{k_t^2} \tag{B.67}$$

The definition of the function, F_1 is modified to:

$$F_1(R_i,\psi) = k_x^{R_i}\, \mathrm{Cos}\, k_x^{R_i}(x-\psi) \tag{B.68}$$

The remainder of the functions, F_2, F_3 and F_4 remain unchanged and given by the expressions in Equations B.63 to B.65.

B.4 Derivation of Mode Admittance Functions

The Green's Function Admittance Operators are derived from the mode admittance functions, $\mathcal{Y}(n)$ (Equation 3.30). These functions are based on the general y parameter representation of a two port network.

B.4.1 General Form of Y Parameters

The y parameters of a general two port network (Figure B.1) are given by the following relationships:

$$y_{11} = \left.\frac{I_1}{V_1}\right|_{V_2=0} \qquad y_{12} = \left.\frac{I_1}{V_2}\right|_{V_1=0}$$

$$y_{21} = \left.\frac{I_2}{V_1}\right|_{V_2=0} \qquad y_{22} = \left.\frac{I_2}{V_2}\right|_{V_1=0}$$

Representing the voltages and currents by the $e_{xk}(y)$ and $h_{zk}(y)$ fields respectively, and considering their general forms $\hat{y}$ directed forms for a transmission line of length, ψ

$$h_{zk}^{R_i}(y) = \frac{1}{jk_y^{R_i}} \left[\frac{\text{Exp}\left[jk_y^{R_i}(y-\frac{\psi}{2})\right] + \rho\text{Exp}\left[-jk_y^{R_i}(y-\frac{\psi}{2})\right]}{\text{Exp}\left[-jk_y^{R_i}\frac{\psi}{2}\right] + \rho\text{Exp}\left[jk_y^{R_i}\frac{\psi}{2}\right]} \right] \tag{B.69}$$

$$e_{xk}^{R_i}(y) = \left[\frac{\text{Exp}\left[jk_y^{R_i}(y-\frac{\psi}{2})\right] - \rho\text{Exp}\left[-jk_y^{R_i}(y-\frac{\psi}{2})\right]}{\text{Exp}\left[-jk_y^{R_i}\frac{\psi}{2}\right] + \rho\text{Exp}\left[jk_y^{R_i}\frac{\psi}{2}\right]} \right] \tag{B.70}$$

Using the above expressions for the y parameters, the y_{11} and y_{12} parameters for the TE modes are found:

$$y_{11} = \left.\frac{h_{zk}(0)}{e_{xk}(0)}\right|_{e_{xk}(\frac{\psi}{2})=0} \tag{B.71}$$

$$y_{12} = \left.\frac{h_{zk}(0)}{e_{xk}(\frac{\psi}{2})}\right|_{e_{xk}(0)=0} \tag{B.72}$$

Substituting the expressions for the electric and magnetic fields:

$$y_{11} = \frac{1}{k_y^{R_i}} \left[\frac{\text{Exp}\left[-jk_y^{R_i}\frac{\psi}{2}\right] + \rho\text{Exp}\left[jk_y^{R_i}\frac{\psi}{2}\right]}{\text{Exp}\left[jk_y^{R_i}(-\frac{\psi}{2})\right] - \rho\text{Exp}\left[-jk_y^{R_i}(-\frac{\psi}{2})\right]} \right] \Bigg|_{\rho=+1} \tag{B.73}$$

$$= \frac{\text{Cot}\, k_y^{R_i}\frac{\psi}{2}}{jk_y^{R_i}(\frac{\psi}{2})} \tag{B.74}$$

$$y_{12} = \frac{1}{k_y^{R_i}} \left[\frac{\text{Exp}\left[-jk_y^{R_i}\frac{\psi}{2}\right] + \rho\text{Exp}\left[jk_y^{R_i}\frac{\psi}{2}\right]}{1-\rho} \right] \Bigg|_{\rho=\frac{\text{Exp}jk_y^{R_i}(-\frac{\psi}{2})}{\text{Exp}jk_y^{R_i}(\frac{\psi}{2})}} \tag{B.75}$$

$$= \frac{\text{Cosec}\, k_y^{R_i}\frac{\psi}{2}}{jk_y^{R_i}(\frac{\psi}{2})} \tag{B.76}$$

The corresponding expressions for the y_{21} and y_{22} parameters can be derived in a similar manner.

The expressions for the "terminating" admittances in the networks at the boundary of Regions I and II; and Regions IV and V are given as a ratio of the h_{zk} and e_{xk} fields.

The expressions for the TM modes can be derived in a similar manner, leading to

the y parameters:

$$y_{11} = jk_y^{R_i} \text{ Cot } k_y^{R_i}\frac{\psi}{2} \tag{B.77}$$

$$y_{12} = jk_y^{R_i} \text{ Cosec } k_y^{R_i}\frac{\psi}{2} \tag{B.78}$$

B.4.2 Mode Admittance Functions

The mode admittances for the sixteen sub-regions shown in Figure 3.1 can be derived from the above equations. The admittances are defined across the entire interface, hence each of the y parameters has contributions from each sub-region adjacent to the boundary.

The mode admittance functions for the TE modes are derived as:

$$\mathcal{Y}_1^I(n) = \frac{1}{jk_y^{R_1}} + \frac{1}{jk_y^{R_2}} \tag{B.79}$$

$$\mathcal{Y}_{11}^{II}(n) = \frac{\text{Cot}k_y^{R_3}\frac{w_1}{2}}{jk_y^{R_3}} + \frac{\text{Cot}k_y^{R_4}\frac{w_1}{2}}{jk_y^{R_4}} \tag{B.80}$$

$$\mathcal{Y}_{12}^{II}(n) = \frac{\text{Cosec } k_y^{R_3}\frac{w_1}{2}}{jk_y^{R_3}} + \frac{\text{Cosec } k_y^{R_4}\frac{w_1}{2}}{jk_y^{R_4}} \tag{B.81}$$

$$\mathcal{Y}_{21}^{II}(n) = \frac{\text{Cosec } k_y^{R_5}\frac{w_1}{2}}{jk_y^{R_5}} + \frac{\text{Cosec } k_y^{R_6}\frac{w_1}{2}}{jk_y^{R_6}} \tag{B.82}$$

$$\mathcal{Y}_{22}^{II}(n) = \frac{\text{Cot } k_y^{R_5}\frac{w_1}{2}}{jk_y^{R_5}} + \frac{\text{Cot } k_y^{R_6}\frac{w_1}{2}}{jk_y^{R_6}} \tag{B.83}$$

$$\mathcal{Y}_{11}^{III}(n) = \frac{\text{Cot } k_y^{R_7}\frac{s}{2}}{jk_y^{R_7}} + \frac{\text{Cot } k_y^{R_8}\frac{s}{2}}{jk_y^{R_8}} \tag{B.84}$$

$$\mathcal{Y}_{12}^{III}(n) = \frac{\text{Cosec } k_y^{R_7}\frac{s}{2}}{jk_y^{R_7}} + \frac{\text{Cosec } k_y^{R_8}\frac{s}{2}}{jk_y^{R_8}} \tag{B.85}$$

$$\mathcal{Y}_{21}^{III}(n) = \frac{\text{Cosec } k_y^{R_9}\frac{s}{2}}{jk_y^{R_9}} + \frac{\text{Cosec } k_y^{R_{10}}\frac{s}{2}}{jk_y^{R_{10}}} \tag{B.86}$$

$$\mathcal{Y}_{22}^{III}(n) = \frac{\text{Cot } k_y^{R_9}\frac{s}{2}}{jk_y^{R_9}} + \frac{\text{Cot } k_y^{R_{10}}\frac{s}{2}}{jk_y^{R_{10}}} \tag{B.87}$$

$$\mathcal{Y}_{11}^{IV}(n) = \frac{\text{Cot } k_y^{R_{11}}\frac{w_2}{2}}{jk_y^{R_{11}}} + \frac{\text{Cot } k_y^{R_{12}}\frac{w_2}{2}}{jk_y^{R_{12}}} \tag{B.88}$$

$$\mathcal{Y}_{12}^{IV}(n) = \frac{\text{Cosec } k_y^{R_{11}}\frac{w_2}{2}}{jk_y^{R_{11}}} + \frac{\text{Cosec } k_y^{R_{12}}\frac{w_2}{2}}{jk_y^{R_{12}}} \tag{B.89}$$

$$\mathcal{Y}_{21}^{IV}(n) = \frac{\text{Cosec } k_y^{R_{13}} \frac{w_2}{2}}{jk_y^{R_{13}}} + \frac{\text{Cosec } k_y^{R_{14}} \frac{w_2}{2}}{jk_y^{R_{14}}} \quad \text{(B.90)}$$

$$\mathcal{Y}_{22}^{IV}(n) = \frac{\text{Cot } k_y^{R_{13}} \frac{w_2}{2}}{jk_y^{R_{13}}} + \frac{\text{Cot } k_y^{R_{14}} \frac{w_2}{2}}{jk_y^{R_{14}}} \quad \text{(B.91)}$$

$$\mathcal{Y}_1^{V}(n) = \frac{1}{jk_y^{R_{15}}} + \frac{1}{jk_y^{R_{16}}} \quad \text{(B.92)}$$

The mode admittance functions for the TM modes are derived in a similar manner for the expressions for y_{11} and y_{12} in Equations B.77 and B.78.

Appendix C

Derivation of the Inner Products for the TRD Formulation

C.1 Form of Basis Functions

The basis functions are defined as a product of an orthonormalisation coefficient, a weight function, and an orthogonal polynomial.

The choice of the orthogonal polynomial will be dependent on the order of the field singularity, ν, present on the edge of the central conductor. This has been investigated by Collin [19], and analytical results have shown that the minimum order of the singularity is given as $\nu = -\frac{1}{3}$, for a finite thickness stripline and $\nu = -\frac{1}{2}$, for an infinitely thin stripline.

The theory will assume that the stripline is of finite thickness, i.e $\nu = -\frac{1}{3}$, although substituting the value of $\nu = -\frac{1}{2}$ does provide a useful limiting case to verify results.

Weight Function

The weight function is used to give the basis function the correct order of singularity, and is derived by considering the singularities on the edge of the central conductor. The analysis assumes a pair of image singularities with a symmetrical weight function as shown in Figure C.1.

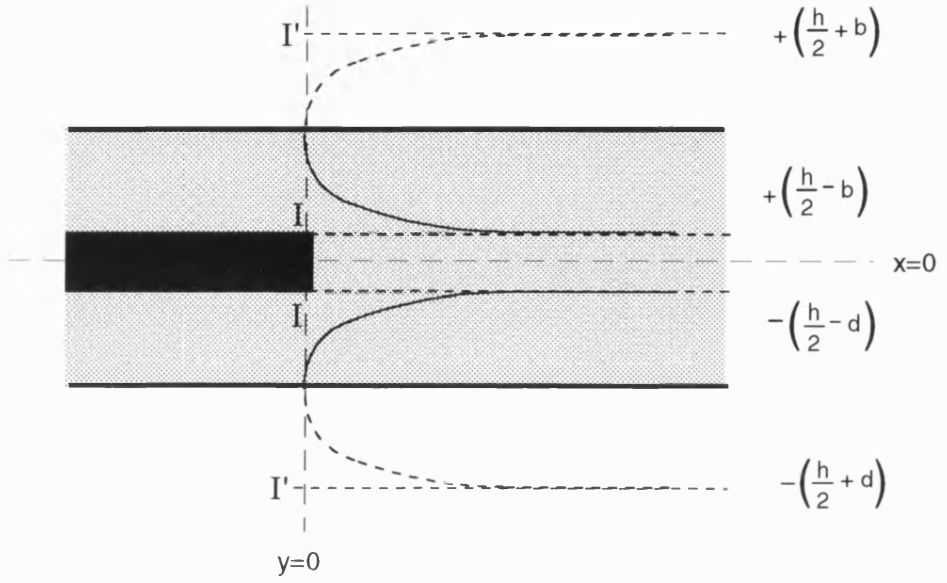

Figure C.1: Formulation of Weight Functions for the Problem

The weight functions are required in the form:

$$W(x,\nu) = (1-x^2)^{\nu} \tag{C.1}$$

The weight function is of the form, $W(x,\nu) = \mid r_1 \mid^{\nu} \mid r_2 \mid^{\nu}$, where r is the distance from the singularities, for the singularities at $y = -(\frac{s}{2})$ and $y = -(\frac{s}{2} + w_1)$

$$W(x,\nu) = \left|\left(\frac{h}{2} + b_1\right) - x\right|^{\nu} \left|\left(\frac{h}{2} - b_1\right) - x\right|^{\nu} \tag{C.2}$$

Rearranging and considering the remainder of the singularities, the weight functions

for the strips can be written down by inspection as:

$$W(x,\nu) = b_i^{2\nu}\left[1-\left(\frac{x-\frac{h}{2}}{b_i}\right)^2\right]^{\nu} \qquad x > \left(\frac{h}{2}-\left(b_i+\frac{t_i}{2}\right)\right) \quad \text{(C.3)}$$

$$= d_i^{2\nu}\left[1-\left(\frac{x+\frac{h}{2}}{d_i}\right)^2\right]^{\nu} \qquad x < \left(\frac{h}{2}-\left(b_i+\frac{t_i}{2}\right)\right) \quad \text{(C.4)}$$

Orthonormalisation Coefficient

In order to maintain the correct field scaling the basis functions are orthonormalised such that:

$$A_p^2\int_{-\infty}^{+\infty} W(x,\nu)\left[C_p^{\nu}(x)\right]^2 dx = 1 \quad \text{(C.5)}$$

Stating a standard result from [77]:

$$\int_{-1}^{+1}(1-x^2)^{\nu-\frac{1}{2}}\left[C_p^{\nu}(x)\right]^2 dx = \frac{\pi\, 2^{1-2\nu}\,\Gamma(p+2\nu)}{p!\,(p+\nu)[\Gamma(\nu)]^2} \quad \text{(C.6)}$$

$$Re(\nu) > -\frac{1}{2}$$

Using a variable substitution, Equation C.6 can be rewritten:

$$\int_{-(\frac{h}{2}+d_i)}^{-(\frac{h}{2}-d_i)}\left[1-\left(\frac{x+\frac{h}{2}}{d_i}\right)^2\right]^{\nu-\frac{1}{2}}\left[C_p^{\nu}\left(\frac{x+\frac{h}{2}}{d_i}\right)\right]^2\frac{dx}{d_i} = \frac{\pi\, 2^{1-2\nu}\,\Gamma(p+2\nu)}{p!\,(p+\nu)[\Gamma(\nu)]^2} \quad \text{(C.7)}$$

Substituting an expression for $W(x,\nu)$ into Equation C.5 and evaluating for a sub-region, i, $x < (\frac{h}{2}-(b_i+\frac{t_i}{2}))$:

$$A_p^2\int_{-(\frac{h}{2}+d_i)}^{-(\frac{h}{2})} d_i^{2\nu}\left[1-\left(\frac{x+\frac{h}{2}}{d_i}\right)^2\right]^{\nu}\left[C_p^{\nu+\frac{1}{2}}\left(\frac{x+\frac{h}{2}}{d_i}\right)\right]^2 dx = 1 \quad \text{(C.8)}$$

Hence,

$$A_p^2\frac{d_i^{2\nu+1}}{2}\frac{\pi\, 2^{-2\nu}\,\Gamma(p+2\nu+1)}{p!\,(p+\nu+\frac{1}{2})[\Gamma(\nu+\frac{1}{2})]^2} = 1 \quad \text{(C.9)}$$

Rearranging in terms of the orthonormalisation coefficient, A_p for the sub-regions $x < (\frac{h}{2} - (b_i + \frac{t_i}{2}))$:

$$A_p^{R_i} = d_i^{-(1+2\nu)} \left[\frac{p!\,(p+\nu+\frac{1}{2})\,[\Gamma(\nu+\frac{1}{2})]^2}{\pi\, 2^{-(1+2\nu)}\,\Gamma(p+2\nu+1)} \right]^{-\frac{1}{2}} \tag{C.10}$$

Similarly for the sub-regions $x > (\frac{h}{2} - (b_i + \frac{t_i}{2}))$:

$$A_p^{R_i} = b_i^{-(1+2\nu)} \left[\frac{p!\,(p+\nu+\frac{1}{2})\,[\Gamma(\nu+\frac{1}{2})]^2}{\pi\, 2^{-(1+2\nu)}\,\Gamma(p+2\nu+1)} \right]^{-\frac{1}{2}} \tag{C.11}$$

C.2 Derivation of Inner Products

Recalling the definition of the inner products required to evaluate the TRD Admittance Matrix Equation, and rewriting for sub-region, i:

$$P_{pn} = < \phi_{h,e}(n,x)\ ;\ f_p(x) > \tag{C.12}$$

$$= \int_{-\infty}^{+\infty} \phi_{h,e}(n,x)\, f_p(x) \tag{C.13}$$

$$= A_p\, A_n^{R_i} \int_{-\infty}^{+\infty} W(x,\nu)\, C_p^{\nu}(x)\, \mathrm{Cos}\, k_x^{R_i}(x-\psi_i)\, dx \qquad \text{TE Modes} \tag{C.14}$$

$$= A_p\, A_n^{R_i} \int_{-\infty}^{+\infty} W(x,\nu)\, C_p^{\nu}(x)\, \frac{\mathrm{Sin}\, k_x^{R_i}(x-\psi_i)}{n^2}\, dx \qquad \text{TM Modes} \tag{C.15}$$

Stating two standard results from [77]:

$$\int_0^{+1} (1-x^2)^{\nu-\frac{1}{2}}\, C_{2p}^{\nu}(x)\, \mathrm{Cos}\, \varrho x\, dx = \frac{(-1)^p\, \Gamma(2p+2\nu)\, \pi}{(2p)!\, \Gamma(\nu)\, (2\varrho)^{\nu}}\, J_{2p+\nu}(\varrho) \tag{C.16}$$

$$\int_0^{+1} (1-x^2)^{\nu-\frac{1}{2}}\, C_{2p+1}^{\nu}(x)\, \mathrm{Sin}\, \varrho x\, dx = \frac{(-1)^p\, \Gamma(2p+2\nu+1)\, \pi}{(2p+1)!\, \Gamma(\nu)\, (2\varrho)^{\nu}}\, J_{2p+1+\nu}(\varrho) \tag{C.17}$$

$$\varrho > 0,\ Re\,\nu > -\frac{1}{2}$$

Considering the expression for the TE modes first, and substituting for the weight function, and undertaking a variable substitution in Equation C.16:

$$\int_{-(\frac{h}{2})}^{-(\frac{h}{2}-d_i)} \left[1-\left(\frac{x+\frac{h}{2}}{d_i}\right)^2\right]^{\nu-\frac{1}{2}} C_{2p}^{\nu}\left(\frac{x+\frac{h}{2}}{d_i}\right) \mathrm{Cos}\varrho\left(\frac{x+\frac{h}{2}}{d_i}\right)\frac{dx}{d_i}$$

$$= \frac{\pi\,(-1)^p, \Gamma(2p+2\nu)}{(2p)!\,\Gamma(\nu)\,(2\varrho)^{\nu}} J_{2p+\nu}(\varrho) \qquad \text{(C.18)}$$

Substituting Equation C.18 into the expression for the inner product,

$$P_{pn}^{R_i} = A_{2p}A_n^{R_i}\int_{-(\frac{h}{2})}^{-(\frac{h}{2}-d_i)} d_i^{2\nu}\left[1-\left(\frac{x+\frac{h}{2}}{d_i}\right)^2\right]^{\nu} C_{2p}^{\nu+\frac{1}{2}}\left(\frac{x+\frac{h}{2}}{d_i}\right)\mathrm{Cos}\,k_x^{R_i}\left(x+\frac{h}{2}\right)dx \qquad \text{(C.19)}$$

$$= A_{2p}A_n^{R_i}\,d_i^{1+2\nu}\frac{\pi\,(-1)^p\,\Gamma(2p+2\nu+1)}{(2p)!\,\Gamma(\nu+\frac{1}{2})\,(2k_x^{R_i}d_i)^{\nu}} J_{2p+\nu+\frac{1}{2}}\left(k_x^{R_i}d_i\right) \qquad \text{(C.20)}$$

The inner product for the sub-regions, $x > (\frac{h}{2} - (b_i + \frac{t_i}{2}))$ are given by:

$$P_{pn} = A_{2p}A_n^{R_i}\,b_i^{1+2\nu}\frac{\pi\,(-1)^p\,\Gamma(2p+2\nu+1)}{(2p)!\,\Gamma(\nu+\frac{1}{2})\,(2k_x^{R_i}b_i)^{\nu}} J_{2p+\nu+\frac{1}{2}}(k_x^{R_i}b_i) \qquad \text{(C.21)}$$

The corresponding expressions for TM modes are:

$$P_{pn} = A_{2p+1}A_n^{R_i}\,b_i^{1+2\nu}\frac{\pi\,(-1)^p\,\Gamma(2p+2\nu+2)}{(2p+1)!\,\Gamma(\nu+\frac{1}{2})\,(2k_x^{R_i}b_i)^{\nu}} J_{2p+\nu+\frac{3}{2}}(k_x^{R_i}b_i) \qquad \text{(C.22)}$$

$$x > \left(\frac{h}{2} - \left(b_i + \frac{t_i}{2}\right)\right)$$

$$= A_{2p+1}A_n^{R_i}\,d_i^{1+2\nu}\frac{\pi\,(-1)^p\,\Gamma(2p+2\nu+2)}{(2p+1)!\,\Gamma(\nu+\frac{1}{2})\,(2k_x^{R_i}d_i)^{\nu}} J_{2p+\nu+\frac{3}{2}}(k_x^{R_i}d_i) \qquad \text{(C.23)}$$

$$x < \left(\frac{h}{2} - \left(b_i + \frac{t_i}{2}\right)\right)$$

Appendix D

Derivation of Voltage, Current, Power Flow and Dissipation Terms

D.1 Derivation of Voltage Terms

The voltage between two conductors is determined from the equation:

$$V = \int \underline{e_{tk}}\, \underline{dl} \tag{D.1}$$

In the case of the stripline structures, the voltage exists between the stripline and ground plane. The chosen path of integration is in the $\hat{x}$ direction thus:

$$V = \int_x e_{xk}(x, y)\, dx \tag{D.2}$$

The form of the $e_{xk}(x, y)$ field, set by the boundary conditions (Appendix B) gives the voltage:

$$V = \left[E_{xo}\psi_i + \sum_{n=1}^{n=N} E_{xn}\ \mathrm{Sin}(n\pi) \right]\ \partial_y \phi_{h,e}(n, y) \tag{D.3}$$

$$V = E_{xo}\psi_i \qquad \text{for TEM Mode} \qquad \text{(D.4)}$$

D.2 Derivation of Current Terms

The current flowing around a conductor is determined from Ampere's Law:

$$I = \oint \underline{h_k}\ \underline{dl} \qquad \text{(D.5)}$$

Figure D.1 shows the contributions for a single strip, and the path of integration used. For the coupled stripline structure the current contributions are evaluated as:

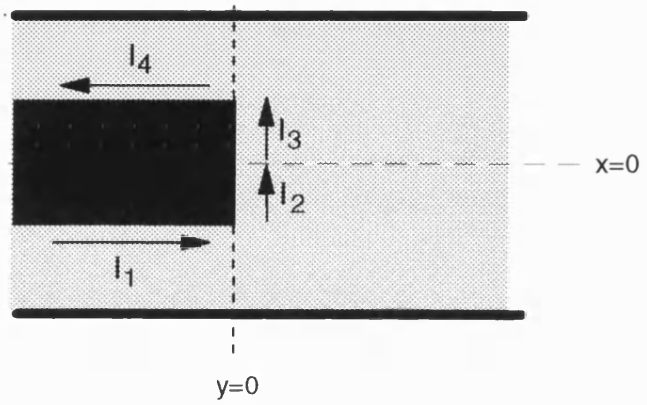

Figure D.1: Integration Contributions for the Current Integral

$$\begin{aligned} I_{2,3} &= \int h_{xk}(x, y_o)\, dx \\ &= \frac{\beta_k}{\omega\mu_o} \sum_{n=0}^{n=N} A_n^{R_i}\ V_{xkn}^{R_i}\ \frac{1}{jk_y^{R_i}} \left[\frac{(1-\rho) - (\text{Exp}\ [jk_y^{R_i} w_i]\ -\ \rho\ \text{Exp}\ [-jk_y^{R_i} w_i])}{\text{Exp}\ [-jk_y^{R_i} w_i]\ +\ \rho\ \text{Exp}\ [jk_y^{R_i} w_i]} \right] \end{aligned} \qquad \text{(D.6)}$$

$$\begin{aligned} I_{1,4} &= \int h_{yk}(x_o, y)\, dy \\ &= \frac{\beta_k}{\omega\mu_o} \sum_{n=0}^{n=N} A_n^{R_i}\ V_{xkn}^{R_i}\ \frac{1}{jk_y^{R_i}} \left[\text{Cos}\ k_x^{R_i}\psi_i\ -\ \text{Cos}\ n\pi\right] \end{aligned} \qquad \text{(D.7)}$$

where the constant ψ_i is defined:

$$\psi_i = \begin{cases} b_i & x > \left(\frac{h}{2} - b_i\right) \\ d_i & x < \left(\frac{h}{2} - b_i\right) \end{cases} \tag{D.8}$$

D.3 Derivation of Power Flow Terms

The power flow is a structure is given by the Poynting Vector, hence the $\hat{z}$ directed power flow is given by:

$$S_z = \int_{CrossSection} \underline{e_{tk}} \wedge \underline{h^*_{tk}} \; \underline{da} \tag{D.9}$$

Noting the relationships for the fields defined in Chapter 3 and Appendix B:

$$S_z = \frac{\beta_k}{\omega\mu_o} \int_{CrossSection} \mid e_{xk}(x,y) \mid^2 + \mid e_{yk}(x,y) \mid^2 \; \underline{da} \tag{D.10}$$

Evaluating the above integral for the subregions, the expressions for the power flow are derived as:

$$S_z^{R_i} = \frac{1}{4}\left(\frac{\beta_k}{\omega\mu_o}\right) \sum_{n=1}^{n=N} \left[A_n^{R_i}\right]^2 V_{xkn}^{R_i} \; \frac{\psi_i + \frac{t_i}{2}}{k_y^{R_i}} \left[1 - \left(\frac{k_x^{R_i}}{k_y^{R_i}}\right)^2\right] \tag{D.11}$$

Regions I, III and V

$$S_z^{R_i} = \frac{1}{4}\left(\frac{\beta_k}{\omega\mu_o}\right) \sum_{n=0}^{n=N} \left[A_n^{R_i}\right]^2 V_{xkn}^{R_i} \; \frac{\psi_i}{2} \; \frac{1}{2jk_y^{R_i}} \left[1 - \left(\frac{k_x^{R_i}}{k_y^{R_i}}\right)^2\right] \times \left(\frac{1 - \rho^2}{(\mathrm{Exp}[jk_y^{R_i} w_i] + \rho \, \mathrm{Exp}[-jk_y^{R_i} w_i])^2} - \frac{\mathrm{Exp}[j2k_y^{R_i} w_i] - \rho^2 \, \mathrm{Exp}[-j2k_y^{R_i} w_i]}{(\mathrm{Exp}[jk_y^{R_i} w_i] + \rho \, \mathrm{Exp}[-jk_y^{R_i} w_i])^2}\right) \tag{D.12}$$

Regions II and IV

D.4 Derivation of Power Dissipation Terms

The power dissipation in the structure is derived from the equation:

$$P_{dis} = \frac{1}{2} R_s \int_{CrossSection} \left(\hat{n} \wedge \underline{h_{tk}}\right)^2 \; \underline{da} \tag{D.13}$$

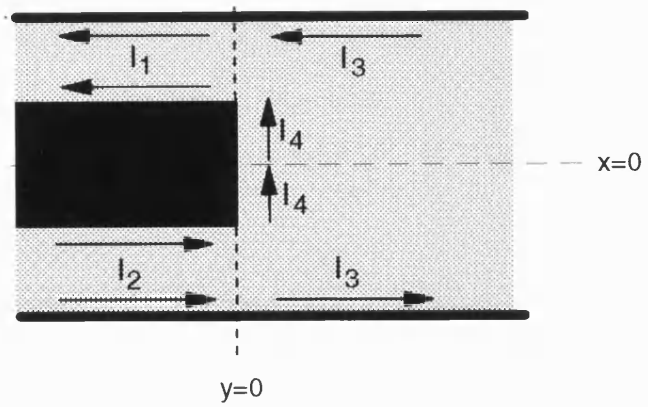

Figure D.2: Integration Contributions for the Power Dissipation Integral

There will be contributions to the integral from the strip and the two ground planes (Figure D.2). Substituting the expressions for the fields derived in Appendix B into Equation D.13:

$$P_{dis} = \frac{1}{2} R_s \left(\frac{\beta_k}{\omega \mu_o} \right)^2 \int_{Cross\underline{Section}} \underline{e_{tk}} \, \underline{e^*_{tk}} \, \underline{dl} \tag{D.14}$$

Evaluating the integrals for the sub-regions the terms defined in Figure D.2 are given by:

$$I_{1,2} = \left(\frac{\beta_k}{\omega \mu_o} \right)^2 R_s \sum_{n=0}^{n=N} \left[V_{xkn}^{R_i} \right]^2 \left[A_n^{R_i} \right]^2 \times \left(\frac{1 - \rho^2}{(\mathrm{Exp}[j k_y^{R_i} w_i] + \rho \, \mathrm{Exp}[-j k_y^{R_i} w_i])^2} - \frac{\mathrm{Exp}[j 2 k_y^{R_i} w_i] - \rho^2 \, \mathrm{Exp}[-j 2 k_y^{R_i} w_i]}{(\mathrm{Exp}[j k_y^{R_i} w_i] + \rho \, \mathrm{Exp}[-j k_y^{R_i} w_i])^2} \right) \tag{D.15}$$

$$I_3 = \left(\frac{\beta_k}{\omega \mu_o} \right)^2 R_s \sum_{n=0}^{n=N} \left[V_{xkn}^{R_i} \right]^2 \left[A_n^{R_i} \right]^2 \frac{1}{k_y^{R_i}} \tag{D.16}$$

$$I_4 = \left(\frac{\beta_k}{\omega \mu_o} \right)^2 R_s \sum_{n=0}^{n=N} \left[V_{xkn}^{R_i} \right]^2 \left[A_n^{R_i} \right]^2 \left(\frac{k_x^{R_i}}{k_y^{R_i}} \right)^2 \left[\frac{t_i}{2} - \frac{\mathrm{Sin} \, k_x^{R_i} t_i}{k_x^{R_i}} \right] \tag{D.17}$$

Appendix E

Derivation of Orthonormalisation Coefficients and Inner Products for the Discontinuity Analysis

E.1 Evaluation of Orthonormalisation Coefficients

The expressions for the orthonormalisation coefficients are derived in general, and can be modified according to the discontinuity analysed.

The expression between the orthonormalisation coefficients and the cross section fields was stated in Equation 6.4:

$$\left[A_k^{A,B}\right]^2 \int_{CrossSection} \left[\sum_{n=0}^{n=\infty} U_{kn}\ u_k(n,x,y)\right]^2 d\underline{a} = 1 \qquad \text{(E.1)}$$

In practice, the integral is sub-divided into the sixteen sub-regions shown in Figure 3.1. The field shape that is denoted by $\sum U_{kn}\ u_k(n,x,y)$ corresponds to the $e_{xk}(x,y)$ fields derived in Chapter 3, and Appendix B.

Recalling the general form of the fields as:

$$e_{xk}^{R_i}(x,y) = \sum_{n=0}^{n=\infty} A_n^{R_i}\ V_{xkn}^{R_i}\ F_1(R_i,\psi)\ F_m(R_i,\psi) \tag{E.2}$$

rewriting the integral in terms of a summation of contributions from the sub-regions, R_i, as:

$$\left[A_k^{A,B}\right]^2 \sum_{i=1}^{i=16} \left[\sum_{n=0}^{n=\infty} \left(\frac{A_n^{R_i}\ V_{xkn}^{R_i}}{j\omega\mu_o}\right)^2 \int_x [F_1(R_i,\psi)]^2\ dx \int_y [F_{2,3,4}(R_i,\psi)]^2\ dy\right] = 1 \tag{E.3}$$

Evaluating the integrals for the functions, F_1 to F_4 (Equations B.54 to B.57)

$$\int_x [F_1(R_i,\psi)]^2\ dx = \int_x \left[\text{Cos } k_x^{R_i}(x-\psi)\right]^2\ dx = \frac{1}{2}\left[x + \frac{\text{Sin } [2k_x^{R_i}(x-\psi)]}{2k_x^{R_i}}\right]_x \tag{E.4}$$

$$\int_y [F_2(R_i,\psi)]^2\ dy = \int_y \left[\text{Exp } jk_y^{R_i}(y-\psi)\right]^2\ dy = \left[\frac{\text{Exp } [2jk_y^{R_i}(y-\psi)]}{2jk_y^{R_i}}\right]_y \tag{E.5}$$

$$\begin{aligned}\int_y [F_3(R_i,\psi)]^2\ dy &= \int_y \left[\frac{\text{Exp } [jk_y^{R_i}(y-\psi)] + \rho\ \text{Exp } [-jk_y^{R_i}(y-\psi)]}{\text{Exp } [-jk_y^{R_i}\psi] + \rho\ \text{Exp } [jk_y^{R_i}\psi]}\right]^2 dy \\ &= \left[\frac{(1-\rho^2)}{2jk_y^{R_i}\ [C_\psi^{R_i}]^2} - \frac{\text{Exp}[2jk_y^{R_i}\psi]\ +\ \rho^2\text{Exp}[-2jk_y^{R_i}\psi]}{2jk_y^{R_i}\ [C_\psi^{R_i}]^2} + \frac{2\rho\psi}{[C_\psi^{R_i}]^2}\right]_y\end{aligned} \tag{E.6}$$

$$\int_y [F_4(R_i,\psi)]^2\ dy = \left[\frac{(1-\rho^2)}{2jk_y^{R_i}\ [C_{-\psi}^{R_i}]^2} - \frac{\text{Exp}[2jk_y^{R_i}\psi]\ +\ \rho^2\text{Exp}[-2jk_y^{R_i}\psi]}{2jk_y^{R_i}\ [C_{-\psi}^{R_i}]^2} + \frac{2\rho\psi}{[C_{-\psi}^{R_i}]^2}\right]_y \tag{E.7}$$

where the constant, $C_\psi^{R_i}$, is given by:

$$C_\psi^{R_i} = \text{Exp } [-jk_y^{R_i}\psi] + \rho\ \text{Exp } [jk_y^{R_i}\psi] \tag{E.8}$$

The orthonormalisation coefficient is found by evaluating Equation E.3 using the results of the above integrals for the appropriate sub-regions. The orthonormalisation coefficient cannot be expressed analytically due to its complexity hence the value is found numerically.

E.2 Evaluation of Inner Product Terms

The evaluation of the amplitude terms X_{pk} (Equation 6.45) require that a set of inner product terms are calculated, which are of the form:

$$X_{pk} = \sum_{n=0}^{n=\infty} U_{kn} P_{pn} \tag{E.9}$$

Separating the $\hat{x}$ and $\hat{y}$ variations of the field shape function, the inner product, P_{pn}, that is required is given by:

$$P_{pn} = \int_x u_k(n,x) f_p(x)\, dx \int_y u_k(n,y) f_p(y)\, dy \tag{E.10}$$

$$= P_{pn(x)} P_{pn(y)} \tag{E.11}$$

The inner products are evaluated using Chebyshev polynomials for the $\hat{x}$ directed dependence, and generalised Laguerre polynomials, Jacobi polynomials and Gegenbauer Polynomials for the $\hat{y}$ dependence. The $\hat{x}$ directed inner products with Gegenbauer polynomials can be derived from the corresponding $\hat{y}$ directed inner products.

E.2.1 $\hat{x}$ Directed Inner Product with Chebyshev Polynomials

The inner product with Chebyshev polynomials is only encountered in the $\hat{x}$ direction of the problem, hence the derivation is carried out for the $F_1(R_i, \psi)$ field shape function.

Substituting the general form of the basis function into Equation E.10 and recalling the form of the $\hat{x}$ directed field from Equations E.2 and E.4:

$$P_{pn(x)} = \int_x A_p\, W(x,\nu)\, f_p(x)\, F_1(R_i,\psi) dx \tag{E.12}$$

Using the $\hat{x}$ dependence of the field shape, the singularity behaviour of the field and the weight functions derived in Appendix C for $x > (\frac{h}{2} - b_i)$, the inner product is given by:

$$P_{pn(x)} = \int_x A_p b_i^{-1} \left[1 - \left(\frac{x-\psi}{b_i}\right)^2\right]^{-\frac{1}{2}} T_p\left(\frac{x-\psi}{b_i}\right) \text{Cos}\, k_x^{R_i}(x-\psi)\, dx \tag{E.13}$$

Stating a standard result from [77]:

$$\int_0^1 (1-x^2)^{-\frac{1}{2}}\ T_n(x)\ \mathrm{Cos}\ \varrho x\ dx = (-1)^n \left[\frac{\pi}{2}\right]\ J_{2n}(\varrho) \tag{E.14}$$

Undertaking a variable substitution into the equation above:

$$\int_{\psi}^{\psi+b_i} \left[1-\left(\frac{x-\psi}{b_i}\right)^2\right]^{-\frac{1}{2}}\ T_p\left(\frac{x-\psi}{b_i}\right)\ \mathrm{Cos}\varrho\left(\frac{x-\psi}{b_i}\right)\ dx = (-1)^p \left[\frac{\pi}{2}\right]\ J_{2p}(\varrho) \tag{E.15}$$

Rearranging Equations E.13 and E.15, the inner product is found for $x > (\frac{h}{2} - b_i)$ and the corresponding expression for $x < (\frac{h}{2} - b_i)$ written down by inspection:

$$P_{pn(x)} = A_{2p}\ (-1)^p \left[\frac{\pi}{2}\right]\ J_{2p}(b_i k_x^{R_i}) \qquad x > \left(\frac{h}{2} - b_i\right) \tag{E.16}$$

$$= A_{2p}\ (-1)^p \left[\frac{\pi}{2}\right]\ J_{2p}(d_i k_x^{R_i}) \qquad x < \left(\frac{h}{2} - b_i\right) \tag{E.17}$$

The orthonormalisation coefficient of the basis function, A_p, is found from the relation:

$$A_p^2 \int_{\psi}^{\psi+b_i} (b_i)^{-1} \left[1-\left(\frac{x-\psi}{b_i}\right)^2\right]^{-\frac{1}{2}} \left[T_p\left(\frac{x-\psi}{b_i}\right)\right]^2\ dx = 1 \tag{E.18}$$

Again quoting a result from [77]:

$$\int_{-1}^{+1} (1-x^2)^{-\frac{1}{2}}\ [T_n(x)]^2\ dx = \begin{cases} \frac{\pi}{2} & n \neq 0 \\ \pi & n = 0 \end{cases} \tag{E.19}$$

Hence by variable substitution and rearranging:

$$A_p = 2\sqrt{\frac{2}{\pi}}\delta_p \qquad \delta_p = \begin{cases} \frac{1}{2} & p = 0 \\ \frac{1}{\sqrt{2}} & p \neq 0 \end{cases} \tag{E.20}$$

E.2.2 $\hat{y}$ Directed Inner Product with Laguerre Polynomials

The $\hat{y}$ directed inner product is evaluated for the generalised Laguerre polynomials, for Regions I and V, and Jacobi and Gegenbauer polynomials for Regions II, III, and IV.

Substituting the form of the Laguerre polynomial with the expression for the inner

products (Equation E.10):

$$P_{pn(y)} = \int_y A_p \; W(y,\nu) \; f_p(y) \; F_2(R_i,\psi) \; dy \tag{E.21}$$

Using the appropriate field shape and weight function for the region the inner product is given by:

$$P_{pn(y)} = \int_\psi^\infty A_p \left(\frac{y-\psi}{\Psi}\right)^\nu \text{Exp} \left[-\left(\frac{y-\psi}{\Psi}\right)\right] \; L_p^\nu \left(\frac{y-\psi}{\Psi}\right) \; \text{Exp} \; \left[-jk_y^{R_i}(y-\psi)\right] \; dy \tag{E.22}$$

where the constant, Ψ is introduced to aid convergence of the approximation. The calculation of this parameter will be discussed later in this section.

The inner product is evaluated in terms of trigonometrical functions, with standard results quoted from [77]:

$$\int_0^\infty x^{\chi-2p-1}\text{Exp} \; [-(\varphi x)] \; L_{2p}^{\chi-2p-1}(\varphi x) \; \text{Cos} \; \vartheta x \; dx$$

$$= (-1)^p \Gamma(\chi) \vartheta^{2p} \frac{[(\varphi + j\vartheta)^{-\chi} + (\varphi - j\vartheta)^{-\chi}]}{2(2p)!} \tag{E.23}$$

$$\int_0^\infty x^{\chi-2p-1}\text{Exp} \; [-(\varphi x)] \; L_{2p}^{\chi-2p-1}(\varphi x) \; \text{Sin} \; \vartheta x \; dx$$

$$= (-1)^p \; j \; \Gamma(\chi) \vartheta^{2p} \frac{[(\varphi - j\vartheta)^{-\chi} - (\varphi + j\vartheta)^{-\chi}]}{2(2p)!} \tag{E.24}$$

$$Re \; \varphi > 0, \; \vartheta > 0, \; Re \; \chi > 2p$$

The results in the equations above can be combined to evaluate the integral:

$$\int_0^\infty x^{\chi-2p-1}\text{Exp} \; [-(\varphi - j\vartheta)x] \; L_{2p}^{\chi-2p-1}(\varphi x) \; dx = (-1)^p \frac{\Gamma(\chi)\vartheta^{2p}}{(2p)!}[(\varphi - j\vartheta)^{-\chi}]$$

$$Re \; \varphi > 0, \; \vartheta > 0, \; Re \; \chi > 2p \tag{E.25}$$

Taking Equation E.25 and performing a variable substitution, the left hand side of the equation is transformed to:

$$\int_\psi^\infty \left(\frac{y-\psi}{\Psi}\right)^{\chi-2p-1} \text{Exp} \; \left[[\varphi - j\vartheta]\left(\frac{y-\psi}{\Psi}\right)\right] \; L_{2p}^{\chi-2p-1}\left[\varphi\left(\frac{y-\psi}{\Psi}\right)\right] \; \frac{dy}{\Psi} \tag{E.26}$$

Equating coefficients in the above equation with those in Equation E.22:

$$\begin{aligned} \varphi &= 1 \\ \vartheta &= -\Psi k_y^{R_i} \\ \chi &= \nu + 2p + 1 \end{aligned}$$

The inner product is therefore given by Equation E.27:

$$P_{pn(y)} = A_{2p}\Psi(-1)^p \frac{\Gamma(\nu+2p+1)}{(2p)!}\left[\frac{(\Psi k_y^{R_i})^{2p}}{(1+jk_y^{R_i})^{\nu+2p+1}}\right] \tag{E.27}$$

The orthonormalisation coefficient for the Laguerre polynomials is given by the relationship:

$$A_p^2 \int_0^\infty \left(\frac{y-\psi}{\Psi}\right)^\nu \text{Exp}\left[-\left(\frac{y-\psi}{\Psi}\right)\right]\left[L_p^\nu\left(\frac{y-\psi}{\Psi}\right)\right]^2 dy = 1 \tag{E.28}$$

Again from a result in [77]:

$$A_p^2 \int_0^\infty \text{Exp}(-x)\, x^\nu\, [L_p^\nu(x)]^2\, dx = \frac{\Gamma(\nu+p+1)}{p!} \tag{E.29}$$

Hence the orthonormalisation coefficient is obtained by variable substitution and found as:

$$A_p = \left[\Psi\, \frac{\Gamma(\nu+p+1)}{p!}\right]^{-\frac{1}{2}} \tag{E.30}$$

The constant, Ψ, improves the convergence of the approximation used to discretise the field, and is determined by minimising the error function [73]:

$$f_{err} = \sum_{k=1}^{k=K}\left(||< F_2(R_i,\psi); F_2(R_i,\psi) >||^2 - \sum_{p=1}^{p=P} ||< F_2(R_i,\psi); f_p(y) >||^2\right) \tag{E.31}$$

In effect the minimisation of the above function is equivalent to minimising the mean square error between the field shape and the approximation.

Evaluating the inner product, $< F_2(R_i,\psi); F_2(R_i,\psi) >$ and using the previously derived expression for the $\hat{y}$ directed inner product, the error function can be expressed

as:

$$f_{err} = -\sum_{k=1}^{k=K}\sum_{n=1}^{n=N}\left[\frac{1}{4[k_y^{R_i}]^2} + \Psi^2 \sum_{p=0}^{p=P} A_p^2 \frac{[\Gamma(\nu+2p+1)]^2}{[(2p)!]^2}\left(\frac{(\Psi k_y^{R_i})^{2p}}{(1+jk_y^{R_i})^{\nu+2p+1}}\right)^2\right] \tag{E.32}$$

The minimisation is carried out numerically using an interval halving technique as described in Chapter 3.

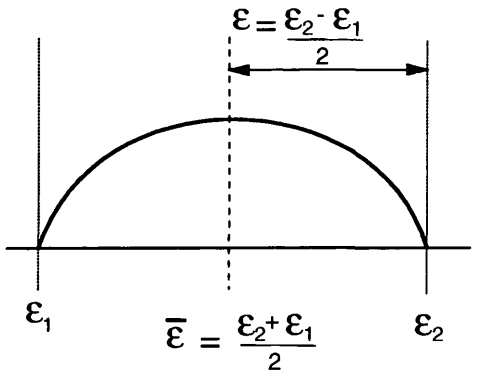

Figure E.1: Definition of the Constants used in the Derivation of the $\hat{y}$ Directed Inner Product with Jacobi Polynomials

E.2.3 $\hat{y}$ Directed Inner Product with Jacobi Polynomials

The field in Regions II to IV are expressed in terms of Jacobi polynomials which model the field behaviour with different field singularities at the ends of the basis functions. Recalling the form of the $\hat{y}$ directed inner products in terms of the basis functions and field shapes.

$$P_{pn(y)} = \int_y A_p \, W(y,\nu,\eta) \, f_p(y) \, F_3(R_i,\psi) \, dy \tag{E.33}$$

Substituting the form of the field shape function (Equation E.6), and the general function (Figure E.1) into Equation E.33:

$$P_{pn(y)} = \int_y A_p \, \varepsilon^{\nu} \, \varepsilon^{\eta} \left[1 - \left(\frac{y-\overline{\varepsilon}}{\varepsilon}\right)\right]^{\nu} \left[1 - \left(\frac{y-\overline{\varepsilon}}{\varepsilon}\right)\right]^{\eta} P_p^{\nu,\eta}\left(\frac{y-\overline{\varepsilon}}{\varepsilon}\right) \left[\frac{\text{Exp } [jk_y^{R_i}(y-\psi)] + \rho\text{Exp } [-jk_y^{R_i}(y-\psi)]}{C_{\psi}^{R_i}}\right] dy \quad \text{(E.34)}$$

The inner product is evaluated by first considering a binomial expansion of the exponential function in terms of $[1+y]$:

$$\text{Exp } j\varphi y = \text{Exp } (-j\varphi) \text{ Exp}(j\varphi[1+y]) \quad \text{(E.35)}$$

$$= \text{Exp } (-j\varphi) \left[\sum_{i=0}^{i=\infty} \frac{(j\varphi)^i}{(i)!}[1+y]^i\right] \quad \text{(E.36)}$$

Using a previously derived result from [77]:

$$\int_{-1}^{+1} (1-x)^{\nu}(1+x)^{\eta+i} P_n^{\nu,\eta}(x)\, dx = 2^{\nu+\eta+i+1} \frac{\Gamma(i+\eta+1)\Gamma(\nu+1)\Gamma(i+1)}{\Gamma(i+1-n)\Gamma(i+\nu+\eta+n+2)}$$
$$Re\ \nu > -1,\ Re\ \eta + i > -1 \quad \text{(E.37)}$$

The inner product in Equation E.34 can be evaluated by first considering the following integral:

$$I = \int_{-1}^{+1} (1-x)^{\nu}(1+x)^{\eta} P_p^{\nu,\eta}(x) \text{ Exp } [j\varphi x] \quad dx \quad \text{(E.38)}$$

Substituting the expression for the exponential into Equation E.38, and evaluating using Equation E.37:

$$I = \text{Exp } (-j\varphi) \sum_{i=0}^{i=\infty} \frac{(j\varphi)^i}{(i)!} \int_{-1}^{+1} (1-x)^{\nu}(1+x)^{\eta+i} P_p^{\nu,\eta}(x) \quad dx$$

$$= 2^{\nu+\eta+1} \text{ Exp } (-j\varphi) \sum_{i=0}^{i=\infty} \frac{\Gamma(i+\eta+1)\Gamma(\nu+1)\Gamma(i+1)}{\Gamma(i+1-n)\Gamma(i+\nu+\eta+n+2)} \frac{(2j\varphi)^i}{(i)!}$$

$$= 2^{\nu+\eta+1} \text{ Exp } (-j\varphi) \frac{\Gamma(\eta+1)\Gamma(\nu+1)\Gamma(1)}{\Gamma(1-n)\Gamma(\nu+\eta+n+2)}$$
$$ {}_2F_2[1+\eta, 1\ ;\ 1-n, \nu+\eta+2\ ;\ 2j\varphi] \quad \text{(E.39)}$$

where ${}_nF_m\ (a_n\ ;\ b_m\ ;\ z)$ denotes a hyper-geometrical function, and is defined as follows:

$$
\begin{aligned}
&{}_nF_m\left[a_{n-1}, a_{n-2}, \cdots, a_0\ ;\ b_{m-1}, b_{m-2}, \cdots, b_0\ ;\ z\right] = \\
&\quad \frac{\Gamma(b_{m-1})\Gamma(b_{m-2})\cdots\Gamma(b_0)}{\Gamma(a_{n-1}\Gamma(a_{n-2})\cdots\Gamma(a_0)} \sum_{i=0}^{i=\infty} \frac{\Gamma(i+a_{n-1}\Gamma(i+a_{n-2})\cdots\Gamma(i+a_0)}{\Gamma(i+b_{m-1})\Gamma(i+b_{m-2})\cdots\Gamma(i+b_0)} \ \frac{z^i}{i!}
\end{aligned}
\tag{E.40}
$$

Using a variable substitution the inner product in Equation E.34 can be evaluated by rewriting the integral, I:

$$
I = \int_{\bar{\varepsilon}-\varepsilon}^{\bar{\varepsilon}+\varepsilon} \left[1 - \left(\frac{y-\bar{\varepsilon}}{\varepsilon}\right)\right]^{\nu} \left[1 + \left(\frac{y-\bar{\varepsilon}}{\varepsilon}\right)\right]^{\eta} P_p^{\nu,\eta}\left(\frac{y-\bar{\varepsilon}}{\varepsilon}\right)\ \text{Exp}\ \left[j\varphi\left(\frac{y-\bar{\varepsilon}}{\varepsilon}\right)\right] \frac{dy}{\varepsilon}
\tag{E.41}
$$

Recalling the form of Equation E.34 for the inner product, $P_{pn(y)}$, and rearranging in terms of the integral, I:

$$
P_{pn(y)} = A_p\ [I]\ \varepsilon^{1+\nu+\eta} \left[\frac{\text{Exp}\ \left[-jk_y^{R_i}\psi + j\varphi\frac{\bar{\varepsilon}}{\varepsilon}\right] + \rho\text{Exp}\ \left[-\left(-jk_y^{R_i}\psi + j\varphi\frac{\bar{\varepsilon}}{\varepsilon}\right)\right]}{C_\psi^{R_i}}\right]\Bigg|_{\varphi=k_y^{R_i}\varepsilon}
\tag{E.42}
$$

Therefore, evaluating the above expression using Equation E.39, the inner product is found as:

$$
\begin{aligned}
P_{pn(y)} \quad = \quad & A_p\ 2^{\nu+\eta+1}\ \frac{\Gamma(\eta+1)\Gamma(1)\Gamma(\nu+1)}{\Gamma(1-p)\Gamma(\nu+\eta+p+2)} \\
& {}_2F_2[1+\eta, 1\ ;\ 1-p, \nu+\eta+p+2\ ;\ 2jk_y^{R_i}\varepsilon] \\
& \left[\frac{\text{Exp}\ \left[jk_y^{R_i}(\bar{\varepsilon}-\psi)\right] + \rho\ \text{Exp}\ \left[-jk_y^{R_i}(\bar{\varepsilon}-\psi)\right]}{C_\psi^{R_i}}\right]
\end{aligned}
\tag{E.43}
$$

The orthonormalisation coefficient for the Jacobi polynomials, A_p is determined from the condition:

$$
[A_p]^2 \int_{\bar{\varepsilon}-\varepsilon}^{\bar{\varepsilon}+\varepsilon} \varepsilon^{\nu+\eta}\ \left[1 - \left(\frac{y-\bar{\varepsilon}}{\varepsilon}\right)\right]^{\nu} \left[1 + \left(\frac{y-\bar{\varepsilon}}{\varepsilon}\right)\right]^{\eta} \left[P_p^{\nu,\eta}\left(\frac{y-\bar{\varepsilon}}{\varepsilon}\right)\right]^2 dy = 1
\tag{E.44}
$$

Using a result quoted from [77]:

$$
\int_{-1}^{+1} (1-x)^{\nu}\ (1+x)^{\eta}\ [P_n^{\nu,\eta}]^2\, dx = \frac{2^{1+\nu+\eta}\ \Gamma(\nu+n+1)\ \Gamma(\eta+n+1)}{n!\ (\nu+\eta+1+2n)\ \Gamma(\nu+\eta+n+1)}
$$
$$
Re\ \nu > -1,\ Re\ \eta > -1
\tag{E.45}
$$

Again performing a variable substitution, the orthonormalisation coefficient can be found as:

$$A_p = \left[\frac{(2\varepsilon)^{1+\nu+\eta}\ \Gamma(\nu+p+1)\Gamma(\eta+p+1)}{p!\ (\nu+\eta+1+2p)\ \Gamma(\nu+\eta+p+1)}\right]^{-\frac{1}{2}} \tag{E.46}$$

E.2.4 $\hat{y}$ Directed Inner Product with Gegenbauer Polynomials

The $\hat{y}$ directed inner products for Gegenbauer polynomials is given by the expression:

$$P_{pn(y)} = \int_y A_p\ \varepsilon^{\nu}\ \varepsilon^{\eta}\ \left[1-\left(\frac{y-\bar{\varepsilon}}{\varepsilon}\right)^2\right]^{\nu-\frac{1}{2}}\ C_p^{\nu}\left(\frac{y-\bar{\varepsilon}}{\varepsilon}\right) \left[\frac{\text{Exp}\ \left[jk_y^{R_i}(y-\psi)\right]+\rho\ \text{Exp}\ \left[-jk_y^{R_i}(y-\psi)\right]}{C_{\psi}^{R_i}}\right] dy \tag{E.47}$$

which can be evaluated from the standard result given in [77]:

$$\int_{-1}^{+1}(1-x^2)^{\nu-\frac{1}{2}}C_n^{\nu}(x)\ \text{Exp}\ [j\varphi x]\ dx = \left[j^n\frac{\pi 2^{1-\nu}\ \Gamma(2\nu+n)}{n!\ \Gamma(\nu)}\right]\varphi^{-\nu}\ J_{n+\nu}(\varphi) \qquad Re\ \nu > -\frac{1}{2} \tag{E.48}$$

Hence the inner product is given by:

$$P_{pn(y)} = A_p\ j^p\ \left[\frac{\pi 2^{1-\nu}\ \Gamma(2\nu+p)}{p!\ \Gamma(\nu)}\right]\left(k_y^{R_i}\varepsilon\right)^{-\nu}\ J_{p+\nu}\left(k_y^{R_i}\varepsilon\right) \left[\frac{\text{Exp}\ \left[jk_y^{R_i}\left(\bar{\varepsilon}-\psi\right)\right]+\rho\ \text{Exp}\ \left[-jk_y^{R_i}\left(\bar{\varepsilon}-\psi\right)\right]}{C_{\psi}^{R_i}}\right] \tag{E.49}$$

The orthonormalisation coefficient, A_p is derived in Appendix C.

References

[1] Silvester P. and Csendes Z.J. Numerical modeling of passive microwave devices. *IEEE Transactions on Microwave Theory and Techniques*, MTT-22:190–201, March 1974.

[2] Saad S.M. Review of numerical methods for the analysis of arbitrarily-shaped microwave and optical dielectric waveguides. *IEEE Transactions on Microwave Theory and Techniques*, MTT-33:894–899, October 1985.

[3] Sorrentino R. Numerical methods for passive components. In *IEEE MTT-S Digest*, volume 1, pages 619–622, 1988.

[4] Itoh T., editor. *Numerical Techniques for Microwave and Millimeter Wave Passive Structures.* Wiley, 1989.

[5] Brebbia C.A. and Ferrante A.J. *Computational Methods for the Solution of Engineering Problems.* Pentech Press, 1986.

[6] Brebbia C.A. *Boundary Element Method for Engineers.* Pentech Press, 1980.

[7] Plott C. EM design tool extends power of circuit simulators. *Microwaves and RF*, pages 217–220, May 1993.

[8] Bates R.H.T. The characteristic impedance of shielded slab line. *IEEE Transactions on Microwave Theory and Techniques*, MTT-4:28–33, January 1956.

[9] Ramo J. Whinnery J.R. and Van Duzer T. *Fields and Waves in Communications Engineering.* Wiley, 1984.

[10] Costamagna E. On the numerical inversion of the schwartz-christoffel conformal transformation. *IEEE Transactions on Microwave Theory and Techniques*, MTT-35:35–40, January 1987.

[11] Oliner A.A. Equivalent circuits for discontinuities in balanced strip transmission lines. *IEEE Transactions on Microwave Theory and Techniques*, MTT-3:134–143, March 1955.

[12] Baratt R.M. Microwave printed circuits - a historical survey. *IEEE Transactions on Microwave Theory and Techniques*, MTT-3:1–9, March 1955.

[13] Cohn S.B. Problems in strip transmission lines. *IEEE Transactions on Microwave Theory and Techniques*, MTT-3:119–126, March 1955.

[14] Cohn S.B. Characteristic impedance of shielded strip transmission line. *IEEE Transactions on Microwave Theory and Techniques*, MTT-2:52–57, July 1954.

[15] Wheeler H.A. Formulas for the skin effect. *Proceedings of the IRE*, 30:412–424, September 1942.

[16] Hilberg W. From approximations to exact relations for characteristic impedances. *IEEE Transactions on Microwave Theory and Techniques*, MTT-17:259–265, May 1969.

[17] Gunston M.A.R. *Microwave Transmission Line Impedance Data.* Van Nostrand Reinhold, 1972.

[18] Rawal S. and Jackson D.R. An exact TEM calculation of loss in a stripline of arbitrary dimensions. *IEEE Transactions on Microwave Theory and Techniques*, MTT-39:694–699, April 1991.

[19] Collin R.E. *Field Theory of Guided Waves.* Mc Graw-Hill, 1960.

[20] Richardson J.K. An approximate formula for calculating z_o of a symmetric stripline. *IEEE Transactions on Microwave Theory and Techniques*, MTT-15:130–131, February 1967.

[21] Chen T.S. Determination of the capacitance, inductance and characteristic impedance of rectangular lines. *IEEE Transactions on Microwave Theory and Techniques*, MTT-8:510–519, September 1960.

[22] Guckel H. Characteristic impedances of generalised rectangular stripline. *IEEE Transactions on Microwave Theory and Techniques*, MTT-13:270–274, May 1965.

[23] Wheeler H.A. Transmission line properties of a stripline between parallel planes. *IEEE Transactions on Microwave Theory and Techniques*, MTT-26:866–876, November 1978.

[24] Chang K. *Handbook of Microwave and Optical Components Volume 1 Microwave Passive and Antenna Components.* Wiley, 1989.

[25] Nauwelaers B. and Van De Capelle A. Characteristic impedance of stripline. *Electronics Letters*, 23:930–931, August 1987.

[26] Rao J.S. and Das B.N. Analysis of asymmetrical stripline by conformal mapping. *IEEE Transactions on Microwave Theory and Techniques*, MTT-27:299–303, April 1979.

[27] Chang .W.H. Analytical IC metal-line capacitance formulas. *IEEE Transactions on Microwave Theory and Techniques*, MTT-24:608–611, September 1976.

[28] Robrish P. An analytic algorithm for unbalanced stripline impedance. *IEEE Transactions on Microwave Theory and Techniques*, MTT-38:1011–1016, August 1990.

[29] Canright R. Comments on an analytic algorithm for unbalanced stripline impedance. *IEEE Transactions on Microwave Theory and Techniques*, MTT-40:177–179, January 1992.

[30] Costamagna E. and Fanni A. Comments on an analytic algorithm for unbalanced stripline impedance. *IEEE Transactions on Microwave Theory and Techniques*, MTT-41:173–174, January 1993.

[31] Gupta K.C. Garg R. and Chadha R., editors. *Computer Aided Design of Microwave Circuits.* Artech House, 1981.

[32] Rautio J.C. A precise benchmark for numerical validation. In *IEEE MTT-S Workshop Session WSMK*, volume 1, 1993.

[33] Green H.E. The numerical solution of some important transmission line problems. *IEEE Transactions on Microwave Theory and Techniques*, MTT-13:676–692, September 1965.

[34] Schneider M.V. Computation of impedance and attenuation of TEM lines by finite difference methods. *IEEE Transactions on Microwave Theory and Techniques*, MTT-13:793–800, November 1965.

[35] Metcalf W.S. Characteristic impedance of rectangular transmission lines. *Proceedings of the IEE*, 112:2033–2039, November 1965.

[36] Carson C.T. and Cambren G.K. Upper and lower bounds on the characteristic impedance of TEM mode transmission lines. *IEEE Transactions on Microwave Theory and Techniques*, MTT-14:497–498, October 1966.

[37] Pantic Z. and Mittra R. Quasi-TEM analysis of microwave transmission lines by the finite element method. *IEEE Transactions on Microwave Theory and Techniques*, MTT-34:1096–1103, November 1986.

[38] Costache G.I. Finite element method applied to skin-effect problems in strip transmission line. *IEEE Transactions on Microwave Theory and Techniques*, MTT-35:1009–1013, November 1987.

[39] Kiang J.F. Integral equation solution to the skin effect problem in conductor strips of finite thickness. *IEEE Transactions on Microwave Theory and Techniques*, MTT-39:452–460, March 1991.

[40] Dillon B.M. Gibson A.A.P. and Paul D.K. Finite element analysis of high power stripline for beamformers. In *Proceedings of the 1st International Conference on Computation in Electromagnetics*, volume 1, pages 10–13. IEE, 1991.

[41] Gibson A.A.P. Tsitsos S. and McCormick A.H. Numerical solutions of open wall stripline geometries. In *Proceedings of the 8th International Conference on Antennas and Propagation*, volume 1, pages 30–33. IEE, 1993.

[42] Cohn S.B. Shielded coupled-strip transmission line. *IEEE Transactions on Microwave Theory and Techniques*, MTT-3:29–38, October 1955.

[43] Getsinger W. Coupled rectangular bars between parallel plates. *IEEE Transactions on Microwave Theory and Techniques*, MTT-10:65–72, January 1962.

[44] Shelton J.P. Impedances of offset parallel-coupled strip transmission lines. *IEEE Transactions on Microwave Theory and Techniques*, MTT-14:7–15, January 1966.

[45] *EEsof Element Catalog Version 3.0*, October 1991.

[46] Cristal E.G. Coupled-transmission-line directional couplers with coupled lines of unequal characteristic impedances. *IEEE Transactions on Microwave Theory and Techniques*, MTT-14:337–346, July 1966.

[47] Tripathi V.K. Asymmetric coupled transmission lines in an inhomogeneous medium. *IEEE Transactions on Microwave Theory and Techniques*, MTT-23:734–739, September 1975.

[48] Linner L.J.P. A method for the computation of characteristic immittance matrix of multi-conductor striplines with arbitrary widths. *IEEE Transactions on Microwave Theory and Techniques*, MTT-22:930–937, November 1974.

[49] Bedair S.S. Characteristics of some asymmetrical coupled transmission lines. *IEEE Transactions on Microwave Theory and Techniques*, MTT-32:108–110, January 1984.

[50] Perlow S.M. Analysis of edge-coupled shielded strip and slabline structures. *IEEE Transactions on Microwave Theory and Techniques*, MTT-35:522–529, May 1987.

[51] Koul S.K. and Bhat B. Broadside, edge coupled, symmetric strip transmission lines. *IEEE Transactions on Microwave Theory and Techniques*, MTT-30:1874–1880, November 1982.

[52] Das B.N. and Prasad K.V.S.V.R. A general formulation of electromagnetically coupled striplines. *IEEE Transactions on Microwave Theory and Techniques*, MTT-32:1427–1433, November 1984.

[53] Kitazawa T. and Mittra R. Analysis of asymmetrical coupled striplines. *IEEE Transactions on Microwave Theory and Techniques*, MTT-33:643–646, July 1985.

[54] Medina F. and Horno M. Capacitance and inductance matrices for multistrip structures in multilayered anisotropic dielectrics. *IEEE Transactions on Microwave Theory and Techniques*, MTT-35:1002–1008, November 1987.

[55] Diaz R.E. The discrete variational conformal technique for the calculation of strip transmission line parameters. *IEEE Transactions on Microwave Theory and Techniques*, MTT-34:714–722, June 1986.

[56] Gupta R.R. Accurate impedance determination of coupled TEM conductors. *IEEE Transactions on Microwave Theory and Techniques*, MTT-17:479–489, August 1969.

[57] Edwards T.C. *Foundations for Microstrip Circuit Design.* Wiley, 1992.

[58] Altschuler H.M. and Oliner A.A. Discontinuities in the center conductor of symmetric strip transmission line. *IEEE Transactions on Microwave Theory and Techniques*, MTT-8:328–339, January 1960.

[59] Nalbandian V. and Steenaart W. Discontinuities in symmetric striplines due to impedance steps and their compensations. *IEEE Transactions on Microwave Theory and Techniques*, MTT-20:573–578, September 1972.

[60] Hedges S.J. and Rozzi T.E. Rigorous analysis and network modeling of the inset dielectric guide. *IEEE Transactions on Microwave Theory and Techniques*, MTT-35:823–834, September 1987.

[61] Boscovic D. Pennock S.R. and Rozzi T.E. Analysis of coupled inset dielectric guides under LSE and LSM polarisation. *IEEE Transactions on Microwave Theory and Techniques*, MTT-40:916–924, May 1992.

[62] Rozzi T.E. and De. Leo R. Rigorous analysis of the GTEM cell. *IEEE Transactions on Microwave Theory and Techniques*, MTT-39:488–499, March 1991.

[63] Rozzi T.E. Moglie F. Morini A. Politi M. and Marchionna E. Hybrid modes, substrate leakage and losses of slotline at millimeter-wave frequencies. *IEEE Transactions on Microwave Theory and Techniques*, MTT-38:1069–1078, August 1990.

[64] Rozzi T.E. Rigorous analysis of the step discontinuity in a planar dielectric waveguide. *IEEE Transactions on Microwave Theory and Techniques*, MTT-26:738–746, October 1978.

[65] Jones D.S. *Methods in Electromagnetic Wave Propagation Volume 1 Theory and Guided Waves.* Oxford University Press, 1987.

[66] *NAG FORTRAN Library Manual Mk14 Volume 5*, 1987.

[67] Rayna G. *REDUCE: Software for Algebraic Computation.* Springer-Verlag, 1987.

[68] Collin R.E. *Foundations for Microwave Engineering.* Mc Graw-Hill, 1966.

[69] Pennock S.R. Izzat N.and Rozzi T.E. Very wideband operation of twin layer inset dielectric guide. *IEEE Transactions on Microwave Theory and Techniques*, MTT-40:1910–1917, October 1992.

[70] Burchett M.H. Pennock S.R. and Shepherd P.R. A rigorous analysis of the higher order modes and attenuation of stripline of arbitrary dimensions. In *IEEE MTT-S Digest*, volume 3, pages 1451–1454, 1993.

[71] Marchetti S. and Rozzi T.E. Electric field singularities at sharp edges of planar conductors. *IEEE Transactions on Antennas and Propagation*, AP-39:1312–1320, September 1991.

[72] Abramowitz M. and Stegun I.A., editors. *Handbook of Mathematical Functions.* US Department of Commerce, 1965.

[73] Boskovic D. *Investigation of Coupled Line Structures in Inset Dielectric Guide.* PhD thesis, University of Bath, 1991.

[74] *HP85180A High Frequency Structure Simulator User's Reference Version A2.00 Edition I*, May 1992.

[75] Anger A. Software computes maxwell's equations. *Microwave Journal*, 2:170–178, February 1990.

[76] *HP85180A High Frequency Structure Simulator Release Notes Version A2.06*, April 1993.

[77] Gradshteyn I.S. and Rhyzhik I.M., editors. *Table of Integrals, Series and Products.* Academic Press, 1963.